Heterometallic MFU-4*large* Frameworks: Activation of Small Molecules and Catalytic Properties

Kumulative Dissertation

zur Erlangung des akademischen Grades
Dr. rer. nat.

Eingereicht an der
Mathematisch-Naturwissenschaftlich-Technischen Fakultät
der Universität Augsburg von

Dipl. Chem. Dmytro Denysenko

Augsburg, Oktober 2015

Erstgutachter:	Prof. Dr. Dirk Volkmer
Zweitgutachter:	Prof. Dr. Leo van Wüllen
Tag der mündlichen Prüfung:	11.12.2015

Für meine Familie und mein Land

Danksagung

Zuerst möchte ich mich bei Herrn Prof. Dirk Volkmer für die Betreuung der Arbeit, ein interessantes, abwechslungsreiches und fruchtbares Thema sowie für die große Freiheit in der Bearbeitung meiner Projekte bedanken.

Für die Übernahme des Zweitgutachtens möchte ich Herrn Prof. Leo van Wüllen danken.

Des Weiteren bedanke ich mich bei der Deutschen Forschungsgemeinschaft für die Finanzierung meiner Arbeit während der gesamten Promotionszeit.

Meinen beiden ehemaligen Kollegen aus der Universität Ulm, Dr. Shyam Biswas und Dr. Markus Tonigold, danke ich für die Einführung in das MOF Gebiet und Unterstützung meiner ersten Schritte in diesem für mich neuen Forschungsbereich.

Ein besonderer Dank gilt allen meinen Arbeitskollegen aus dem Lehrstuhl für Festkörperchemie. Meinen Laborkollegen Dr. Maciej Grzywa und Phillip Schmieder danke ich für eine entspannte Atmosphäre und eine immer ordentliche Laborhaltung. Dr. Björn Bredenkötter danke ich für die Hilfe bei allen organisatorischen Fragen. Andreas Kalytta-Mewes danke ich für die ständige Bereitschaft, bei allen technischen Angelegenheiten zu helfen. Silke Weigel danke ich für viele sorgfältige EDX-Messungen und ESEM-Aufnahmen. Peter Gross, Andreas Schaller, Sebastian Spirkl, Manuel Hambach und allen anderen Kollegen danke ich für viele unterhaltsame Feierabende.

Ebenfalls möchte ich mich bei unseren Projektpartnern aus München (Prof. Karsten Reuter und Dr. Jelena Jelic), Stuttgart (Dr. Michael Hirscher, Dr. Julia Teufel, Dr. Barbara Streppel, Dr. Hyunchul Oh, Ingrid Weinrauch, Dr. Robert Dinnebier, Dr. Oxana Magdysyuk) und Bremen (Prof. Thomas Heine und Ievgeniia Savchenko) für eine erfolgreiche und angenehme Zusammenarbeit bedanken. Auch unseren Kollegen aus dem Arbeitskreis von Prof. Alois Loidl (Dr. Peter Lunkenheimer, Pit Sippel und Jonas Fischer) danke ich für eine nette und gewinnbringende Kooperation.

Zu guter Letzt danke ich ganz herzlich meinen Eltern, meinem Bruder sowie allen meinen Freunden für die ständige mentale Unterstützung und Motivation auf meinem langen Bildungsweg.

Content

List of Abbreviations

BET	Brunauer-Emmett-Teller
DFT	Density Functional Theory
DMA	N,N-Dimethylacetamide
DMF	N,N-Dimethylformamide
DRIFT	Diffuse Reflectance Infrared Fourier Transform
EDX	Energy Dispersive X-Ray
FT-IR	Fourier Transform Infrared
GC/MS	Gas Chromatography / Mass Spectrometry
IUPAC	International Union of Pure and Applied Chemistry
MOF	Metal-Organic Framework
NHPI	N-Hydroxyphthalimide
Q_{st}	Isosteric Heat of Adsorption
SBU	Secondary Building Unit
SEM	Scanning Electron Microscopy
TGA	Thermogravimetric Analysis
TPO	Temperature-Programmed Oxidation
TPR	Temperature-Programmed Reduction
TPSR	Temperature-Programmed Surface Reaction
UV-vis-NIR	Ultraviolet-Visible-Near Infrared
VTXRPD	Variable-Temperature X-Ray Powder Diffraction
XRPD	X-Ray Powder Diffraction

1 Motivation

Heterogeneous catalysis plays a crucial role in chemical and petroleum industry and is regarded as one of the most important research fields in chemistry. Several scientists have been honored with a Nobel Prize for their investigations in the field of heterogeneous catalysis – Fritz Haber in 1918, Irving Langmuir in 1932 and Gerhard Ertl in 2007. Due to advantages such as simple separation from the reaction mixture and high stability, heterogeneous catalysts often are technically more attractive as their homogeneous analogues. One major requirement for an efficient heterogeneous catalyst is a high volume density of catalytically active sites which can be achieved by increasing the available specific surface area. Several approaches have been developed in order to create high surface area values, such as usage of nanoparticles, impregnation of porous materials with catalytically active particles or usage of active carbon as a template matrix for the preparation of highly porous metal oxides.[1,2] Due to their high surface area, porous materials are especially interesting for heterogeneous catalysis. The introduction of zeolites has allowed to increase the efficiency of several industrial processes.[2,3] Due to their well-defined pores, zeolites have also been used for size- or shape-selective catalytic transformations.[2,3] Besides Lewis-acidic centers, transition metal ions belong to the most important catalytically active sites. In recent years, porous coordination frameworks, or metal-organic frameworks, have been developed as a promising novel class of highly porous materials. The construction principle allows to design frameworks with desired properties, pore structure and active metal sites. The use of ubiquitous small molecules such as O_2, N_2 or H_2 for selective catalytic transformations is particularly interesting. Binding of small molecules at the active metal site is a crucial step in heterogeneous catalysis and thus studying interactions between small molecules and metal centers in metal-organic frameworks represents an important and challenging task.

A general goal of this work was the development of a framework with accessible coordinatively unsaturated redox-active metal sites which is catalytically active in heterogeneous gas-phase oxidation reactions with molecular oxygen. As an especially challenging target, the selective oxidation of aliphatic C–H bonds was projected. Although heterogeneous catalysis was one of the earliest proposed applications for porous coordination frameworks[4] and was first demonstrated already in 1994 (liquid-phase cyanosilylation of aldehydes catalyzed by a cadmium-containing framework),[5] the number of publications describing catalytic reactions with MOFs, at the beginning of this work in 2009, remained still very small (approx. 30).[6] Most of the described catalytic oxidation reactions involved peroxides such as hydrogen peroxide[7] and *t*-butylhydroperoxide[8] or iodosylbenzene[9] which had been employed as oxidants in liquid-phase reactions. In several cases MOF-catalyzed liquid-phase oxidation reactions with molecular oxygen have been performed in the presence of co-catalysts such as isobutyraldehyde[10] or N-hydroxyphthalimide (NHPI).[11] Only few liquid-phase catalytic oxidation reactions employing molecular oxygen without a co-catalyst were reported: an oxidation of sulfides to disulfides catalyzed by vanadium-containing framework,[12] oxidation of cinnamylalcohol to

cinnamilaldehyde catalyzed by palladium-containing MOF[13] and oxidation of tetralin to tetralon catalyzed by cobalt- and copper-containing frameworks.[14] MIL-101 framework, which is itself not redox active, has been used as a host material for immobilization of Keggin-type anions $[PW_{11}CoO_{39}]^{5-}$. The catalyst, prepared is this way, has been used for the allylic oxidation of α-pinene by molecular oxygen.[15] Oxidation of CO to CO_2 in continuous gas flow over a nickel-containing framework was until 2009 the only example for heterogeneous gas-phase oxidation reaction catalyzed by a MOF material.[16] Thus, development of a stable framework, which is catalytically active in heterogeneous oxidation reaction with molecular oxygen, was and still remains a challenging task.

A suitable framework must possess readily accessible coordinatively unsaturated redox active metal sites. However, the presence of such metal sites leads to an increased sensitivity of the framework towards hydrolysis or reactions with other coordinating molecules which can be present in the reaction mixture. Thus, a robust framework with strong coordination bonds and possibility to coordinate additional molecules without significant distortion of framework-constituting bonds is required. Moreover, in efficient catalytic transformations normally more than a single free coordination site is required per metal center, so that the oxidant (i.e. O_2) and the substrate can bind to the catalytically active site at the same time. Such properties are not straight-forwardly to implement into novel framework designs. For instance, MFU-1, a cobalt-containing framework, developed previously in our group, possesses coordinatively unsaturated Co(II) sites.[11] However, these sites are not accessible due to a steric hindrance provided by organic ligands. A catalytic activity found for this framework in the liquid-phase oxidation reactions (with *t*-butylhydroperoxide or O_2/NHPI combination as oxidants) could be caused by a partial dissociation of coordinative bonds, making Co(II) sites accessible for oxidant or substrate molecules. However, such dissociation is not possible without a solvent and thus this framework is not suitable as a catalyst for heterogeneous gas-phase reactions. The second problem for oxidation reactions arises from the fact that of MOFs – owing to the presence of organic ligands – are only metastable with respect to complete oxidation of the constituting organic ligands. In this context, either ligands which show enhanced robustness against oxidation (for instance, partially or completely halogenated) or highly active metal sites, allowing to perform the reaction at mild conditions, are required. In the latter case, oxidation-sensitive C–H bonds in organic ligands should not come too close to the active metal sites, in order to prevent self-oxidation. Additionally to these requirements, preparation of porous crystalline frameworks containing redox active metal ions is not a trivial task, since a direct synthesis from the metal salt and organic ligand is often limited to a small number or even to only one kind of metal ion. For this reason, a postsynthetic metal exchange, which would allow to insert different metal ions, was projected in this work. At the beginning of this work, only very few examples of postsynthetic metal exchange in MOFs had been described. The first exchange reaction had been demonstrated in 2007 for the $Mn_3[(Mn_4Cl)_3(BTT)_8(CH_3OH)_{10}]_2$ framework (BTT = benzotristetrazolate), where Mn^{2+} guest ions were substituted by Li^+, Fe^{2+}, Co^{2+}, Ni^{2+}, Cu^{2+}, and Zn^{2+}, Fe^{2+}, ions.[17] However, in this case only guest cations, occupying the voids in an anionic

framework, were exchanged. An exchange of framework-constituting metal ions was first described a few months later, followed by several other examples.[18] Thus, development of the framework with exchangeable, accessible and coordinatively unsaturated metal ions was the premier challenge in this work.

MFU-4 was chosen as a model compound for the development of the desired framework, since its structural features, including coordinatively unsaturated metal ions (as described in section 2.2), seemed to be suitable for postsynthetic metal exchange. An appropriate large organic ligand was necessary in order to construct the desired framework, since MFU-4 itself has very small pore apertures and thus doesn't allow the diffusion of molecules with a kinetic diameter larger than approx. 3.5 Å.

As redox active metal sites, the late 3*d* transition metal ions (Mn up to Zn) were considered, because an oxidation state +2, characteristic for Zn-centers in MFU-4, is easily adapted by all of them. Special focus was laid upon Co(II), since there exist a range of metal complexes that are known to bind molecular oxygen reversibly, thus forming either superoxide or peroxide species,[19] which are able to oxygenate aliphatic C–H bonds.[20] It should be, however, noted that many Co–O_2 complexes have been synthesized using hydrogen peroxide instead of oxygen. Another advantage of Co(II) ions is the formation of stable complexes with nitrogen-containing ligands, which are present in MFU-4 structure. In contrast, V(II), Cr(II), Mn(II) and Fe(II) normally do not form stable complexes with N-donor ligands. Additionally, these metal ions are highly oxygen-sensitive, which would result in a difficult handling and, possibly, irreversible oxidation upon exposure to oxygen. On the other side, Ni(II) and Cu(II) form stable complexes with N-donors as well, but are much harder to oxidize. Thus, based on literature-known properties, within the row of 3*d* transition metal ions Co(II) remains an optimal candidate for reversible oxygen binding.

A framework, suitable for the desired catalytic application, should be able to activate molecular oxygen which can be seen by an increased heat of adsorption. Although several MOF structures featuring coordinatively unsaturated metal sites have been described previously, no example of a framework, demonstrated to bind oxygen, can be found in the literature up to 2010. Moreover, only very few examples of reversible oxygen binding within a porous material have been reported until 2010. A partially reversible oxygen binding has been found in Cr(II)[21] and Cu(I)[22] exchanged zeolites. Fully reversible O_2 binding on Fe(II) and Co(II) centers has been described for microporous porphyrin solids.[9a] Thus, this property is very rare and difficult to achieve. Since the MFU-4 structure allows to vary a coordination environment of unsaturated metal sites (by changing side-ligands, as described in sections 2.2 and 2.4.2), a screening approach was suggested, in order to find a framework which offers reversible oxygen binding.

2 Introduction

2.1 Metal-Organic Frameworks

2.1.1 General Remarks

According to the IUPAC recommendation, metal-organic frameworks (MOFs) are defined as coordination networks with organic ligands, containing potential voids.[23] Coordination networks form a subset in a large area of coordination polymers. Thus, MOFs belong to the field of coordination chemistry and combine organic and inorganic chemistry. The term “MOF” was first introduced in 1995,[24] although several potentially porous coordination polymers, such as bis(adiponitrilo)copper (I) nitrate[25] or prussian blue[26] have been described earlier. Starting from 2001, the field of MOFs has been growing exponentially and it has become now one of the most important research fields in chemistry (Figure 1). For the reason of convenience, trivial names instead of systematic ones are used for MOFs. These can be simple names with numbers like MOF-5, abbreviations pointing out an institution, where the framework was synthesized for the first time (such as HKUST-1 = Hong Kong University of Science and Technology - 1) or just net composition including abbreviation for the organic linker (HKUST-1 = CuBTC = $Cu_3(btc)_2$, where btc = 1,3,5-benzenetricarboxylate). Some frameworks may have several different abbreviations assigned by different groups which coincidentally have been working on the same MOF structure (i.e. MOF-74 = CPO-27, CPO = Coordination Polymer of Oslo).

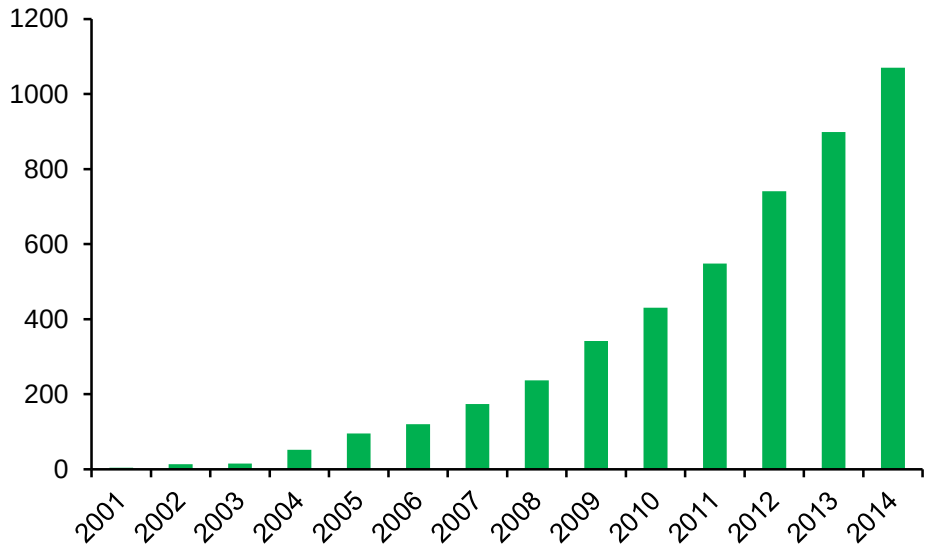

Figure 1. Number of citations per year, containing the key word “metal organic framework” in the years 2001-2014 (from SciFinder Scholar).

2.1.2 Framework Design and Common Structures

Combination of different metal-containing nodes, termed SBUs (secondary building units), with organic linkers allows to obtain a large topologic variety of frameworks, some of which are shown in Figure 2. In more complicated cases, two different linkers can be combined, or the second linker can be used in order to extend a 2D-framework into a 3D-structure. Additionally, the length of the linker can be varied. Thus, this approach allows an exceptionally flexible design of frameworks with desired structure and properties. The most commonly used ligands are either O-donors (such as aromatic carboxylates) or N-donors (pyrazolates, imidazolates, triazolates, tetrazolates etc.). A selection of the most widely investigated MOFs is shown in Figure 3.

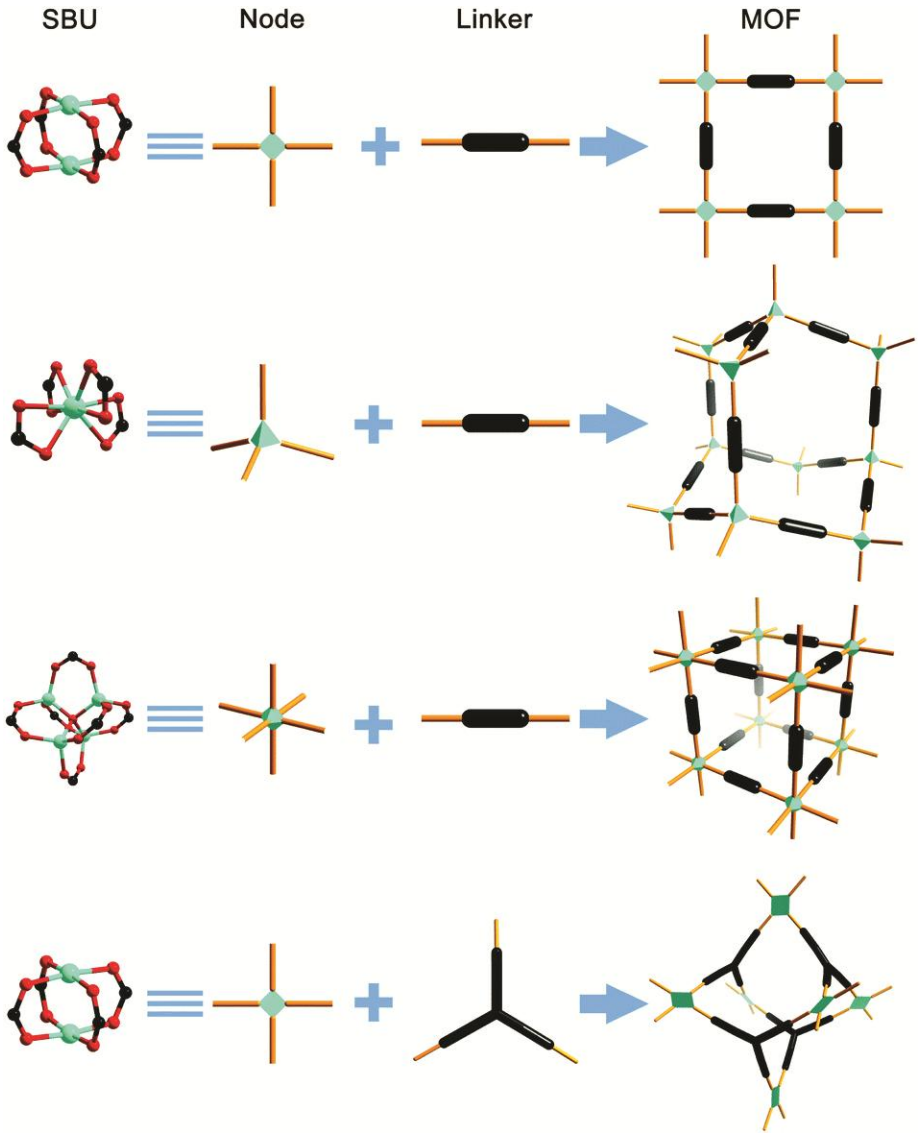

Figure 2. Different framework topologies obtained by combining square-planar (a), tetrahedral (b) or octahedral (c) nodes with linear linkers and square-planar nodes with trigonal linkers (d).[27]

MOF-5, first described in 1999,[28] is a cubic framework built from tetrahedral $\{Zn_4O\}^{6+}$ units and linear 1,4-benzenedicarboxylate ligands (Figures 2c and 3a). MOF-5 has been among the first coordination frameworks to remain crystalline and permanently porous upon solvent removal.

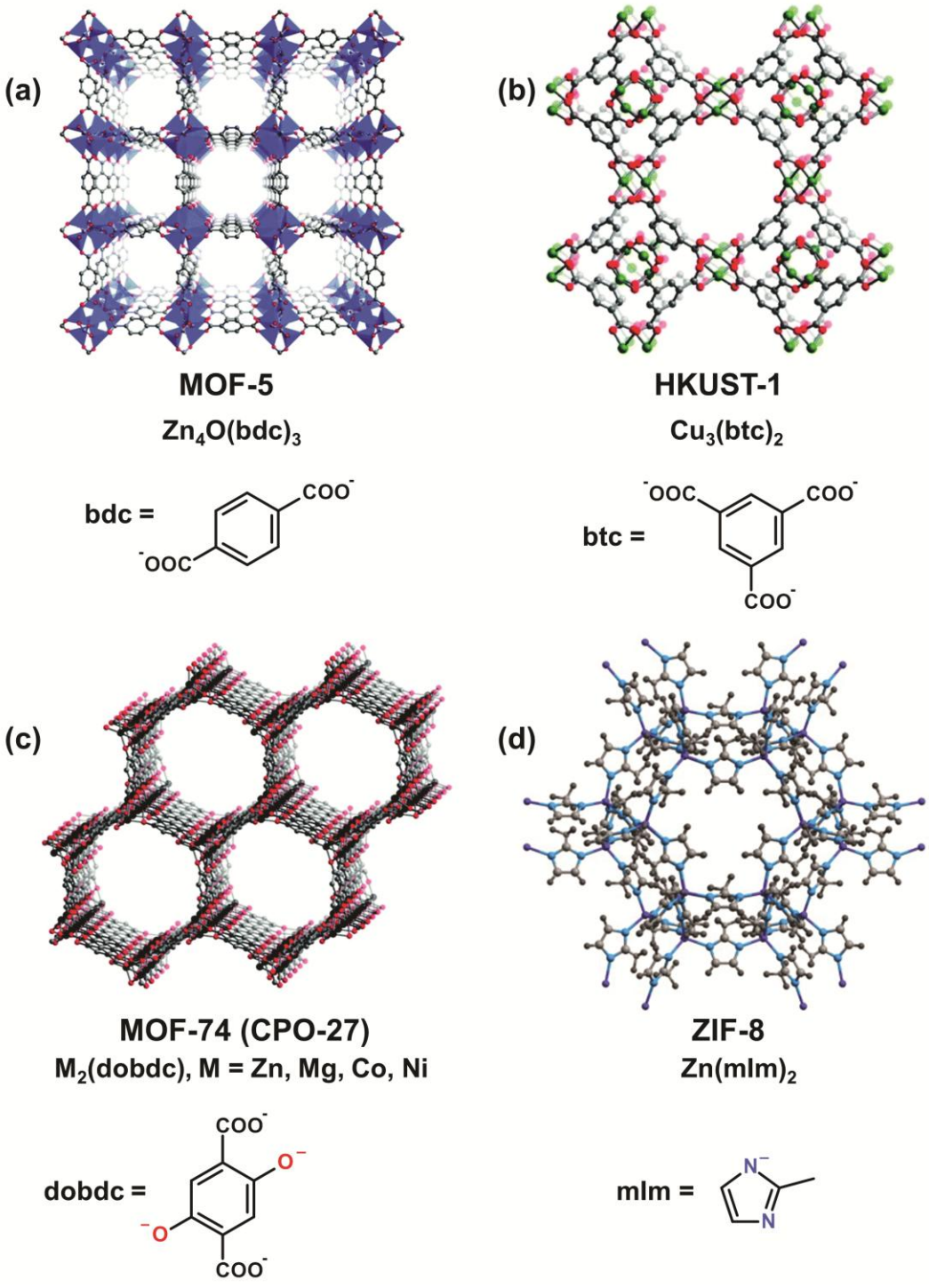

Figure 3. Structures of carboxylate-based (a-c)[29] and imidazolate-based (d) frameworks.[30]

Based on this parent compound a series of isoreticular[a] frameworks (IRMOFs) was developed, containing functionalized or extended linear aromatic biscarboxylate ligands.[31] HKUST-1, built from the dimeric Cu(II) paddlewheel units and benzene-1,3,5-tricarboxylate ligands (Figures 2d and 3b), is another early member and extensively studied example of a rigid porous framework.[32] MOF-74 is a rigid framework, constructed from 2,5-dioxidobenzene-1,4-dicarboxylate and different metal ions, which features easily accessible coordinatively unsaturated metal sites.[33] ZIF-8 is a member of large family of highly stable zeolitic imidazolate frameworks, built from imidazole or benzimidazole derivatives and different metal ions such as Zn^{2+}, Cd^{2+}, Fe^{2+}, Co^{2+}, Cu^{2+}. The main feature of ZIFs is their topological relation to zeolites since the bond angle M-Im-M (Im = imidazolate) is very close to the Si-O-Si dihedral bond angle in zeolites (Figure 4).[34]

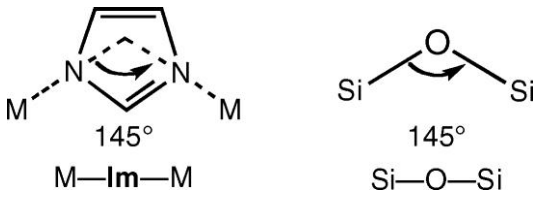

Figure 4. Structural features of ZIFs (left) and zeolites (right).[34]

2.1.3 Framework Description

In the MOF field, the term SBU has first been invented by Yaghi et al. for MOF-5.[28] However, the meaning of SBU for MOFs is not the same, as for zeolites, where this term is actually coming from. In zeolite chemistry, secondary building units are derived assuming that the entire framework can be derived of one type of SBU only. Up to 2007, 23 different SBUs have been observed in zeolite structures.[35] These units have do rarely exist as chemically stable entities, however they are merely useful for exploring possible structural relationships between different zeolites.[36] This kind of formal approach is generally not possible for the description of metal-organic frameworks. Even in the case of highly symmetric frameworks, which can be reduced to only one kind of building unit, each framework will have its own unique SBU, which can be quite large. For these reasons, such description of MOF structures is not practicable. According to Yaghi et al., MOFs are made up of two kinds of secondary building units – organic and metal-containing. Organic SBUs, also called linkers, may be ditopic or polytopic. The second kind of SBU can be simply a metal ion or (most commonly) a finite polyatomic cluster containing two or more metal atoms or an infinite unit such as a one-periodic rod of atoms.[37] Such polyatomic metal-containing clusters are based on stable coordination units, which are extended by organic linkers at their points of extension. Frequently such units are also found in molecular complexes. For instance, tetranuclear $[Zn_4O(COO)_6]$ units, which represent the metal-containing SBU of MOF-5 (Figure 2c, left side), can be found in many stable basic zinc carboxylates such as

[a] i.e. having the same topology

acetate, pivalate or benzoate.[38] Replacing monocarboxylates by 1,4-benzenedicarboxylate leads to the formation of a 3D-framework. This approach allows a rational framework design based on chemically realistic construction units. However, the problem of a formal description is that metal-containing SBUs and organic ligands share the same donor atoms, which leads to some inconsistencies in the formal structural description of a MOF. Organic ligands, for instance, from which a MOF structure is constructed, in literature are very often considered as linkers. However, linkers should be only referred to as interconnecting parts between points of extension of metal-containing SBUs. Thus, the MOF-5 structure is build up from $[Zn_4O(COO)_6]$ units and 1,4-phenylene linkers (Figure 5a). The deconstruction of a ZIF-8 framework in this way will result in separated organic fragments, which serve as organic linkers and interconnect metal-containing $[ZnN_4]$ SBUs. Another deconstruction possibility, which seems more logical in this case, would be to use only Zn^{2+} ions as metal-containing SBUs, which are interconnected by 2-methylimidazolate ligands (Figure 5b). Such approach is also suitable for MOF-5, where tetrahedral $\{Zn_4O\}^{6+}$ units can be considered as metal-containing SBUs and 1,4-phenylenedicarboxylate ligands as interconnecting linkers. However, both approaches are not optimal in the case of MFU-4 structure, described in the section 2.2, since both will lead to artificially separated fragments either in the organic linker or in a metal-containing SBU. Thus, the reduction of MOF structures to chemically meaningful SBUs in general still remains an ill-defined task in MOF nomenclature and structural description. For this reason, a topologic approach, where organic linkers are seen only as imaginary connectors and not as real molecules or fragments, has been established.[39] In this approach, the RCSR (Reticular Chemistry Structure Resource) symbols are used for the characterization of framework nets.[40]

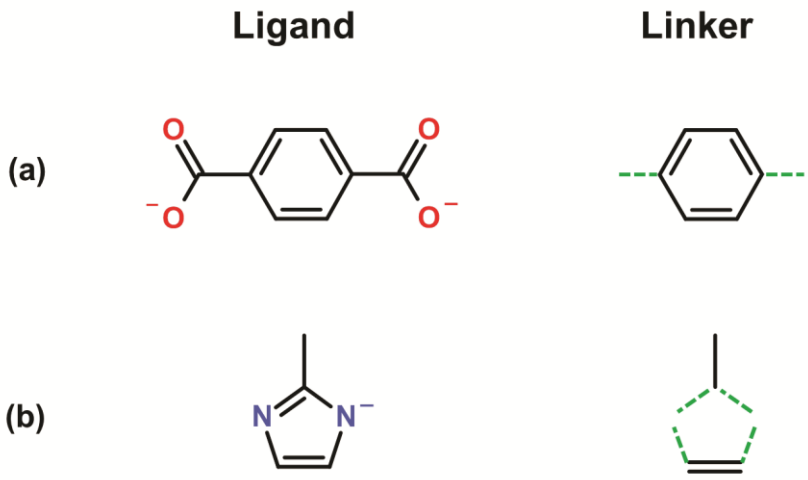

Figure 5. A comparison of organic parts assigned as ligand and linker in MOF-5 (a) and ZIF-8 (b); green dashed lines show the connectivity of the linker.

2.1.4 Functional Properties and Applications

The main common property of MOFs is their permanent[b] porosity. Owing to this technical feature, MOFs were first suggested for gas sorption applications such as gas capture,[41] storage, separation or purification.[42] Many frameworks are flexible and show a so-called "breathing effect" – meaning reversible structural changes upon loading with guest molecules.[43] Most of the hitherto described MOFs belong to microporous materials, i.e. featuring pore sizes below 2 nm. However, applying very long linkers allows to obtain frameworks with a pore size up to 9.8 nm (e.g. IRMOF-74-XI).[44] The BET surface area of MOFs typically ranges from 1000 to 4000 $m^2\ g^{-1}$, however some MOFs have been shown to exceed the upper value of this range significantly.[29] Thus, MOFs clearly constitute a class of compounds possessing the highest specific surface area among all known porous materials. Up to now, the highest BET surface area of 7140 $m^2\ g^{-1}$ was found for the NU-110E framework.[45] Selected properties of typical MOFs including pore size, pore volume and BET surface area, are summarized in Table 1.

Catalysis is the second important application field for MOFs which was extensively studied in the recent years.[46] The main advantage of MOFs being used as heterogeneous catalysts is their high surface area combined with the possibility of introducing active metal sites. However, an insufficient stability is often a limiting factor. For instance, MOF-5, formed by relatively weak coordination bonds between Zn^{2+} ions and carboxylate anions, is moisture-sensitive.[47] Also thermal stability is considerably lower, as, for instance, in the case of zeolites. In contrast to MOFs, which contain organic ligands and thus can be oxidized quite easily at high temperature, zeolites are oxidation-stable. Nevertheless, catalysis remains an important research topic in MOF chemistry, including biomimetic[48] and chiral[49] catalysis. Recently, MOFs were also considered for many other application fields such as sensing,[50] luminescent[51] and ferroelectric[52] materials, non-linear optics[53] and biomedicine.[54]

Table 1. Selected properties of typical MOFs.

Framework	**MOF-5**	**HKUST-1**	**CPO-27-Mg**	**ZIF-8**
Pore size / Å	11.0 / 15.1[28]	5.0 / 9.0[32]	12.0[55]	11.6[34]
Pore volume / $cm^3\ g^{-1}$	1.55[45]	0.76[29]	0.63[29]	0.71[29]
BET surface area / $m^2\ g^{-1}$	3800[45]	1502[29]	1542[29]	1770[29]

[b] i.e. remaining after removal of guest molecules

2.2 MFU-4-Type Frameworks

MFU-4 (Metal-Organic Framework Ulm University-4), first described in 2009, is a cubic framework constructed from 1*H*,5*H*-benzo(1,2-d:4,5-d')bistriazolate ($BBTA^{2-}$) ligands (Figure 6b) with the net composition $[Zn_5Cl_4(BBTA)_3]$.[56] The metal-containing SBU of MFU-4 with the composition $[Zn^oZn^t_4(ta)_6]^{4+}$ (o – octahedral, t – tetrahedral, ta – triazolate) includes one octahedrally coordinated (central) Zn(II) ion and four tetrahedrally coordinated (peripheral) Zn(II) ions which are connected to six triazolate ligands (Figure 6a). These SBUs have six points of extension, which are interconnected by two CH fragments of a benzene ring, respectively, into a cubic system. Peripheral zinc(II) ions in the SBU of MFU-4 are additionally coordinated by negatively charged chloride side-ligands, forming in total a neutral node. Such pentanuclear clusters, termed Kuratowski-units, can be also found in several discrete coordination compounds.[57] The main advantage of this coordination unit is its high hydrolytic stability, in contrast to many carboxylate-based MOFs. MFU-4 remains crystalline and porous after solvent removal and is stable up to 400 °C. This framework crystallizes in the space group $Fm\bar{3}m$ (no. 225) and includes two types of voids with the diameter of 3.9 Å and 11.9 Å, respectively, which are interconnected thus forming very small apertures with 2.5 Å diameter (Figure 7). Due to the narrow pore openings, MFU-4 allows only diffusion of atoms and molecules with a small kinetic diameter, such as He, H_2, H_2O or CO_2, whereas larger molecules and atoms (Ar, N_2, CH_4) are excluded from uptake or diffuse very slowly. This property allows a kinetic separation of small molecules, for instance CO_2 and N_2.[58] At low temperatures (< 70 K), interesting tunneling effects occur in small apertures of MFU-4 allowing highly efficient separation of isotopologues such as H_2 and D_2 (this approach is called “quantum sieving”).[59] However, for catalytic applications, a framework with large pore apertures allowing free diffusion of different molecules, is required. For this purpose, a structural analogue of MFU-4, called MFU-4*l* (*l* = large), based on an extended linear bistriazolate ligand, has been developed.

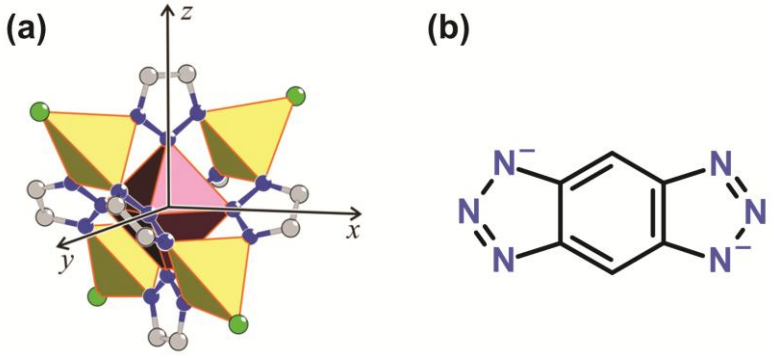

Figure 6. (a) The SBU of MFU-4 featuring a central metal ion (shown as magenta octahedron) and four peripheral metal ions (shown as yellow tetrahedra) with chloride side-ligands (green); (b) $BBTA^{2-}$ ligand.[56]

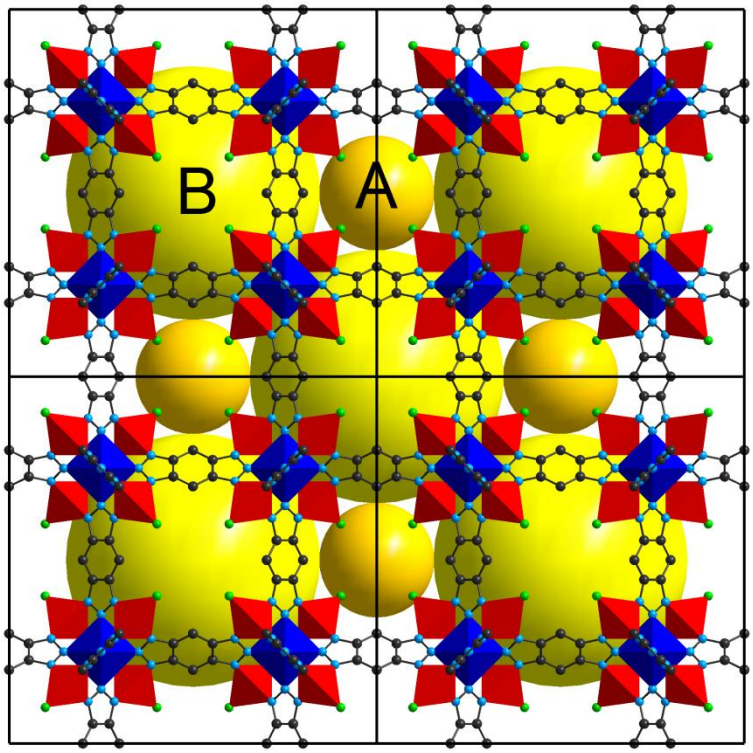

Figure 7. The structure of MFU-4 featuring small (A) and large (B) voids.[56]

2.3 MFU-4*l* Framework

2.3.1 Synthesis

Dibenzo-[1,4]-dioxin (**1**) was chosen as an aromatic system since it can be selectively nitrated giving 2,3,7,8-tetranitrodibenzo-[1,4]-dioxin (**2**), which is a suitable precursor for the desired bistriazolate ligand. Since the literature-described nitration procedure, employing a mixture of sulfuric and nitric acid, gives very low yield (17 %),[60] a mixture of fuming nitric acid with trifluoroacetic anhydride was applied. This modified procedure allows to perform the nitration with nearly quantitative yield. The second reduction step was conducted according to a previously published procedure[61] yielding 2,3,7,8-tetraaminodibenzo-[1,4]-dioxin tetrahydro-chloride (**3**). The last diazotization step leads to the desired bis-(1*H*-1,2,3-triazolo-[4,5-b],[4',5'-i])dibenzo-[1,4]-dioxin (H_2-BTDD) ligand (Scheme 1). In summary, the H_2-BTDD ligand can be efficiently synthesized using this optimized three-step procedure in about 83 % overall yield. Similar to MFU-4, the solvothermal synthesis starting from $ZnCl_2$ and H_2-BTDD ligand in N,N-dimethylformamide (DMF) leads to MFU-4*l* obtained in high yield as a pale-yellow precipitate. SEM images show that MFU-4*l* forms cubic crystals with a typical size ranging from 1 to 5 μm (Scheme 2).[A1]

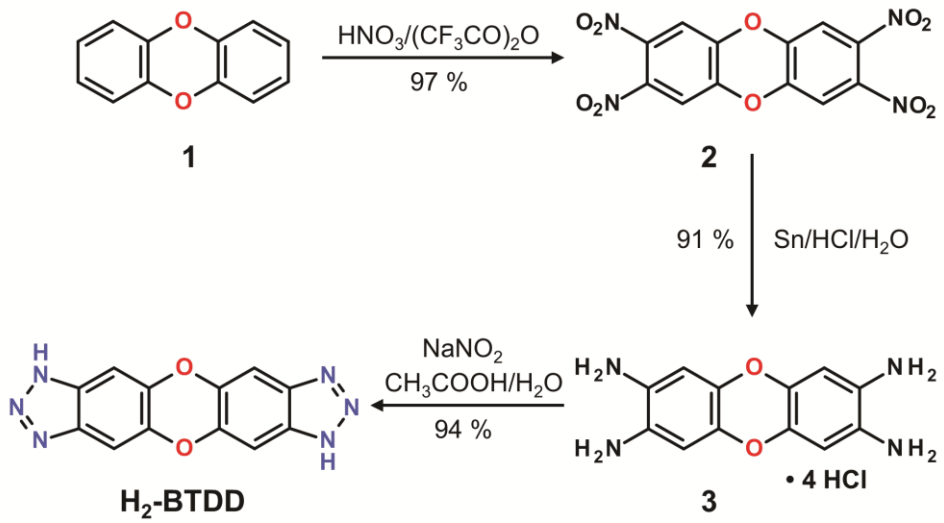

Scheme 1. Synthesis of H_2-BTDD, the ligand of MFU-4*l*.[A1]

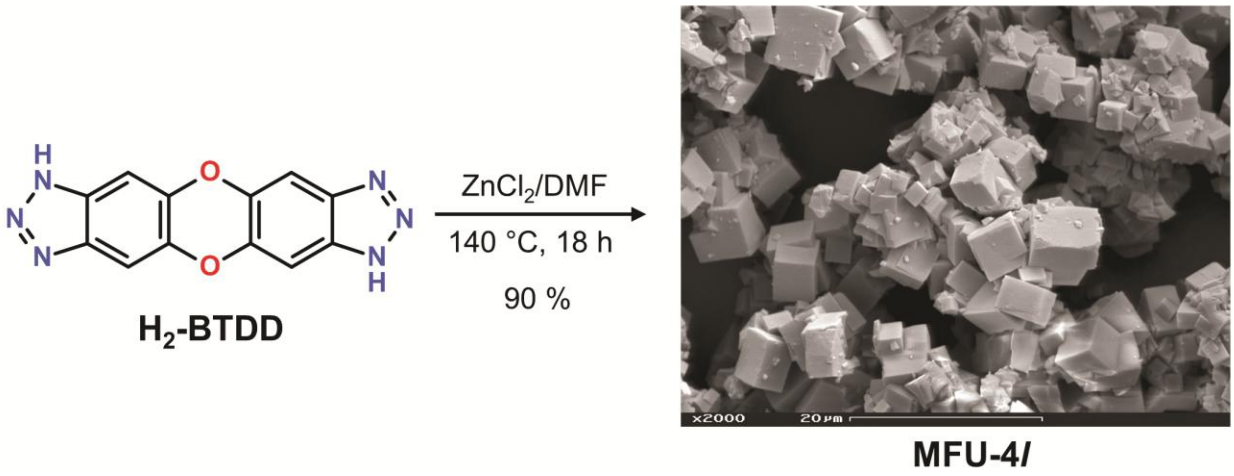

Scheme 2. Synthesis of MFU-4*l* and SEM image of agglomerated MFU-4*l* crystals.[A1]

2.3.2 Crystal Structure and Characteristics

The structure of solvent-free MFU-4*l* has been solved from X-Ray powder diffraction (XRPD) data. Similar to MFU-4, MFU-4*l* has a composition $[Zn_5Cl_4(BTDD)_3]$ and crystallizes in the space group $Fm\bar{3}m$ (no. 225) with cell axes lengths of 31.057(1) Å and a unit cell volume of 29955(4) $Å^3$. Two kinds of voids with a maximal diameter of 12 Å and 18.6 Å, respectively, are interconnected by apertures with 9.1 Å diameter (Figure 8).[A1] After solvent removal, MFU-4*l* remains permanently porous and stable up to 500 °C under nitrogen and 350 °C under air, as revealed from TGA and VTXRPD analysis. The argon sorption isotherm recorded at 87.3 K shows that MFU-4*l* is a typical microporous material with a BET surface area of 3580 $m^2\ g^{-1}$ and a pore volume of 1.42 $cm^3\ g^{-1}$ and thus belongs to a smaller sub-class of stable frameworks

featuring very high permanent porosity.[A1] The metal-containing SBU in MFU-4*l* is the same as in MFU-4 and features coordinatively unsaturated peripheral Zn(II) ions (Figure 6). The coordination environment of each of these ions is similar to those of well-known scorpionate complexes (Figure 9a).[62] In contrast to scorpionates, the coordination sites in a rigid MFU-4*l* framework do not have to be protected from dimerization by bulky substituents R and thus are easily accessible for substrate molecules allowing catalytic applications (Figure 9b).

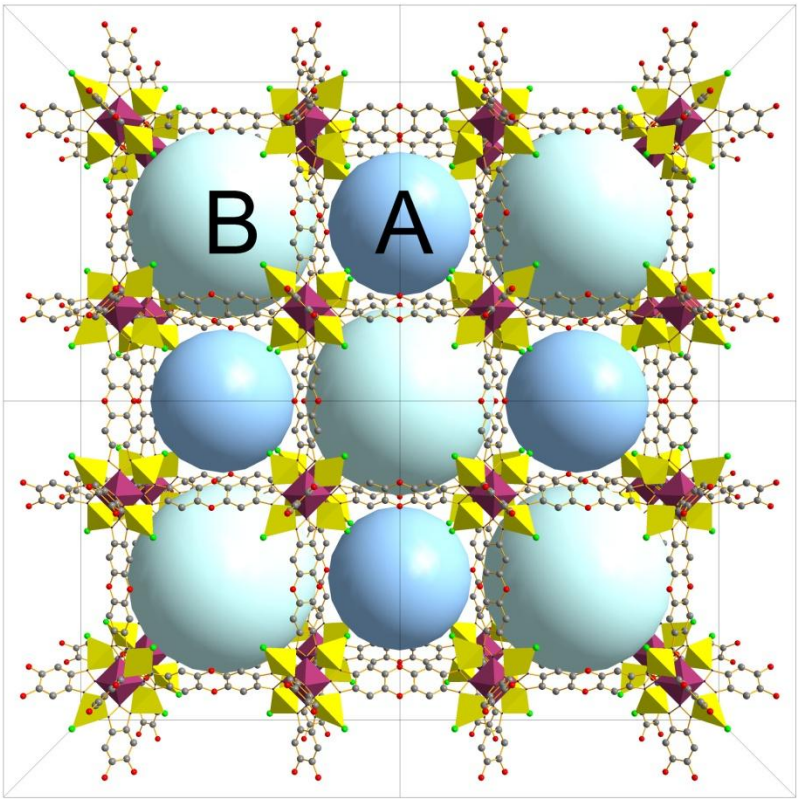

Figure 8. The structure of MFU-4*l* featuring small (A) and large (B) voids.[A1]

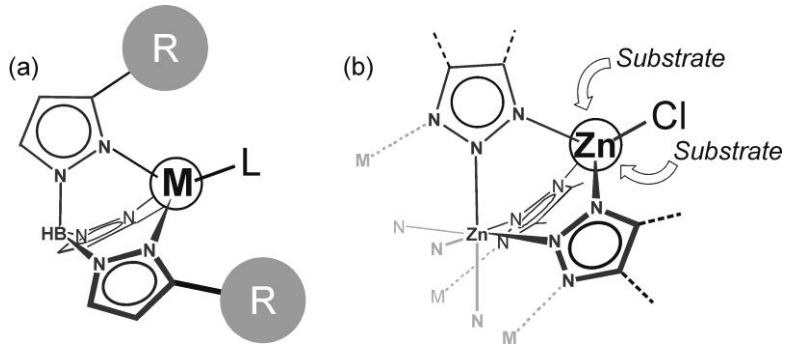

Figure 9. (a) Scorpionate complex (M = metal ion, L = ligand, R = bulky substituent, e.g. *tert*-Bu); (b) Part of the metal-containing SBU in MFU-4*l* comprising coordinatively unsaturated and substrate-accessible coordination sites.[A3]

2.4 Metal and Ligand Exchange in MFU-4*l*

2.4.1 Metal Exchange

A postsynthetic metal exchange in SBUs has been developed and described in the recent years for several MOF families, thus allowing the preparation of frameworks with the desired properties.[63] With respect to catalytic applications and activation of small molecules, redox active transition metal ions are particularly interesting.[64] The coordination principle in the SBU of MFU-4*l* allows for the stepwise exchange of peripheral metal ions, whereas the central octahedrally coordinated Zn^{2+} ion remains unchanged and the SBU remains intact (Figure 10a). It was shown that Mn^{2+}, Fe^{2+}, Co^{2+}, Ni^{2+} and Cu^{2+} ions can be introduced postsynthetically into MFU-4*l*.[A4] However, a complete exchange of peripheral Zn^{2+} ions is only possible with Co^{2+}. Thus, treatment of MFU-4*l* with a $CoCl_2$ solution in DMF at 140 °C leads to Co-MFU-4*l* with the composition $[ZnCo_4Cl_4(BTDD)_3]$.[A2] The dependence of the number *x* of exchanged Zn(II) ions in the $[Zn^oZn^t_4(ta)_6]^{4+}$ unit on the initial Co/Zn molar ratio (Figure 10b) converges towards a plateau at *x* = 4 (and not 5), suggesting that the central octahedrally coordinated Zn center cannot be replaced under the chosen experimental conditions.[A2] Additionally, spectroscopic studies didn't show any evidence for the presence of octahedrally coordinated Co^{2+} ions in Co-MFU-4*l*. Exchange reactions tested with other transition metal ions cannot be performed at the same high temperature due to amorphization of MFU-4*l* or precipitation of by-products. However, an almost complete Zn/Ni exchange can be achieved with $NiCl_2$ in DMF at 80 °C, whereas Zn/Cu exchange can only be conducted at 60 °C and leads in average to the substitution of 2-2.5 zinc centers per $[Zn^oZn^t_4(ta)_6]^{4+}$ unit (Figure 10b). Similar results were obtained with $MnCl_2$ and $FeCl_2$ at 60 °C.[A4]

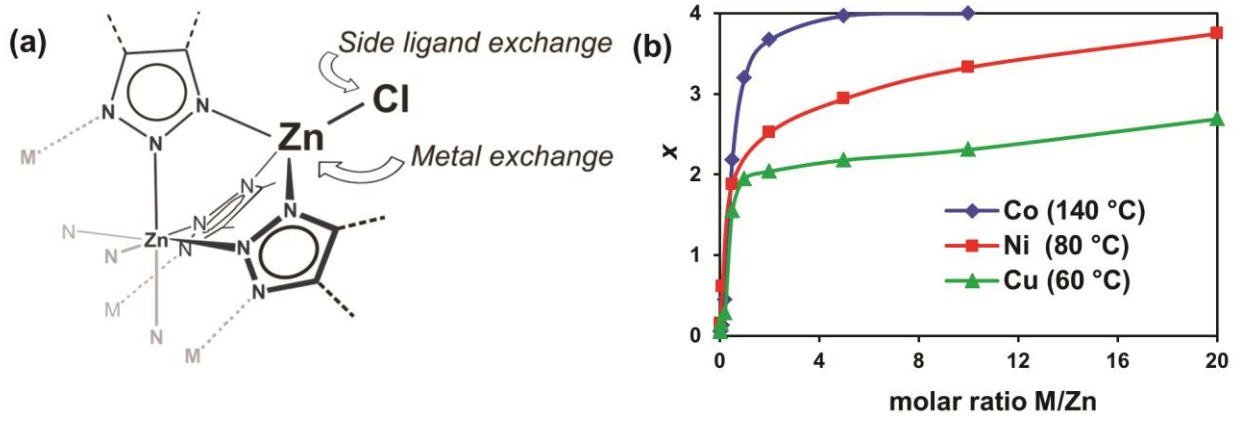

Figure 10. (a) Metal- and side-ligand exchange on the peripheral position in the SBU of MFU-4*l*; (b) Number *x* of exchanged Zn(II) ions per $[Zn^oZn^t_4(ta)_6]^{4+}$ unit as a function of the (M/Zn) molar ratio in the starting MCl_2 / MFU-4*l* reaction mixture (right).[A2,A4]

2.4.2 Ligand Exchange

Postsynthetic metal exchange in MFU-4*l* can be augmented by an exchange of the chloride side ligand (Figure 10, left) by other singly charged anionic ligands. In this way, a number of different anions such as nitrite (NO_2^-), nitrate (NO_3^-), azide (N_3^-), triflate ($CF_3SO_3^-$), isocyanate (NCO^-), formate ($HCOO^-$), acetate (CH_3COO^-) or fluoride (F^-) were introduced as side-ligands into MFU-4*l* frameworks. The exchange reaction proceeds smoothly at room temperature employing methanolic or acetonitrile solutions of well soluble lithium salts (except fluoride, where methanol-soluble CsF was applied). All attempts to introduce strongly coordinating or highly basic ligands such as cyanide (CN^-) or hydroxide (OH^-), respectively, failed leading to the decomposition of the framework.[A4]

The described metal and ligand exchange reactions proceed without significant change of the framework crystallinity and porosity. Thus, the family of MFU-4*l* frameworks represents a modular "construction kit" which allows fine adjustments of the framework properties towards a desired application. A summary of postsynthetic metal and ligand exchange reactions in MFU-4*l* is shown in Figure 11 (ligand exchange is exemplified for Co-MFU-4*l*).[A4]

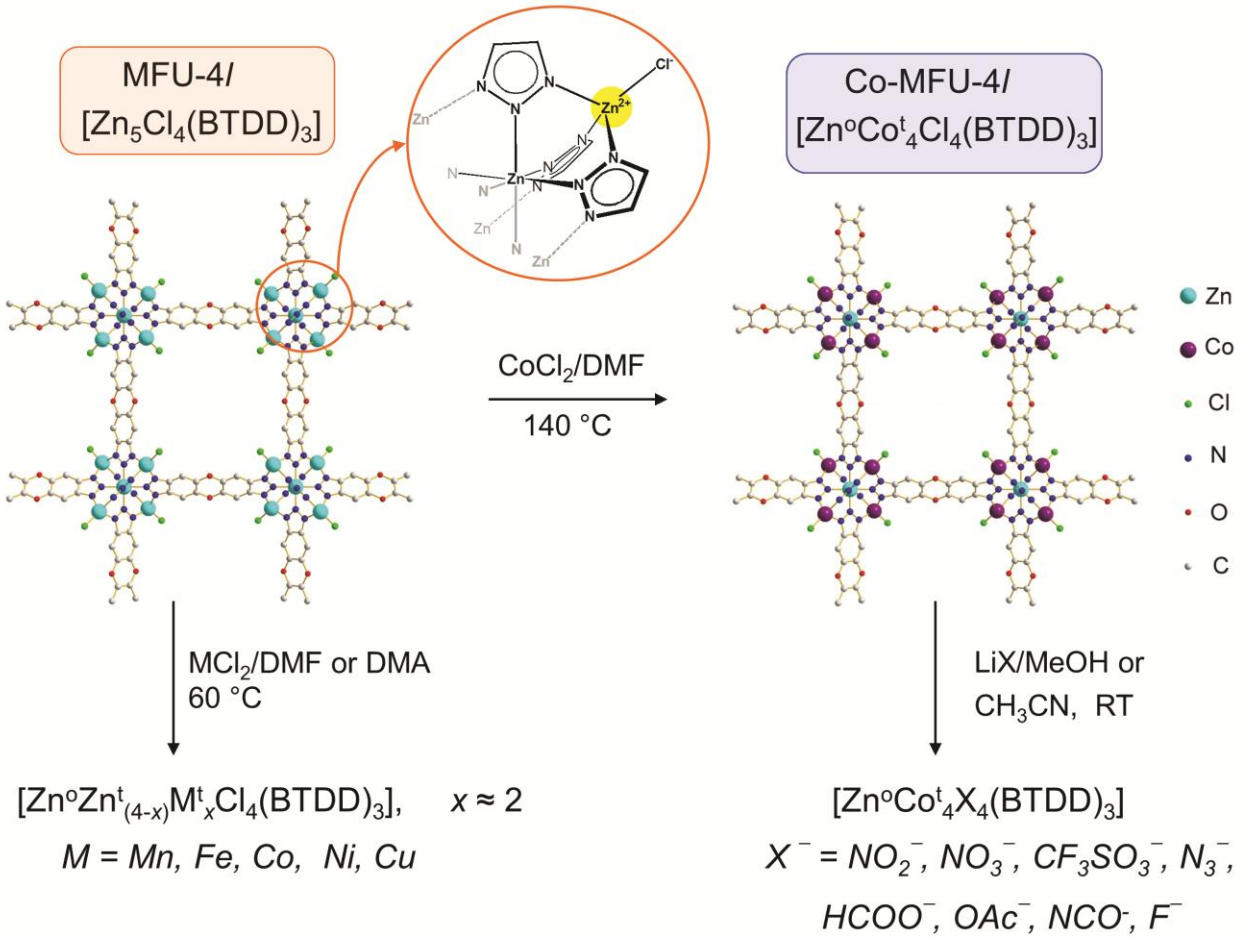

Figure 11. Postsynthetic metal and ligand exchange in MFU-4*l* (DMA = N,N-dimethylacetamide).[A4]

2.5 Catalytic Properties of Heterometallic MFU-4*l* Frameworks

2.5.1 Gas Phase Oxidation of Carbon Monoxide

Temperature-programmed-oxidation (TPO) and -reduction (TPR) studies on Co-MFU-4*l* have shown that the framework consumes molecular oxygen at ca. 80 and 190 °C (Figure 12a) and reacts then with hydrogen at ca. 190 °C. This cycle can be repeated at least three times showing, that the gas phase oxidation/reduction sequence is reversible. MFU-4*l*, in contrast, shows no such behaviour which allows to assume that Co(II) centers are responsible for the redox activity of Co-MFU-4*l*. Heating the Co-MFU-4*l* sample, pre-oxidized at 200 °C, under carbon monoxide gas flow results in formation of carbon dioxide in the temperature range 120–180 °C, as shown by TPSR (temperature-programmed surface reaction) curve (Figure 12b).[A2] These results show clearly that Co-MFU-4*l* is catalytically active in heterogeneous oxidation of carbon monoxide. The reaction temperature range is considerably higher than the one reported for Co_3O_4 nanoparticles (-77°C).[65] However, CO oxidation catalysts containing Co_3O_4 usually require much higher pre-treatment temperatures (450–550°C),[65] whereas in the case of Co-MFU-4*l*, 200°C is sufficient for catalyst activation. This points to an advantage of Co-MFU-4*l* as compared to conventional cobalt oxide-based catalysts and shows its potential as a heterogeneous catalyst for gas phase oxidation reactions.[A2] An exact reaction mechanism cannot be proposed, based on the available experimental data, since Co-MFU-4*l* doesn't show oxygen chemisorption at low temperatures, as revealed from the measurements of the isosteric heat of oxygen adsorption.[A4] Binding of oxygen on Co(II) centers must be also detectable by UV-vis-NIR spectroscopy. However, spectroscopic measurements performed on Co-MFU-4*l* at temperatures up to 280 °C under oxygen (where the decomposition of the framework starts), didn't show significant changes allowing to assume that the reactivity is rather related to the active Co-sites which are present as defects in the framework and not to the regular Co–Cl units.

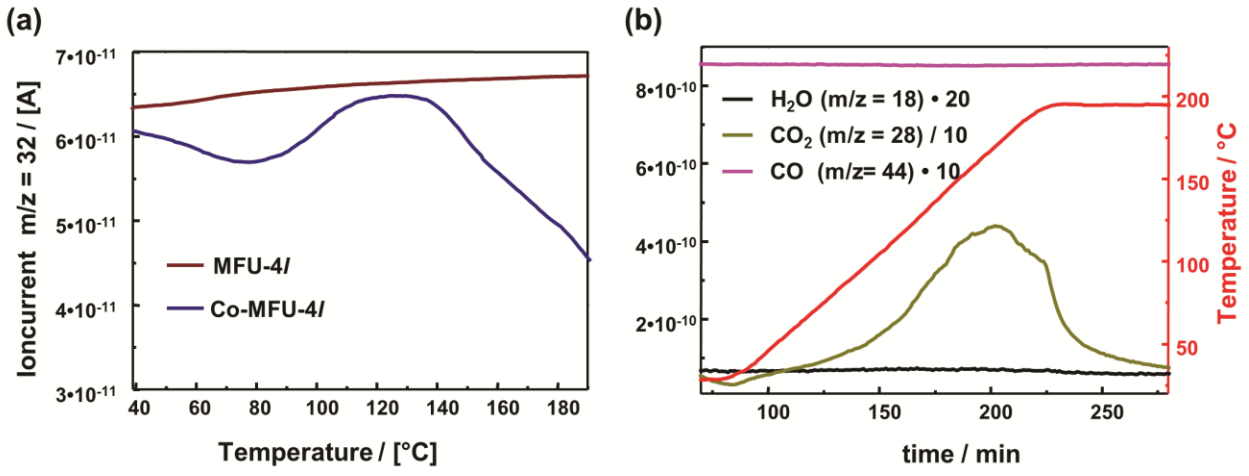

Figure 12. (a) TPO curves for MFU-4*l* and Co-MFU-4*l*; (b) CO-TPSR curve for Co-MFU-4*l*.[A2]

2.5.2 Liquid Phase Oxidation of Ethylbenzene

Although all investigated heterometallic MFU-4*l* frameworks with different side-ligands didn't show oxygen chemisorption (as revealed from the measurements of isosteric heats of adsorption), some of them still can activate molecular oxygen in a liquid phase and thus show catalytic activity in the oxidation of ethylbenzene with air under mild conditions.[A4] NHPI was used as a co-catalyst in this reaction (Scheme 3). This strategy has been successfully applied with homogeneous catalysts such as acetates or acetylacetonates of V(IV), Mo(VI), Mn(III), Fe(III), Co(II), Co(III) and Cu(II),[66] as well as with some MOFs, such as Co(II)-containing MFU-1[11] and Co-BTT[67].

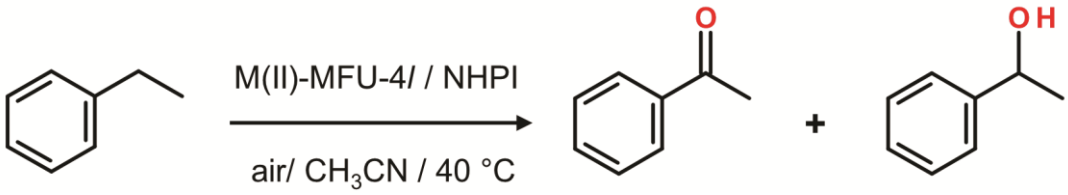

Scheme 3. Liquid-phase NHPI-mediated oxidation of ethylbenzene catalyzed by MFU-4*l* derivatives.[A4]

The highest conversion is achieved with Cu-MFU-4*l*, Co-MFU-4*l* and Co-MFU-4*l*-acetate (Table 2). Introduction of weakly coordinating side-ligands into Co-MFU-4*l* (such as nitrate and triflate) leads to a strongly reduced activity. A possible reason might be that in this case, the Co–nitrate (or Co–triflate) bond dissociates in solution and the remaining positively charged Co-species are much less active. Ni-MFU-4*l* shows low activity, whereas Mn-MFU-4*l* and Fe-MFU-4*l* are not stable under reaction conditions: a fast oxidation of Mn^{2+} or Fe^{2+} ions (as seen by colour change) and no conversion of ethylbenzene were observed. In the case of Co-MFU-4*l*, the heterogeneous character of catalysis was confirmed by the hot filtration test, performed after 8 h reaction time (Figure 13).

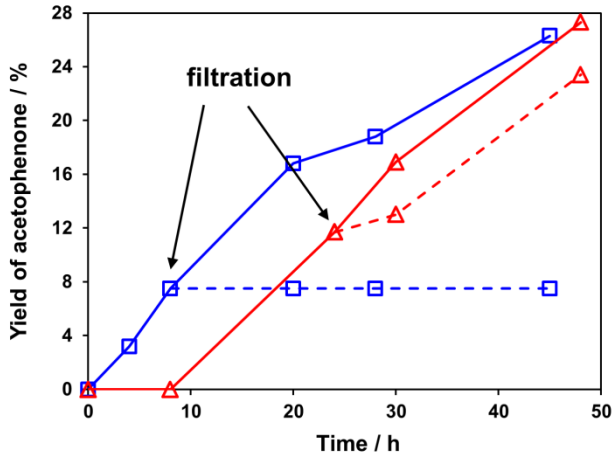

Figure 13. Time-dependent formation of acetophenone in the NHPI-mediated oxidation of ethylbenzene catalyzed by Co-MFU-4*l* (blue) and Cu-MFU-4*l* (red). Dashed lines show the reaction progress after hot filtration.[A4]

Considering the absence of metal leaching during the reaction, Co-MFU-4*l* remains stable during the catalytic tests. However, XRPD and porosity measurements indicate that both, its crystallinity and its porosity decrease gradually. The EDX (Energy-dispersive X-Ray) analysis of Co-MFU-4*l* recovered after catalysis shows an unchanged Zn/Co ratio which also proves a heterogeneous character of catalysis. Cu-MFU-4*l* remains as well highly crystalline and porous after the reaction, but the hot filtration test, performed after 24 h reaction time, indicates a probable leaching of Cu^{2+} ions: the conversion in the filtrate continues with time at a similar rate as in the unfiltered reaction mixture (Figure 15). Assuming that metal leaching occurs in the case of Cu-MFU-4*l* is further supported by the prolonged induction period of the reaction (Figure 13). GC/MS analysis shows the formation of 1-phenylethanol as a by-product in all cases. However, the ketone/alcohol selectivity is very high (≥ 95 %) in all cases (Table 2).[A4] Co-MFU-4*l* shows similar activity and selectivity in this reaction as described previously for MFU-1.[11]

Table 2. Conversions and selectivities for liquid-phase oxidation of ethylbenzene catalyzed by heterometallic MFU-4*l* frameworks after 48 h reaction time.[A4]

Framework	**Peripheral Metal Ion**	**Side-Ligand**	**Conversion of ethylbenzene / %**	**Selectivity ketone/alcohol[a]**
Co-MFU-4*l*	Co^{2+}	Cl^-	27±3	97
Co-MFU-4*l*-acetate	Co^{2+}	CH_3COO^-	26±3	95
Co-MFU-4*l*-nitrate	Co^{2+}	NO_3^-	8±1	95
Co-MFU-4*l*-triflate	Co^{2+}	$CF_3SO_3^-$	3.0±0.5	-
Mn-MFU-4*l*	Mn^{2+}	Cl^-	0	-
Fe-MFU-4*l*	Fe^{2+}	Cl^-	0	-
Ni-MFU-4*l*	Ni^{2+}	Cl^-	9±1	-
Cu-MFU-4*l*	Cu^{2+}	Cl^-	28±3	95

[a] the selectivity for Ni-MFU-4*l* and Co-MFU-4*l*-triflate could not be estimated due to very low content of alcohol.

2.6 Thermal Transformations of Side-Ligands

2.6.1 Formate Ligand

Bulk metal formates can be easily decomposed at 200–300 °C, the formate anion often serves as a reducing agent at the same time. For instance, thermal decomposition of copper(II) formate results in the formation of reduced copper species – Cu_2O and Cu.[68] This lead us to the idea that formate side-ligands in heterometallic MFU-4*l* frameworks could be used as precursors for the generation of active metal sites.

Table 3. Temperature ranges for the thermal decomposition of formate side ligands in heterometallic MFU-4*l* frameworks determined by TGA under N_2 flow with 5 K min^{-1} heating rate.[A4]

Framework	Peripheral Metal Ion	Start / °C	End / °C
MFU-4*l*	Zn^{2+}	195	280
Mn-MFU-4*l*	Mn^{2+}	330	370
Fe-MFU-4*l*	Fe^{2+}	195	325
Co-MFU-4*l*	Co^{2+}	195	325
Ni-MFU-4*l*	Ni^{2+}	180	280
Cu-MFU-4*l*	Cu^{2+}	120	180

Thermogravimetric (TGA) studies show that the coordinated formate side-ligands can be decomposed selectively, before the decomposition of the MFU-4*l* framework starts, the suitable temperature range depending strongly on the peripheral metal ion (Table 3). XRPD measurements show that the crystallinity of MFU-4*l* and its Fe, Ni and Cu derivatives is completely retained upon decomposition of the coordinated formate side ligands, whereas the crystallinity of Co-MFU-4*l*-formate becomes lower and Mn-MFU-4*l*-formate shows only a few X-ray reflexes after thermal treatment.[A3,A4] FT-IR spectra show clearly the formation of Zn–H species after thermal treatment of MFU-4*l*-formate. Thus, a characteristic Zn-formate stretching vibration, which appears as shoulder in the FT-IR spectrum at 1610 cm^{-1}, disappears completely after heating at 300 °C and three new bands appear upon heat treatment: at 1793, 482 and 453 cm^{-1} (Figure 14a). DFT calculations, conducted in the working group of Prof. Karsten Reuter (TU München), show that all these bands belong to the Zn–H species.[A3]

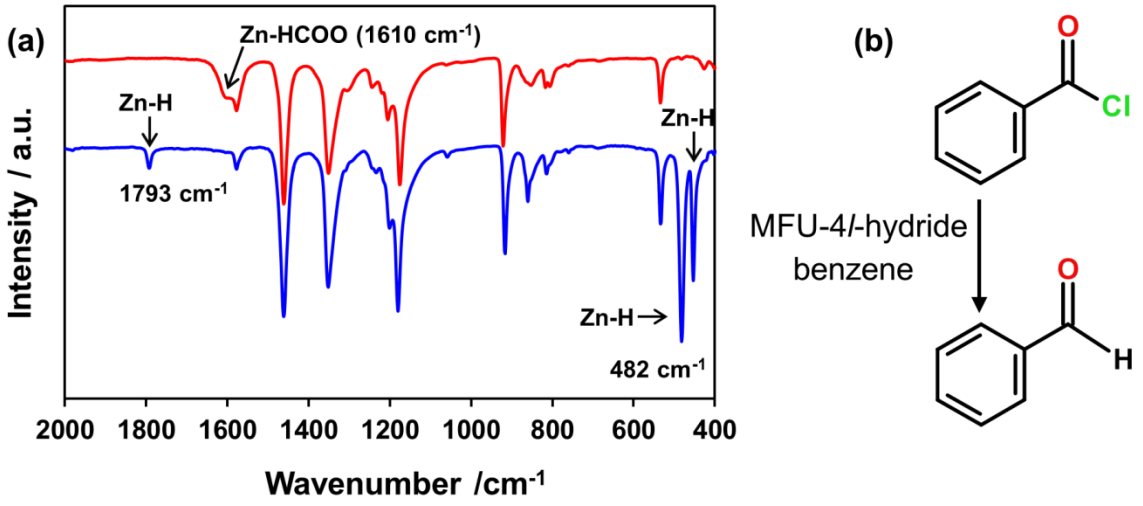

Figure 14. (a) FT-IR spectra of Cu-MFU-4*l*-formate (red) and MFU-4*l*-hydride (blue); (b) Conversion of benzoyl chloride to benzaldehyde.[A3]

Molecular hydride complexes of zinc scorpionates were shown to react with various electrophiles such as CO_2, CS_2, RNCS, RI and CH_3COCl.[69] As shown by GC/MS analysis, MFU-4*l*-hydride reacts with benzoyl chloride in benzene solution at room temperature, yielding benzaldehyde as the main product (Figure 14b). This test case indicates the potential of MFU-4*l*-hydride as a hydride transfer and reducing agent.[A3]

Thermal decomposition of formate side-ligands bound to Cu(II) centers in MFU-4*l* framework results in the formation of highly active trigonal-pyramidal Cu(I) centers, as revealed from the gas sorption and spectroscopic studies.[A3] The resulting framework, termed Cu(I)-MFU-4*l*, shows unique chemisorption properties and will be discussed in detail in section 2.7. The formation of metal(I) sites was also observed in the case of Co-MFU-4*l*-formate. However, due to their very high reactivity, Co(I) centers could only be characterized spectroscopically. Thus, the product, obtained after heating of Co-MFU-4*l*-formate under CO gas flow at 325 °C, shows a characteristic band at 1971 cm^{-1} (Scheme 4),[A4] which corresponds to the CO stretch and is very similar to a CO vibrational frequency in Co(I)-containing scorpionate complex [$Tp^{i\text{-Pr,Me}}$Co(CO)] (1940 cm^{-1}, $Tp^{i\text{-Pr,Me}}$ = hydrotris(3-isopropyl-5-methyl-1-pyrazolyl)borate).[70]

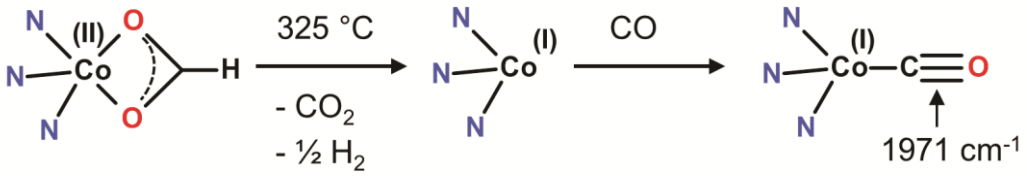

Scheme 4. Schematic representation for the formation of Co(I)-CO species after thermal treatment of Co-MFU-4*l*-formate under CO gas flow.[A4]

2.6.2 Azide Ligand

Azide is another example for reactive ligands that undergo thermal transformations. For instance, aryl-substituted bis(imino)pyridine cobalt azide complexes ($^{i\text{-Pr}}$BPDI)CoN_3 and (^{Mes}BPDI)CoN_3 have been shown to generate a nitrene intermediate under photolytic or thermal (215 °C) conditions which then undergoes an intramolecular insertion into aliphatic C–H bond.[71] Co-MFU-4*l*-azide undergoes a clean transformation to Co-MFU-4*l*-isocyanate when heated up to 300 °C under a CO gas flow. Thus, a characteristic IR-band at 2068 cm^{-1}, which corresponds to the azide stretch mode, disappears completely and a new band at 2217 cm^{-1} appears. This new band corresponds to the isocyanate stretch mode, as shown by comparison to a Co-MFU-4*l*-isocyanate sample, independently prepared from Co-MFU-4*l* *via* the postsynthetic side-ligand exchange (Figure 15).[A4] According to DFT calculations, this reaction most probably proceeds *via* the nitrene intermediate (Scheme 5). This test reaction indicates that Co-MFU-4*l*-azide could be potentially interesting as an N-atom transfer reagent.

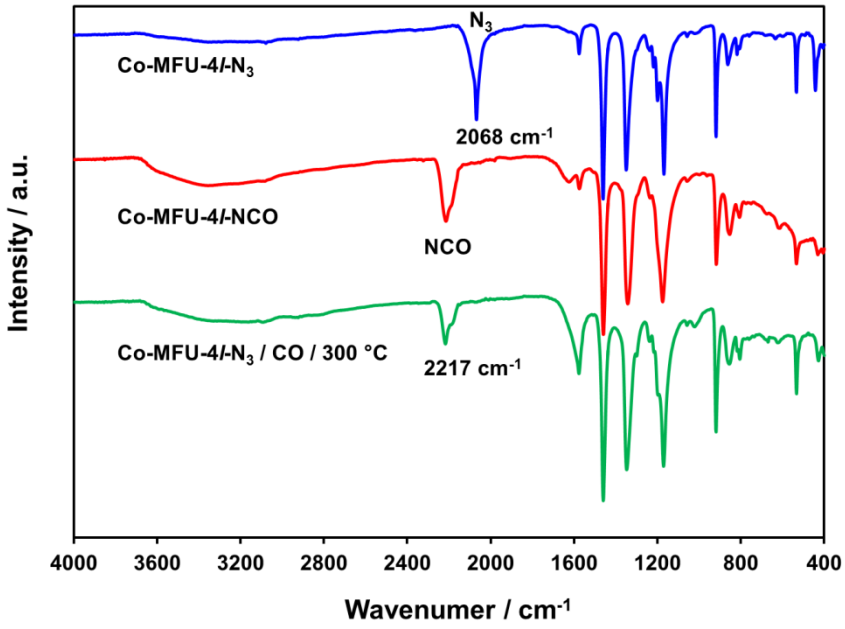

Figure 15. FT-IR spectra of Co-MFU-4*l*-azide (blue), Co-MFU-4*l*-isocyanate (red) and of the product obtained from Co-MFU-4*l*-azide after heating under CO flow at 300 °C (green).[A4]

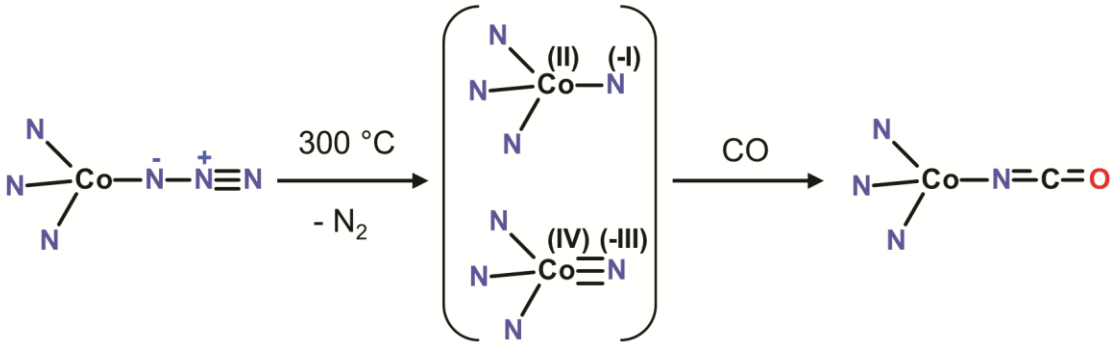

Scheme 5. Schematic representation of the conversion of the Co-azide moiety to Co-isocyanate within the MFU-4*l* framework through a nitrene intermediate.[A4]

2.6.3 Fluoride Ligand

As shown by thermogravimetric studies, heating of Cu-MFU-4*l*-fluoride under hydrogen gas flow at 240 °C results in a weight loss corresponding to the loss of fluoride side-ligands, at which conditions the crystallinity and porosity of the framework are retained. As revealed from the sorption and spectroscopic studies, the product contains the same trigonal-pyramidal Cu(I) centers, as obtained after thermal decomposition of formate side-ligands in Cu-MFU-4*l*-formate. According to DFT calculations, this transformation most probably proceeds *via* heterolytic hydrogen cleavage and involves a copper hydride intermediate (Scheme 6).[A4]

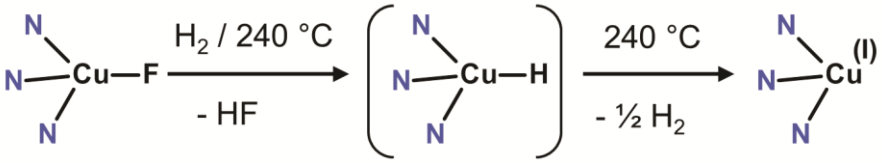

Scheme 6. Schematic representation of the conversion of Cu(II)–F units to Cu(I) in Cu-MFU-4*l*-fluoride through a Cu(II)–H intermediate.[A4]

Heterolytic cleavage of the H_2 molecule has been described for several molecular complexes. For instance, Cu(I) *t*-butoxide reacts with H_2 in the presence of phosphine ligands in a THF solution leading to a hexameric Cu(I)-hydride complex.[72] This complex was shown to reduce α,β-unsaturated carbonyl compounds with high yields and selectivities.[73] The heterogeneous reaction of Cu-MFU-4*l*-fluoride with hydrogen represents the first example for the heterolytic cleavage of the H_2 molecule on single-site active centers within a metal-organic framework indicating a potential of this compound as a catalyst for hydrogenation reactions.[A4]

2.7 Binding of Small Molecules at Cu(I) Centers in MFU-4*l*

2.7.1 Preparation of Cu(I)-MFU-4*l*

As already mentioned above, Cu(I)-MFU-4*l* can be prepared either by heating of Cu-MFU-4*l*-formate under vacuum or inert gas flow at 180 °C, or by heating Cu-MFU-4*l*-fluoride under hydrogen gas flow at 240 °C (Scheme 7, paths (a) and (b), respectively). Alternatively, Cu(I) centers in MFU-4*l* can be generated by direct heating of Cu-MFU-4*l* in DMF at 140 °C (path c in Scheme 7). However, the material, prepared in this way, shows much lower content of active Cu(I) sites, as demonstrated by sorption measurements. Pathway (d), presented in Scheme 7, shows a direct transformation of peripheral Zn–Cl units into Cu(I) sites, for the purpose of which lithium chloride is added in order to form soluble chlorocuprates from insoluble CuCl. This route, again, leads to a framework with lower content of active Cu(I) sites, due to low metal exchange degree.[A4]

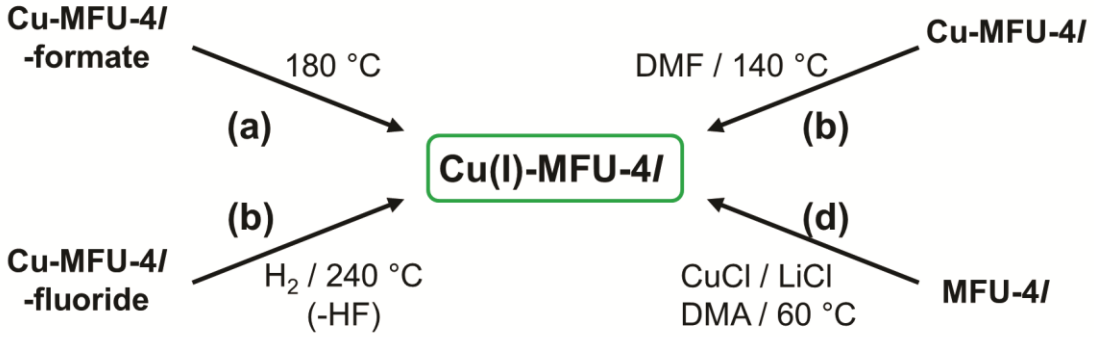

Scheme 7. Different ways for the preparation of Cu(I)-MFU-4*l*.[A4]

2.7.2 Complexes of Cu(I)-MFU-4*l* with Carbon Monoxide and Ethylene

As proven by gas sorption measurements, Cu(I)-MFU-4*l* forms very stable complexes with CO and C_2H_4. The quantity of bound species (approx. 38 $cm^3\ g^{-1}$) is nearly identical for both gases and very close to the calculated value (37.8 $cm^3\ g^{-1}$) based on the analytically determined Cu-content, suggesting formation of stable 1:1 Cu(I)-CO and Cu(I)-C_2H_4 coordination units (Figure 16). The isosteric heat of ethylene chemisorption, as calculated from the adsorption isotherms using the Clausius-Clapeyron equation, is 88±4 kJ mol^{-1}, stays in very good agreement with the DFT-calculated value of 84 kJ mol^{-1} (Table 4).[A3] The binding enthalpy of carbon monoxide is too high and cannot be determined by this method.

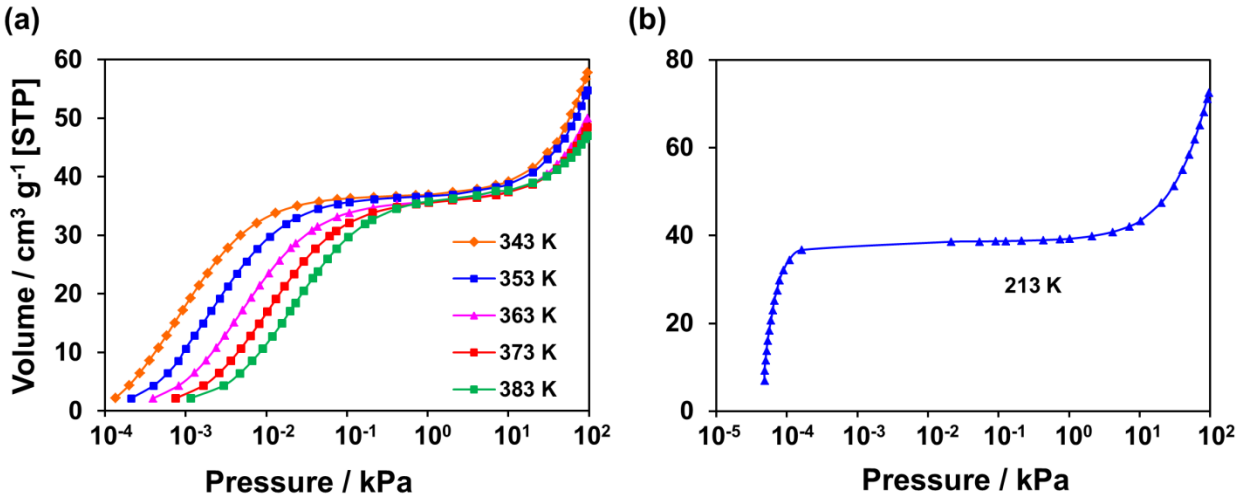

Figure 16. C_2H_4 (a) and CO (b) adsorption isotherms for Cu(I)-MFU-4*l*.[A3]

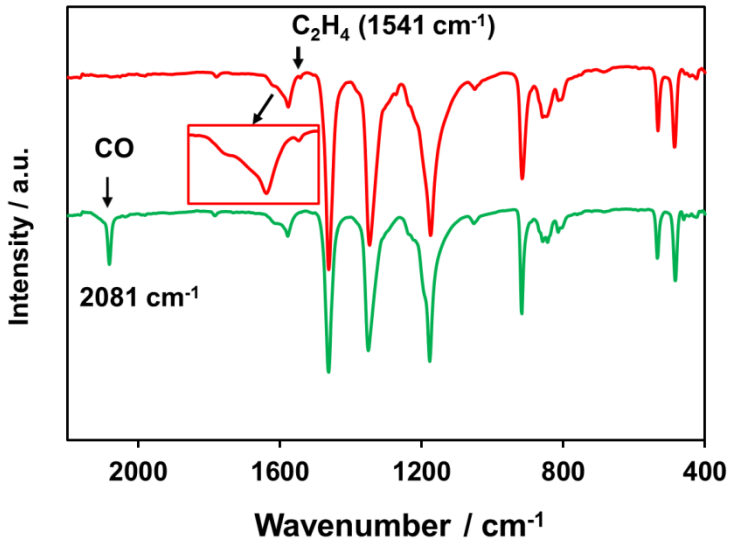

Figure 17. FT-IR spectra of C_2H_4 (red) and CO (green) complexes of Cu(I)-MFU-4*l*.[A3]

The corresponding stretch modes of coordinatively bound CO and C_2H_4 molecules can be observed in the FT-IR spectra at 2081 cm^{-1} and 1541 cm^{-1}, respectively (Figure 17), which stands in good agreement with the DFT-calculated values (2056 and 1517 cm^{-1}, respectively).[A3] Both vibrational frequencies are shifted to lower wavenumbers, as compared to free gas molecules (2143 cm^{-1} for CO and 1623 cm^{-1} for C_2H_4).[74]

2.7.3 Binding of Oxygen, Nitrogen and Hydrogen

An especially interesting property of Cu(I)-MFU-4*l* is the rather strong and reversible binding of small molecules such as O_2, N_2 and H_2. Molecular dioxygen,[75] dinitrogen[75] and dihydrogen[76] complexes have attracted significant attention in coordination chemistry. Up to now, only very few stable MOFs with open metal centers have been described, which are able to bind these molecules. The structural analogue of CuBTC, $Cr_2(BTC)_3$, containing dinuclear Cr(II) paddle wheel units, was shown to bind oxygen at room temperature.[77] However, after the first adsorption step, only approx. 82 % of the total amount of oxygen can be desorbed, indicating, that 18 % of O_2 binds irreversibly. CPO-27 (or MOF-74) represents another well-established MOF family with interesting chemisorption properties. CPO-27-Fe, for instance, shows reversible chemisorption of O_2 and N_2 with initial heats of adsorption of 41 and 35 kJ mol^{-1}, respectively. However, O_2 chemisorption is reversible at -62 °C, whereas at room temperature an irreversible formation of a dimeric Fe(III) peroxide is observed.[78] A weak chemisorption of hydrogen with well-defined 1:1 Ni/H_2 stoichiometry has been reported for CPO-27-Ni, with the initial heat of adsorption of 13.5 kJ mol^{-1},[79] which ranked among the highest values reported for MOFs until the invention of hydrogen complex of Cu(I)-MFU-4*l*,[A3] described in this work.

As shown by gas sorption measurements (Figure 18a-c), the chemisorbed amount for O_2, N_2 and H_2 is the same as for CO and C_2H_4 (38 cm^3 g^{-1}), which indicates a 1:1 stoichiometry of the Cu(I)–A_2 (A_2 = O_2, N_2, H_2) coordination units (see also Figure 18c). The adsorption/desorption isotherms measured at 273–293 K demonstrate full binding reversibility (as exemplified for H_2, Figure 18d). The isosteric heats of O_2, N_2 and H_2 chemisorption (53, 42 and 32 kJ mol^{-1}, respectively), calculated from the measured isotherms, stay in very good agreement with the DFT-calculated values (Table 4). These values lie far over the corresponding physisorption heats, observed at higher loading (> 1.8 mmol g^{-1}, Figure 19). Methane, in contrast, shows only physisorption as indicated by the low value of the heat of adsorption (15 kJ mol^{-1}, Figure 19). This fact suggests Cu(I)-MFU-4*l* as a potential candidate for CH_4/N_2 separation with highly selective N_2 uptake.[A3] In the case of physisorption, CH_4 is adsorbed preferentially over N_2.[80]

Table 4. Experimental and DFT-calculated isosteric heats of adsorption in kJ mol^{-1} in Cu(I)-MFU-4*l*.[A3]

	H_2	**N_2**	**O_2**	**C_2H_4**	**CH_4**
Experiment	32.3±0.4	41.6±0.6	52.6±0.6	88±4	14.9±0.4
DFT-B3LYP	25	44	46	84	15

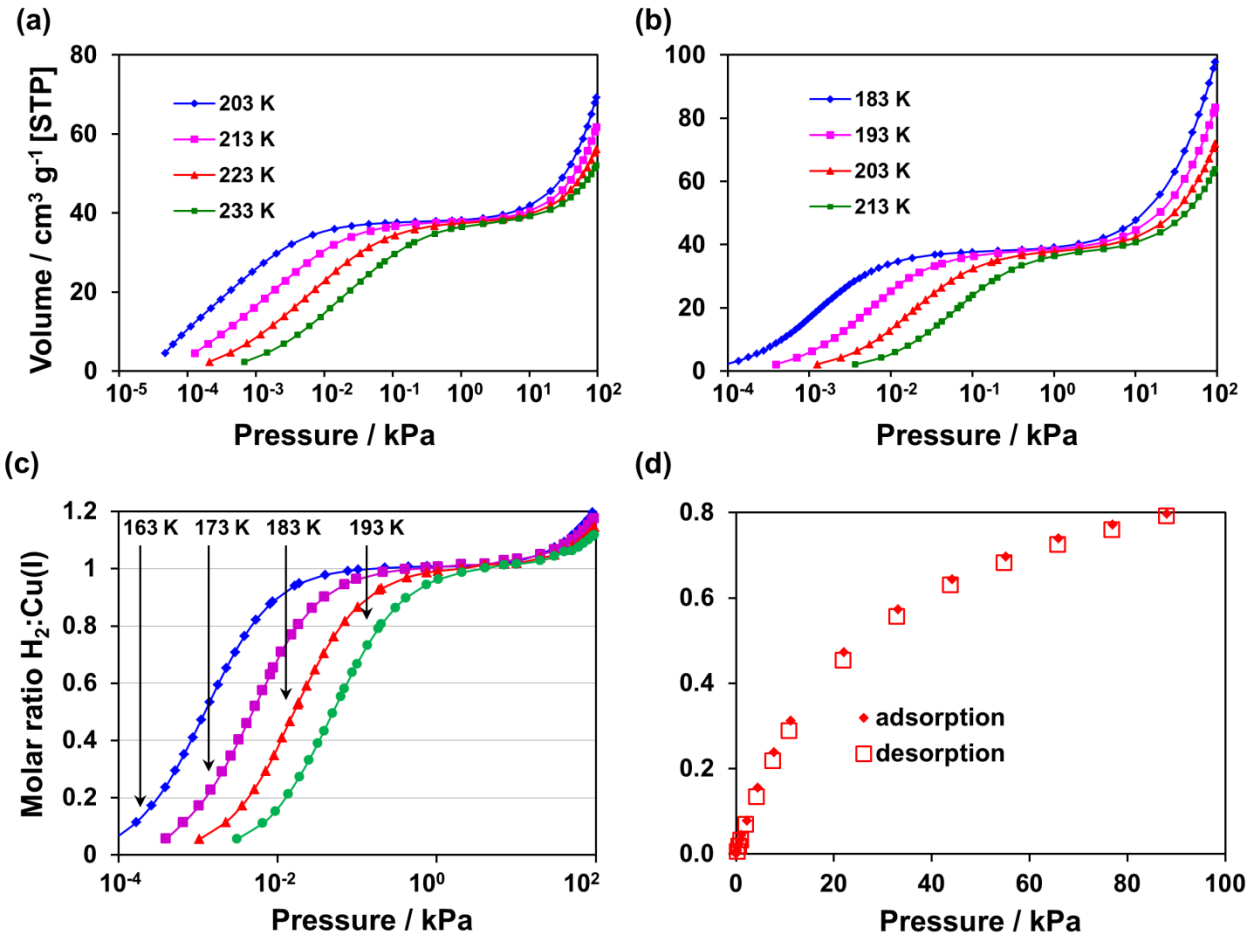

Figure 18. O_2 (a), N_2 (b) and H_2 (c) adsorption isotherms for Cu(I)-MFU-4*l*; (d) H_2 adsorption/desorption isotherms at 273 K for Cu(I)-MFU-4*l*.[A3]

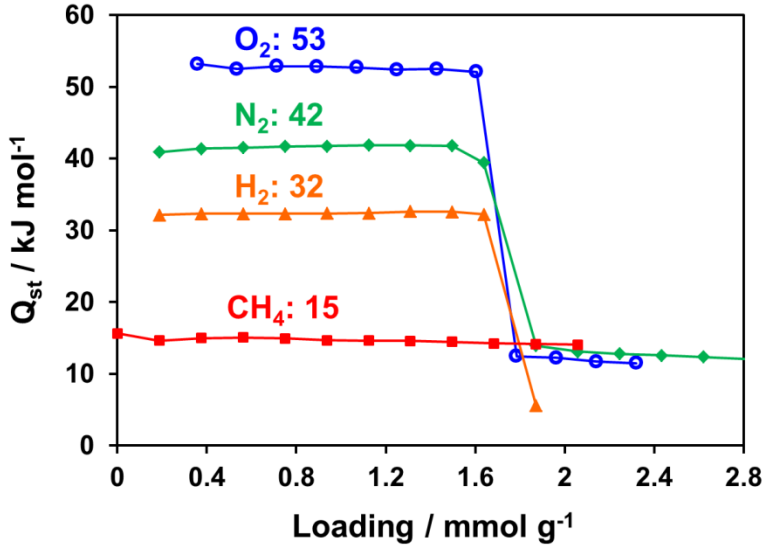

Figure 19. Loading-dependent isosteric heats of adsorption (Q_{st}) for different gases in Cu(I)-MFU-4*l*.[A3]

The unprecedented strong and reversible chemisorption of H_2 is particularly interesting. The Cu(I)–H_2 bonding energy in Cu(I)-MFU-4*l* is significantly higher than typical values for H_2 physisorption (5-10 kJ mol^{-1}),[81] but also significantly lower than in ionic metal hydrides or Kubas-type metal dihydrogen complexes, which normally require high desorption temperatures of 150-400 °C.[82] The hydrogen binding at the Cu(I) centers matches well a suggested optimal binding energy of approx. 25 kJ mol^{-1} for hydrogen storage, allowing accumulation and release of hydrogen at temperatures close to ambient.[81] Thus, hydrogen adsorption/desorption isotherms show, that approx. 80 % of Cu(I) centers are saturated with hydrogen at 0 °C and 1 bar H_2 pressure (Figure 18d). Albeit the amount of chemisorbed hydrogen in Cu(I)-MFU-4*l* is not high (0.34 wt%) due to the low gravimetric density of Cu(I) centers, this value can be achieved at temperature and pressure conditions close to ambient, indicating great potential of Cu(I)-containing materials with higher density of active metal sites for hydrogen storage.[A3]

2.7.4 Spectroscopic Characterization and Structural Models of Bound Molecules

Cu(I)-MFU-4*l*, being air-stable (meaning, that it is not oxidized irreversibly or destroyed in air like many Cu(I)-containing compounds), changes its color reversibly from slightly yellow (in vacuum or under inert gas) to dark-grey in air, which indicates reversible binding of O_2 molecules at the Cu^{I} centers. This process can be followed by *in situ* UV-vis-NIR spectroscopy. Thus, changing argon gas flow to oxygen leads to additional absorption bands in the UV-vis spectrum (Figure 20). The difference spectrum clearly shows two absorption bands, typical for Cu(I)–O_2 complexes: a d→d transition of Cu^{2+} ions at 581 nm and a π^*→d ligand-to-metal charge transfer (LMCT) transition at ca. 457 nm (such species are normally considered as Cu(II) superoxides Cu(II)–$O_2^{\bullet}$).[83] Due to very low reflectance of Cu(I)-MFU-4*l* under oxygen atmosphere at wavelength below 500 nm, the position of the CT band cannot be determined accurately.[A3]

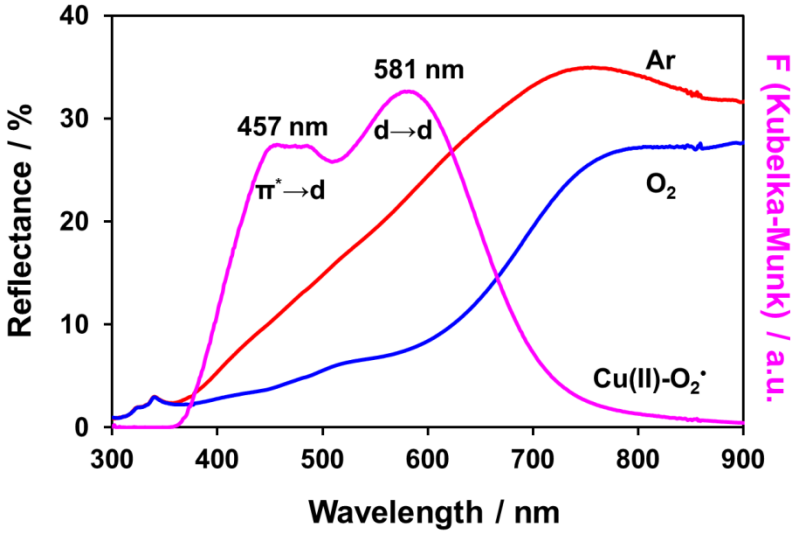

Figure 20. In situ UV-vis-NIR spectra of Cu(I)-MFU-4*l* under argon and oxygen gas flow at room temperature and the difference spectrum, showing the absorbance of the Cu(I)–O_2 complex.[A3]

The binding of nitrogen can be followed by diffuse reflectance infrared Fourier transform (DRIFT) spectroscopy. Thus, changing argon gas flow to nitrogen leads to a significant increase of the intensity of the absorption band at 2242 cm^{-1} (Figure 21). This band is also visible under Ar, which is probably due to a nitrogen impurity in argon gas. This band corresponds to the IR-active N–N bond stretch and is typical for Cu(I)–N_2 adducts, as previously described in the literature.[84] Similar value of 2215 cm^{-1} was also obtained from the DFT calculations. Similar to CO and C_2H_4, the observed N–N vibrational frequency is shifted to lower wavenumbers as compared to the free N_2 molecule (2331 cm^{-1}).[74]

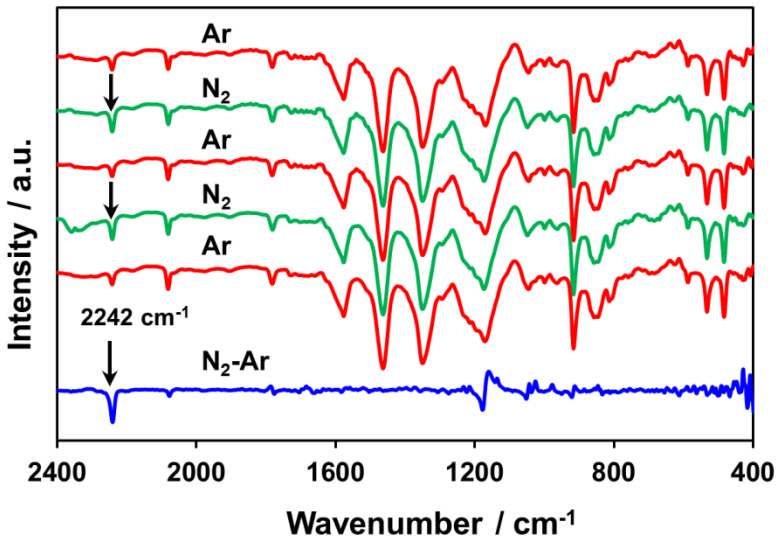

Figure 21. In situ DRIFT spectra of Cu(I)-MFU-4*l* under Ar (red) and N_2 (blue) gas flow at room temperature the difference spectrum, showing the absorbance of the Cu(I)–N_2 complex.[A3]

DFT-calculated geometries of the observed Cu(I)–H_2, N_2, O_2 and C_2H_4 complexes in the Kuratowski unit are presented in Figure 28. According to these, H_2 binds in the η^2 (side-on) mode with a H–H bond distance of 0.83 Å and a Cu–H bond distance of 1.66 Å (Figure 22a). N_2 binds in the η^1 (end-on) mode with a N–N bond distance of 1.12 Å and a Cu–N bond distance of 1.83 Å , the Cu–N–N angle in the latter compound is 180° (Figure 22b). O_2 binds also in the η^1 (end-on) mode with a O–O bond distance of 1.29 Å , a Cu–O bond distance of 1.92 Å and a Cu–O–O angle of 105.7° (Figure 22c). C_2H_4 forms a η^2 (side-on) complex with a C–C bond distance of 1.39 Å and a Cu–C bond distance of 2.03 Å (Figure 22d). All bond distances within the coordinated species are elongated as compared to corresponding free molecules (0.74, 1.10, 1.21 and 1.34 Å for H_2, N_2, O_2 and C_2H_4, respectively),[74] which stays in agreement with the experimentally observed red shifts of the stretch frequencies for N_2 and C_2H_4.[A3]

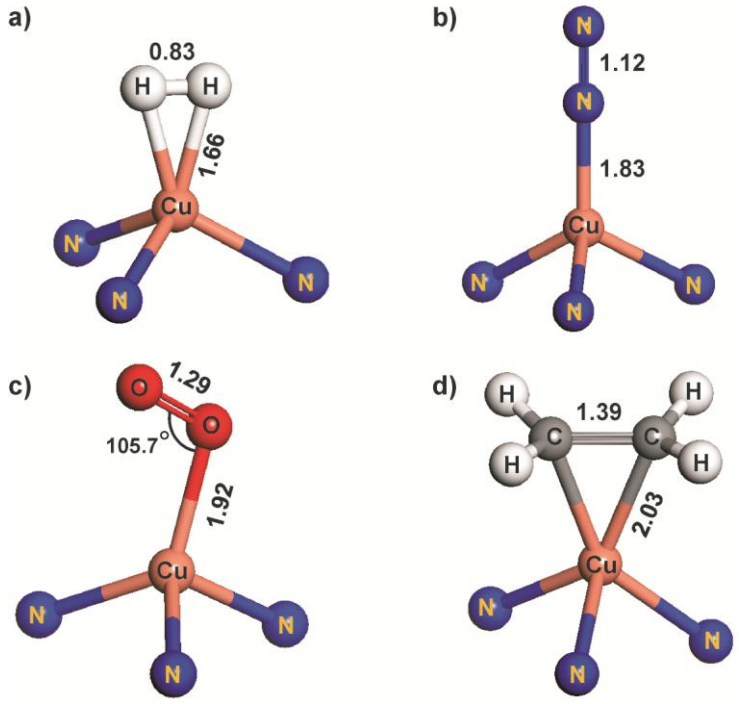

Figure 22. Binding geometries for H_2 (a), N_2 (b), O_2 (c) and C_2H_4 (d) at the Cu(I) sites within the Kuratowski unit of MFU-4*l* as obtained from the DFT calculations (atomic distances in Å).[A3]

These studies represent the first characterization of Cu(I)–H_2 and Cu(I)–N_2 complexes formed on chemically well-defined Cu(I) centers in a porous material. Also molecular dihydrogen and dinitrogen complexes of Cu(I) are not known up to now. The first experimental proof for the formation of a Cu(I)–H_2 complex has been obtained by IR investigations on monomeric CuCl embedded in an Ar matrix, which suggested that H_2 binds in the side-on coordination mode.[85] H_2[86,87] and N_2[84] chemisorption has also been described on copper-exchanged zeolites. Cu(I)–H_2 and Cu(I)–N_2 adducts in zeolites have been characterized by spectroscopic methods (mainly IR spectroscopy)[84,86] and inelastic neutron scattering (INS).[87] The isosteric heat of H_2 adsorption in Cu(I)-ZSM-5 decreases from 73 kJ mol^{-1} at lowest loading to 40 kJ mol^{-1} at higher loading,[88] indicating that Cu(I) sites are not uniform (in contrast to Cu(I)-MFU-4*l*, where the isosteric heat of adsorption is nearly constant over the whole chemisorption range).

2.8 Binding of N_2O and CO_2 at Cu(I) and Li(I) Centers in MFU-4*l*

Since N_2O, possessing only a weak dipole moment (0.161 D), is isoelectronic with CO_2 and has very similar physical and physisorption properties,[89] a comparison of the interaction strengths of N_2O and CO_2 molecules with coordinatively unsaturated Cu(I) and Li(I) centers in MFU-4*l* framework can help to elucidate the Lewis-acidic properties of these metal ions and to find an optimized framework for selective N_2O adsorption. An advantage of such studies *via* the gas sorption in a metal-organic framework is that the coordination environment of the metal sites is well defined and not influenced by the solvent molecules, so that the Lewis acidity can be assessed directly. Additionally, N_2O is one of the most powerful greenhouse[90] and ozone-depleting[91] gases and thus its removal from industrial waste gases remains an important task.[92] However, adsorption of N_2O has only rarely been studied so far. To the best of my knowledge, it was only once described for MOFs (MOF-5 and MOF-177)[93] and a few times for other porous materials such as active carbons[94] and zeolites.[93,95]

Li-MFU-4*l*, containing trigonal-pyramidally coordinated Li^+ ions (similarly to Cu^+ in Cu(I)-MFU-4*l*), was prepared *via* postsynthetic metal exchange from MFU-4*l* and LiCl in DMF at 60 °C. Similar to a previously described metal exchange with other metal salts, approx. 2 of 4 Zn^{2+} ions in the SBU are substituted under these exchange conditions leading to a framework with the composition $[Li_2Zn_3Cl_2(BTDD)_3]$.[A5]

As revealed from the adsorption isotherms, the isosteric heats of CO_2 adsorption in MFU-4*l* and Cu(I)-MFU-4*l* are nearly the same, amounting to ca. 16 kJ mol^{-1} (Figure 23). This low value is typical for physisorption and indicates that no chemical bond is established between the metal sites and the CO_2 molecules. Li-MFU-4*l*, in contrast, shows considerably higher isosteric heat of CO_2 adsorption (22.7 kJ mol^{-1} at 0.35 mmol g^{-1} loading, Table 5 and Figure 23).

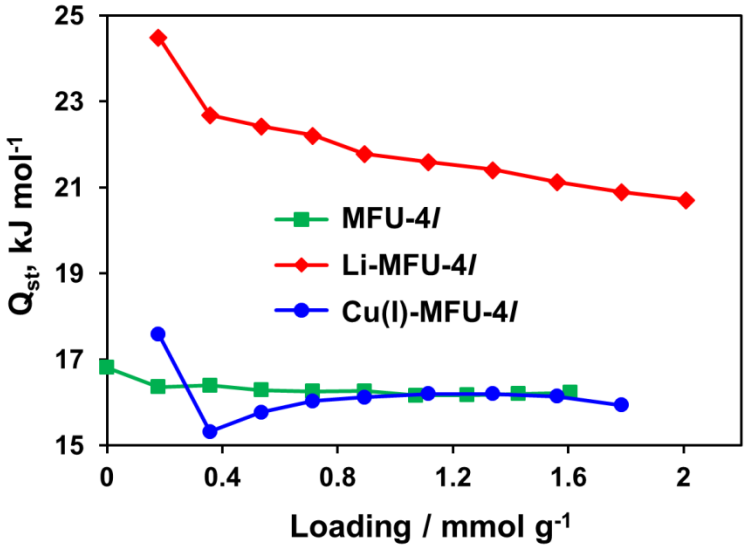

Figure 23. Dependencies of the isosteric heat of CO_2 adsorption on loading in MFU-4*l* frameworks.[A5]

Table 5. Experimental and DFT-calculated binding energies for CO_2 and N_2O in MFU-4*l* derivatives.[A5]

Framework	Peripheral unit	CO_2 binding energy		N_2O binding energy	
		experimental[a]	DFT	experimental[a]	DFT
MFU-4*l*	Zn–Cl	16.4±0.1	17	17.9±0.3	18
Li-MFU-4*l*	Li(I)	22.7±0.9	25	23.6±0.2	25
Cu(I)-MFU-4*l*	Cu(I)	15.3±0.5	18	30.8±1.4	33

[a] isosteric heat of adsorption at 0.35 mmol g^{-1} loading.

This higher value corresponds to a weak interaction of CO_2 molecules with Li^+ ions. The situation is different in the case of N_2O. MFU-4*l* shows again quite low value of ca. 17 kJ mol^{-1}, corresponding to physisorption (Figure 24). Such behavior of MFU-4*l* can be easily understood, taking into account the fact that Zn(II)–Cl units would require an energetically unfavorable distortion of the tetrahedral coordination geometry upon coordination of CO_2 or N_2O. Li-MFU-4*l* shows isosteric heat of N_2O adsorption similar to the value for CO_2 (23.6 kJ mol^{-1} at 0.35 mmol g^{-1} loading, Table 5 and Figure 24). The behavior of Li-MFU-4*l* can be well explained within the HSAB (hard and soft (Lewis) acids and bases) concept.[96] Due to this concept, Li^+ ions are hard Lewis acids with high charge density (chemical hardness η = 35.12 eV), whereas CO_2 and N_2O possess quite similar moderate chemical hardness as Lewis bases (8.8 and 7.6 eV, respectively).[97] This results in a similar moderate binding of CO_2 and N_2O to Li^+ ions, as also confirmed by DFT calculations (Table 5).[A5]

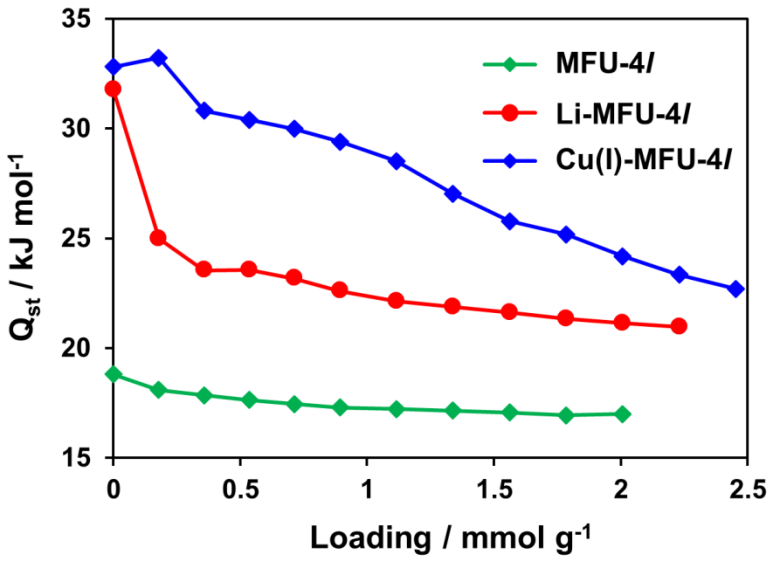

Figure 24. Dependencies of the isosteric heat of N_2O adsorption on loading in MFU-4*l* frameworks.[A5]

Cu(I)-MFU-4*l*, in contrast, shows the highest isosteric heat of N_2O adsorption (30.8 kJ mol^{-1} at 0.35 mmol g^{-1} loading, Table 5 and Figure 24). In terms of the HSAB concept, Cu(I) is a soft Lewis acid with low charge density (chemical hardness η = 6.28 eV)[97] and thus it is not surprising that CO_2 doesn't bind to Cu(I). However, a relatively strong binding of N_2O on Cu(I) centers cannot be explained easily within the HSAB concept unless N_2O is a slightly softer Lewis base as compared to CO_2. This fact underscores the specific character of the Cu(I)–N_2O bonding interaction. The high binding energy for N_2O on Cu(I) centers is also confirmed by DFT (Table 5). The calculated binding geometry reveals an almost linear orientation of the N_2O molecule (with respect to the Cu–N bond) and a Cu–N distance of 1.94 Å (Figure 25a), in contrast to Li-MFU-4*l* with 2.35 Å Li–N distance and binding geometry rather typical for Van der Waals interactions (Figure 25b). These results speak for a weak coordinative bond between Cu(I) and N_2O, which might be related to the charge-donating properties of Cu(I) as well as to the electron accepting properties of N_2O.[97] Weak binding of N_2O molecules to Cu(I) sites in Cu(I)-ZSM-5 has been observed previously by IR spectroscopy at 110–120 K.[98] Due to its poor coordination strength (N_2O possesses a low dipole moment and weak σ-donor and π-acceptor properties),[99] N_2O complexes are very rare and have so far only been described for Ru^{II} and V^{III}.[100] Thus, binding of N_2O on Cu(I) centers in MFU-4*l* is of general interest for coordination chemistry and should be considered in the design of frameworks for the selective N_2O adsorption.[A5]

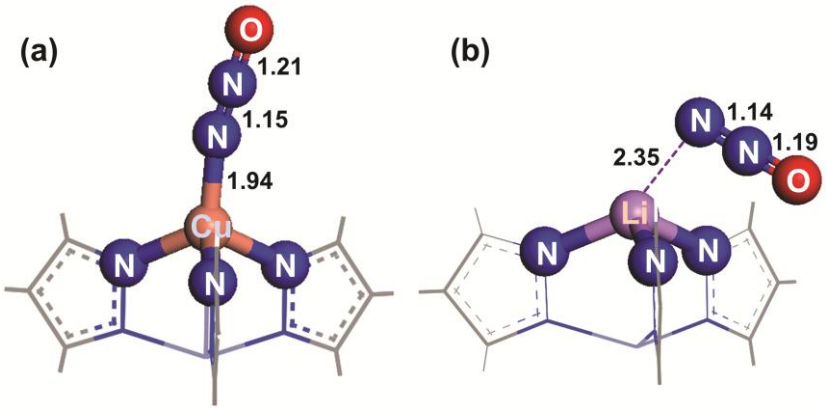

Figure 25. N_2O binding geometries for the Cu(I) (a) and Li(I) (b) sites within the Kuratowski unit of MFU-4*l* as obtained from DFT calculations (atomic distances in Å).[A5]

3 Conclusions and Outlook

This work represents the synthesis and systematic study of heterometallic derivatives of MFU-4*l* – a novel metal-organic framework, which was synthesized and characterized for the first time. The desired large bistriazolate H_2-BTDD ligand was successfully synthesized in a highly efficient three-step procedure. Starting from this ligand, the MFU-4*l* framework, a large-pore member of the MFU-4 family, was prepared in high yield. MFU-4*l* possesses large apertures (9.1 Å), allowing free diffusion of typical substrate molecules. Moreover, MFU-4*l* is highly porous and shows high hydrolytic and thermal stability. These properties, combined with the presence of coordinatively unsaturated, substrate-accessible metal sites, show that MFU-4*l* framework is a generally suitable candidate for catalytic applications (section 2.3).

All attempts to synthesize a Co-analogue of MFU-4*l* directly, starting from the H_2-BTDD ligand and different cobalt salts, were unsuccessful. However, another synthetic approach, based on postsynthetic metal exchange, led to the desired Co-substituted MFU-4*l* framework. In a similar way, Mn-, Fe-, Ni-, Cu- and Li-derivatives of MFU-4*l* were also prepared. These exchange reactions in MFU-4*l* were augmented by the substitution of chloride side-ligands by different monoanionic ligands. Using this strategy, a large variety of heterometallic MFU-4*l* frameworks of the general formula $[M_xZn_{(5-x)}L_4(BTDD)_3]$, where M = Mn(II), Fe(II), Co(II), Ni(II) or Cu(II) and L = NO_2^-, NO_3^-, $CF_3SO_3^-$, N_3^-, $HCOO^-$, CH_3COO^-, NCO^- and F^-, was prepared (section 2.4).

Measurements of the isosteric heat of oxygen adsorption have shown that none of these frameworks is able to bind oxygen at low temperature. Nevertheless, Co-, Ni- and Cu-derivatives of MFU-4*l* showed catalytic activity in the liquid-phase oxidation of ethylbenzene with air under mild conditions. Additionally, Co-MFU-4*l* was found to be catalytically active in the heterogeneous gas-phase oxidation of carbon monoxide with molecular oxygen, as described in the section 2.5. Taking into account the fact that Co(II) centers in Co-MFU-4*l* are not able to bind oxygen, as shown by sorption and spectroscopic measurements, it can be assumed that the reactivity in the last case is rather related to the active Co-sites which are present as defects in the framework and not to the regular Co(II)–Cl units. Besides the lack of reactivity of Co–Cl units in the MFU-4*l* framework, the problem of unselective oxidation with a Co-containing catalyst was realized, after the same reaction was performed with methane instead of CO. It resulted in a full oxidation of methane and formation of CO_2, which is not surprising, since the mechanism of oxidation reactions, catalyzed by Co(II), normally involves highly active radical species, which react unselectively. In the case of CH_4, CO_2 is formed, because all intermediate oxidation products (CH_3OH, CH_2O and HCOOH) react faster than CH_4.

The first problem (low reactivity of the M(II)–Cl units in the MFU-4*l* framework) can be understood, when referring to the results described in section 2.8. Li-MFU-4*l*, containing trigonal-pyramidally coordinated Li^+ ions without a side-ligand, showed an enhanced heat of adsorption for CO_2 and N_2O molecules, which is ascribed to a Lewis-acidic character of Li^+ ions. MFU-4*l*, in contrast, showed only physisorption for both molecules, although Zn^{2+} itself is a stronger Lewis

acid (possessing higher charge density) as Li^+. The reason for such behavior is that Zn(II)–Cl units in the MFU-4*l* framework require an energetically unfavorable distortion from the tetrahedral coordination geometry upon binding of additional molecules. Another reason for the inertness of the Co(II)–Cl units towards oxygen binding was discovered by DFT calculations, described in reference [A4]. According to these studies, binding of the O_2 molecule at the Co(II) center would result in a change of the spin state from high-spin to low-spin, which involves a quite high energetic barrier. However, DFT results also indicate that even Mn(II)–Cl and Fe(II)–Cl units, which would not require a change of the spin state upon oxygen binding, will not form thermodynamically stable complexes with O_2. DFT calculations predict that only strongly basic side-ligands such as hydroxide, hydride or amide at M(II) sites (where M = Mn, Fe and Co) in the MFU-4*l* framework would enable oxygen binding. Unfortunately, all attempts to prepare such derivatives failed so far since strongly basic ligands destroy the MFU-4*l* framework. All these observations point out that M(II)–Cl units are not the best choice for binding of small molecules and catalytic applications, and trigonal-pyramidally coordinated M(I) ions (where M is a redox active metal ion) should be more preferable as active sites in the MFU-4*l* framework.

In the row of 3*d* transition metal ions, which were introduced into the MFU-4*l* framework, an oxidation state of +1 is most common for copper. Although conventional synthetic methods such as heterogeneous reduction of Cu(II)-MFU-4*l* in a liquid phase or direct metal exchange in MFU-4*l* allowed to introduce Cu(I) ions into the MFU-4*l* framework, the products thus obtained were not analytically pure. Searching for an alternative method for the generation of Cu(I) sites, a thermal transformation of formate side-ligands was considered as a possible preparative route. This approach led indeed to a selective formation of Cu(I) sites from the Cu(II)-formate units in the MFU-4*l* framework. At the same time, the parent Zn-formate moieties were selectively transformed to Zn–H species upon thermal treatment, the latter were shown to act as a hydride-transfer and reducing agent. Thus, thermal transformation of formate ligands represents a novel powerful approach for the generation of active metal sites. Reaction products in the case of other studied transition metal ions could not be characterized clearly and require further investigations. Only in the case of Co, a Co(I) species, stabilized by CO ligands, could be detected (section 2.6).

Further investigations on thermal transformations of side-ligands in the MFU-4*l* framework have shown that the same Cu(I) centers can be generated from Cu(II)-fluoride units upon heterogeneous reaction with H_2 gas at 240 °C. According to DFT calculations, this transformation most probably proceeds *via* heterolysis of H_2 molecule, involving a Cu(II)-hydride intermediate, and thus represents the first example for the heterolytic hydrogen cleavage on a single-site active center within a metal-organic framework indicating a potential of Cu-MFU-4*l*-fluoride as a catalyst for hydrogenation reactions. Interestingly, Cu(II)–Cl units undergo the same transformation, but at considerably higher temperature (350 °C), which causes a partial decomposition of the framework. The reason for higher reactivity of fluoride ligands in this transformation is that heterolytic hydrogen cleavage at a single-site active center requires a Lewis-acidic metal site and a basic ligand. Both properties are more pronounced in the case of

fluoride, due to its higher electronegativity and basicity. The high stability of the H–F bond also contributes to the reduction of activation energy. Another example of the selective transformation at the single-site active center was the heterogeneous conversion of Co-azide moiety to Co-isocyanate at 300 °C under CO gas. This transformation most probably proceeds *via* a nitrene intermediate and thus indicates that Co-MFU-4*l*-azide could be potentially interesting as an N-atom transfer reagent (section 2.6).

Detailed investigations on Cu(I)-MFU-4*l* showed that this framework possesses unique chemisorption properties, described in the section 2.7. Thus, with respect to Cu(I) sites, it forms very stable 1:1 complexes with ethylene and carbon monoxide. Moreover, trigonal-pyramidally coordinated Cu(I) centers in MFU-4*l* show quite strong and reversible binding of oxygen, nitrogen and hydrogen, upon which complexes with the same 1:1 stoichiometry are being formed. These studies represent an important characterization of chemically well-defined Cu(I)–H_2 and Cu(I)–N_2 complexes, which have never been described before. Particularly interesting is an unusually strong and reversible chemisorption of H_2. The Cu(I)–H_2 binding energy in Cu(I)-MFU-4*l* (32 kJ mol^{-1}) is significantly higher than all the values reported for fully reversible H_2 adsorption before (for instance, 13.5 kJ mol^{-1} for CPO-27-Ni - the single reported example of weak hydrogen chemisorption in a MOF material) and matches well a suggested optimal binding energy of approx. 25 kJ mol^{-1} for hydrogen storage, allowing accumulation and release of hydrogen at temperatures close to ambient. Finally, as described in the section 2.8, Cu(I)-MFU-4*l* shows quite strong binding of N_2O, which is a very weak ligand and has been only very rarely shown to build structurally well-defined metal complexes. All this observations underscore a unique character of trigonal-pyramidally coordinated Cu(I) sites and show that Cu(I)-MFU-4*l* is an exceptional framework with a large potential for applications such as sensing, selective adsorption or hydrogen storage.

Unfortunately, all attempts to use Cu(I)-MFU-4*l* as a catalyst in heterogeneous gas-phase oxidation reactions, failed so far. Thus, treatment of the oxygen complex of this framework under methane, ethylene or carbon monoxide gas flow resulted either in a simple removal of O_2 molecule from Cu(I) sites (in the case of CH_4) or in the substitution of O_2 bound at Cu(I) sites by C_2H_4 or CO molecules. Similar results were obtained, when the reaction was performed in a reversed way. In this case, a treatment of a Cu(I)-MFU-4*l* complex with C_2H_4 or CO under oxygen gas flow resulted only in evolution of ethylene or carbon monoxide. Also the usage of a CH_4/O_2 gas mixture flowed over Cu(I)-MFU-4*l* didn't result in the oxidation of methane. The first reason for the missing reactivity might be an insufficient stability of the Cu(I)–O_2 complex, which results in its dissociation before it can react. The second reason is that a trigonal-pyramidally coordinated Cu(I) site in MFU-4*l* can obviously coordinate only one molecule – even in the case of such strongly coordinating ligand as CO, the second molecules doesn't bind at the same Cu(I) site. However, binding of both, substrate and oxidant, molecules (for instance, C_2H_4 and O_2) at the same Cu(I) site would be necessary in order to achieve a reaction under conditions, where a Cu(I)–O_2 complex remains stable. Another possibility would be a binding of these molecules at the neighboring Cu(I) sites, but the distance between these sites in the MFU-4*l* framework is too

large in order to allow a reaction between bound molecules. It should be also noted, that a Cu(I)–O_2 complex in the MFU-4*l* framework is actually a superoxide Cu(II)–$O_2^{\bullet}$, as revealed from spectroscopic measurements. Thus, even if it would be active in any oxidation reaction, the problem of non-selective oxidation, described previously for Co-MFU-4*l*, could still remain, due to a radical character of the reaction. For this reason, an alternative approach is required, in order to achieve a successful heterogeneous oxidation catalysis by a Cu(I)-MFU-4*l* framework. One possible way could be a pre-oxidation of Cu(I) sites by N_2O gas, occasionally practiced in zeolite chemistry. First studies, not presented in this work, have shown, that Cu(I)-MFU-4*l* reacts with N_2O at 260 °C forming highly active species, which then react with H_2 already at -33 °C. The formation of Cu(III)=O species, suggested by some investigators but never characterized in substance, is supposed. Such species could be able to perform a selective oxygenation of aliphatic C–H bonds in a non-radical way, as it is done by FeO^+ species, supposed in the soluble methane monooxygenase and Fe-zeolites.[101]

In conclusion, the MFU-4*l* family represents a versatile “construction kit” which allows to build a broad range of robust and readily available metal-organic frameworks with desired composition and reactivity. Some heterometallic MFU-4*l* derivatives show exciting features such as a heterolytic hydrogen cleavage or reversible binding of H_2, N_2 and O_2 molecules, providing motivation for further investigations. For instance, the catalytic activity of Cu-MFU-4*l*-fluoride in heterogeneous hydrogenation reactions should be tested. Characterization of copper species, obtained after heterogeneous oxidation of Cu(I)-MFU-4*l* by N_2O gas, and investigations on their reactivity are highly interesting. Another highly rewarding research direction might be to introduce low-valent metal sites from transition metal elements frequently employed in organometallic catalytic transformations, such as Mn(I) or Rh(I), which could enable a dissociative hydrogen binding or even activation of aliphatic hydrocarbons.

4 Zusammenfassung und Ausblick

Die vorliegende Arbeit beschreibt Synthesen und systematische Untersuchungen von heterometallischen Derivaten von MFU-4*l*, einer neuartigen erstmal synthetisierten und charakterisierten Metall-organischen Gerüstverbindung. Der entsprechend große H_2-BTDD Bis-triazolat-Ligand konnte in einer hocheffizienten Dreistufensynthese wie geplant hergestellt werden. Ausgehend von diesem Liganden wurde MFU-4*l* mit hoher Ausbeute erfolgreich synthetisiert. MFU-4*l* ist ein großporiges Mitglied der MFU-4 Familie, welches 9.1 Å große Porenöffnungen besitzt und damit eine freie Diffusion von typischen Substratmolekülen erlaubt. Außerdem ist MFU-4*l* hochporös und weist eine hohe hydrolytische und thermische Stabilität auf. Diese Eigenschaften, zusammen mit zugänglichen koordinativ ungesättigten Metallzentren, zeigen, dass MFU-4*l* für katalytische Anwendungen grundsätzlich geeignet ist (Abschnitt 2.3).

Sämtliche Versuche, ein Cobalt-Analogon von MFU-4*l* ausgehend von dem H_2-BTDD Ligand und unterschiedlichen Kobaltsalzen, direkt zu synthetisieren, waren erfolglos. Jedoch führte ein anderer Ansatz, basierend auf einem postsynthetischen Metallaustausch, zum gewünschten Co-substituierten MFU-4*l*-Netzwerk. In einer ähnlichen Weise wurden auch Mn-, Fe-, Ni-, Cu- und Li-Derivate von MFU-4*l* hergestellt. Diese Austauschreaktionen in MFU-4*l* wurden ergänzend mit der Substitution der Chlorid-Seitenliganden durch unterschiedliche monoanionische Liganden erweitert. Mit Hilfe dieser Strategie wurde eine große Vielfalt von heterometallischen MFU-4*l*-Netzwerken mit der Zusammensetzung $[M_xZn_{(5-x)}L_4(BTDD)_3]$ (M = Mn(II), Fe(II), Co(II), Ni(II) oder Cu(II) und L = NO_2^-, NO_3^-, $CF_3SO_3^-$, N_3^-, $HCOO^-$, CH_3COO^-, NCO^-, F^-) hergestellt (Abschnitt 2.4).

Messungen der isosteren Sorptionswärme von Sauerstoff haben gezeigt, dass keines von diesen Netzwerken in der Lage ist, Sauerstoff bei tiefen Temperaturen zu binden. Dennoch zeigten Co-, Ni-, und Cu-Derivate von MFU-4*l* katalytische Aktivität in der Flüssigphasen-Oxidation von Ethylbenzol mit Luft unter milden Bedingungen. Co-MFU-4*l* war außerdem katalytisch aktiv in der heterogenen Gasphasenoxidation von Kohlenmonoxid mit molekularem Sauerstoff (Abschnitt 2.5). Unter Berücksichtigung der Tatsache, dass Co(II)-Zentren in Co-MFU-4*l* keinen Sauerstoff binden, was durch Sorptions- und spektroskopische Messungen bewiesen wurde, kann vermutet werden, dass die Reaktivität im letzteren Fall eher auf aktive Co-Zentren zurückzuführen ist, die als Defekte im Netzwerk vorliegen und nicht auf die regulären Co(II)–Cl-Einheiten. Neben der ungenügenden Reaktivität der Co–Cl-Einheiten im MFU-4*l*-Netzwerk, stellte die unselektive Oxidation ein Problem dar. So führte der Versuch in der gleichen Reaktion Methan anstatt von CO einzusetzen zu einer kompletten Oxidation und Bildung von CO_2. Dieses Ergebnis ist nicht verwunderlich, da die Co(II)-katalysierten Oxidationsreaktionen in der Regel über hochreaktive Radikalspezies laufen, was zu unselektiven Reaktionen führt. Im Fall von CH_4, wird CO_2 als Produkt gebildet, da sämtliche Zwischenprodukte (CH_3OH, CH_2O und HCOOH) schneller oxidiert werden als Methan.

Die Ursache für die geringe Reaktivität von M(II)–Cl-Einheiten im MFU-4*l*-Netzwerk kann mit Hilfe von Ergebnissen, welche im Abschnitt 2.8 beschrieben sind, verstanden werden. Li-MFU-

4*l*, welches trigonal-pyramidal koordinierte Li^+-Ionen ohne Seitenliganden enthält, zeigte eine erhöhte Sorptionswärme für CO_2 und N_2O Moleküle, was auf Lewis-saure Eigenschaften von Li^+-Ionen zurückzuführen ist. MFU-4*l* zeigte im Gegensatz dazu nur eine Physisorption von beiden Molekülen, obwohl Zn^{2+} eine höhere Ladungsdichte als Li^+ besitzt und somit eine stärkere Lewis-Säure sein sollte. Ein Grund für dieses Verhalten liegt darin, dass die Bindung von zusätzlichen Molekülen an die Zn(II)–Cl-Einheiten im MFU-4*l*-Netzwerk zu einer energetisch ungünstigen Verzerrung der tetraedrischen Koordinationsumgebung von Zn^{2+}-Ionen führen würde. Ein weiterer Grund für die Trägheit von Co(II)–Cl-Einheiten gegenüber O_2-Bindung wurde mit Hilfe von DFT-Rechnungen, beschrieben in Referenz [A4], entdeckt. Laut diesen Untersuchungen würde die Bindung eines O_2-Moleküls an das Co(II)-Zentrum zu einer Änderung des Spinzustands von high-spin zu low-spin führen, welche eine hohe Energiebarriere aufweist. Des Weiteren zeigten DFT-Rechnungen, dass selbst die Mn(II)–Cl- und Fe(II)–Cl-Einheiten, bei welchen die Sauerstoffbindung keine Änderung des Spinzustands zur Folge hätte, keine thermodynamisch stabilen O_2-Komplexe bilden würden. Laut diesen Rechnungen würden nur stark basische Seitenliganden wie Hydroxid, Hydrid oder Amid an Mn(II)-, Fe(II)- und Co(II)-Zentren im MFU-4*l*-Netzwerk eine Sauerstoffbindung ermöglichen. Solche Derivate konnten jedoch nicht hergestellt werden, da stark basische Liganden das MFU-4*l* Netzwerk zerstören. Diese Beobachtungen weisen darauf hin, dass die M(II)–Cl-Einheiten nicht die beste Wahl für die Bindung von kleinen Molekülen und katalytische Anwendungen darstellen. Basierend auf den bereits erwähnten Eigenschaften von Li^+-Ionen im MFU-4*l*-Netzwerk, sollten trigonal-pyramidal koordinierte redoxaktive M(I)-Ionen als aktive Zentren die bessere Wahl sein.

In der Reihe der 3*d* Übergangsmetalle, die in das MFU-4*l* Netzwerk eingeführt wurden, ist die Oxidationszahl +1 am meisten bei Cu verbreitet. Auch wenn konventionelle Synthesemethoden, wie die heterogene Reduktion von Cu(II)-MFU-4*l* in der Flüssigphase oder der direkte Metallaustausch im MFU-4*l*, Cu(I)-haltige Netzwerke lieferten, so waren die gewonnenen Produkte analytisch nicht rein. Auf der Suche nach einer alternativen Methode zur Generierung von Cu(I)-Zentren, wurde die thermochemische Umwandlung von Formiat-Seitenliganden als eine mögliche präparative Route in Betracht bezogen. Diese Strategie führte tatsächlich zu einer selektiven Bildung von Cu(I)-Zentren aus Cu(II)-Formiat-Einheiten im MFU-4*l*-Netzwerk. Gleichzeitig wurden Zn-Formiat-Einheiten durch thermische Behandlung selektiv in Zn–H Spezies umgewandelt. Letztere agieren als Hydrid-Transfer- und Reduktionsmittel, was mit der selektiven Umsetzung von Benzoylchlorid zum Benzaldehyd gezeigt wurde. Somit stellt die thermische Umwandlung von Formiat-Liganden einen neuartigen Ansatz zu Generierung von aktiven Metallzentren dar. Im Fall von anderen Übergangsmetallionen konnten die Produkte nicht eindeutig charakterisiert werden und benötigen daher weitere Untersuchungen. Einzig im Fall von Cobalt konnten stabilisierte Co(I)–CO-Spezies nachgewiesen werden (Abschnitt 2.5).

Weitere Untersuchungen von thermischen Umwandlungen der Seitenliganden im MFU-4*l* Netzwerk haben gezeigt, dass die gleichen Cu(I)-Zentren auch durch die heterogene Reaktion von Cu(II)-Fluorid Einheiten mit Wasserstoff bei 240 °C generiert werden können. Laut DFT-Rechnungen verläuft diese Umsetzung am wahrscheinlichsten über das Cu(II)-Hydrid-

Intermediat und stellt somit das erste Beispiel der heterolytischen Wasserstoffspaltung an einem „single-site“ aktiven Zentrum in einem MOF dar. Damit wird das Potential von Cu-MFU-4*l*-Fluorid als Katalysator für heterogene Hydrierungsreaktionen sichtbar. Interessanterweise unterliegen die Cu(II)–Cl Einheiten der gleichen Transformation, allerdings bei einer wesentlich höheren Temperatur (350 °C), was zu einer partiellen Zersetzung des Netzwerkes führt. Die Ursache für eine höhere Reaktivität der Fluorid-Liganden in der heterolytischen Wasserstoffspaltung an einem „single-site“ aktiven Zentrum liegt daran, dass für diese Reaktion ein Lewis-saures Metallzentrum und ein basischer Ligand erforderlich sind. Beide Eigenschaften sind beim Fluorid aufgrund höherer Elektronegativität wesentlich stärker ausgeprägt. Auch die hohe Stabilität der H–F Bindung trägt zur Reduzierung der Aktivierungsenergie bei. Ein weiteres Beispiel für eine selektive Transformation an einem „single-site“ aktiven Zentrum stellt die heterogene Umsetzung der Co-Azid Einheit zum Co-Isocyanat in CO-Gasatmosphäre bei 300 °C dar. Diese Transformation, welche vermutlich über das Nitren-Intermediat verläuft, zeigt das Potential von Co-MFU-4*l*-Azid als N-Übertragungsreagenz (Abschnitt 2.6).

Detaillierte Untersuchungen am Cu(I)-MFU-4*l* haben gezeigt, dass dieses Netzwerk einzigartige Chemisorptionseigenschaften aufweist (Abschnitt 2.7). Bezogen auf Cu(I)-Zentren, bildet es sehr stabile 1:1 Komplexe mit Ethen und Kohlenmonoxid. Des Weiteren zeigen trigonal-pyramidal koordinierte Cu(I) Zentren in MFU-4*l* eine ziemlich starke und reversible Bindung von Sauerstoff, Stickstoff und Wasserstoff, bei der Komplexe mit der gleichen 1:1 Stöchiometrie gebildet werden. Diese Studien stellen eine wichtige Charakterisierung chemisch gut definierter, einheitlicher Cu(I)–H_2 und Cu(I)–N_2 Komplexe dar, welche vorher noch nie in der Literatur beschrieben wurden. Besonders interessant ist dabei die ungewöhnlich starke und reversible Bindung von H_2. Die Cu(I)–H_2 Bindungsenergie in Cu(I)-MFU-4*l* (32 kJ mol^{-1}) ist wesentlich höher als alle bisher berichteten Werte für eine vollständig reversible H_2-Adsorption (z. B. 13.5 kJ mol^{-1} für CPO-27-Ni – das bisher einzige beschriebe Beispiel für eine schwache Wasserstoff-Chemisorption in einem MOF) und entspricht sehr gut der vorgeschlagenen optimalen Sorptionswärme von ca. 25 kJ mol^{-1}, welche eine Speicherung und Freisetzung des Wasserstoffs bei Raumtemperatur erlauben würde. Abschließend, wie im Abschnitt 2.8 beschrieben, zeigt Cu(I)-MFU-4*l* eine relativ starke Bindung von N_2O. Distickstoffmonoxid ist ein sehr schwacher Ligand und bildet nur sehr selten strukturell gut definierte Komplexe mit Metallionen. All diese Beobachtungen unterstreichen den einzigartigen Charakter der trigonal-pyramidal koordinierten Cu(I)-Zentren und zeigen, dass Cu(I)-MFU-4*l* ein beispielhaftes Netzwerk mit großem Potential für technologische Anwendungen wie Sensorik, selektive Adsorption und Wasserstoffspeicherung ist.

Leider blieben alle Versuche, Cu(I)-MFU-4*l* als Katalysator in heterogenen Gasphasen-Oxidationsreaktionen anzuwenden, erfolglos. So endeten die Versuche, den O_2-Komplex von Cu(I)-MFU-4*l* mit Methan-, Ethen- oder Kohlenmonoxid-Gas umzusetzen, entweder in der einfachen Dissoziation des Komplexes (im Fall von CH_4) oder in der Substitution von O_2 an Cu(I)-Zentren durch C_2H_4- bzw. CO-Moleküle. Ähnliche Ergebnisse wurden erzielt, als die Reaktion in umgekehrter Weise versucht wurde. In diesem Fall führte das Erhitzen der

Komplexe von Cu(I)-MFU-4*l* mit C_2H_4 bzw. CO unter O_2-Gasfluss ebenfalls nur zur Dissoziation des jeweiligen Komplexes. Auch die Nutzung eines CH_4/O_2-Gasgemisches, welches über Cu(I)-MFU-4*l* geleitet wurde, führte nicht zur Oxidation von Methan. Der erste Grund für die fehlende Reaktivität könnte in einer ungenügenden Stabilität des Cu(I)–O_2 Komplexes liegen, sodass der Komplex dissoziiert, bevor es zur Reaktion kommen kann. Der zweite Grund liegt darin, dass trigonal-pyramidal koordinierte Cu(I) Zentren im MFU-4*l* offensichtlich nur ein Molekül koordinieren können – sogar im Fall von einem so stark koordinierenden Liganden wie CO. Das zweite Molekül bindet nicht am gleichen Cu(I)-Zentrum. Die Bindung beider Moleküle (Substrat und Oxidans – z. B., C_2H_4 und O_2) am gleichen Cu(I)-Zentrum ist jedoch nötig, um die Reaktion unter milden Bedingungen zu ermöglichen, sodass der Cu(I)–O_2 Komplex stabil bleibt. Eine andere Möglichkeit wäre, diese zwei Moleküle an benachbarten Cu(I)-Zentren zu binden. Allerdings ist der Abstand zwischen solchen Zentren im MFU-4*l* Netzwerk zu groß, um die Reaktion zwischen den gebundenen Molekülen zu erlauben. Es muss auch erwähnt werden, dass der Cu(I)–O_2 Komplex in MFU-4*l* als Superoxid Cu(II)–$O_2^{\bullet}$ vorliegt, was durch spektroskopische Messungen belegt wurde. Daher würde dieser Komplex, wenn überhaupt, eine radikale und möglicherweise unselektive Oxidationsreaktion bewirken. Damit wäre das Problem der unselektiven Oxidation, welches für Co-MFU-4*l* bereits erwähnt wurde, immer noch nicht gelöst. Deswegen ist eine alternative Strategie nötig, um eine erfolgreiche heterogene Oxidationskatalyse mit dem Cu(I)-MFU-4*l*-Netzwerk zu erzielen. Ein möglicher Ansatz wäre eine Voroxidation der Cu(I)-Zentren mit N_2O Gas, was in der Zeolithchemie gelegentlich praktiziert wird. Erste Untersuchungen, die in dieser Arbeit nicht beschrieben sind, haben gezeigt, dass Cu(I)-MFU-4*l* mit N_2O bei 260 °C reagiert. Dabei entstehen hochreaktive Spezies, welche bereits bei -33 °C mit H_2 reagieren. Die Bildung von Cu(III)=O Spezies, welche von einigen Forschern vorgeschlagen aber nie charakterisiert wurden, wird in dieser Reaktion vermutet. Solche Spezies sollten eine nichtradikale selektive Oxidation von aliphatischen C–H Bindungen ermöglichen. So eine Reaktion ist für FeO^+ Spezies, welche in der löslichen Methan-Monooxygenase vermutet werden, bekannt.[101]

Zusammenfassend stellt die MFU-4*l*-Familie ein sehr vielseitiges System dar, welches erlaubt eine breite Palette an robusten und leicht zugänglichen Metall-organischen Gerüstverbindungen gezielt in gewünschter Zusammensetzung und Reaktivität zu konstruieren. Einige heterometallische MFU-4*l*-Derivate zeigen eindrucksvolle Eigenschaften, wie heterolytische Wasserstoffspaltung oder reversible Bindung von H_2, N_2 und O_2, was Anlass für weitere Untersuchungen an MFU-4*l*-Netzwerken gibt. Beispielsweise sollte zukünftig die katalytische Aktivität von Cu-MFU-4*l*-fluorid in heterogenen Hydrierungsreaktionen getestet werden. Die Charakterisierung und Reaktivitätsstudien an Kupferspezies, welche bei der heterogenen Oxidation von Cu(I)-MFU-4*l* mit N_2O entstehen, sind ebenfalls sehr interessant. Eine weitere sehr lohnende Forschungsrichtung wäre die Synthese von MFU-4*l*-Netzwerken mit anderen niedervalenten Metallzentren wie z.B. Mn(I) oder Rh(I), welche eine dissoziative Wasserstoffbindung oder sogar Alkanaktivierung ermöglichen könnten.

5 References

[1] P.B. Weisz, *Annu. Rev. Phys. Chem.* **1970**, *21*, 175-196.

[2] F. Schüth, *Chem. Ing. Tech.* **2005**, *77*, 1399-1416.

[3] C. Perego, R. Millini, *Chem. Soc. Rev*. **2013**, *42*, 3956-3976.

[4] B.F. Hoskins, R. Robson, *J. Am. Chem. Soc.* **1990**, *112*, 1546-1554.

[5] M. Fujita, Y.J. Kwon, S. Washizu, K. Ogura, *J. Am. Chem. Soc.* **1994**, *116*, 1151-1152.

[6] J. Lee, O.K. Farha, J. Roberts, K.A. Scheidt, S.T. Nguyen, J.T. Hupp, *Chem. Soc. Rev*. **2009**, *38*, 1450-1459.

[7] a) S. De Rosa, G. Giordano, T. Granato, A. Katovic, A. Siciliano, F. Tripicchio, *J. Agric. Food Chem*. **2005**, *53*, 8306-8309; b) F. Gándara, A. García-Cortés, C. Cascales, B. Gómez-Lor, E. Gutiérrez-Puebla, M. Iglesias, A. Monge, N. Snejko, *Inorg. Chem*. **2007**, *46*, 3475-3484; c) B. Xiao, H. Hou, Y. Fan, *J. Organomet. Chem*. **2007**, *692*, 2014-2020.

[8] a) M.J. Ingleson, J.P. Barrio, J.-B. Guilbaud, Y.Z. Khimyak, M.J. Rosseinsky, *Chem. Commun*. **2007**, 2680-2682; b) M.H. Alkordi, Y. Liu, R.W. Larsen, J.F. Eubank, M. Eddaoudi, *J. Am. Chem. Soc*. **2008**, *130*, 12639-12641; c) Y. Lu, M. Tonigold, B. Bredenkötter, D. Volkmer, J. Hitzbleck, G. Langstein, *Z. Anorg. Allg. Chem*. **2008**, *634*, 2411-2417; d) M. Tonigold, Y. Lu, B. Bredenkötter, B. Rieger, S. Bahnmüller, J. Hitzbleck, G. Langstein, D. Volkmer, *Angew. Chem.* **2009**, *121*, 7682-7687; *Angew. Chem. Int. Ed.* **2009**, *48*, 7546-7550.

[9] a) K.S. Suslick, P. Bhyrappa, J.-H. Chou, M.E. Kosal, S. Nakagaki, D.W. Smythenry, S.R. Wilson, *Acc. Chem. Res*. **2005**, *38*, 283-291; b) S.-H. Cho, B. Ma, S.T. Nguyen, J.T. Hupp, T.E. Albrecht-Schmitt, *Chem. Commun*. **2006**, 2563-2565.

[10] A. Pramanik, S. Abbina, G. Das, *Polyhedron* **2007**, *26*, 5225-5234.

[11] M. Tonigold, Y. Lu, A. Mavrandonakis, A. Puls, R. Staudt, J. Möllmer, J. Sauer, D. Volkmer, *Chem. Eur. J.* **2011**, *17*, 8671-8695.

[12] J.W. Han, C.L. Hill, *J. Am. Chem. Soc.* **2007**, *129*, 15094-15095.

[13] F.X. Llabrés i Xamena, A. Abad, A. Corma, H. Garcia, *J. Catal.* **2007**, *250*, 294-298.

[14] F.X. Llabrés i Xamena, O. Casanova, R.G. Tailleur, H. Garcia, A. Corma, *J. Catal.* **2008**, *255*, 220-227.

[15] N.V. Maksimchuk, M.N. Timofeeva, M.S. Melgunov, A.N. Shmakov, Yu.A. Chesalov, D.N. Dybtsev, V.P. Fedin, O.A. Kholdeeva, *J. Catal.* **2008**, *257*, 315-323.

[16] R.-Q. Zou, H. Sakurai, Q. Xu, *Angew. Chem.* **2006**, *118*, 2604-2608; *Angew. Chem. Int. Ed.* **2006**, *45*, 2542-2546.

[17] O.M. Yaghi, H. Li, *J. Am. Chem. Soc.* **1995**, *117*, 10401-10402.

[18] a) L. Mi, H. Hou, Z. Song, H. Han, H. Xu, Y. Fan, S.-W. Ng, *Cryst. Growth Des*. **2007**, *7*, 2553-2561; b) L. Mi, H. Hou, Z. Song, H. Han, Y. Fan, *Chem. Eur. J*. **2008**, *14*, 1814-1821; c) J. Zhao, L. Mi, J, Hu, H. Hou, Y. Fan, *J. Am. Chem. Soc.* **2008**, *130*, 15222-15223; d) J. Li, L. Li, H. Hou, Y. Fan, *Cryst. Growth Des*. **2009**, *9*, 4504-4513; e) S. Das, H. Kim, K. Kim, *J. Am. Chem. Soc.* **2009**, *131*, 3814-3815.

[19] a) R.D. Jones, D.A. Summerville, F. Basolo, *Chem. Rev*. **1979**, *79*, 139-179; b) E.C. Niederhoffer, J.H. Timmons, A.E. Martell *Chem. Rev*. **1984**, *84*, 137-203.

[20] S. Hikichi, H. Komatsuzaki, M. Akita, Y. Moro-Oka, *J. Am. Chem. Soc.* **1998**, *120*, 4699-4710.

[21] R. Kellerman, P.J. Hutta, K.J. Klier, *J. Am. Chem. Soc.* **1974**, *96*, 5946-5947.

[22] S. Santra, T. Archipov, A.B. Ene, H. Komnik, H. Stoll, E. Roduner, G. Rauhut, *Phys. Chem. Chem. Phys.* **2009**, *11*, 8855-8866.

[23] S.R. Batten, N.R. Champness, X.-M. Chen, J. Garcia-Martinez, S. Kitagawa, L. Öhrström, M. O'Keeffe, M. Paik Suh, J. Reedijk, *Pure Appl. Chem.* **2013**, *85*, 1715-1724.

[24] O.M. Yaghi, H. Li, *J. Am. Chem. Soc.* **1995**, *117*, 10401-10402.

[25] Y. Kinoshita, I. Matsubara, T. Higuchi, Y. Saito, *Bull. Chem. Soc. Jpn.* **1959**, *32*, 1221-1226.

[26] H.J. Buser, D. Schwarzenbach, W. Petter, A. Ludi, *Inorg. Chem.* **1977**, *16*, 2704-2710.

[27] W. Lu, Z. Wei, C.-Y. Gu, T.-F. Liu, J. Park, J. Park, J. Tian, M. Zhang, Q. Zhang, T. Gentle III, M. Bosch, H.-C. Zhou, *Chem. Soc. Rev*. **2014**, *43*, 5561-5593.

[28] H. Li, M. Eddaoudi, M. O'Keeffe, O.M. Yaghi, *Nature* **1999**, *402*, 276-279.

[29] J.A. Mason, M. Veenstra, J.R. Long, *Chem. Sci.* **2014**, *5*, 32-51.

[30] O. Karagiaridi, M.B. Lalonde, W. Bury, A.A. Sarjeant, O.K. Farha, J.T. Hupp, *J. Am. Chem. Soc.* **2012**, *134*, 18790-18796.

[31] M. Eddaoudi, J. Kim, N. Rosi, D. Vodak, J. Wachter, M. O'Keeffe, O.M. Yaghi, *Science* **2002**, *295*, 469-472.

[32] S.S.-Y. Chui, S.S.-F. Lo, J.P.H. Charmant, A.G. Orpen, I.D. Williams, *Science* **1999**, *283*, 1148-1150.

[33] N.L. Rosi, J. Kim, M. Eddaoudi, B. Chen, M. O'Keeffe, O.M. Yaghi, *J. Am. Chem. Soc.* **2005**, *127*, 1504-1518.

[34] A. Phan, C.J. Doonan, F.J. Uribe-Romo, C.B. Knobler, M. O'Keeffe, O.M. Yaghi, *Acc. Chem. Res.* **2010**, *43*, 58-67.

[35] Ch. Baerlocher, L.B. McCusker, D.H. Olson, *Atlas of Zeolite Framework Types,* 6th revised Edn.; Elsevier, Amsterdam, **2007**.

[36] N.A. Anurova, V.A. Blatov, G.D. Ilyishin, D.M. Proserpio, *J. Phys. Chem. C* **2010**, *114*, 10160-10170.

[37] a) M. O'Keeffe, O.M. Yaghi, *Chem. Rev*. **2012**, *112*, 675-702.

[38] W. Clegg, D.R. Harbron, C.D. Homan, P.A. Hunt, I.R. Little, B.P. Straughan, *Inorg. Chim. Acta* **1991**, *186*, 51-60.

[39] M. Li, D. Li, M. O'Keeffe, O.M. Yaghi, *Chem. Rev*. **2014**, *114*, 1343-1370.

[40] M. O'Keeffe, M.A. Peskov, S.J. Ramsden, O.M. Yaghi, *Acc. Chem. Res*. **2008**, *41*, 1782-1789.

[41] a) K. Sumida, D.L. Rogow, J.A. Mason, T.M. McDonald, E.D. Bloch, Z.R. Herm, T.-H. Bae, J.R. Long, *Chem. Rev*. **2012**, *112*, 724-781; b) E. Barea, C. Montoro, J.A.R. Navarro, *Chem. Soc. Rev*. **2014**, *43*, 5419-5430.

[42] a) J.-R. Li, J. Sculley, H.-C. Zhou, *Chem. Rev*. **2012**, *112*, 869-932; b) M.P. Suh, H.J. Park, T.K. Prasad, D.-W. Lim, *Chem. Rev*. **2012**, *112*, 782-835; c) Y. Peng, V. Krungleviciute, I. Eryazici, J.T. Hupp, O.K. Farha, T. Yildirim, *J. Am. Chem. Soc*. **2013**, *135*, 11887-11894.

[43] A. Schneemann, V. Bon, I. Schwedler, I. Senkowska, S. Kaskel, R.A. Fischer, *Chem. Soc. Rev*. **2014**, *43*, 6062-6096.

[44] H. Deng, S. Grunder, K.E. Cordova, C. Valente, H. Furukawa, M. Hmadeh, F. Gándara, A.C. Whalley, Z. Liu, S. Asahina, H. Kazumori, M. O'Keeffe, O. Terasaki, J.F. Stoddart, O.M. Yaghi, *Science* **2012**, *336*, 1018-1023.

[45] O.K. Farha, I. Eryazici, N.C. Jeong, B.G. Hauser, C.E. Wilmer, A.A.Sarjeant, R.Q. Snurr, S.T. Nguyen, A.Ö. Yazaydın, J.T. Hupp, *J. Am. Chem. Soc*. **2012**, *134*, 15016-15021.

[46] a) J. Gascon, A. Korma, F. Kapteijn, F.X. Llabrés i Xamena, *ACS Catal*. **2014**, *4*, 361-378; b) P. García-García, M. Müller, A. Corma, *Chem. Sci*. **2014**, *5*, 2979-3007.

[47] L. Huang, H. Wang, J. Chen, Z. Wang, J. Sun, D. Zhao, Y. Yan, *Microporous Mesoporous Mater*. **2003**, *58*, 105-114.

[48] Z.-Y. Gu, J. Park, A. Raiff, Z. Wei, H.-C. Zhou, *ChemCatChem* **2014**, *6*, 67-75.

[49] K. Leus, Y.-Y. Liu, P. Van Der Voort, *Catal. Rev*. **2014**, *56*, 1-56.

[50] L.E. Kreno, K. Leong, O.K. Farha, M. Allendorf, R.P. Van Duyne, J.T. Hupp, *Chem. Rev*. **2012**, *112*, 1105-1125.

[51] Y. Cui, Y. Yue, G. Qian, B. Chen, *Chem. Rev*. **2012**, *112*, 1126-1162.

[52] W. Zhang, R.-G. Xiong, *Chem. Rev*. **2012**, *112*, 1163-1195.

[53] C. Wang, T. Zhang, W. Lin, *Chem. Rev*. **2012**, *112*, 1084-1104.

[54] P. Horcajada, R. Gref, T. Baati, P.K. Allan, G. Maurin, P. Couvreur, G. Férey, R.E. Morris, C. Serre, *Chem. Rev*. **2012**, *112*, 1232-1268.

[55] P.D.C. Dietzel, R. Blom, H. Fjellvåg, *Eur. J. Inorg. Chem.* **2008**, 3624-3632.

[56] S. Biswas, M. Grzywa, H.P. Nayek, S. Dehnen, I. Senkovska, S. Kaskel, D. Volkmer, *Dalton Trans*. **2009**, 6487-6495.

[57] a) S. Biswas, M. Tonigold, D. Volkmer, *Z. Anorg. Allg. Chem*. **2008**, *634*, 2532–2538; b) S. Biswas, M. Tonigold, M. Speldrich, P. Kögerler, M. Weil, D. Volkmer, *Inorg. Chem*. **2010**, *49*, 7424–7434.

[58] G. Sastre, J. van den Bergh, F. Kapteijn, D. Denysenko, D. Volkmer, *Dalton Trans*. **2014**, *43*, 9612-9619.

[59] J. Teufel, H. Oh, M. Hirscher, M. Wahiduzzaman, L. Zhechkov, A. Kuc, T. Heine, D. Denysenko, D. Volkmer, Adv. Mater. **2013**, *4*, 635-639.

[60] H. Gilman, J. J. Dietrich, *J. Am. Chem. Soc.* **1958**, *80*, 366-368.

[61] K. Chichak, U. Jacquemard, N.R. Branda, *Eur. J. Inorg. Chem.* **2002**, 357-368.

[62] S. Trofimenko, *Chem. Rev.* **1993**, *93*, 943–980.

[63] C.K. Brozek, M. Dincâ, *Chem. Soc. Rev*. **2014**, *43*, 5456-5467.

[64] V. Colombo, S. Galli, H. J. Choi, G. D. Han, A. Maspero, G. Palmisano, N. Masciocchi, J.R. Long, *Chem. Sci.*, **2011**, *2*, 1311-1319.

[65] (a) J. Jansson, A. E. C. Palmqvist, E. Fridell, M. Skoglundh, L. Österlund, P. Thormählen and V. Langer, *J. Catal.*, 2002, **211**, 387-397; (b) X. Xie, Y. Li, Z.-Q. Liu, M. Haruta and W. Shen, *Nature*, 2009, **458**, 746-749.

[66] Y. Ishii, S. Sakaguchi, **T**. Iwahama, *Adv. Synth. Catal.* **2001**, *343*, *393-427.*

[67] S. Biswas, M. Maes, A. Dhakshinamoorthy, M. Feyand, D.E. De Vos, H. Garcia, N. Stock, *J. Mater. Chem.* **2012**, *22*, 10200-10209.

[68] A.K. Galwey, D.M. Jamieson, M.E. Brown, *J. Phys. Chem*. **1974**, *78*, 2664–2670.

[69] a) R. Han, I.B. Gorrell, A.G. Looney, G. Parkin, *J. Chem. Soc. Chem. Commun*. **1991**, 717–719; b) A. Looney, R. Han, I.B. Gorrell, M. Cornebise, K. Yoon, G. Parkin, A.R. Rheingold, *Organometallics* **1995**, *14*, 274–278; c) M. Rombach, H. Brombacher, H. Vahrenkamp, *Eur. J. Inorg. Chem*. **2002**, 153–159.

[70] O.M. Reinaud, K.H. Theopold, *J. Am. Chem. Soc.* **1994**, *116*, 6979-6980.

[71] C.C.H. Atienza, A.C. Bowman, E. Lobkovsky, P.J. Chirik, *J. Am. Chem. Soc.* **2010**, *132*, 16343-16345.

[72] G.V. Goeden, K.G. Kaulton, *J. Am. Chem. Soc.* **1981**, *103*, 7355-7357.

[73] W.S. Mahoney, D.M. Brestensky, J.M. Stryker, *J. Am. Chem. Soc.* **1988**, *110*, 291-293.

[74] NIST Computational Chemistry Comparison and Benchmark Database. NIST Standard Reference Database Number 101. Release 16a, August 2013, Editor: Russell D. Johnson III. http://cccbdb.nist.gov.

[75] P.L. Holland, *Dalton Trans*. **2010**, *39*, 5415-5425.

[76] G.J. Kubas, *Metal dihydrogen and σ-bond complexes*; Kluwer Academic Publishers, New-York, **2001**.

[77] L.J. Murray, M. Dinca, J. Yano, S. Chavan, S. Bordiga, C.M. Brown, J.R. Long, *J. Am. Chem. Soc.* **2010**, *132*, 7856-7857.

[78] E.D. Bloch, L.J. Murray, W.L. Queen, S. Chavan, S.N. Maximoff, J.P. Bigi, R. Krishna, V.K. Peterson, F. Grandjean, G.J. Long, B. Smit, S. Bordiga, C.M. Brown, J.R. Long, *J. Am. Chem. Soc.* **2011**, *133*, 14814-14822.

[79] P.D.C. Dietzel, P.A. Georgiev, J. Eckert, R. Blom, T. Strässle, T. Unruh, *Chem. Commun*. **2010**, *46*, 4962-4964.

[80] B. Liu, B. Smit, *Langmuir* **2009**, *25*, 5918-5926.

[81] Y.-S. Bae, R.Q. Snurr, *Microporous Mesoporous Mater*. **2010**, *132*, 1121-1140.

[82] B. Sakintuna, F. Lamari-Darkrim, M. Hirscher, *Int. J. Hydrogen Energ*. **2007**, *32*, 1121-1140.

[83] L.M. Mirica, X. Ottenwaelder, T.D.P. Stack, *Chem. Rev.* **2004**, *104*, 1013-1045.

[84] a) A.I. Serykh, M.D. Amiridis, *Micropor. Mesopor. Mat*. **2006**, *94*, 320-324; b) Y. Kuroda, Y. Yoshikawa, S.-i. Konno, H. Hamano, H. Maeda, R. Kumashiro, M. Nagao, *J. Phys. Chem*. **1995**, *99*, 10621-10628; c) Y. Kuroda, Y. Yoshikawa, S. Emura, R. Kumashiro, M. Nagao, *J. Phys. Chem*. **1999**, *103*, 2155-2164; d) Y. Kuroda, S.-i. Konno, K. Morimoto, Y. Yoshikawa, *J. Chem. Soc. Chem. Commun*. **1993**, 18-20; e) G. Spoto, S. Bordiga, G. Ricchiardi, D. Scarano, A. Zecchina, F. Geobaldo, *J. Chem. Soc. Faraday Trans*. **1995**, *91*, 3285-3290.

[85] H.S. Plitt, M.R. Bär, R. Ahlrichs, H. Schnöckel, *Angew. Chem*. **1991**, *103*, 848-850; *Angew. Chem. Int. Ed.* **1991**, *30*, 832-834.

[86] a) A.I. Serykh, V.B. Kazansky, *Phys. Chem. Chem. Phys*. **2004**, *6*, 5250-5255; b) X. Solans-Monfort, V. Branchadell, M. Sodupe, C.M. Zicovich-Wilson, E. Gribov, G. Spoto, C. Busco, P. Ugliengo, *J. Phys. Chem. B*. **2004**, *108*, 8278-8286; c) G. Spoto, E. Gribov,

S. Bordiga, C. Lamberti, G. Ricchiardi, D. Scarano, A. Zecchina, *Chem. Commun*. **2004**, 2768-2769.

[87] P.A. Georgiev, A. Albinati, B.L. Mojet, J. Ollivier, J. Eckert, *J. Am. Chem. Soc.* **2007**, *129*, 8086-8087.

[88] P.A. Georgiev, A. Albinati, J. Eckert, *Chem. Phys. Lett.* **2007**, *449*, 182-185.

[89] M.W. Ackley, S.U. Rege, H. Saxena, *Micropor. Mesopor. Mat*. **2003**, *61*, 25-42.

[90] D.A. Lashof, D.R. Ahuja, *Nature* **1990**, *344*, 529-531.

[91] A.R. Ravishankara, J.S. Daniel, R.W. Portmann, *Science* **2009**, *326*, 123-125.

[92] V.I. Sobolev, L.V. Pirutko, in: J.C. Taylor (Ed.), *Advances in Chemistry Research, Vol. 19*; Nova Science Publishers, New York, **2013**, pp. 1-24.

[93] D. Saha, Z. Bao, F. Jia, S. Deng, *Environ. Sci. Technol.* **2010**, *44*, 1820-1826.

[94] a) D.O. Shiels, *J. Phys. Chem*. **1929**, *33*, 1386-1397; b) H. Marsh, T.E. O'Hair, *Fuel* **1966**, *45*, 301-309; c) Y. Peng, F. Zhang, C. Xu, Q. Xiao, Y. Zhong, W. Zhu, *J. Chem. Eng. Data* **2009**, *54*, 3079-3081.

[95] a) V. Rakić, V. Dondur, S. Gajinov, A. Auroux, *Thermochim. Acta* **2004**, *420*, 51-57; b) V. Rakić, V. Rac, V. Dondur, A. Auroux, *Catal. Today* **2005**, *110*, 272-280; c) B.R. Wood, J.A. Reimer, A.T. Bell, *J. Catal*. **2002**, *209*, 151-158; d) Y. Wang, Z. Lei, B. Chen, Q. Guo, N. Liu, *Appl. Surf. Sci*. **2010**, *256*, 4042-4047; e) G. Domínguez, R. Hernández-Huesca, G. Aguilar-Armenta, *J. Mex. Chem. Soc*. **2010**, *54*, 111-116.

[96] R.G. Pearson, *J. Am. Chem. Soc*. **1963**, *85*, 3533-3539.

[97] R.G. Pearson, *Inorg. Chem*. **1988**, *27*, 734-740.

[98] C. Lamberti, S. Bordiga, M. Salvalaggio, G. Spoto, A. Zecchina, F. Geobaldo, G. Vlaic, M. Bellatreccia, *J. Phys. Chem. B* **1991**, *101*, 344-360.

[99] W.B. Tolman, *Angew. Chem*. **2010**, *122*, 1034–1041; *Angew. Chem. Int. Ed*. **2010**, *49*, 1018-1024.

[100] a) J.N. Armor, H. Taube, *J. Am. Chem. Soc*. **1969**, *91*, 6874-6876; b) C.B. Pamplin, E.S.F. Ma, N. Safari, S.J. Rettig, B.R. James, *J. Am. Chem. Soc*. **2001**, *123*, 8596-8597; c) N.A. Piro, M.F. Lichterman, W.H. Harman, C.J. Chang, *J. Am. Chem. Soc*. **2011**, *133*, 2108-2111.

[101] K. Yoshizawa, *Acc. Chem. Res*. **2006**, *39*, 375-382.

6 Appendix Publications

A1 *Elucidating Gating Effects for Hydrogen Sorption in MFU-4-Type Triazolate-Based Metal–Organic Frameworks Featuring Different Pore Sizes*
D. Denysenko, M. Grzywa, M. Tonigold, B. Streppel, I. Krkljus, M. Hirscher, E. Mugnaioli, U. Kolb, J. Hanss, D. Volkmer, *Chem. Eur. J.* **2011**, *17*, 1837–1848. Copyright Wiley-VCH Verlag GmbH & Co. KGaA. Reproduced with permission.

A2 *Reversible gas-phase redox processes catalyzed by Co-exchanged MFU-4l(arge)*
D. Denysenko, T. Werner, M. Grzywa, A. Puls, V. Hagen, G. Eickerling, J. Jelic, K. Reuter, D. Volkmer, *Chem. Commun.* **2012**, *48*, 1236-1238. Reproduced by permission of The Royal Society of Chemistry. http://pubs.rsc.org/en/content/articlepdf/2012/cc/c2cc16235k.

A3 *Scorpionate-Type Coordination in MFU-4l Metal–Organic Frameworks: Small-Molecule Binding and Activation upon the Thermally Activated Formation of Open Metal Sites*
D. Denysenko, M. Grzywa, J. Jelic, K. Reuter, D. Volkmer, *Angew. Chem.* **2014**, *126*, 5942-5946; *Angew. Chem. Int. Ed.* **2014**, *53*, 5832-5836. Copyright Wiley-VCH Verlag GmbH & Co. KGaA. Reproduced with permission.

A4 *Postsynthetic Metal and Ligand Exchange in MFU-4l: a Screening Approach toward Functional Metal-Organic Frameworks Comprising Single-Site Active Centers*
D. Denysenko, J. Jelic, K. Reuter, D. Volkmer, *Chem. Eur. J.* **2015**, *21*, 8188-8199. Copyright Wiley-VCH Verlag GmbH & Co. KGaA. Reproduced with permission.

A5 *Elucidating Lewis Acidity of Metal Sites in MFU-4l Metal-Organic Frameworks: N_2O and CO_2 adsorption in MFU-4l, Cu^{I}-MFU-4l and Li-MFU-4l*
D. Denysenko, J. Jelic, O.V. Magdysyuk, K. Reuter, D. Volkmer, *Micropor. Mesopor. Mat.* **2015**, *216*, 146-150. doi:10.1016/j.micromeso.2015.03.014. Reproduced with permission.

DOI: 10.1002/chem.201001872

Elucidating Gating Effects for Hydrogen Sorption in MFU-4-Type Triazolate-Based Metal–Organic Frameworks Featuring Different Pore Sizes

Dmytro Denysenko,[a] Maciej Grzywa,[a] Markus Tonigold,[b] Barbara Streppel,[c] Ivana Krkljus,[c] Michael Hirscher,[c] Enrico Mugnaioli,[d] Ute Kolb,[d] Jan Hanss,[a] and Dirk Volkmer*[a, b]

Abstract: A highly porous member of isoreticular MFU-4-type frameworks, $[Zn_5Cl_4(BTDD)_3]$ (MFU-4*l*(arge)) (H_2-BTDD = bis(1*H*-1,2,3-triazolo[4,5-*b*],-[4′,5′-*i*])dibenzo[1,4]dioxin), has been synthesized using $ZnCl_2$ and H_2-BTDD in *N*,*N*-dimethylformamide as a solvent. MFU-4*l* represents the first example of MFU-4-type frameworks featuring large pore apertures of 9.1 Å. Here, MFU-4*l* serves as a reference compound to evaluate the origin of unique and specific gas-sorption properties of MFU-4, reported previously. The latter framework features narrow-sized pores of 2.5 Å that allow passage of sufficiently small molecules only (such as hydrogen or water), whereas molecules with larger kinetic diameters (e.g., argon or nitrogen) are excluded from uptake. The crystal structure of MFU-4*l* has been solved ab initio by direct methods from 3D electron-diffraction data acquired from a single nanosized crystal through automated electron diffraction tomography (ADT) in combination with electron-beam precession. Independently, it has been solved using powder X-ray diffraction. Thermogravimetric analysis (TGA) and variable-temperature X-ray powder diffraction (XRPD) experiments carried out on MFU-4*l* indicate that it is stable up to 500 °C (N_2 atmosphere) and up to 350 °C in air. The framework adsorbs 4 wt % hydrogen at 20 bar and 77 K, which is twice the amount compared to MFU-4. The isosteric heat of adsorption starts for low surface coverage at 5 kJ mol^{-1} and decreases to 3.5 kJ mol^{-1} at higher H_2 uptake. In contrast, MFU-4 possesses a nearly constant isosteric heat of adsorption of ca. 7 kJ mol^{-1} over a wide range of surface coverage. Moreover, MFU-4 exhibits a H_2 desorption maximum at 71 K, which is the highest temperature ever measured for hydrogen physisorbed on metal–organic frameworks (MOFs).

Keywords: adsorption · hydrogen · metal–organic frameworks · thermal desorption spectroscopy · triazolates

Introduction

Hydrogen is an attractive energy carrier that could replace petroleum in the future. However, hydrogen storage is a difficult problem that still has to be solved. Investigation of metal–organic frameworks (MOFs) as porous materials for hydrogen storage is currently an important research field.[1] Due to a recent requirement of the United States Department of Energy, a hydrogen storage tank must contain 6 wt % of hydrogen. Hydrogen uptake depends on several properties of porous material. At low pressure, hydrogen uptake correlates with the heat of adsorption. At intermediate pressure (30 bar), uptake correlates with the surface area, and at high pressure (100 bar and more), uptake correlates with the free volume.[2] Uptake values up to 10 wt % H_2 at 100 bar and 77 K were reported for MOF-5.[3] However, a material with a high surface area or free volume alone is not necessarily a good candidate for hydrogen storage.

[a] D. Denysenko, Dr. M. Grzywa, Dr. J. Hanss, Prof. Dr. D. Volkmer
Institute of Physics
Chair of Solid State and Material Science
Augsburg University
Universitätsstrasse 1, 86135 Augsburg (Germany)
Fax: (+49) 821-598-5955
E-mail: dirk.volkmer@physik.uni-augsburg.de

[b] M. Tonigold, Prof. Dr. D. Volkmer
Institute of Inorganic Chemistry II—Materials and Catalysis
Ulm University
Albert-Einstein-Allee 11, 89081 Ulm (Germany)

[c] B. Streppel, I. Krkljus, Dr. M. Hirscher
Max Planck Institute for Metals Research
Heisenbergstrasse 3, 70569 Stuttgart (Germany)

[d] Dr. E. Mugnaioli, Dr. U. Kolb
Institute of Physical Chemistry
Johannes Gutenberg-University Mainz
Welderweg 11, 55099 Mainz (Germany)

Supporting information for this article is available on the WWW under http://dx.doi.org/10.1002/chem.201001872.

Relatively high adsorption enthalpy is required for successful application. Calculations[4] show that the adsorption enthalpy of 15 kJ mol^{-1} would be optimal for a reversible adsorption–desorption cycle at room temperature. However, due to very weak van der Waals interactions of H_2 molecules, the heat of hydrogen physisorption typically ranges from 4 to 7 kJ mol^{-1}. Metal–organic frameworks with unsaturated metal sites can reach an adsorption enthalpy of over 10 kJ mol^{-1}.[5] The pore-size distribution of a MOF strongly influences the heat of adsorption. Thus, frameworks with smaller pore sizes have higher heat of adsorption due to a stronger interaction between adsorbed hydrogen molecules and cavities.[6] The desorption temperature of hydrogen likewise increases with decreasing pore size.[7] Monte Carlo calculations have been used to show that pores with a diameter of 7 Å should be optimal for hydrogen adsorption.[8] However, these calculations did not consider the important gating effects of very small apertures or narrow channels interconnecting the internal voids of the storage material. Finally, the stability of a metal–organic framework plays a very important role for its potential use as a hydrogen-storage material as well as for other applications. Thus, the performance of MOF-5 in hydrogen adsorption depends strongly on the preparation and handling conditions since this framework is not stable under ambient conditions owing to its sensitivity towards hydrolytic decomposition.[3]

In a general sense, the success of inventing functional MOFs will rely on a systematic development of suitable secondary building units (SBUs) from which a structurally and functionally diverse class of novel materials might evolve.[9a,b] Herein we present a unique "solid-state construction kit" that is based on novel pentanuclear SBUs, for which the term "Kuratowski-type" SBUs is proposed. We have recently developed two major lines of functional MOF compounds, termed MFU-1 and MFU-4, respectively. MFU-1 is a pyrazolate-based redox-active analogue of the famous MOF-5[9c] featuring four tetrahedrally coordinated Co^{II} centers that are connected by a central μ_4-bridging oxide anion (Figure 1, left). This compound shows enhanced stability against hydrolytic and oxidative decomposition and it can be employed as catalyst in a range of radical-centered oxidation reactions.[10] Since the particular SBU of MFU-1 seems to be limited to the presence of a $\{Co_4O\}$ core, we have developed a modular MOF family (MFU-4),[11] which is based on Kuratowski-type pentanuclear SBUs of the general formula $[M^{II}Zn_4X_4(\mathbf{L}_6)]$ (Figure 1, right). These feature a central metal ion coordinated to six triazolate ligands (**L**) that span a Cartesian system and can either be assembled into discrete coordination compounds[12] or into porous cubic frameworks.[11] The central metal ion in the octahedral coordination environment can be varied[12] giving the opportunity of potentially obtaining redox-active SBUs that are also Lewis acidic, with chemical properties that can be fine-tuned by selecting appropriate metal ions. Changing the Zn^{2+} ions in tetrahedral positions to other transition-metal ions could improve hydrogen-sorption properties.[5]

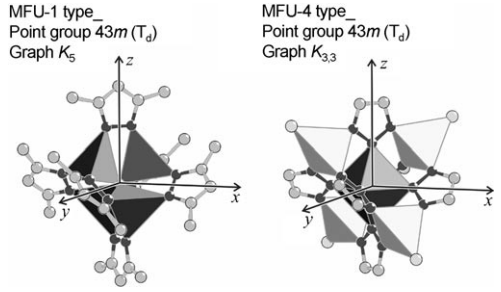

Figure 1. Structural features of SBUs found in MFU-1 and MFU-4.

The graph theoretical analysis proves that $[M^{II}Zn_4X_4(\mathbf{L}_6)]$ units contain the nonplanar $K_{3,3}$ graph. According to a theorem of C. Kuratowski,[13] a finite graph is planar only if it does not contain a subgraph that is a subdivision of K_5 (the complete graph on five vertices) or $K_{3,3}$ (a complete bipartite graph on six vertices, three of which connect to each of the other three). As can be seen in Figure 2, the molecular

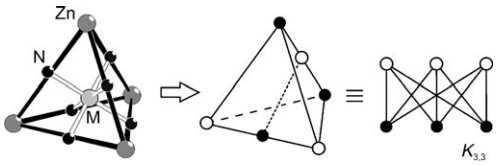

Figure 2. Formal derivation of the $K_{3,3}$ graph, which can be used to represent the connectivity scheme in Kuratowski-type SBUs.

graph of $[M^{II}Zn_4X_4(\mathbf{L}_6)]$ units in fact contains a subgraph of $K_{3,3}$. Accordingly, there is no way to draw $[M^{II}Zn_4X_4(\mathbf{L}_6)]$ as a planar graph and thus we propose a pseudoperspective skeletal formula as derived in Figure 3 to represent Kuratowski-type coordination compounds in this paper and in the future.

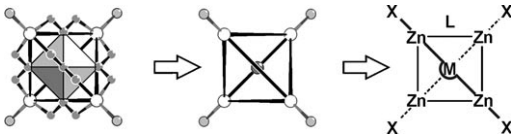

Figure 3. Derivation of a skeletal formula representing the connectivity of $[M^{II}Zn_4X_4(\mathbf{L}_6)]$ units (X: terminal ligand; **L**: 1,2,3-triazolate-type ligand).

The first triazolate-based MOF featuring Kuratowsky-type secondary building units, MFU-4, was constructed from benzobistriazolate linkers and $\{Zn_5Cl_4\}^{6+}$ cores featuring a very high thermal and hydrolytic stability. Due to its small pore apertures (2.5 Å) it is highly selective for the adsorption of atoms or small molecules such as H_2 and it can therefore be applied in molecular sieving applications, some of which are hard to achieve with other kinds of porous materials. However, to separate mixtures of larger molecular adsorbates or for catalytic transformations a porous frame-

work featuring large pore apertures is required. Herein we describe MFU-4*l*(arge) constructed from bis(1*H*-1,2,3-triazolo[4,5-*b*],[4′,5′-*i*])dibenzo[1,4]dioxin linkers (H_2-BTDD, **2**), which is a novel member of isoreticular MFU-4-type frameworks (Scheme 1).

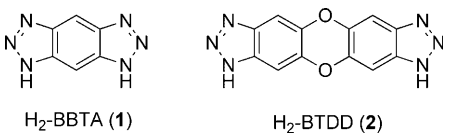

Scheme 1. Triazolate linker **1** for MFU-4 and **2** for MFU-4*l*.

Comparing hydrogen-sorption properties of MFU-4 and MFU-4*l* featuring small and large pores, respectively, might help to improve present concepts about the influence of pore size on the potential of a porous material for hydrogen storage by means of physisorption. In the following we will demonstrate that small pore apertures are responsible for selective hydrogen adsorption in MFU-4. Its small pore diameters result in a higher heat of adsorption due to a stronger interaction between adsorbed molecules and the MOF. This desirable property of MFU-4, however, is compromised by a reduced void volume if compared with MFU-4*l*, which features larger pores and a higher surface area, which allow for uptake of a larger total amount of hydrogen at high pressure. Only a few studies with accurate determination of the isosteric heat of adsorption from isotherms have been reported so far.[6] A powerful tool that can help us to understand the mechanism of adsorption and diffusion of hydrogen in MOFs is thermal desorption spectroscopy (TDS).[7] Herein we present hydrogen-adsorption isotherms for MFU-4 and MFU-4*l* measured over a wide temperature range (77–298 K) as well as TDS studies at low temperatures between 20 and 120 K.

Results and Discussion

Synthesis and characterization: The bis(1*H*-1,2,3-triazolo-[4,5-*b*],[4′,5′-*i*])dibenzo[1,4]dioxin (H_2-BTDD, **2**) ligand was synthesized in three steps starting from dibenzo[1,4]dioxin (see Scheme 2). The nitration of dibenzo[1,4]dioxin described in the literature[14] gives a very low yield (17%) of the desired product and requires several purification steps. Therefore, we have developed an improved and simple procedure that allowed us to obtain 2,3,7,8-tetranitrodibenzo-[1,4]dioxin (**3**) in good yield. The reduction of the nitro compound was carried out according to the literature procedure.[15]

MFU-4*l* can be synthesized in high yield using solvothermal or microwave methods and *N*,*N*-dimethylformamide (DMF) as a solvent (see Scheme 3).

Different ratios of $ZnCl_2$/**2** (from 2:1 to 40:1) can be used for MOF synthesis. However, a large excess amount of zinc chloride is preferable to avoid the formation of amorphous

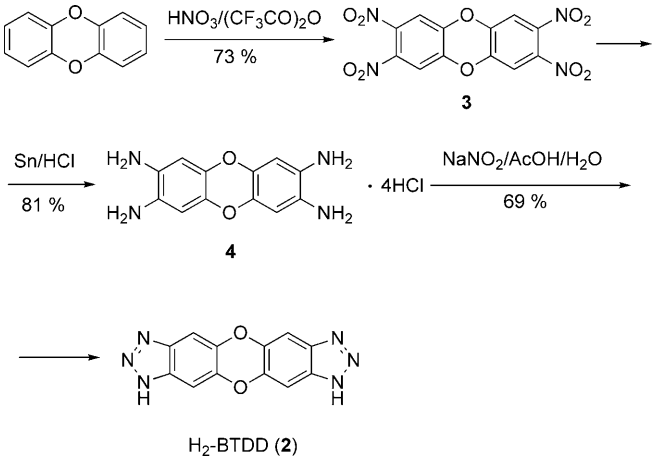

Scheme 2. Synthesis of ligand **2**.

Scheme 3. Synthesis of MFU-4*l*.

byproducts that have been observed when using low metal/ligand ratios. The ratio of 20:1 was found to be optimal. MFU-4*l* was obtained as a microcrystalline powder with typical crystal sizes ranging from 1 to 5 μm (Figure 4). Crystals of this size are not suitable for single-crystal X-ray structure analysis, thus powder X-ray diffraction and single-crystal electron diffraction have been used for structural characterization.

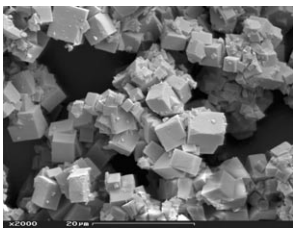

Figure 4. SEM image of MFU-4*l* prepared by the solvothermal method (scale bar: 20 μm).

The use of *N*-methylpyrrolidone (NMP) as solvent offers the advantage of a higher solubility of the linker. Also, some larger crystals, up to 40 μm, could be obtained in NMP under solvothermal conditions. However, the yield was very poor and the product contains a considerable amount of amorphous impurities.

Structure solution by electron diffraction: Automated electron diffraction tomography (ADT)[16–18] is a new technique in which the reciprocal space is sampled by tilting a nanosized single crystal in small steps over the full tilt range ac-

cessible in the transmission electron microscope. We used nanobeam electron diffraction to create a low-dose, small, semiparallel electron beam and scanning TEM to image and track the crystal; this technique is particularly suitable for beam-sensitive materials that are normally not accessible by conventional electron-diffraction techniques.[19] After reconstruction of the 3D reciprocal space, cell parameter determination with a maximum error of 5% is possible. The intensities that can be observed after indexing are already quasi-kinematical and cover most of the symmetrically independent reciprocal space. ADT can be combined with precession electron diffraction (PED), thus integrating the space between the tilts to enhance intensity quality further. Based on ADT data sets, the full structure can be found ab initio by direct methods in a pure kinematical approach. This technique was able to solve complex nanoporous structures such as charoite.[20]A cubic face-centered cell ($a=32.0(4)$ Å) was automatically determined. No further extinction was detected in the reconstructed three-dimensional reciprocal space (Figure 5). All independent reflections up to a resolution of

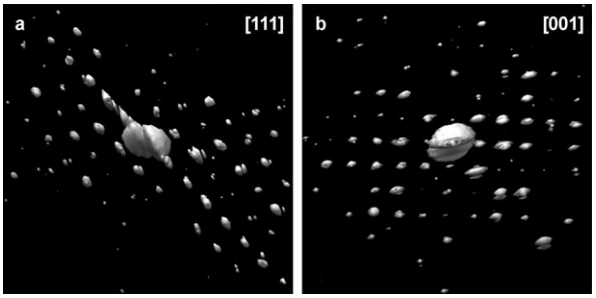

Figure 5. Projections of three-dimensional reconstructed reciprocal space by ADT data: a) [111] projection; b) [001] projection.

1.3 Å were sampled and integrated. Intensities collected in such a way were quasi-kinematical because they were integrated from nonoriented diffraction patterns. The amount and quality of the data obtained by ADT is remarkably superior to any previous electron-diffraction experiment performed on MOFs, for which cell parameters were determined by single-oriented projections.[21] Ab initio structure solution delivered the complete structure directly except for one carbon atom. The structure was refined by imposing a rigid benzene ring and soft bond restraints. The final residual R value was 32.1%, which is in an acceptable range for electron-diffraction data.

Crystal structure description: The crystal structure of MFU-4*l* has been independently solved ab initio from powder X-ray diffraction data by direct methods. Both structure solutions—from powder X-ray and ADT diffraction data, respectively—deliver almost identical structures, which show small differences in bond lengths only. The maximum deviation in atom positions from the ADT solution is 0.2 Å. The crystal structure of MFU-4*l* is similar to that of MFU-4 (Figure 6) in that it possesses a cubic six-connected net. This

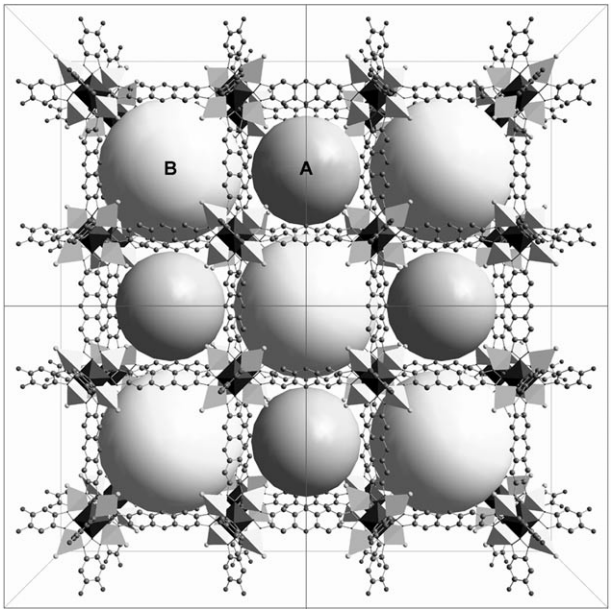

Figure 6. Ball-and-stick representation of the MFU-4*l* framework along the crystallographic *a* direction (octahedrally coordinated Zn^{2+}: dark-gray octahedra; tetrahedrally coordinated Zn^{2+}: pale-gray tetrahedra). All hydrogen atoms are omitted for clarity. The larger spheres represent the cavities of **B** cells, whereas the smaller spheres represent the cavities of **A** cells.

can be described as follows: the nodes (vertices) are represented by cationic pentanuclear $\{Zn_5Cl_4\}^{6+}$ clusters and the links (edges) of the net are represented by finite rods of $BTDD^{2-}$ anions. There are two types of Zn ions: first, a tetrahedrally coordinated zinc atom (Zn1) with $3m$ site symmetry is surrounded by three N atoms from BTDD ligands (forming the base of the tetrahedron) and one Cl atom (constituting the apex of the tetrahedron); second, an octahedrally coordinated zinc atom (Zn2), with $\bar{4}3m$ site symmetry surrounded by six N atoms from six hexadentate-coordinated BTDD ligands. All BTDD ligands are twisted around their coordinative bonds to the central Zn2 ions. In the solution from the powder X-ray diffraction data, the distances Zn–N for a tetrahedrally coordinated Zn atom are smaller (2.010(5) Å) than those between octahedrally coordinated Zn atoms and nitrogen donors (2.0414(9) Å). In the ADT solution, the distances Zn–N for a tetrahedrally coordinated Zn atom are 2.09(3) Å and for a octahedrally coordinated Zn atom are 2.12(4) Å, respectively. These values are in good agreement with other Zn–triazolate complexes (1.98–2.05 Å for tetrahedral coordination and 2.14–2.22 Å for octahedral coordination).[11]

According to the results obtained by using the PLATON/SQUEEZE[22] program, the total potentially accessible void volume is 23563.2 Å^3, which is 78.7% of the unit-cell volume.

Analogously to MFU-4, the framework of MFU-4*l* has two different types of cavities (the smaller and the larger ones are referred to as **A** and **B** cells, respectively) arranged in an alternating fashion (Figure 6). The **A** cells are repre-

sented by the cubic arrangement of eight chlorine atoms that have a minimum nonbonding distance of 8.9320(2) Å from each other. Taking the van der Waals radii of Cl atoms (1.75 Å) into account, imaginary spheres with a diameter of 11.97 Å could fit into the **A** cells. Each of the larger **B** cells, on the other hand, is surrounded by twelve dioxin rings and an imaginary sphere with a diameter of 18.56 Å would fit into it, taking the van der Waals radii of the C atoms into account. The aperture between **A** and **B** cells would admit the passage of an imaginary sphere with a diameter of 9.13 Å (taking the van der Waals radii of Cl atoms into account.

Large pore apertures in MFU-4*l* allow the adsorption and free diffusion of larger molecules. Table 1 shows selected structural parameters of MFU-4 and MFU-4*l* for comparison.

Table 1. Selected structural features of MFU-4 and MFU-4*l*.

	MFU-4	MFU-4*l*
space group	$Fm\bar{3}m$ (225)	$Fm\bar{3}m$ (225)
cell length $a=b=c$ [Å]	21.6265(9)	31.057(1)
V [Å^3]	10114(9)	29955(4)
ρ_{calcd} [g cm^{-3}]	1.23	0.56
void volume [%]	53.1	78.7
diameter **A** cells [Å]	3.88	11.97
diameter **B** cells [Å]	11.94	18.56
aperture [Å]	2.52	9.13

Thermal analyses: Due to a larger pore size, MFU-4*l* loses solvent molecules much easier then MFU-4. Thus, MFU-4*l* heated in a vacuum at 180 °C contains no solvent as observed by thermogravimetric analysis (TGA) and shows no weight loss up to 500 °C (Figure 7). In contrast, MFU-4 must be heated at 250 °C under vacuum to remove DMF molecules, which cannot pass through small apertures easily.

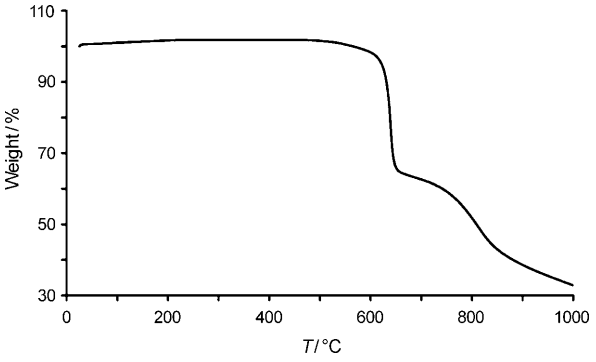

Figure 7. Temperature-dependent weight-loss of MFU-4*l* (sample exposed to flowing nitrogen gas).

By using more accurate TGA/MS measurements on the sample stored in air, traces of adsorbed molecules were detected (Figure 8). Weight loss below 200 °C corresponds to water (m/z 18). The second peak with m/z 44 observed in

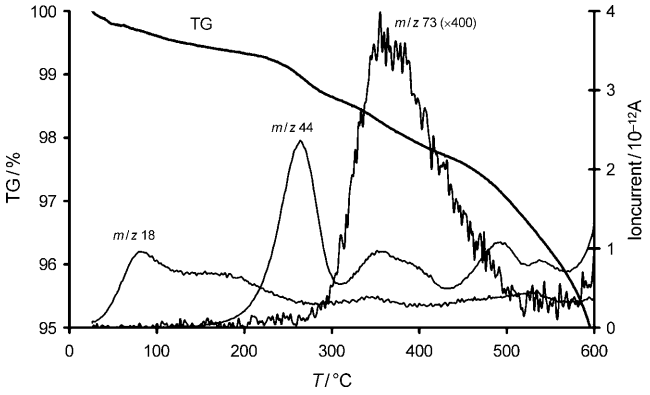

Figure 8. TGA/MS data of MFU-4*l*.

the temperature range between 200 and 300 °C corresponds to CO_2, which was also identified by TGA/IR spectroscopy. The third peak is DMF (m/z 73 for the molecular ion and m/z 44 for $(CH_3)_2N^+$).

The presence of DMF was further confirmed by using a thermodesorption GC-MS trace of volatile products formed after heating MFU-4*l* at 260 °C.

Variable-temperature X-ray powder diffraction (VTXRPD) studies (Figure 9a) showed that MFU-4*l* is stable up to 350 °C in air, which is similar to the stability of MFU-4. Small differences in the intensities of the reflections are observed at higher temperatures due to the removal of residual solvent molecules. At 400 °C, zinc oxide (PDF no. 36-1451) appears as a new crystal phase that predominates

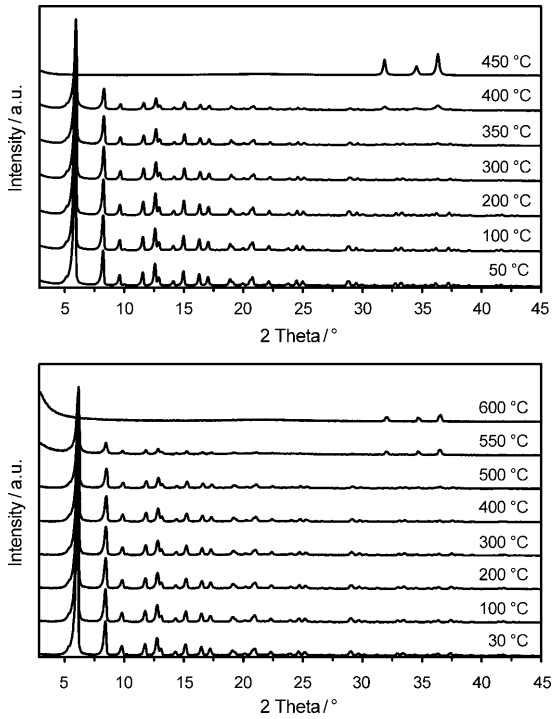

Figure 9. VTXRPD plots of MFU-4*l* in the range of a) 50–450 °C under air and b) 30–600 °C under a nitrogen atmosphere.

above 450 °C, at which the framework is completely decomposed. Under a nitrogen atmosphere it is stable even up to 500 °C (Figure 9b), which is in agreement with TGA measurements.

Physisorption results: MFU-4*l* exhibits permanent porosity, which was confirmed by argon gas sorption. Prior to measurement, the sample was suspended multiple times in dichloromethane, which led to solvent exchange of less-volatile DMF molecules. The sorption isotherm of MFU-4*l* obtained with Ar gas reveals a type-I sorption behavior, which is characteristic of microporous solids (Figure 10). The pore

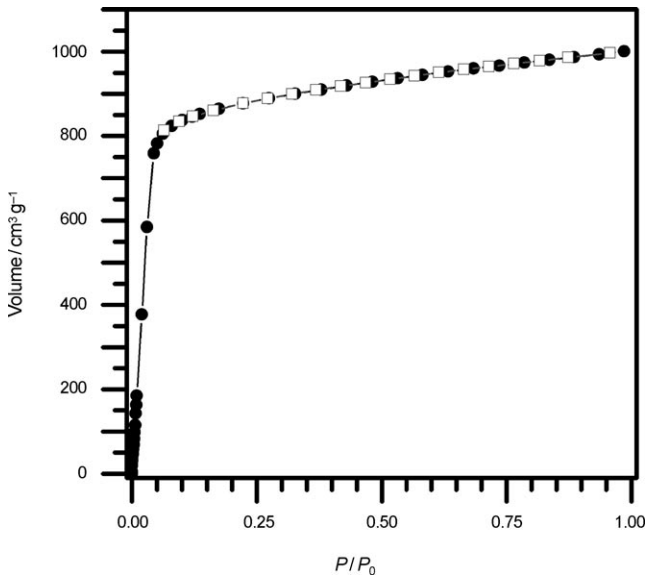

Figure 10. Representative argon adsorption isotherm at 77 K for a desolvated sample of MFU-4*l* (●: adsorption, □: desorption).

volume obtained from the sorption isotherm at $P/P_0 = 0.9$ is 1.26 $cm^3 g^{-1}$ (1.15 $cm^3 g^{-1}$ pore volume and 1.93 nm pore diameter determined by the Dubinin–Radushkevich equation),[23] which is close to the value expected from the crystallographic data (1.42 $cm^3 g^{-1}$ for the solvent-free crystal and 1.86 nm pore diameter). The adsorption data was fitted to the BET equation to give a surface area of 2750 $m^2 g^{-1}$ for MFU-4*l*,[24] which is close to the theoretical values of the specific surface area of 2987 $m^2 g^{-1}$ as derived from the crystal structure by a Monte Carlo integration technique (in which a probe molecule, here argon, is "rolled" over the surface).[24] Experimental values of MFU-4 and MFU-4*l* are compared in Table 2.

Table 2. Measured and calculated[24] specific surface areas.

Framework	Adsorbate	Specific surface area [$m^2 g^{-1}$]	
		Calculated	Measured
MFU-4	H_2	1736	
MFU-4	Ar	1350	ca. 0
MFU-4*l*	H_2	3095	
MFU-4*l*	Ar	2987	2750

To evaluate the pore-size distribution of MFU-4*l*, the argon-sorption isotherms sampled at 77 K were analyzed using nonlocal density functional theory (NLDFT)[25] implementing a carbon equilibrium transition kernel for argon adsorption at 77 K based on a slit-pore model.[26] The distributions calculated by fitting the adsorption data (Figure 11)

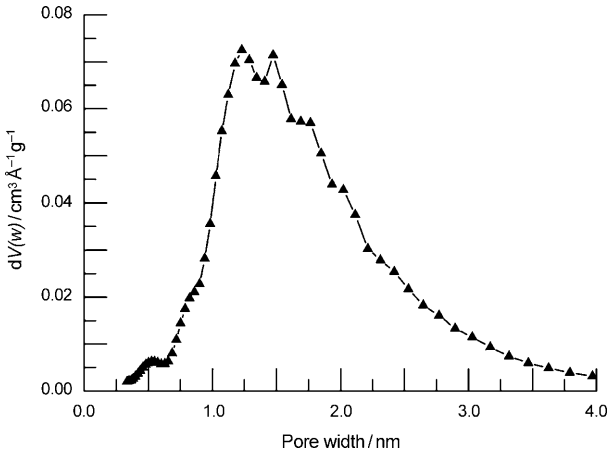

Figure 11. Pore-size distribution for MFU-4*l* calculated by fitting NLDFT models to the argon-adsorption data.

are indicative of micropores with average aperture diameters between 1.1–2.0 nm for MFU-4*l*. These values are in good agreement with the average pore diameters calculated from crystallographic data (1.2 nm for the pores in the **A** cell and 1.86 nm for pores in the **B** cell).[27]

However, both the results of the pore geometries derived from NLDFT calculations and the Dubinin–Radushkevich (DR) equation have to be regarded with caution and should not be over-interpreted, since the available slit-pore model in the case of NLDFT is slightly erroneous due to wrong pore geometry assumptions, and DR suffers from the fact that is does not give a realistic description of micropore filling because it is derived from classical, macroscopic theories.[23]

Hydrogen adsorption: Excess hydrogen-adsorption isotherms of MFU-4*l* up to 20 bar for temperatures between 77 K and room temperature are shown in Figure 12. At 77 K, a typical type-I isotherm is observed but saturation is not reached up to 20 bar. At 20 bar the excess hydrogen uptake is 4 wt % for 77 K and decreases with rising temperature. At room temperature the hydrogen uptake increases linearly with the pressure up to 0.1 wt %. The temperature and pressure dependence of the hydrogen uptake for MFU-4*l* is very similar to MOF-5, which shows an uptake of 4.5 wt % at 77 K and also no saturation up to 20 bar.[6] The investigated MOF-5 reference sample had a specific surface area of 2360 $m^2 g^{-1}$ (nitrogen BET), which is comparable to the surface area of MFU-4*l* of 2750 $m^2 g^{-1}$ (argon BET).

In Figure 13a the excess hydrogen uptake of MFU-4*l* and MFU-4 (all isotherms measured for MFU-4 are given in the

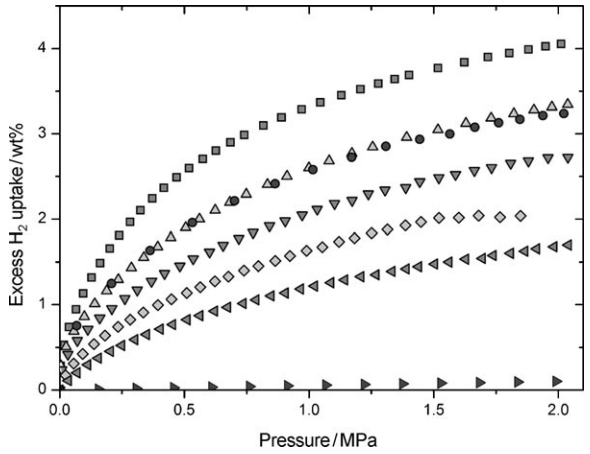

Figure 12. Excess hydrogen adsorption isotherms for MFU-4*l* at 77 K (liquid nitrogen, ■), 87 K (liquid argon, ▲), 87 K (cooling system (CS), ●), 97 K (CS, ▼), 107 K (CS, ◆), 117 K (CS, ◀), and 298 K (▶).

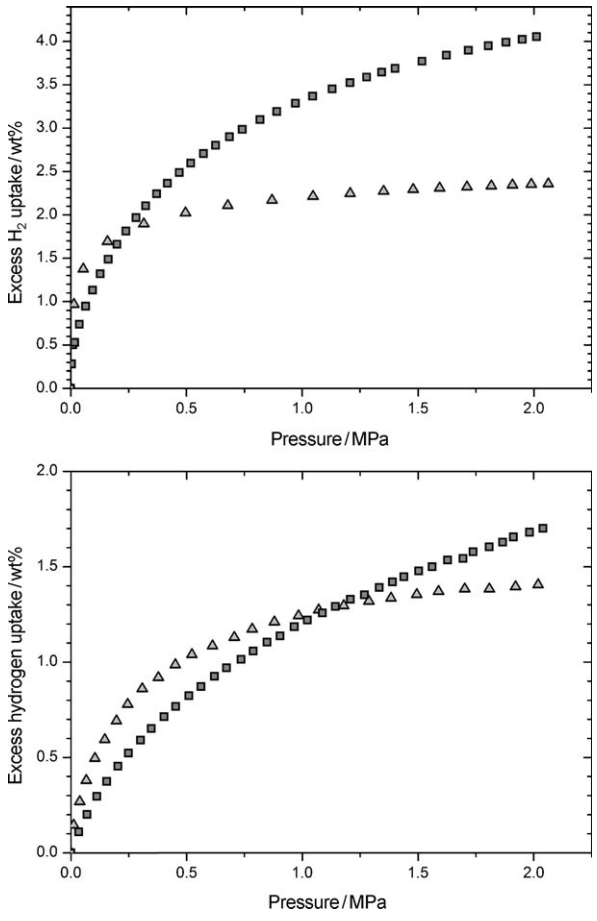

Figure 13. Excess hydrogen uptake at a) 77 K and b) 117 K for MFU-4 (triangles) and MFU-4*l* (squares).

Supporting Information) at 77 K are shown. The two isotherms cross each other at 0.24 MPa. MFU-4 stores more hydrogen at pressures below 0.24 MPa, while at higher pressures MFU-4*l* does not reach saturation and stores up to twice as much hydrogen as MFU-4 (4 wt% at 20 bar). The temperature dependence of the maximum hydrogen uptake is different for MFU-4 and MFU-4*l*. This leads to a shift of the crossover to higher pressures at higher temperatures. For example, at 117 K the crossover is shifted from 0.24 to 1.2 MPa (Figure 13b). At 117 K and 20 bar, MFU-4 stores 1.3 wt% and MFU-4*l* just slightly more with 1.8 wt%.

The difference in the shape of the isotherm is reflected in the heat of adsorption (Figure 14). The isosteric heat of adsorption is calculated from a variant of the Clausius–Clapeyron equation from high pressures (0–2 MPa) isotherms for intermediate surface coverage. For MFU-4 the isosteric heat of adsorption is constant within the experimental uncertainty at 7 kJ mol^{-1}, which is one of the highest heat of adsorption ever observed over such a wide range of surface coverage for hydrogen physisorption in porous materials.[6] For MFU-4*l*, the isosteric heat of adsorption at low surface coverage is approximately 5 kJ mol^{-1} and strongly decreases with hydrogen uptake. Above 30% surface coverage the heat of adsorption remains constant at 3.5 kJ mol^{-1}. This difference in the isosteric heat of adsorption is caused by the pore structure, as smaller pores lead to higher overlap of the van der Waals potentials of the wall and therefore higher heat of adsorption.[6]

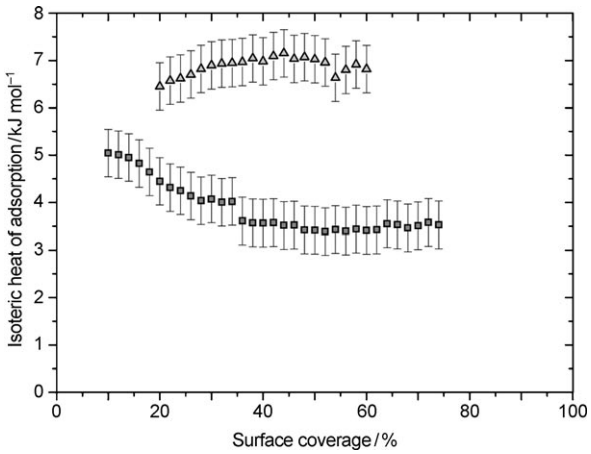

Figure 14. Isosteric heat of adsorption for hydrogen in MFU-4 (triangles) and MFU-4*l* (squares) normalized to the hydrogen uptake at 20 bar and 77 K.

Thermal desorption spectroscopy: Figure 15 shows thermal desorption spectra of hydrogen for MFU-4 and MFU-4*l* for two different heating rates, 0.1 and 0.01 Ks^{-1} in a temperature range between 20 and 120 K. At higher temperatures no hydrogen was desorbed. The TDS spectra show distinct differences in the temperature profile and in the magnitude of the signal between MFU-4 and MFU-4*l*. Furthermore, the desorption spectra measured with a slower heating rate are slightly shifted toward lower temperatures, which indicates that the hydrogen release is thermally activated. For MFU-4*l*, the majority of the adsorbed hydrogen molecules were desorbed below 60 K, whereas for MFU-4 the major hydrogen desorption just began at this temperature. The

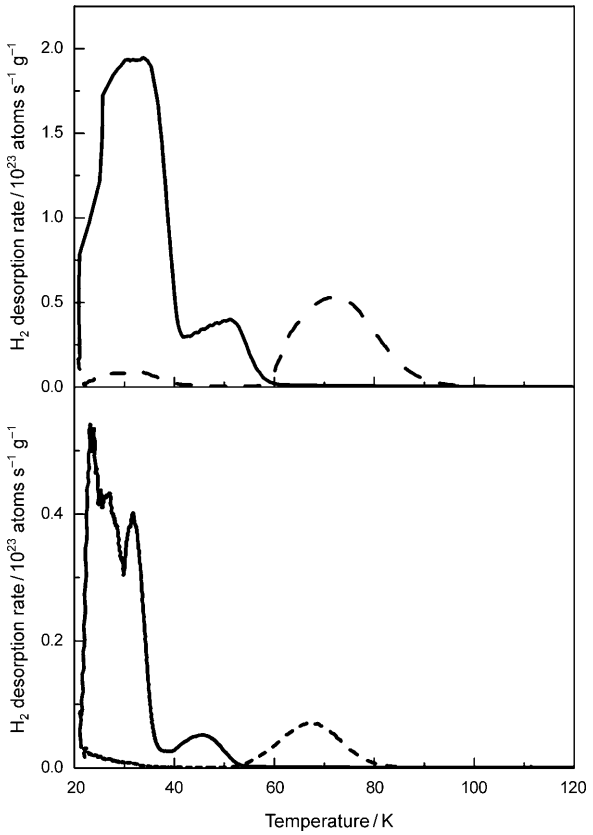

Figure 15. Hydrogen thermal desorption spectra of MFU-4 (-----) and MFU-4*l* (——) recorded with a heating rate of 0.1 Ks^{-1} (top) and 0.01 Ks^{-1} (bottom).

total amount of desorbed gas, corresponding to the area under the desorption curve, was about 2.5 and 1 wt% for MFU-4*l* and MFU-4, respectively.

MFU-4*l* exhibits two hydrogen-desorption maxima, one broad and large maximum centered at approximately 32 K and a smaller maximum centered at 51 K (for a heating rate of 0.1 Ks^{-1}). During cooling under a hydrogen atmosphere a certain amount of gas is liquefied or adsorbed in multilayers giving rise to additional desorption in this low-temperature region.[7,28] For MFU-4*l* this effect gives rise to the low-temperature shoulder and the first large desorption peak for a heating rate of 0.1 and 0.01 Ks^{-1}, respectively. Nevertheless, the presence of two distinct desorption maxima for MFU-4*l* indicates clearly the presence of two hydrogen adsorption sites possessing different heats of adsorption. The larger first desorption peak at about 32 K can be assigned to hydrogen adsorbed in the cavities. The smaller maximum at about 51 K corresponds to stronger binding sites as already indicated by the higher heat of adsorption for low surface coverage in the pressure–capacity–temperature (PCT) measurements (Figure 14).

In contrast, for MFU-4 one dominant desorption maximum is observed at 71 K and a smaller signal around 30 K. The desorption signal in the low-temperature region may be caused by gas liquefied or adsorbed in multilayers. Most of the hydrogen is desorbing at temperatures above 60 K, which is much higher than that of the other MOFs.[9] Indeed MFU-4 exhibits a desorption maximum with the highest temperature ever measured for physisorbed hydrogen on MOFs. The MFU-4 framework is constructed from smaller and larger cavities, arranged in an alternate fashion.[11] Owing to this structure, hydrogen molecules moving from one larger cavity to another must pass through a smaller cavity. Therefore, the diffusion of the hydrogen molecule through the aperture of the small cavities, with a diameter of approximately 2.52 Å, is the limiting factor for the degassing of hydrogen and gives rise to the high desorption temperature.

The total hydrogen uptake was calculated to about 1 wt% for MFU-4, in comparison to 2.5 wt% for MFU-4*l*. These values are lower than the maximum excess adsorption at high pressures and 77 K, which typically, for MOFs are correlated to the specific surface area and are independent of the compound.[7,29] The results obtained from TDS are sometimes lower, and especially if the heat of adsorption is low, part of the adsorbed hydrogen will be pumped away during evacuation already at 20 K. The lower value for MFU-4 may be caused by a partial filling of the cavities at 700 mbar and cooling down to 20 K, because the kinetics of the filling is limited by the diffusion through the small window of the smaller cavity.

Conclusion

We have successfully prepared and characterized a novel member of isoreticular MFU-4-type cubic frameworks, MFU-4*l*, constructed from $BTDD^{2-}$ dianions and $\{Zn_5Cl_4\}^{6+}$ coordination units. The linker can be easily synthesized in three steps. Compared to solvothermal synthesis, the preparation of MFU-4*l* by microwave irradiation leads to a large reduction in reaction time. Thermogravimetric and VTXRPD analyses indicate that MFU-4*l* possesses very high thermal stability (500 °C under nitrogen). Large pore apertures of 9.1 Å allow adsorption and free diffusion of different molecules. In contrast, MFU-4, with small pore apertures of 2.5 Å, is highly selective for the adsorption of atoms or small molecules such as He or H_2 and it can therefore be applied in molecular sieving applications, some of which are hard to achieve with any other kinds of porous materials. MFU-4*l*, which has a much higher surface area, generally is able to adsorb more hydrogen than MFU-4. However, at higher temperatures and lower pressures MFU-4 adsorbs more hydrogen than MFU-4*l*. Moreover, the values of isosteric heat of adsorption, which is constant over a wide range of surface coverage and of desorption temperature, belong to the highest ever observed for hydrogen physisorption on porous materials. This makes MFU-4 more suitable for hydrogen adsorption than MFU-4*l*. These observations demonstrate the importance of pore size in designing new materials for hydrogen storage. Figure 16 shows a comparison of MFU-4 and MFU-4*l* frameworks. The diffusion path

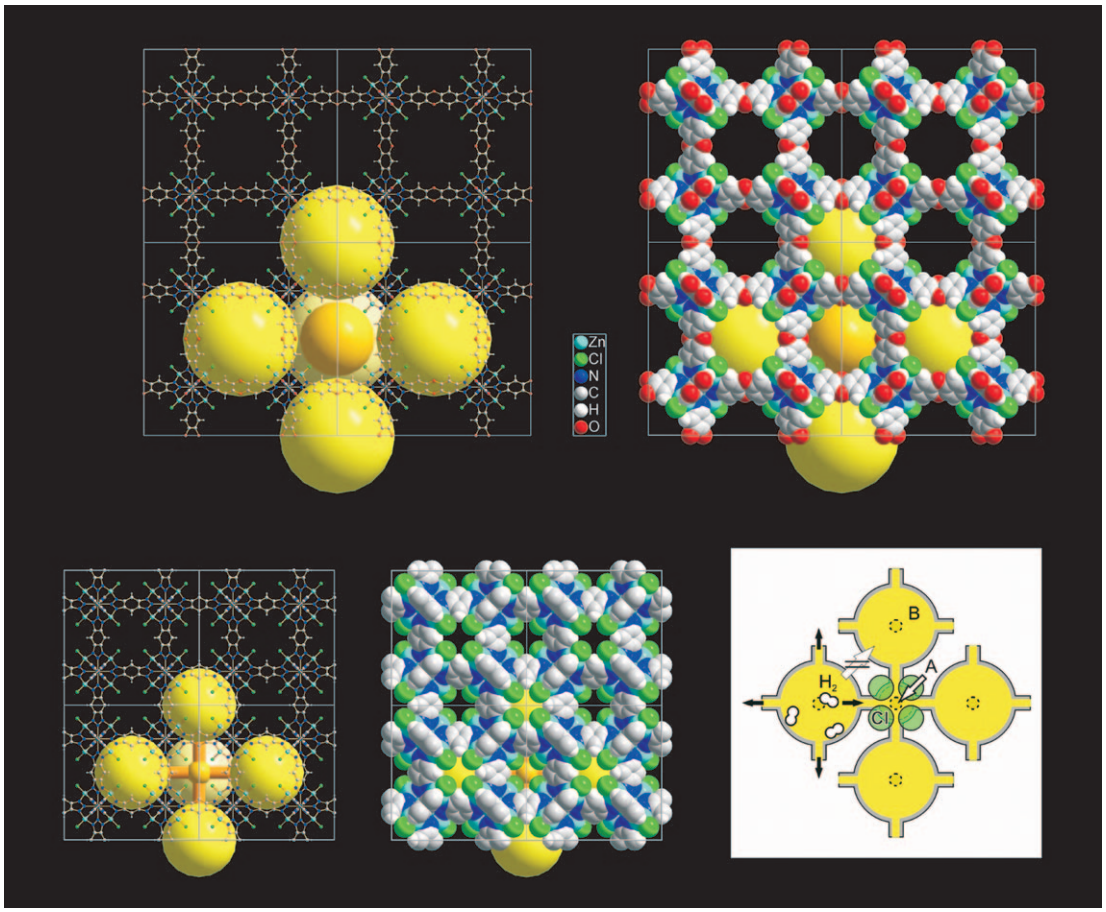

Figure 16. Frameworks of MFU-4*l* (top), MFU-4 (bottom left and middle), and the diffusion path of hydrogen molecules in MFU-4 through the aperture between **A** and **B** cells (bottom right).

of hydrogen molecules in MFU-4 through the aperture between the **A** and **B** cells is shown on the bottom right.

In conclusion, we have demonstrated that MFU-4-type frameworks have a huge potential for the development of functional materials for hydrogen storage, gas separation (MFU-4), and possible catalytic applications (MFU-4*l*). Further investigations of these frameworks are currently underway in our laboratories. For structure solution and refinement of MFU-4*l*, three-dimensional electron-diffraction data acquired by using the ADT technique was used successfully. This is the first ab initio structure solution of an unknown MOF performed with electron-diffraction data. The new ADT method delivers intensity data superior in quality and quantity and has proven to be quick, reliable, and promising for future structural investigations on MOF compounds, in which single crystals of sufficient sizes are notoriously hard to obtain.

Experimental Section

Materials and general methods: All starting materials were of reagent grade and used as received from the commercial supplier. Fourier transform infrared (FTIR) spectra were recorded from KBr pellets in the range 4000–400 cm^{-1} on a Bruker IFS FTIR spectrometer. The following indications are used to characterize absorption bands: very strong (vs), strong (s), medium (m), weak (w), shoulder (sh), and broad (br). Elemental analyses (C, H, N) were carried out on a Perkin–Elmer 2400 elemental analyzer. TGA was performed with a TGA/SDTA851 Mettler Toledo analyzer in the temperature range of 25–1100 °C under flowing nitrogen at a heating rate of 10 K min^{-1}. TGA/MS analysis was carried out using Netsch thermoanalyzer STA 409 C connected to a Balzers QMG mass spectrometer by a Skimmer coupling system in the temperature range of 20–700 °C under a N_2 flow with a heating rate of 10 K min^{-1}. Thermodesorption GC–MS analysis was carried out using Perkin–Elmer ATD 400 inlet and a Varian 3400 gas chromatograph coupled with a Finnigan Mat ITS40 mass spectrometer. The sample was heated in a glass tube at 260 °C for 15 min before measurement. SEM images were recorded using a Zeiss DSM 962 scanning electron microscope. Argon-gas sorption isotherms were measured with a Quantachrome Autosorb-I ASI-CP-8 instrument. Prior to measurements, the samples of dichloromethane-exchanged MFU-4*l* were heated at 180 °C for 24 h under high vacuum to remove the occluded solvent molecules. Argon-sorption experiments were performed at 77.3 K in the range of $5.00\times10^{-5}\leq P/P_0\leq1.00$ with Ar.

2,3,7,8-Tetranitrodibenzo[1,4]dioxin (3):[14] Fuming nitric acid (24 mL) was added to trifluoroacetic acid anhydride (16 mL) under cooling in an ice/water bath. Dibenzo[1,4]dioxin (5 g, 27.2 mmol) was added in small portions to a well-stirred nitration mixture while keeping the temperature below 10 °C. The reaction mixture was stirred for 1.5 h at 60–70 °C at reflux and then poured into ice/water (400 mL) with stirring. The precipitate was removed by filtration, washed well with water, and dried under vacuum over P_4O_{10}. Yield: 7.2 g (73 %); ^{1}H NMR (400 MHz,

[D$_6$]DMSO): $\delta = 8.03$ ppm (s, 4H); ^{13}C NMR (100 MHz, [D$_6$]DMSO): $\delta = 113.8$, 138.7, 143.6 ppm; IR (KBr): $\tilde{\nu} = 3104$ (m), 3055 (m), 1641 (w), 1605 (m), 1558 (s), 1495 (s), 1431 (m), 1376 (s), 1348 (s), 1306 (s), 895 (s), 818 cm^{-1} (s); elemental analysis calcd (%) for $C_{12}H_4N_4O_{10}$: C 39.58, H 1.11, N 15.38; found: C 39.08, H 1.17, N 15.18.

H_2-BTDD·0.5H_2O (2): A well-stirred mixture of compound **4** (7 g, 19.8 mmol), acetic acid (70 mL), and water (10 mL) was cooled in an ice/water bath and a solution of sodium nitrite (2.9 g, 42 mmol) in water (10 mL) was added slowly while keeping the temperature below 10 °C. The mixture was diluted with water (100 mL), the precipitate was removed by filtration, washed well with water and methanol, and dried under vacuum over P_4O_{10}. Yield 3.72 g (69 %); ^{1}H NMR (400 MHz, CF_3COOD): $\delta = 7.85$ ppm (s, 4H); ^{13}C NMR (100 MHz, CF_3COOD): $\delta =$ 99.8, 131.1, 144.7 ppm; IR (KBr): $\tilde{\nu} = 3448$ (br), 3129 (s), 2899 (s), 2803 (s), 1711 (w), 1595 (m), 1480 (s), 1416 (m), 1355 (s), 1218 (s), 1076 (m), 1004 (m), 919 (m), 860 (s), 633 (w), 431 cm^{-1} (w); elemental analysis calcd (%) for $C_{12}H_7N_6O_{2.5}$: C 52.37, H 2.56, N 30.54; found: C 52.45, H 2.52, N 29.91.

[Zn_5Cl_4(BTDD)$_3$] (MFU-4*l*)

Solvothermal method: H_2-BTDD (760 mg, 2.77 mmol) was dissolved in DMF (760 mL) under stirring and heating at 145 °C for 30 min. Anhydrous zinc chloride (7.78 g, 57.2 mmol) was added to a cooled (ca. 50 °C) solution of linker and the mixture was stirred until the zinc chloride was completely dissolved. The resulting solution was heated with stirring under reflux at 145 °C for 18 h and then cooled down to room temperature. The precipitate was removed by filtration, washed slowly with DMF (3 × 50 mL), methanol (3 × 50 mL), and dichloromethane (3 × 50 mL), and dried for 24 h at 180 °C under vacuum (ca. 0.2 mbar). Yield 940 mg (90 % based on ligand) of an almost white microcrystalline powder; IR (KBr): $\tilde{\nu} = 3420$ (br), 3076 (w), 2924 (w), 2854 (w), 1731 (w), 1576 (w), 1460 (s), 1346 (m), 1171 (s), 915 (m), 802 (m), 732 (w), 601 (w), 500 cm^{-1} (m); elemental analysis calcd (%) for $C_{36}H_{12}Cl_4N_{18}O_6Zn_5$: C 34.28, H 0.96, N 19.99; found: C 33.98, H 1.21, N 19.55.

Microwave irradiation method: H_2-BTDD (5 mg, 0.0188 mmol) was dissolved in DMF (5 mL) under stirring and heating at 145 °C for 10 min. A 1 M solution of anhydrous zinc chloride in DMF (0.4 mL, 0.4 mmol) was added to a cooled (ca. 50 °C) solution and the mixture was placed in a Pyrex sample tube (10 mL). The tube was sealed and placed in a microwave synthesizer (CEM, Discover S). The resulting mixture was heated to 155 °C at 300 W, kept under these conditions for 30 min, and then cooled down to room temperature. The precipitate was removed by filtration, washed slowly with DMF (5 mL), methanol (5 mL), and dichloromethane (3 × 10 mL), and dried for 24 h at 180 °C under vacuum (ca. 0.2 mbar). Yield 5.2 mg (73 %) of an almost white microcrystalline powder. This material exhibited the same analytical results as those obtained by the solvothermal method and is phase-pure according to XRPD measurement.

Crystal structure determination by ADT: ADT[16–18] was performed in a FEI F30 TEM. The sample was deposited as a dry powder on a carbon grid and cooled to −160 °C inside the microscope. An area of around 300 × 300 nm, on the edge of a crystal that was 1000 × 600 nm large, was selected for data acquisition. To have a quasi-parallel electron beam of 70 nm in diameter and a low electron dose on the sample, a C2 condenser aperture of 10 μm was inserted and a high gun lens current and spot size were used (respectively 8 and 8 for that microscope). During the tilt, the crystal position was tracked in STEM microprobe mode and the electron-diffraction patterns were collected every 1° of tilt, with an exposure time of 5 s. Two tilt series were collected with and without precession of the beam.[30] The tilt without precession, sampling a range of 60°, was used for cell-parameter determination. The tilt with precession, sampling a range of 66°, was used for intensity extraction.

All the possible 412 independent reflections up to a resolution of 1.3 Å were integrated (coverage of 100 % of the reciprocal space). The internal R_{sym} was 28.63 %. The isotropic thermal factor determined by a Wilson plot was 0.048 Å^2. Ab initio structure solution was performed by direct methods implemented in SIR2008[31] with a fully kinematic approach ($I = F^2$). The almost complete structure was delivered in one run. Inside the first 10 potentials, 9 corresponded to 9 atoms of the structure and 1 potential to a ghost close to a Zn atom. The missing carbon atom (potential 11) was placed in a wrong special position.

The structure was refined by SHELXL.[32] The ghost disappeared during the refinement and the missing carbon atom was placed imposing a rigid benzene group. The final refinement, performed with soft restraints on bond lengths, resulted in a final residual R of 32.1 %.

Crystal structure determination by PXRD: For the PXRD study, a portion of the sample was powdered and placed between two sheets of foil. Intensity data were collected using a STOE STADI P powder diffractometer with germanium monochromator, operated at 40 kV, 40 mA, Cu target; transmission geometry, fixed divergence slit 1/4°. The PXRD pattern was taken at room temperature in the 2θ range from 2.8 to 70°, step size 0.01, and time per step 596.6 s.

Variable-temperature X-ray powder diffraction (VTXRPD) measurements were performed under air or nitrogen with a PANalytical X'Pert PRO diffractometer with a X'Celerator detector operated at 45 kV, 40 mA, with $Cu_{K\alpha}$ radiation, fixed divergence slit $^1/_2$°, equipped with an Anton Paar HTK 1200N reaction chamber. Measurements were performed at a temperature range from 30 to 600 °C, by employing 2θ ranges from 3.0 to 80.0°, step size 0.033° 2θ, time 98 s per step. The heating rate was 5 °C min^{-1}. The sample was heated before measurement at each temperature for 15 min.

Extractions of the peak positions, pattern indexing, and determination of the lattice parameters for MFU-4*l* were carried out with the PROSZKI package.[33] Independently, the indexing process was performed by the N-TREOR09 program implemented in the EXPO2009 package.[34] Space group determination by probabilistic approach was performed by using EXPO2009. The set of the most probable space groups was found: extinction group F; space groups $F23$ (196), $Fm\bar{3}$ (202), $F432$ (209), $F\bar{4}3m$ (216), $Fm\bar{3}m$ (225). The $Fm\bar{3}m$ (225) space group was chosen for further structure determination procedures. During pattern decomposition the lattice parameters were not refined. The positions of heavy atoms Zn and Cl were found by direct methods; missing light atoms O, C, and N were localized on difference Fourier maps. Hydrogen atoms were placed in idealized position in the SHELXL program.[32]

The Rietveld refinement was carried out using the Jana2006 program.[35] Weak geometric restraints on bond lengths were used during the refinement process. No preferred orientation has been observed. Experimental details and crystal data for MFU-4*l* are listed in Table 3. The final Rietveld refinement plots are presented in Figure 17.

CCDC-776578 contains the supplementary crystallographic data for this paper. These data can be obtained free of charge from The Cambridge Crystallographic Data Centre via www.ccdc.cam.ac.uk/data_request/cif.

Hydrogen adsorption measurements: Hydrogen-adsorption measurements were performed with an automated Sieverts' apparatus

Table 3. Crystal and experimental data for MFU-4*l*.

chemical formula	$C_{36}Cl_4N_{18}H_{12}O_6Zn_5$
formula weight	1261.32
T [K]	293(2)
2θ range [°], step size [°]	2.80–70, 0.01
X-ray source, wavelength [Å]	$Cu_{K\alpha}$, $\lambda = 1.54178$
crystal system	cubic
space group	$Fm\bar{3}m$ (225)
a [Å]	31.0569(6)
V [Å^3]	29955.2(5)
M_{30}	75.01 (0.00002, 30)
F_{30}	184.77 (0.00416, 30)
Z, ρ_{calcd} [g cm^{-3}]	8, 0.5592
no. of atoms	5
no. of observations	6720
unique reflections	315
R_p	4.63
R_{wp}	7.16
R_{obs}	5.88
R_{wobs}	5.82

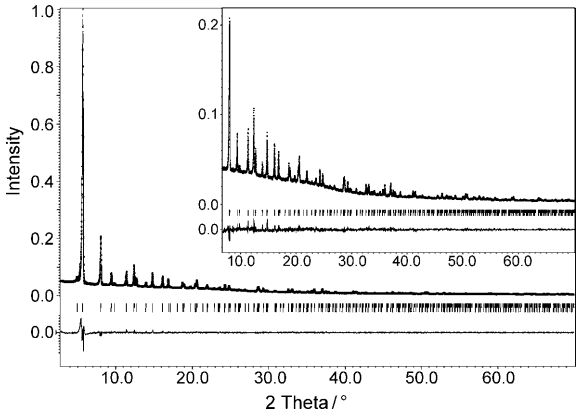

Figure 17. The Rietveld refinement plots for MFU-4*l*. Dotted and solid lines represent observed and calculated patterns, respectively, with peak markers and the difference plot shown at the bottom. For clarity, the inset shows an expanded view in the range 7–70° 2θ.

(PCTPro2000, HY-Energy LLC, Setaram Inc.) and are described in detail elsewhere.[6] MFU-4*l* (115 mg) was evacuated at 180 °C overnight prior to the measurements and between each isotherm for 2 h at 50 °C. Equilibrium was reached for all pressures below 1 min. For MFU-4, two measurements were performed, first at temperatures between 77 and 117 K on a 180 mg sample and later at temperatures between 127 and 177 K on a 216 mg sample. In both experiments the sample was out-gassed overnight prior to the measurement at 250 (first sample) and 180 °C (second sample). Between individual measurements of isotherms the sample was out-gassed at temperatures above 50 °C for more than 1 h. For further analysis, results from both samples were combined.

In porous solids hydrogen is mainly adsorbed as a monolayer on inner surfaces. The amount of hydrogen that is in this adsorbed layer is called absolute adsorbed hydrogen.[36] Whereas, the excess adsorption, typically measured by taking into account the skeletal density of the material, represents the amount of hydrogen that is stored in addition to the amount of hydrogen gas that would be present in the pore volume due to external pressure. The excess adsorption is therefore smaller than the absolute adsorption by the amount of hydrogen gas that would be in the adsorbed layer if no adsorption occurred. Hence the absolute adsorption is calculated from the excess adsorption with the assumption that the adsorbed layer exhibits the density of liquid hydrogen (see the Supporting Information). The isosteric heat of adsorption is calculated from the absolute adsorbed hydrogen according to a variant of the Clausius–Clapeyron equation.[6]

Thermal desorption spectroscopy: The degassing of hydrogen was studied by low-temperature thermal desorption spectroscopy (TDS) using a special apparatus described in detail elsewhere.[28] The typical mass used is about 3 mg and the samples were out-gassed at a temperature of 440 K under high vacuum for approximately 10 h prior to the first measurement and between the measurements for at least 1 h. Then the samples were exposed to a hydrogen atmosphere (purity 99.999 %) of 700 mbar at room temperature and then cooled down to 20 K. After about 30 min at 20 K, the sample cell was evacuated. Following this, the temperature was increased with a linear heating rate (0.1 and 0.01 Ks^{-1}) from 20 to 370 K and the desorbed gases were analyzed by using a quadrupole mass spectrometer. The total number of desorbed hydrogen atoms was derived for each TDS spectrum, since the spectrometer was previously calibrated with Pd.[28]

Acknowledgements

Financial Support by the DFG (Priority Program SPP 1362 "Porous Metal-organic Frameworks" and Sonderforschungsbereich 625 "Von einzelnen Molekülen zu nanoskopisch strukturierten Materialien") is gratefully acknowledged.

[1] L. J. Murray, M. Dincă, J. R. Long, *Chem. Soc. Rev.* **2009**, *38*, 1294–1314.
[2] H. Frost, T. Düren, R. Q. Snurr, *J. Phys. Chem. B* **2006**, *110*, 9565–9570.
[3] S. S. Kaye, A. Dailly, O. M. Yaghi, J. R. Long, *J. Am. Chem. Soc.* **2007**, *129*, 14176–14177.
[4] S. K. Bhatia, A. L. Myers, *Langmuir* **2006**, *22*, 1688–1700.
[5] M. Dinca, J. R. Long, *Angew. Chem.* **2008**, *120*, 6870–6884; *Angew. Chem. Int. Ed.* **2008**, *47*, 6766–6779.
[6] B. Schmitz, U. Müller, N. Trukhan, M. Schubert, G. Férey, M. Hirscher, *ChemPhysChem* **2008**, *9*, 2181–2184.
[7] B. Panella, K. Hönes, U. Müller, N. Trukhan, M. Schubert, H. Pütter, M. Hirscher, *Angew. Chem.* **2008**, *120*, 2169–2173; *Angew. Chem. Int. Ed.* **2008**, *47*, 2138–2142.
[8] M. Rzepka, P. Lamp, M. A. de La Casa-Lillo, *J. Phys. Chem. B* **1998**, *102*, 10894–10898.
[9] a) M. Eddaoudi, D. B. Moler, H. Li, B. Chen, T. M. Reineke, M. O'Keeffe, O. M. Yaghi, *Acc. Chem. Res.* **2001**, *34*, 319–330; b) M. Eddaoudi, J. Kim, N. Rosi, D. Vodak, J. Wachter, M. O'Keeffe, O. M. Yaghi, *Science* **2002**, *295*, 469–472; c) H. Li, M. Eddaoudi, M. O'Keeffe, O. M. Yaghi, *Nature* **1999**, *402*, 276–279.
[10] M. Tonigold, Y. Lu, B. Bredenkötter, B. Rieger, S. Bahnmüller, J. Hitzbleck, G. Langstein, D. Volkmer, *Angew. Chem.* **2009**, *121*, 7682–7687; *Angew. Chem. Int. Ed.* **2009**, *48*, 7546–7550.
[11] S. Biswas, M. Grzywa, H. P. Nayek, S. Dehnen, I. Senkovska, S. Kaskel, D. Volkmer, *Dalton Trans.* **2009**, 6487–6495.
[12] S. Biswas, M. Tonigold, D. Volkmer, *Z. Anorg. Allg. Chem.* **2008**, *634*, 2532–2538.
[13] K. Kuratowski, *Fund. Math.* **1930**, *15*, 271–283.
[14] H. Gilman, J. J. Dietrich, *J. Am. Chem. Soc.* **1958**, *80*, 366–368.
[15] K. Chichak, U. Jacquemard, N. R. Branda, *Eur. J. Inorg. Chem.* **2002**, 357–368.
[16] U. Kolb, T. Gorelik, C. Kübel, M. T. Otten, D. Hubert, *Ultramicroscopy* **2007**, *107*, 507–513.
[17] U. Kolb, T. Gorelik, M. T. Otten, *Ultramicroscopy* **2008**, *108*, 763–772.
[18] E. Mugnaioli, T. Gorelik, U. Kolb, *Ultramicroscopy* **2009**, *109*, 758–765.
[19] U. Kolb, T. E. Gorelik, E. Mugnaioli, A. Stewart, *Polymer Reviews* **2010**, *50*, 385–409.
[20] I. Rozhdestvenskaya, E. Mugnaioli, M. Czank, W. Depmeier, U. Kolb, A. Reinholdt, T. Weirich, *Mineral. Mag.* **2010**, *74*, 159–177.
[21] a) O. I. Lebedev, F. Millange, C. Serre, G. Van Tendeloo, G. Férey, *Chem. Mater.* **2005**, *17*, 6525–6527; b) D. Chandra, M. W. Kasture, A. Bhaumik, *Microporous Mesoporous Mater.* **2008**, *116*, 204–209; c) D. Jiang, T. Mallat, F. Krumeich, A. Baiker, *J. Catal.* **2008**, *257*, 390–395; d) S. Turner, O. I. Lebedev, F. Schröder, D. Esken, R. A. Fischer, G. Van Tendeloo, *Chem. Mater.* **2008**, *20*, 5622–5627; e) F. Schröder, D. Esken, M. Cokoja, M. W. E. van den Berg, O. I. Lebedev, G. Van Tendeloo, B. Walaszek, G. Buntkowsky, H.-H. Limbach, B. Chaudret, R. A. Fischer, *J. Am. Chem. Soc.* **2008**, *130*, 6119–6130; f) S. J. Yang, J. Y. Choi, H. K. Chae, J. H. Cho, K. S. Nahm, C. R. Park, *Chem. Mater.* **2009**, *21*, 1893–1897.
[22] A. L. Spek, *J. Appl. Crystallogr.* **2003**, *36*, 7–13.
[23] F. Rouquerol, J. Rouquerol, K. Sing, *Adsorption by Powders & Porous Solids*, Academic Press, San Diego, **1999**.
[24] a) T. Düren, F. Millange, G. Férey, K. S. Walton, R. Q. Snurr, *J. Phys. Chem. C* **2007**, *111*, 15350–15356; b) K. S. Walton, R. Q. Snurr, *J. Am. Chem. Soc.* **2007**, *129*, 8552–8556.
[25] P. I. Ravikovitch, A. V. Neimark, *Colloids Surf. A* **2001**, *187–188*, 11–21.
[26] J. Jagiello, M. Thommes, *Carbon* **2004**, *42*, 1227–1232.
[27] The van der Waals radii of C (0.17 nm) and Cl (0.175 nm) were used to calculate the width of the apertures: A. Bondi, *J. Phys. Chem.* **1964**, *68*, 441–451.

[28] B. Panella, M. Hirscher, B. Ludescher, *Microporous Mesoporous Mater.* **2007**, *103*, 230–234.
[29] B. Panella, M. Hirscher, H. Puetter, U. Mueller, *Adv. Funct. Mater.* **2006**, *16*, 520–524.
[30] R. Vincent, P. A. Midgley, *Ultramicroscopy* **1994**, *53*, 271–282.
[31] M. C. Burla, R. Caliandro, M. Camalli, B. Carrozzini, G. L. Cascarano, L. De Caro, C. Giacovazzo, G. Polidori, S. Diligi, R. Spagna, *J. Appl. Crystallogr.* **2007**, *40*, 609–613.
[32] G. Sheldrick, *Acta Crystallogr. Sect. A* **2008**, *64*, 112–122.
[33] W. Lasocha, K. Lewinski, *J. Appl. Crystallogr.* **1994**, *27*, 437–438.
[34] A. Altomare, M. Camalli, C. Cuocci, C. Giacovazzo, A. Moliterni, R. Rizzi, *J. Appl. Crystallogr.* **2009**, *42*, 1197–1202.
[35] V. Petricek, M. Dusek, L. Palatinus, Jana2006. The crystallographic computing system. Institute of Physics, Praha, Czech Republic, **2006**.
[36] F. O. Mertens, *Surf. Sci.* **2009**, *603*, 1979–1984.

Received: May 10, 2010
Published online: January 12, 2011

CHEMISTRY
A EUROPEAN JOURNAL

Supporting Information

Elucidating Gating Effects for Hydrogen Sorption in MFU-4-Type Triazolate-Based Metal–Organic Frameworks Featuring Different Pore Sizes

Dmytro Denysenko,[a] Maciej Grzywa,[a] Markus Tonigold,[b] Barbara Streppel,[c] Ivana Krkljus,[c] Michael Hirscher,[c] Enrico Mugnaioli,[d] Ute Kolb,[d] Jan Hanss,[a] and Dirk Volkmer*[a, b]

chem_201001872_sm_miscellaneous_information.pdf

Hydrogen adsorption isotherms of MFU-4

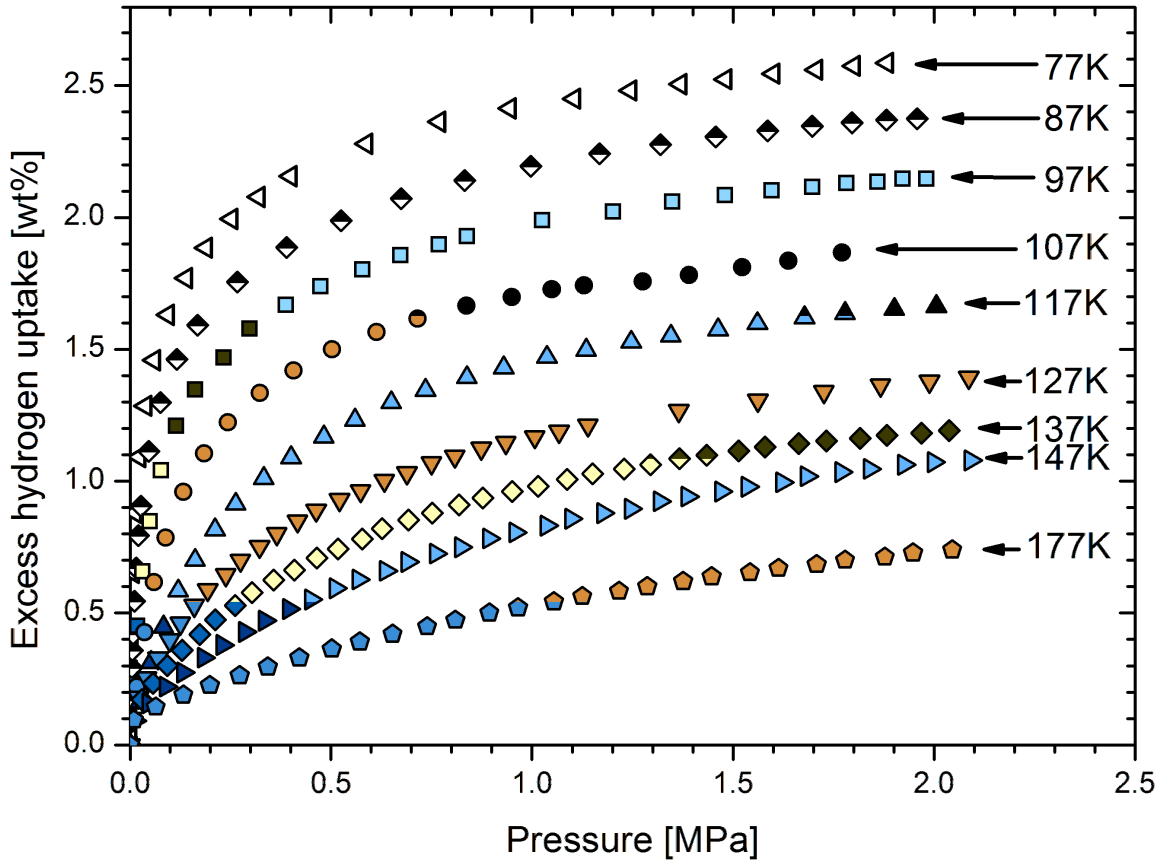

Figure S1. Excess hydrogen uptake of MFU-4 measured at temperatures between 77 K and 177 K. For calculation of the isosteric heat of adsorption isotherms between 97 K and 177 K are used.

Calculation of absolute adsorption out of excess adsorption

For estimating the absolute amount adsorbed the volume of the adsorbed layer (V_{ads}) needs to be known. The density of the adsorbed hydrogen is close to the density of liquid hydrogen ($?_{lq}$) and therefore the volume of the adsorbed layer is $V_{ads} = ?_{lq} \bullet n_{excess} \bullet M_{H_2}$

where M_{H_2} is the molar mass of hydrogen. Owing to the external pressure, in the volume of the adsorbed layer would be the amount of gas (n_{gas}) present if there was no adsorption. This can be calculated from the ideal gas equation including a compression factor Z which is calculated from virial expansion of the van der Waals equation:

$n_{gas} = P \bullet V_{ads}/(Z \bullet R \bullet T)$

with $Z = (1.000547-6.07 \bullet 10^{-7}T+(0.000912-1.0653 \bullet 10^{-6}T) \bullet P+(7.373407-0.0901 \bullet 10^{-7}T) \bullet P^2$

The absolute amount adsorbed n_{ads} is therefore

$n_{ads} = (n_{excess}+n_{gas}) = n_{excess}\bullet(1+P\bullet?_{lq}\bullet M_{H_2}/(Z\bullet R\bullet T))$

Structural parameters of MFU-4*l* from powder X-Ray diffraction data.

Table S1. Atom coordinates and equivalent displacement parameters for MFU-4*l*.

Atom	x	y	z	U
H1	0.4207	0.3037	0.1963	0.038
Zn1	0.31771(19)	0.31771(19)	0.1823	0.021(2)
Cl1	0.3562(4)	0.3562(4)	0.1438	0.052(8)
Zn2	0.25	0.25	0.25	0.031(9)
N1	0.34070(4)	0.27492(3)	0.2251	0.063(13)
C1	0.38265(3)	0.26599(4)	0.234	0.016(9)
N2	0.31573(3)	0.25	0.25	0.063(13)
C2	0.42117(3)	0.28257(3)	0.2174	0.016(9)
C3	0.46096(3)	0.26662(3)	0.2334	0.016(9)
O1	0.5	0.28346(4)	0.2165	0.064(18)

Table S2. Selected bond distances (Å) for MFU-4*l*.

Bond	Distance	Bond	Distance	Bond	Distance
Zn1-Cl1	2.070(11)	Zn2-N2$^{(f)}$	2.0414(9)	C1-C1$^{(h)}$	1.4044(12)
Zn1-N1	2.010(5)	Zn2-N2$^{(g)}$	2.0414(9)	C1-N2	2.1937(12)
Zn1-N1$^{(a)}$	2.010(5)	Zn2-N2$^{(d)}$	2.0414(9)	C1-C2	1.4006(11)
Zn1-N1$^{(b)}$	2.010(6)	N1-N1$^{(h)}$	2.1894(9)	C1-C2$^{(h)}$	2.4453(11)
Zn1-N2	2.974(4)	N1-N1$^{(a)}$	2.8891(14)	C1-C3	2.4323(11)
Zn1-N2$^{(c)}$	2.974(4)	N1-N1$^{(b)}$	2.8891(14)	C1-C3$^{(h)}$	2.8226(11)
Zn1-N2$^{(d)}$	2.974(6)	N1-C1	1.3605(15)	N2-N2$^{(c)}$	2.8870(9)

Zn2-N2	2.0414(9)	N1-C1[(h)]	2.2194(12)	N2-N2[(f)]	2.8870(9)
Zn2-N2[(e)]	2.0414(9)	N1-N2	1.3416(10)	N2-N2[(g)]	2.8870(9)
Zn2-N2[(c)]	2.0414(9)	N1-C2	2.5215(15)		

Symmetry transformations used to generate equivalent atoms:

[(a)] -z+½, x, -y+½

[(b)] y, -z+½, -x+½

[(c)] z, x, y

[(d)] -y+½, z, -x+½

[(e)] -x+½, -y+½, z

[(f)] z, -x+½, -y+½

[(g)] y, z, x

[(h)] x, -y+½, -z+½

[(i)] -x+1, z, y

[(j)] -x+1, -z+½, -y+½

Structural parameters of MFU-4*l* refined by ADT data

Table S3. Atom coordinates and equivalent displacement parameters for MFU-4*l*.

Atom	x	Y	z	U
Zn1	0.3138(6)	0.3138	0.1862	0.23(2)
Cl1	0.354(1)	0.354	0.146	0.36(3)
Zn2	0.25	0.25	0.25	0.05(1)
N1	0.344(1)	0.2730(8)	0.2270	0.22(2)
C1	0.38929	0.26536	0.234464	0.27(3)
N2	0.31627(3)	0.25	0.25	0.27(3)
C2	0.4269	0.28071	0.21929	0.29(3)
C3	0.46452	0.26536	0.23464	0.36(4)
O1	0.5	0.284(2)	0.216	0.40(5)

Table S4. Selected bond distances (Å) for MFU-4*l*.

Bond	Distance
Zn1-Cl1	2.24(6)
Zn1-N1	2.09(3)
Zn2-N2	2.12(4)
N1-C1	1.48(3)
N1-N2	1.37(3)
C1-N2	2.1937(12)
C1-C2	1.39
C3-O1	1.40(4)

ChemComm

Cite this: *Chem. Commun.*, 2012, **48**, 1236–1238

www.rsc.org/chemcomm

COMMUNICATION

Reversible gas-phase redox processes catalyzed by Co-exchanged MFU-4*l*(*arge*)†

Dmytro Denysenko,[a] Tamas Werner,[a] Maciej Grzywa,[a] Angela Puls,[b] Volker Hagen,[c] Georg Eickerling,[d] Jelena Jelic,[e] Karsten Reuter[e] and Dirk Volkmer*[a]

Received 7th October 2011, Accepted 6th December 2011
DOI: 10.1039/c2cc16235k

Postsynthetic metal ion exchange in a benzotriazolate-based MFU-4*l*(*arge*) framework leads to a Co(II)-containing framework with open metal sites showing reversible gas-phase oxidation properties.

Metal–organic frameworks have been suggested for a number of applications such as heterogeneous catalysis, gas storage, gas separation and drug delivery.[1] With respect to catalytic applications MOFs possessing highly accessible, redox active metal centers are particularly interesting.[2] However, besides sustained catalytic activity, production scale applications require processable (*i.e.* moldable) catalyst particles that are solvolytically stable and mechanically robust, and these antithetic requirements seem to drastically limit the number of suitable coordination frameworks. Identifying novel MOF structural families of potential use in catalytic applications thus represents the first and foremost step, preceding further development towards technical applications.[3]

Aiming at MOF oxidation catalysts we have recently reported on MFU-1, which is a cobalt-based structural analogue of MOF-5.[4] Solution impregnation of MFU-1 with a co-catalyst (*N*-hydroxyphthalimide) leads to NHPI@MFU-1, which oxidizes a range of organic substrates under ambient conditions by employing molecular oxygen from air.[5] However, attempts to replace the Co^{2+} ions in MFU-1 by other redox active metal centers as yet were unsuccessful. To overcome this limitation, we here present the first example of a novel redox active MOF, which is derived from MFU-4*l*(arge)[6]—a recent member of the highly modular and robust MFU-4 structural family.[7] MFU-4 type frameworks are based on pentanuclear T_d symmetrical $[Zn^{o}Zn_4^{t}Cl_4(ta)_6]$ coordination units (o—octahedral, t—tetrahedral metal coordination sites, ta—triazolate ligand). In MFU-4-type frameworks rigid benzobistriazolate linkers ($BBTA^{2-}$) occupy the positions of the triazolate (ta) moieties.

MFU-4*l*, constructed from deprotonated bis(1*H*-1,2,3-triazolo-[4,5-*b*],[4′,5′-*i*])dibenzo-[1,4]-dioxin (H_2-BTDD) linkers, constitutes a highly porous framework with large pore apertures (av. dia. 9.1 Å) and coordinatively unsaturated metal coordination sites. Heating up a MFU-4*l* suspension/$CoCl_2$ solution in DMF leads to isostructural replacement of zinc by Co(II) centres (Fig. 1). Depending on the Co/Zn molar ratio of the initial suspension, the total number x of Co(II) replacing zinc in the formula unit $[Co_xZn_{(5-x)}Cl_4(BTDD)_3]$ may differ (Fig. 2). It is clearly seen that the Co/Zn exchange process follows a sigmoidal behaviour: at a Co/Zn molar ratio <0.3 (inset of Fig. 2) the exchange curve indicates a substoichiometric replacement of zinc centers. In order to reach $x = 1$ (*i.e.* on average one Co(II) center per pentanuclear SBU) the initial Co/Zn molar ratio of the suspension has to be adjusted to a value of about 0.30 ± 0.02. The complete exchange of zinc centers requires a huge excess of cobalt ions in the

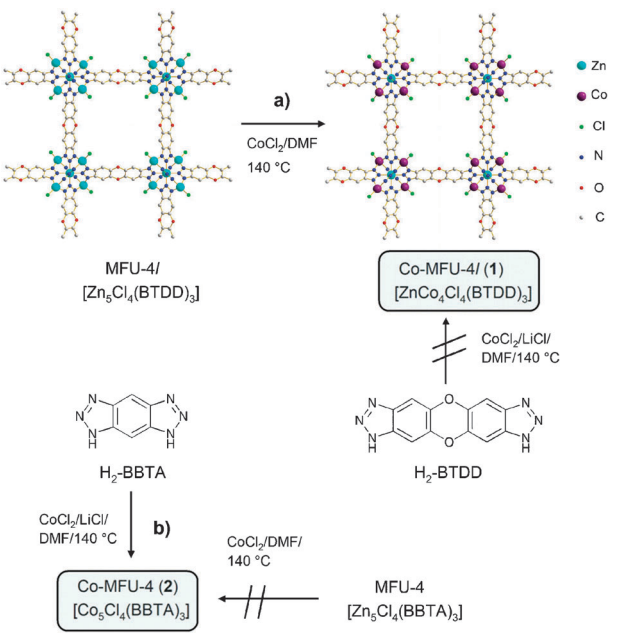

Fig. 1 Synthesis of **1** *via* postsynthetic Co/Zn metal exchange (a) and direct synthesis of **2** (b).

[a] *Institute of Physics, Chair of Solid State and Material Science, Augsburg University, D-86135 Augsburg, Germany. E-mail: dirk.volkmer@physik.uni-augsburg; Fax: +49 (0)821 598-5955*
[b] *Rubotherm GmbH, D-44799 Bochum, Germany*
[c] *Rubokat GmbH, D-44801 Bochum, Germany*
[d] *Institute of Physics, Chair of Chemical Physics and Material Science, Augsburg University, D-86135 Augsburg, Germany*
[e] *Dept. Chemie, Technische Universität München, D-85747 Garching, Germany*

† Electronic supplementary information (ESI) available: Experimental details, spectral data, TGA data, XRPD data and crystal structure data. CCDC 847582 (**1**), CCDC 847583 (**2**) and CCDC 847498 (**3**). For ESI and crystallographic data in CIF or other electronic format see DOI: 10.1039/c2cc16235k

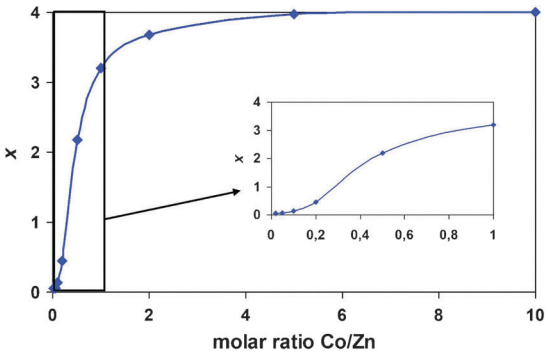

Fig. 2 Total number x of Co(II) ions per $\{Co_xZn_{5-x}Cl_4\}^{6+}$ unit as a function of (Co/Zn) molar ratio under solvothermal reaction conditions, determined by energy-dispersive X-ray spectroscopy (EDX).

suspension (Co/Zn molar ratio > 5). It should be noted that the exchange curve (Fig. 2) converges towards a plateau at $x = 4$ (and not 5!), suggesting that the central octahedrally coordinated Zn center cannot be replaced using the given experimental conditions. Thus, the average chemical formula of cobalt-exchanged MFU-4*l* may be formulated as $[Zn^{o}(Co_x{}^{t}Zn_{(4-x)}{}^{t}Cl_4(BTDD)_3]$ (**1**).

In contrast to these findings, the Co/Zn metathesis starting from MFU-4 failed completely, which is probably due to strong diffusion limitations imposed on solvated metal ions, caused by the very small pore apertures (av. dia. 2.5 Å) of this framework.[7] However, in contrast to **1** an isostructural MFU-4 derivative, termed Co-MFU-4 (**2**), was directly prepared from 1*H*,5*H*-benzo(1,2-*d*:4,5-*d*′)bistriazole (H_2-BBTA) and $CoCl_2$ in DMF in the presence of LiCl under solvothermal reaction conditions, a reaction path that proved unsuccessful in the case of **1** (Fig. 1). Based on powder X-ray diffraction data the crystal structures of both Co-containing frameworks have been refined by the Rietveld method, starting from structural models of the isostructural compounds MFU-4 and MFU-4*l*, respectively (Table 1). Both MOF compounds (**1** and **2**) are thermally stable (up to 450 °C under nitrogen atmosphere), as confirmed by TGA and VT-XRPD analysis. Compound **1** is highly porous with a BET surface area of 3556 $m^2\ g^{-1}$ (Table 1).

In order to ensure that the tetrahedral coordination geometry of the Co(II) centers in **1** and **2** is retained, the discrete pentanuclear "Kuratowski-type" complex[8] of formula $[Co^{o}Co_4{}^{t}Cl_4(Me_2bta)_6)]\cdot 2PhBr$ (**3**, Me_2bta = 5,6-dimethylbenzotriazolate) has been prepared, serving as structural and spectroscopic model of SBUs that are present in **1** and **2**. Its structure has been solved from single crystal X-ray data. Compound **3** crystallizes in the cubic crystal system, space group $Fd\bar{3}m$; it is isostructural with the zinc complex described previously.[8a] An ORTEP style plot of the asymmetric unit of **3** with atom labels and bond lengths is shown in Fig. 3.

The diffuse reflectance UV/vis spectra of compounds **1–3** show strong absorption bands at *ca.* 600 nm, typical for Co(II) centers in tetrahedral coordination environments, and corresponding to the spin-allowed $^4A_2(F) \rightarrow {}^4T_1(P)$ transition. Ligand field splitting energies Δ_t (Co^{2+}) and Racah parameters B_t (Co^{2+}), calculated from the Tanabe–Sugano diagram for tetrahedrally coordinated d^7 metal ions, are similar for all compounds, where **2** has the highest splitting energy. IR spectra

Table 1 Selected features and crystallographic data for compounds **1–3** containing Kuratowski-type coordination units

Compound	**1**	**2**	**3**
Chemical formula	$C_{36}H_{12}Cl_4$ $Co_4N_{18}O_6Zn$	$C_{18}H_6Cl_4$ Co_5N_{18}	$C_{60}H_{58}Br_2Cl_4$ Co_5N_{18}
Formula weight (M)	1235.5	910.8	1627.5
T/K	293(2)	293(2)	100(1)
Crystal system	Cubic	Cubic	Cubic
Space group	$Fd\bar{3}m$ (225)	$Fd\bar{3}m$ (225)	$Fd\bar{3}m$ (227)
Cell length $a = b = c$/Å	30.9950(7)	21.7309(4)	23.5130(1)
Unit cell volume/$Å^3$	29776.6(7)	10262.1(2)	12999.42(10)
Z	8	8	8
Reflections total	—	—	28354
Reflections unique	—	—	999
$R_{int}(F)$	—	—	0.066
$R_1(I(F_o) > 2\sigma(I))$	—	—	0.0358
wR_2 (all data)	—	—	0.0885
$F(000)$	4768	3501	5320
Reflections observed	86	55	—
Number of observ.	4300	4300	—
R_P	1.38	1.30	—
R_{wp}	2.25	1.82	—
R_{wobs}	6.08	13.97	—
Diameter A-cells/Å	11.97	4.43	—
Diameter B-cells/Å	18.52	11.97	—
Aperture/Å	9.14	2.98	—
BET surface area, $m^2\ g^{-1}$ (Ar, 77 K)	3556	1435	—
λ_{max} (Co^{2+})/nm	605	609	624
Δ_t (Co^{2+})/cm^{-1}	4016	4201	3797
B_t (Co^{2+}), cm^{-1}	762	737	747
Vibrational mode including Co–Cl stretch (FTIR)/cm^{-1}	383	415	372

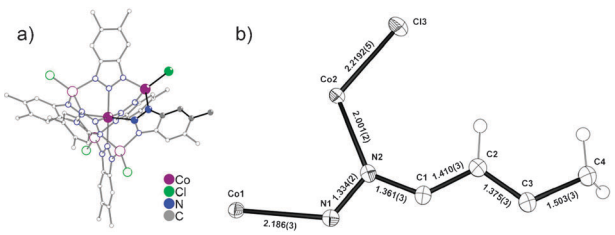

Fig. 3 Structure of **3** (a) and an asymmetric unit of **3** (b). Atoms represented by ORTEP style thermal ellipsoids (50% probability).

recorded at the wavenumber range from 600–180 cm^{-1} show characteristic vibrational modes: out of these, the Co–Cl single bond stretching mode could be unequivocally assigned based on comparison with spectroscopic data gleaned from DFT calculations on **3**. The DFT calculations were performed with the full-potential code FHI-aims,[9] using the GGA–PBE functional[10] to describe electronic exchange and correlation, a tier2 basis set and tight integration settings.

Selected structural and spectroscopic data of compounds **1–3** are given in Table 1.

In summary the structural and spectroscopic data provide sound evidence for the fact that all three compounds possess coordinatively unsaturated Co(II) centers in the (N_3Cl) donor environment typical of Kuratowski-type units.

As a proof-of-concept the gas phase redox activity of MOF compounds **1** and **2** has been investigated by cyclic temperature-programmed oxidation (TPO) and reduction (TPR) monitored by an online mass spectrometer. The TPO curve of **1** shows reversible oxidation with molecular oxygen around approx. 80 °C, whereas **2** shows no oxidation under identical conditions

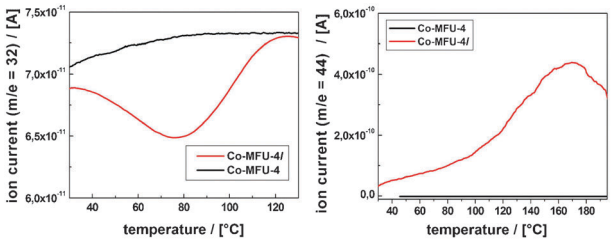

Fig. 4 Left: TPO curves; right: CO-TPSR curves for **1** and **2**.

(Fig. 4, left). Reversibility of these gas phase redox processes has been confirmed by repeating all TPR/TPO experiments for at least three times. Mass spectra concomitantly recorded during O_2 exposition gave no indication of volatile compounds being formed during oxidation of **1** at 80 °C, which suggests a stoichiometric uptake (*i.e.* coordination) of O_2 by Co^{2+} ions. At higher temperatures (not shown) a decomposition of the organic framework indicated by a significant evolution of CO_2 and water is indicated.

The TPSR (**T**emperature **P**rogrammed **S**urface **R**eaction) technique is a suitable method to prove if an adsorbed species (*e.g.* oxygen during TPO) is capable of catalytic (oxidation) reaction. CO oxidation is probably the simplest reaction to indicate if the adsorbed oxygen is also reactive for oxidation reactions. The samples were pretreated during heating in oxygen flow (1000 ppm in He) up to 200 °C and subsequent cooling in the same gas mixture to ambient. Afterwards the samples have been flushed with helium under ambient conditions. The experimental data were recorded during a linear heat-up in a 10% CO/He mixture. **1** shows a significant trace of CO_2 (m/e = 44) while **2** shows no indication for CO_2 formation (Fig. 4, right). This result is clearly corresponding to the observed reversible oxidation behaviour of the two samples. It can be concluded that the open framework structure of the Co-MFU-4*l* sample ensures a sufficient accessibility of catalytically active Co centres, whereas Co-MFU-4, albeit containing similar SBUs, is catalytically inactive owing to hindered diffusion/transport of gas molecules. The reaction temperature range is considerably higher than the one reported for Co_3O_4 nanoparticles (−77 °C). However, CO oxidation catalysts containing Co_3O_4 usually require much higher pre-treatment temperatures (450–550 °C),[11] whereas in the case of **1** 200 °C is sufficient for catalyst activation. This points to an advantage of the new MOF compound **1** compared to conventional cobalt oxide-based catalysts and shows its potential as a heterogeneous catalyst for gas phase reactions.

A few examples of postsynthetic metal exchange in MOFs have been reported by now, such as the partial exchange of Zn^{2+} by Co^{2+} in MOF-5[12] and some others.[13] We demonstrate here that isostructural replacement of Zn^{2+} ions in MFU-4 type frameworks leads to redox active Co(II) derivatives featuring catalytically active metal sites. Postsynthetic metal metathesis therefore may offer a general approach toward redox active frameworks comprising coordinatively unsaturated metal centers that might be difficult to obtain *via* direct synthesis from their components.

Comparative TPO/TPSR studies on **1** and **2** show that only **1** has accessible metal centers that undergo multiple and reversible redox reactions in gas phase TPO and TPR cycles. The striking lack of a similar redox activity in **2** is ascribed to its narrow pore size which limits gas diffusion within the pore volume of this particular MOF. To our understanding Co-MFU-4*l* represents a novel prototypic MOF which comprises all essential properties (*i.e.* redox reversibility, thermal stability, robustness) required for the future development of MOF catalysts suitable for gas phase heterogeneous redox processes.

Notes and references

1 (*a*) G. Ferey, *Chem. Soc. Rev.*, 2008, **37**, 191–214; (*b*) Z. Ma and B. Moulton, *Coord. Chem. Rev.*, 2011, **255**, 1623–1641.
2 V. Colombo, S. Galli, H. J. Choi, G. D. Han, A. Maspero, G. Palmisano, N. Masciocchi and J. R. Long, *Chem. Sci.*, 2011, **2**, 1311–1319.
3 J. Lee, O. K. Farha, J. Roberts, K. A. Scheidt, S. T. Nguyen and J. T. Hupp, *Chem. Soc. Rev.*, 2009, **38**, 1450–1459.
4 M. Tonigold, Y. Lu, B. Bredenkötter, B. Rieger, S. Bahnmüller, J. Hitzbleck, G. Langstein and D. Volkmer, *Angew. Chem.*, 2009, **121**, 7682–7687.
5 M. Tonigold, Y. Lu, A. Mavrandonakis, A. Puls, R. Staudt, J. Möllmer, J. Sauer and D. Volkmer, *Chem.–Eur. J.*, 2011, **17**, 8671–8695.
6 D. Denysenko, M. Grzywa, M. Tonigold, B. Streppel, I. Krkljus, M. Hirscher, E. Mugnaioli, U. Kolb, J. Hanss and D. Volkmer, *Chem.–Eur. J.*, 2011, **17**, 1837–1848.
7 S. Biswas, M. Grzywa, H. P. Nayek, S. Dehnen, I. Senkovska, S. Kaskel and D. Volkmer, *Dalton Trans.*, 2009, 6487–6495.
8 (*a*) S. Biswas, M. Tonigold and D. Volkmer, *Z. Anorg. Allg. Chem.*, 2008, **634**, 2532–2538; (*b*) S. Biswas, M. Tonigold, M. Speldrich, P. Kögerler, M. Weil and D. Volkmer, *Inorg. Chem.*, 2010, **49**, 7424–7434; (*c*) Y.-Y. Liu, M. Grzywa, M. Tonigold, G. Sastre, T. Schüttrigkeit, N. S. Leeson and D. Volkmer, *Dalton Trans.*, 2011, **40**, 5926–5938.
9 V. Blum, R. Gehrke, F. Hanke, P. Havu, V. Havu, X. Ren, K. Reuter and M. Scheffler, *Comput. Phys. Commun.*, 2009, **180**, 2175–2196.
10 J. P. Perdew, K. Burke and M. Ernzerhof, *Phys. Rev. Lett.*, 1996, **77**, 3865–3868.
11 (*a*) J. Jansson, A. E. C. Palmqvist, E. Fridell, M. Skoglundh, L. Österlund, P. Thormählen and V. Langer, *J. Catal.*, 2002, **211**, 387–397; (*b*) X. Xie, Y. Li, Z.-Q. Liu, M. Haruta and W. Shen, *Nature*, 2009, **458**, 746–749.
12 J. A. Botas, G. Calleja, M. Sánchez-Sánchez and M. G. Orcajo, *Langmuir*, 2010, **26**, 5300–5303.
13 (*a*) M. Dincă and J. R. Long, *J. Am. Chem. Soc.*, 2007, **129**, 11172–11176; (*b*) L. Mi, H. Hou, Z. Song, H. Han, H. Xu, Y. Fan and S.-W. Ng, *Cryst. Growth Des.*, 2007, **7**, 2553–2561; (*c*) L. Mi, H. Hou, Z. Song, H. Han and Y. Fan, *Chem.–Eur. J.*, 2008, **14**, 1814–1821; (*d*) S. Das, H. Kim and K. Kim, *J. Am. Chem. Soc.*, 2009, **131**, 3814–3815; (*e*) T. K. Prasad, D. H. Hong and M. P. Suh, *Chem.–Eur. J.*, 2010, **16**, 14043–14050.

Supporting Information

Experimental Section

Materials and General Methods

All starting materials were of reagent grade and used as received from the commercial supplier. Fourier transform infrared (FTIR) spectra were recorded with ATR unit in the range 4000–180 cm^{-1} on a Bruker Equinox 55 FT-IR spectrometer. Diffuse reflectance UV/Vis/NIR spectra were recorded in the range 2000–250 nm on a Perkin Elmer λ 750 s spectrometer. Thermogravimetric analysis (TGA) was performed with a TGA Q500 analyzer in the temperature range of 25-900 °C in flowing nitrogen gas at the heating rate of 10 $Kmin^{-1}$. Energy-dispersive X-Ray spectroscopy (EDX) was performed with a Philips XL 30 scanning electron microscope. Argon gas sorption isotherms were measured with a Quantachrome Autosorb-I ASI-CP-8 instrument. Prior to measurements, the samples were heated at 250 ˚C (**1**) and 280 °C (**2**) for 24h in high vacuum to remove the occluded solvent molecules. Argon sorption experiments were performed at 77 K in the range of $1.00\times10^{-5} \leq P/P_0 \leq 1.00$ with argon gas. Temperature-programmed oxidation (TPO) and reduction (TPR) measurements were carried out with BELCAT-B (Bel. Inc. Japan) instrument coupled with a GAM-400 (IPI, Germany) quadrupole mass spectrometer.

Synthesis of Co-MFU-4*l* (1)

Anhydrous cobalt (II) chloride (5.2 g, 40 mmol) was dissolved in DMF (160 mL) and MFU-4*l* (1 g, 0.8 mmol) was added to the solution. The reaction mixture was stirred for 20 h at 140 °C under reflux. The dark-green or dark-blue precipitate was filtered off, washed with DMF, methanol and dichloromethane and dried at 250 °C under vacuum. Yield 0.92 g (94 %).

Synthesis of Co-MFU-4 (2)

Anhydrous cobalt (II) chloride (3.9 g, 30 mmol), anhydrous lithium chloride (2.55 g, 60 mmol) and 1H,5H-benzo(1,2-d:4,5-d')bistriazole (2.4 g, 15 mmol) were dissolved in DMF (240 mL) and the solution was heated in a sealed tube for 48 h at 140 °C. The dark-blue

precipitate was filtered off, washed with DMF and methanol and dried at 280 °C under vacuum. Yield 1.9 g (42 %).

Synthesis of $[Co_5Cl_4(Me_2bta)_6]$•2PhBr (3)

The solution of 5,6-dimethylbenzotriazol (1.5 g, 10.2 mmol) and 2,6 dimethylpyridin (1.05 mL, 9.04 mmol) in methanol (20 mL) was added in 1 min to the solution of $CoCl_2$•$6H_2O$ in methanol (25 mL). The red precipitate was filtered off and dried under vacuum. The crude product was refluxed in bromobenzene (500 mL) for 3 h and the solution was evaporated to 250 mL. After 3 days at room temperature, green-blue octahedral crystals of **3** crystallized.

Powder X-ray diffraction measurements and crystal structure determination of 1 and 2

Crystalline samples were ground using an agate mortar and pestle, and were deposited in the hollow well of a sample holder. Diffraction data were collected in the 2θ range of 4-90° with 0.02° steps, with an interval of 6 s per step, using a Seifert XRD 3003 TT diffractometer equipped with Meteor 1D detector.

For the thermal stability characterization, the samples were ground using an agate mortar and pestle and were loaded into a glass capillary. The variable temperature XRPD experiment data were collected in the 2θ range of 4 - 60° with 0.02° steps, with an interval of 1 s per step using a Bruker A8 Advance diffractometer equipped with Lynxeye linear position-sensitive detector, mri TCPU1 oven, transmission geometry. The samples were heated from room temperature to 100, 200, 300, 350, 400, 450 and 500 °C, and once the corresponding temperature was reached, the sample was kept at this temperature for 10 min before starting to measure.

Since Co-MFU4 and Co-MFU4*l* are isostructural with MFU-4 and MFU-4*l* compounds, respectively, a Rietveld refinement process was directly carried out starting from the structural models of their isostructural counterparts. The Rietveld refinement was carried out using the Jana2006 program. Weak geometric restraints on bond distances were used during the refinement process. In both cases hydrogen atoms were placed at idealized positions using the SHELXL program. The experimental details and crystal data for Co-MFU4*l* (**1**) and Co-MFU4 (**2**) are listed in Table 1. The final Rietveld refinement plots for **1** and **2** are presented in Fig. 1 and 2, respectively.

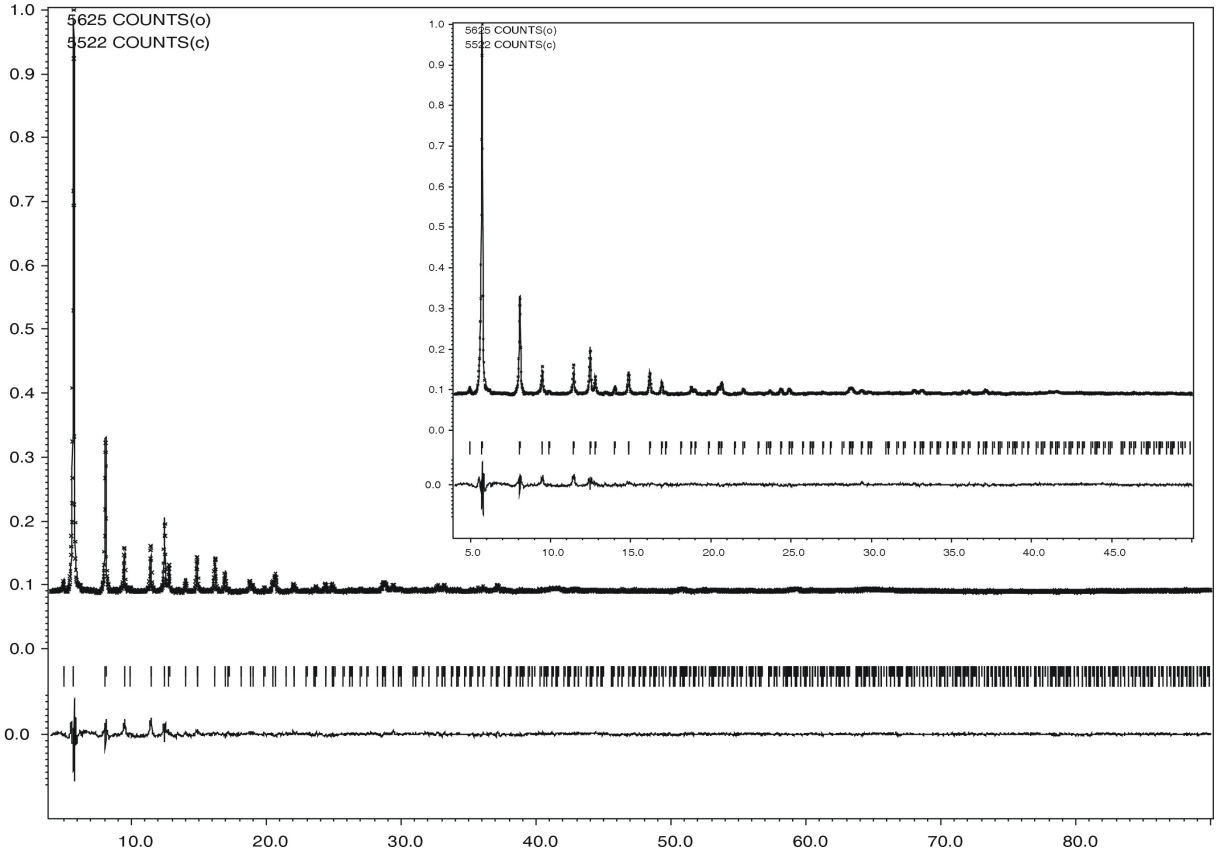

Fig. S1. The Rietveld refinement plots for **Co-MFU4*l***. Dotted and solid lines represent observed and calculated patterns, respectively with peak markers and the difference plot shown at the bottom. For clarity, the insert shows an expanded view in the range 4–50 in 2θ.

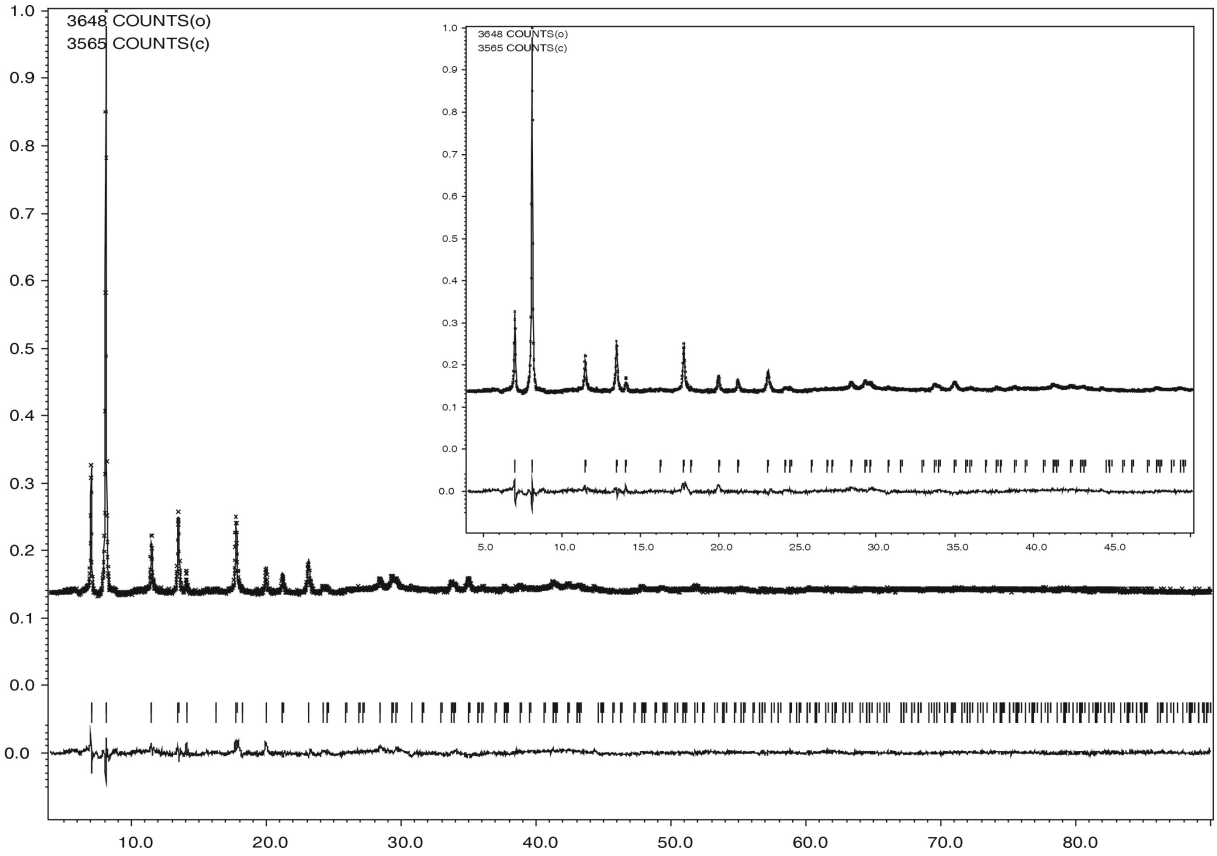

Fig. S2. The Rietveld refinement plots for **Co-MFU4**. Dotted and solid lines represent observed and calculated patterns, respectively with peak markers and the difference plot shown at the bottom. For clarity, the insert shows an expanded view in the range 4–50 in 2θ.

Table 1. Experimental details and crystal data for Co-MFU4*l* (**1**) and Co-MFU4 (**2**)

Compound	**Co-MFU4**	**Co-MFU4*l***
Diffractometer	Seifert XRD 3003 TT	Seifert XRD 3003 TT
X-ray source/wavelength/ Å	Cu, 1.5418	Cu, 1.5418
T/K	293(2)	293(2)
Empirical formula		
Formula	$C_{18}H_6Cl_4Co_5N_{18}$	$C_{36}H_{12}Cl_4Co_4N_{18}O_6Zn$
M_r	910.8	1235.5
Crystal system	cubic	cubic
Space group (no)	$Fd\bar{3}m$ (no. 227)	$Fd\bar{3}m$ (no. 227)
a/Å	21.7309(4)	30.9950(7)
V/Å^3	10262.1(2)	29776.6(7)
Z	8	8
D_c/g cm^{-3}	1.171	0.551
F(000)	3501	4768
2θ Range/°	4-90	4-90
Refls. Obs.	55	86
Number of observation	4300	4300
R_P	1.30	1.38
R_{wp}	1.82	2.25
R_{wobs}	13.97	6.08

Co-MFU4:

Atom	x	y	z	Uiso
Co1	0.25	0.25	0.25	0.014(4)
Co2	0.3411(2)	0.3411(2)	0.3411(2)	0.014(4)
Cl	0.3946(3)	0.3946(3)	0.3946(3)	0.044(10)
N1	0.2863(2)	0.3877(4)	0.2863(2)	0.043(10)
N2	0.25	0.35536(10)	0.25	0.043(10)
C1	0.2741(4)	0.4474(2)	0.2741(4)	0.051(10)
C2	0.2999(6)	0.5	0.2999(6)	0.051(10)
H2	0.3302	0.5	0.3302	0.038

Co1 N2 . . 2.290(2)

Co2 Cl . . 2.014(8)

Co2 N1 . . 1.965(7)

N1 N2 . . 1.319(6)

N1 C1 . . 1.350(10)

C1 C1 . 99_555 1.484(12)

C1 C2 . . 1.391(10)

Co-MFU4*l*:

Atom	x	y	z	Uiso
Co2	0.3185(3)	0.3185(3)	0.181542	0.013(6)
Cl1	0.356(2)	0.356(2)	0.144361	0.05(2)
N1	0.3399(3)	0.2752(2)	0.224812	0.018(10)
C1	0.38267(10)	0.2665(3)	0.233457	0.047(15)
N2	0.3146(6)	0.25	0.25	0.018(10)
C2	0.4215(2)	0.2826(2)	0.217351	0.047(15)
C3	0.4612(2)	0.2669(2)	0.233142	0.047(15)
O1	0.5	0.2834(4)	0.216589	0.04(3)
Zn1	0.25	0.25	0.25	0.04(2)
H1	0.421274	0.303866	0.196134	0.038

Co2 Cl1 . . 2.00(5)

Co2 N1 . . 2.009(9)

N1 C1 . . 1.380(10)

N1 N2 . . 1.355(13)

C1 C2 . . 1.396(7)

N2 Zn1 . . 2.001(19)

C2 C3 . . 1.410(8)

C2 H1 . . 0.930(4)

C3 C3 . 52_555 1.478(6)

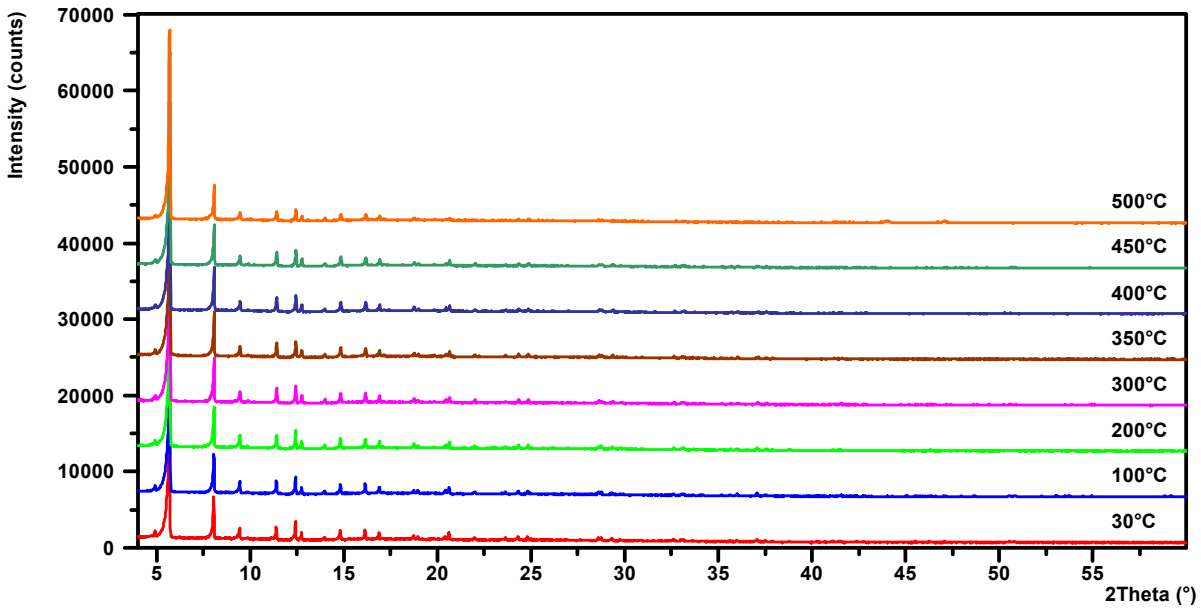

Fig. S3. VT-XRPD measurements of **1**.

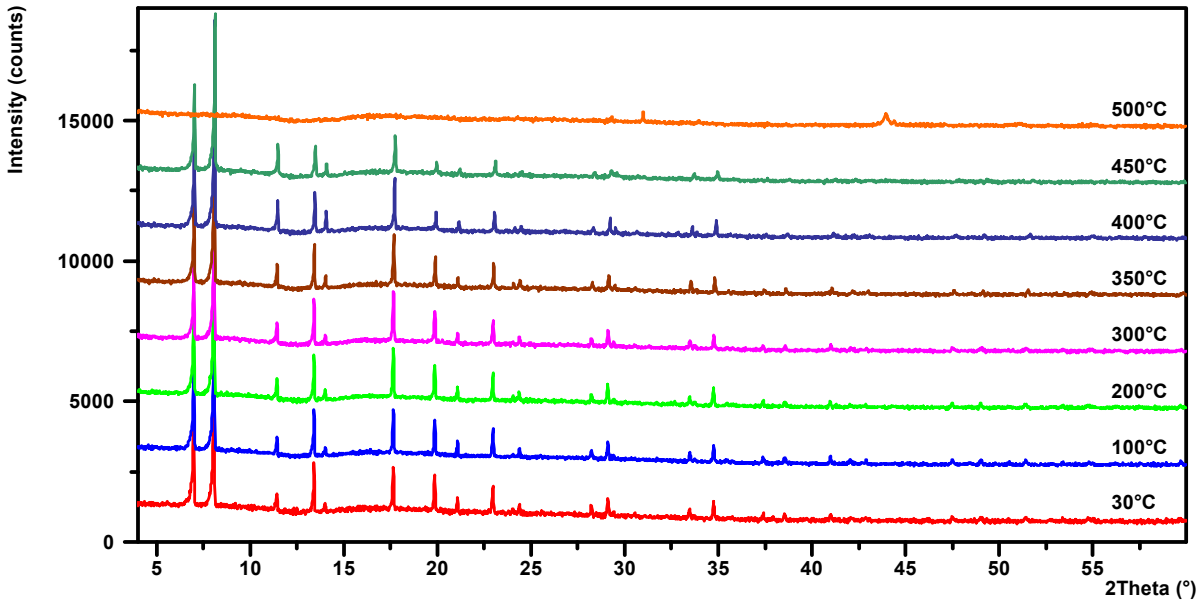

Fig. S4. VT-XRPD measurements of **2**.

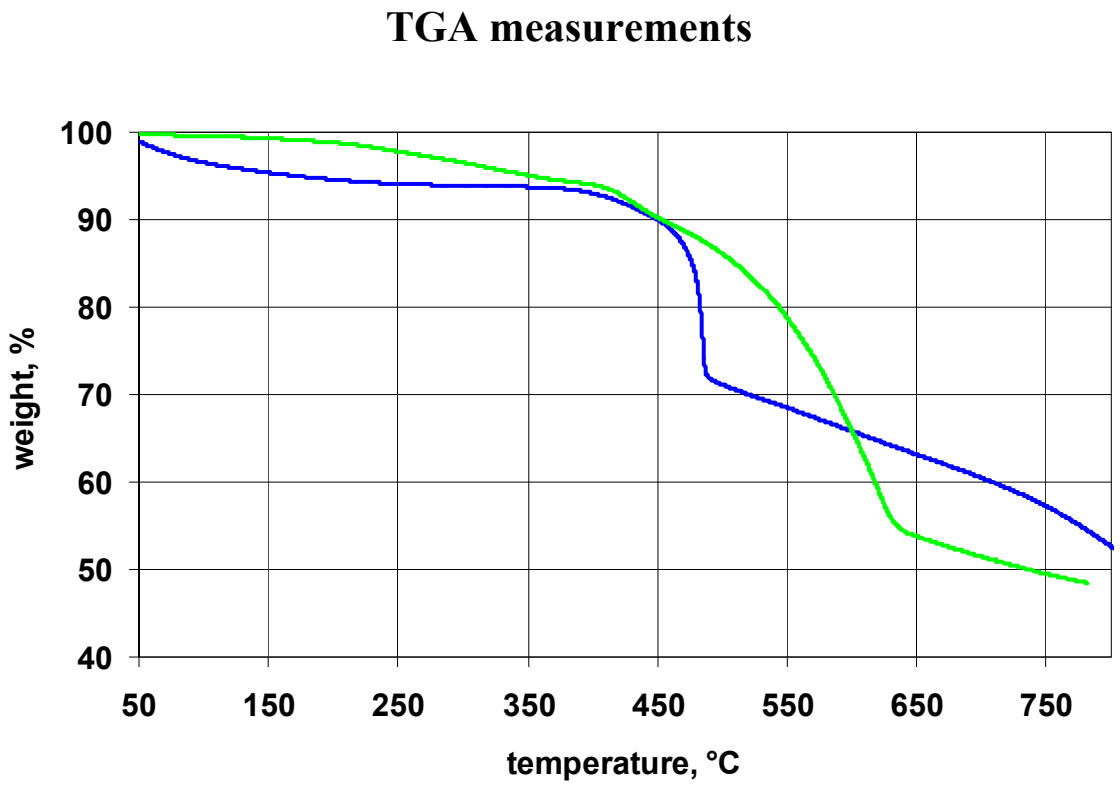

Fig. S5. Temperature-dependent weight-loss of **1** (green) and **2** (blue) under flowing nitrogen gas.

Single crystal structure determination of $[Co_5Cl_4(Me_2bta)_6]$•2PhBr (3)

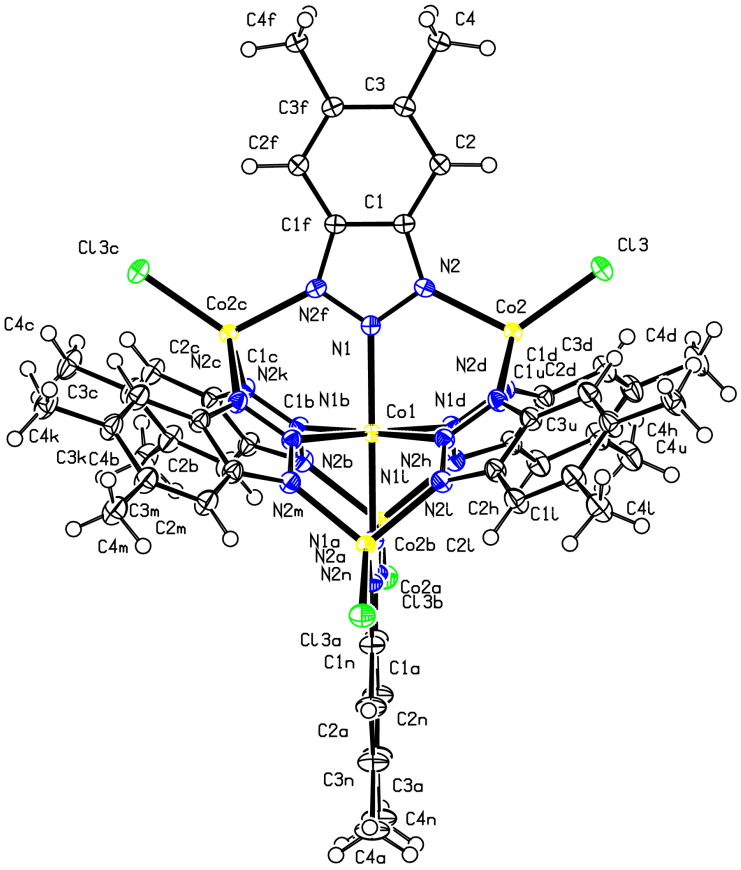

Fig. S6. ORTEP representation of the crystal structure of **3** (50% probability ellipsoids).

Data Collection. A turquoise block-like crystal of **3** with dimensions of 0.08 x 0.07 x 0.07 mm was selected and transferred into a glass capillary which was mounted in a N_2 stream (100(1) K) on a SMART APEX2 fixed-χ goniometer (Bruker). The data collection was carried out at the window of a *IμS* micro-focus sealed tube (50kV, 60 μA; Ag*K*α; λ = 0.56087 Å) equipped with a Montel multilayer-optic (Incoatec).

Intensity data were collected employing a Bruker APEX II CCD-detector and 0.5° ω-scans with a detector-to-sample distance of 50 mm. Two ω-scans (118° and 204.5°, 645 images in total) at a detector off-set angle (2θ) of 17.5° and 25° employing exposure rates of 60 seconds/frame were recorded (correlated exposures). The unit cell parameters were obtained by full-matrix least-squares refinement of 4491 reflections.

Data Reduction. Compound **3** crystallizes in the cubic space group *Fd-3m* (Int. Tables No. 227) with the cell parameter a = 23.5130(1), V = 12999.42(10) Å^3, Z = 8, F(000) = 5320. A total of 28354 Bragg reflections were measured (1.18° < θ < 23.66°). The cell refinement and data reduction were performed using the APEX2 software package. The data was analytically corrected for absorption effects employing crystal faces using SADABS [T_{min} = 0.95520, T_{max} = 0.96133]. Solvent molecule contributions have been removed from the intensity data via the SQUEEZE routine as implemented in PLATON. The internal agreement factor was $R_{int}(F)$ = 0.066 yielding 999 unique reflections. The structure was solved by direct methods and refined with standard Fourier techniques. Full-matrix least square refinements were carried out by minimizing $\Sigma w(F_o^2\text{-}F_c^2)^2$ with the SHELX-97 weighting scheme. The non-hydrogen atoms were refined anisotropically, all hydrogen atoms were located in the difference Fourier map and included in the structure factor calculation employing isotropic thermal parameters. The final refinement converged at R_1 = 0.0425, wR_2 = 0.0885, GooF = 1.056 for all 999 reflections (909 reflections with $I(F_o) > 2\sigma(I)$).

Selected bond lengths:

Atom1	Atom2	Distance [Å]	Atom1	Atom2	Distance [Å]
Co1	N1	2.186(3)	N1	N2_j	1.334(2)
Co1	N1_a	2.186(3)	N2	C1	1.361(3)
Co1	N1_b	2.186(3)	C1	C2	1.410(3)
Co1	N1_d	2.186(3)	C1	C1_j	1.391(2)
Co1	N1_e	2.186(3)	C2	C3	1.375(3)
Co1	N1_h	2.186(3)	C3	C4	1.503(3)
Co2	Cl3	2.2192(5)	C3	C3_j	1.451(2)
Co2	N2	2.0007(15)	C2	H2	0.99(2)
Co2	N2_c	2.0007(15)	C4	H4A	0.98(3)
Co2	N2_e	2.0007(15)	C4	H4B	0.93(3)
N1	N2	1.334(2)	C4	H4B_p	0.93(3)

Selected bond angles:

Atom1	Atom2	Atom3	Angle [°]	Atom1	Atom2	Atom3	Angle [°]
N1	Co1	N1_a	180.00	Co1	N1	N2	124.76(12)
N1	Co1	N1_b	90.00	Co1	N1	N2_j	124.76(12)
N1	Co1	N1_d	90.00	N2	N1	N2_j	110.5(2)
N1	Co1	N1_e	90.00	Co2	N2	N1	118.10(15)
N1	Co1	N1_h	90.00	Co2	N2	C1	134.26(13)
N1_a	Co1	N1_b	90.00	N1	N2	C1	107.65(15)
N1_a	Co1	N1_d	90.00	N2	C1	C2	131.36(16)
N1_a	Co1	N1_e	90.00	N2	C1	C1_j	107.11(18)
N1_a	Co1	N1_h	90.00	C1_j	C1	C2	121.5(2)
N1_b	Co1	N1_d	90.00	C1	C2	C3	117.52(16)
N1_b	Co1	N1_e	90.00	C2	C3	C4	120.60(16)
N1_b	Co1	N1_h	180.00	C2	C3	C3_j	121.0(2)
N1_d	Co1	N1_e	180.00	C3_j	C3	C4	118.45(19)
N1_d	Co1	N1_h	90.00	C1	C2	H2	120.7(19)
N1_e	Co1	N1_h	90.00	C3	C2	H2	121.8(19)
Cl3	Co2	N2	117.59(5)	C3	C4	H4A	110(2)
Cl3	Co2	N2_c	117.59(5)	C3	C4	H4B	112.2(16)
Cl3	Co2	N2_e	117.59(5)	C3	C4	H4B_p	112.2(16)
N2	Co2	N2_c	100.27(6)	H4A	C4	H4B	108(2)
N2	Co2	N2_e	100.27(6)	H4A	C4	H4B_p	108(2)
N2_c	Co2	N2_e	100.27(6)	H4B	C4	H4B_p	106(2)

UV/vis/NIR Spectroscopy

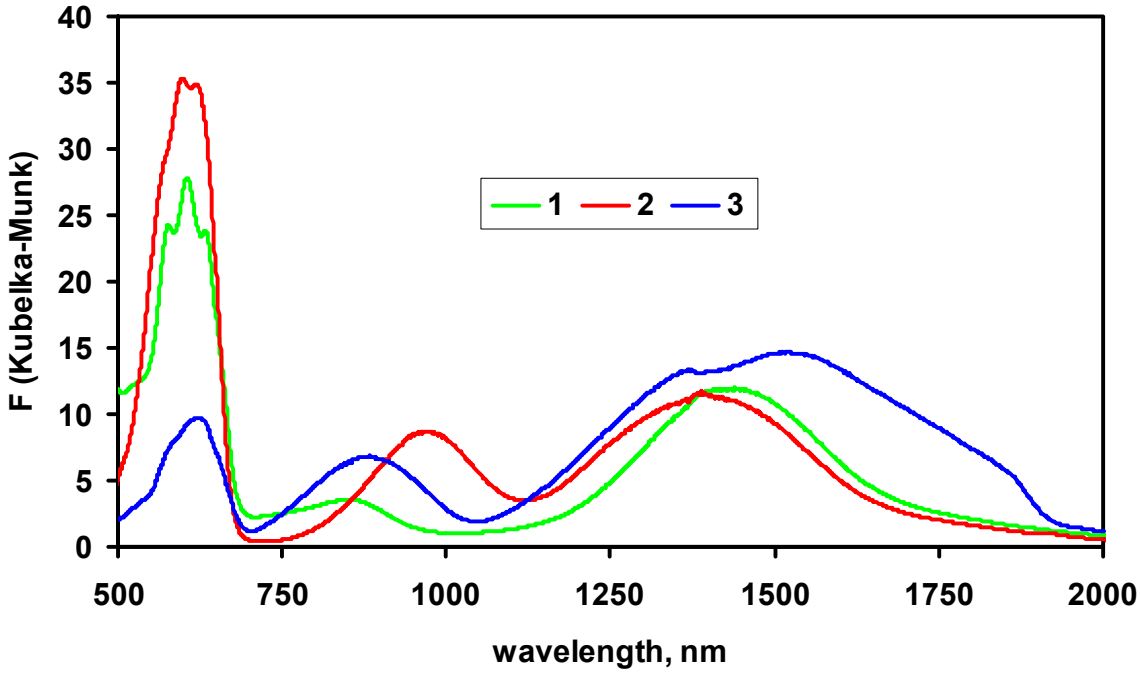

Fig. S7. UV/vis/NIR spectra of compounds **1-3**.

FTIR Spectroscopy

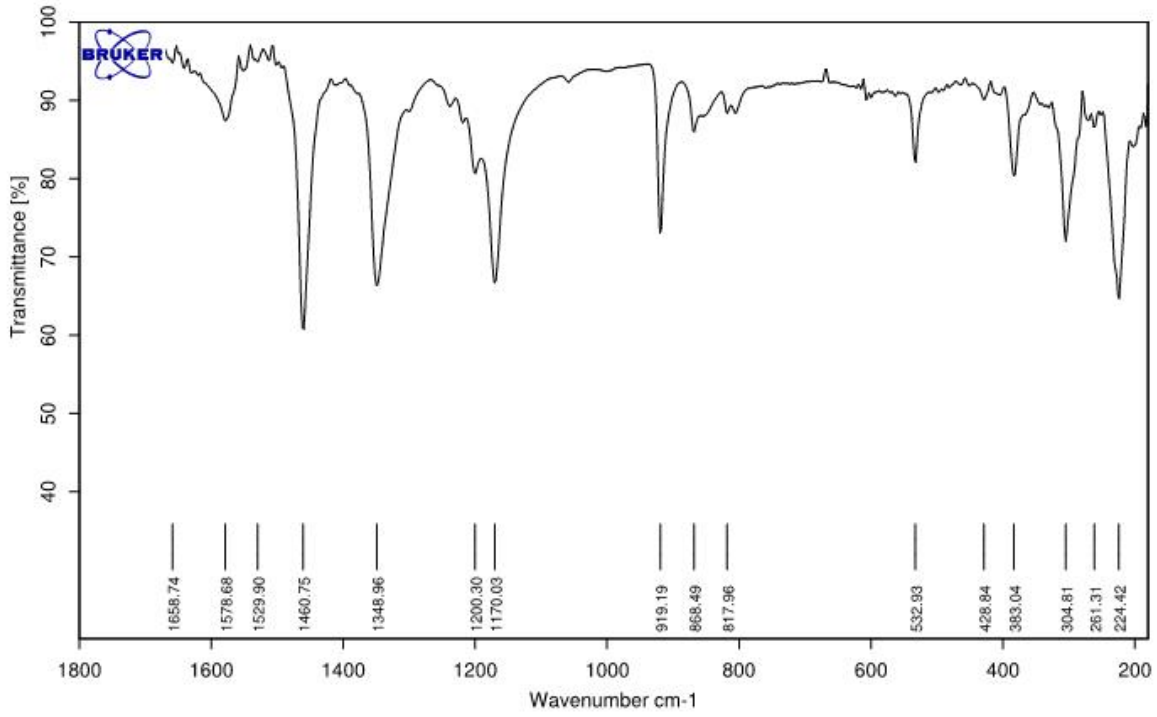

Fig. S8. FTIR spectra of **1**.

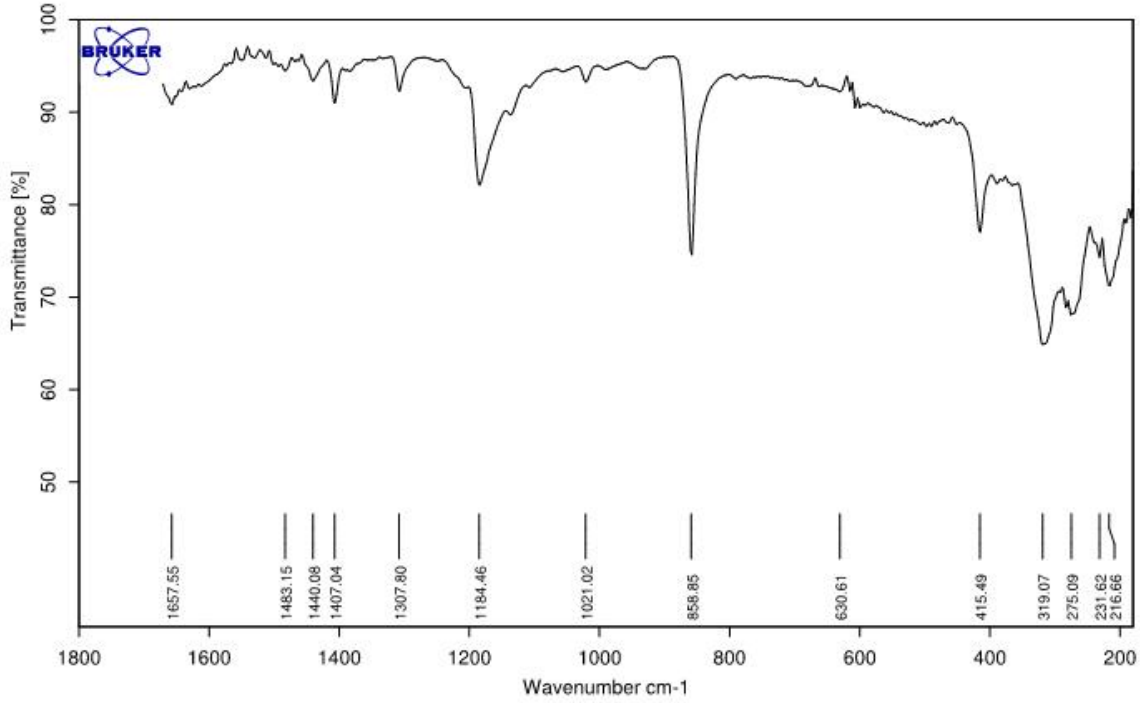

Fig. S9. FTIR spectra of **2**.

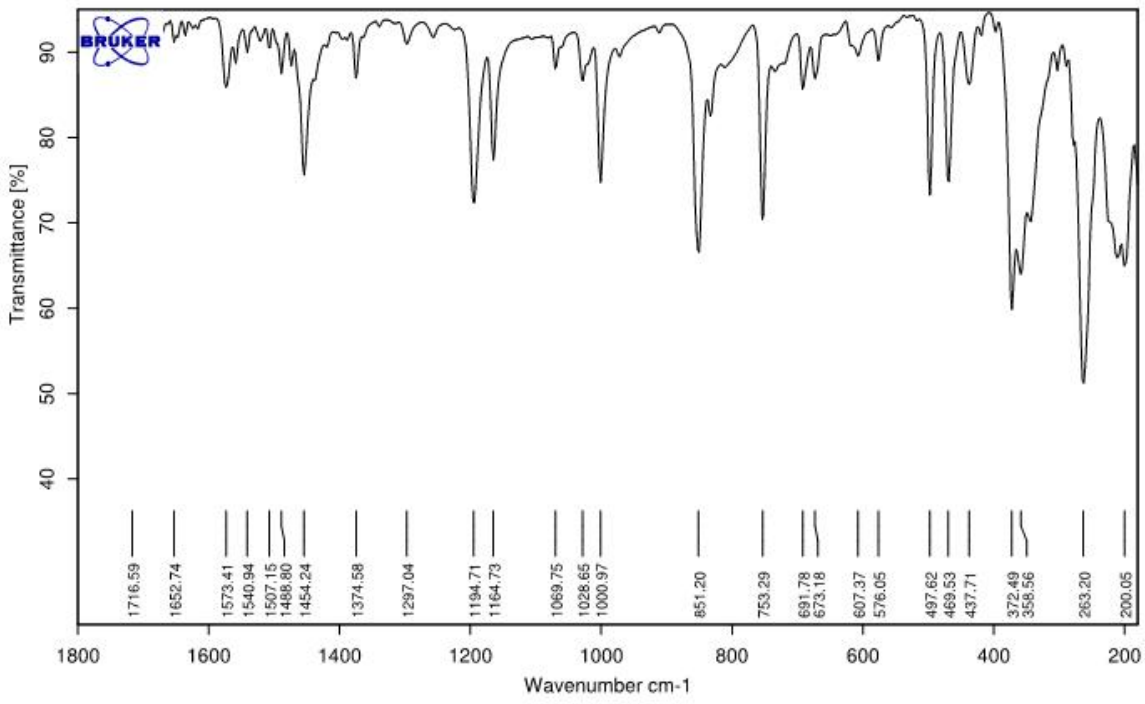

Fig. S10. FTIR spectra of **3**.

Small-Molecule Binding

DOI: 10.1002/anie.201310004

Scorpionate-Type Coordination in MFU-4*l* Metal–Organic Frameworks: Small-Molecule Binding and Activation upon the Thermally Activated Formation of Open Metal Sites**

*Dmytro Denysenko, Maciej Grzywa, Jelena Jelic, Karsten Reuter, and Dirk Volkmer**

Abstract: *Postsynthetic metal and ligand exchange is a versatile approach towards functionalized MFU-4l frameworks. Upon thermal treatment of MFU-4l formates, coordinatively strongly unsaturated metal centers, such as zinc(II) hydride or copper(I) species, are generated selectively. Cu^{I}-MFU-4l prepared in this way was stable under ambient conditions and showed fully reversible chemisorption of small molecules, such as O_2, N_2, and H_2, with corresponding isosteric heats of adsorption of 53, 42, and 32 kJ mol^{-1}, respectively, as determined by gas-sorption measurements and confirmed by DFT calculations. Moreover, Cu^{I}-MFU-4l formed stable complexes with C_2H_4 and CO. These complexes were characterized by FTIR spectroscopy. The demonstrated hydride transfer to electrophiles and strong binding of small gas molecules suggests these novel, yet robust, metal–organic frameworks with open metal sites as promising catalytic materials comprising earth-abundant metal elements.*

Metal–organic frameworks with open metal sites have been proposed for many different applications, such as catalysis,[1] gas storage and capture,[2] separation,[3] and sensing.[4] However, most known MOFs with free metal centers are only able to bind typical Lewis bases, such as CO_2 or H_2O, whereas the activation of unreactive small molecules, such as O_2, N_2, and H_2, still remains a challenge.

Molecular dioxygen,[5] dinitrogen,[5] and dihydrogen[6] complexes have attracted significant attention in coordination chemistry. Only very few stable MOFs with open metal centers have been described that are able to bind these molecules. A structural analogue of CuBTC, $Cr^{II}_2(BTC)_3$, containing dinuclear Cr^{II} paddle-wheel units, was shown to bind oxygen at room temperature.[7] However, after the first adsorption step, only approximately 82% of the total amount of oxygen could be desorbed, thus indicating that 18% of the O_2 binds irreversibly. CPO-27 (also termed MOF-74) is another well-established MOF family with interesting chemisorption properties. CPO-27-Fe, for example, showed reversible chemisorption of O_2 and N_2 with initial heats of adsorption of 41 and 35 kJ mol^{-1}, respectively. However, O_2 chemisorption was reversible at −62 °C, whereas at room temperature the irreversible formation of a dimeric iron(III) peroxide was observed.[8] A weak chemisorption of hydrogen with well-defined 1:1 stoichiometry (metal sites/H_2) was reported for CPO-27-Ni, with an initial heat of adsorption of 13.5 kJ mol^{-1}, which ranks among the highest values reported for a MOF material.[9] In contrast, compound **5**, presented herein, shows fully reversible binding of O_2, N_2, and H_2 molecules under ambient conditions. To the best of our knowledge, no copper(I)-containing metal–organic framework has previously been shown to possess similar chemisorption properties, although IR investigations on monomeric CuCl embedded in an Ar matrix gave first experimental proof of the formation of a Cu^{I}–H_2 complex, in which H_2 binds in a side-on coordination mode.[10] The chemisorption of N_2[11] and H_2[12] on copper-exchanged zeolites has also been described previously. For these microporous compounds, Cu^{I}–N_2 and Cu^{I}–H_2 adducts were characterized by spectroscopic methods (mainly IR spectroscopy). However, presumably as a result of the relatively low Cu^{I} content, no accurate values of N_2 or H_2 binding energies were reported.

We herein describe a new approach towards such highly active metal centers in a metal–organic framework based on MFU-4*l*, constructed from bistriazolate $BTDD^{2-}$ ligands and $\{Zn_5Cl_4\}^{6+}$ building units (Figure 1).[13] Coordination frameworks derived from the MFU-4 family show exceptional robustness against thermal and hydrolytic decomposition[14] and are therefore attractive for technical applications, such as

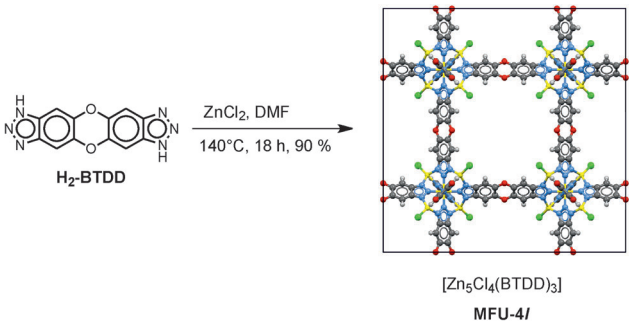

Figure 1. Solvothermal synthesis of MFU-4*l*. Atom colors: Zn (octahedral) pink, Zn (tetrahedral) yellow, Cl green, O red, N blue, C gray, H white. The black square outlines the cubic unit cell of MFU-4*l* (space group: $Fm\bar{3}m$, $a = 31.057$ Å; see Ref. [13]).

[*] D. Denysenko, Dr. M. Grzywa, Prof. Dr. D. Volkmer
Universität Augsburg, Institut für Physik
Lehrstuhl für Festkörperchemie
Universitätsstrasse 1, 86159 Augsburg (Germany)
E-mail: dirk.volkmer@physik.uni-augsburg.de
Dr. J. Jelic, Prof. Dr. K. Reuter
Technische Universität München
Chair of Theoretical Chemistry and Catalysis Research Center
Lichtenbergstrasse 4, 85747 Garching (Germany)

[**] We gratefully acknowledge funding by the priority program 1362 "Porous Metal–Organic Frameworks (MOFs)" of the Deutsche Forschungsgemeinschaft (DFG).

Supporting information for this article is available on the WWW under http://dx.doi.org/10.1002/anie.201310004.

gas separation[15] and catalysis.[16] Their fundamental building units, so-called Kuratowski units,[17] feature coordination sites reminiscent of scorpionate-type complexes.[18] In contrast to the latter, however, the coordination sites in MFU-4 frameworks do not have to be protected from unfavorable side reactions by bulky substituents R (Figure 2a). As a result, frameworks can be generated that contain free metal centers

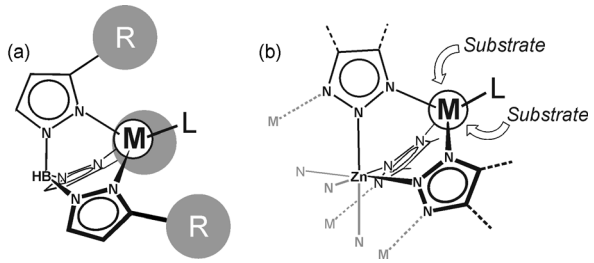

Figure 2. a) Scorpionate complex. b) Part of the fundamental building unit (Kuratowski unit) of MFU-4-type frameworks comprising coordinatively unsaturated, substrate-accessible coordination sites (M = (transition) metal, L = ligand, R = bulky substituent, for example, *t*Bu).

with (almost) unconstrained substrate accessibility (Figure 2b). With the aim of constructing catalytically active frameworks, suitable MFU-4*l* derivatives can be used as starting materials, within which the required coordinatively highly unsaturated metal centers can be formed. The first example, as shown below, establishes the formation of a highly reactive zinc(II) hydride species **2**, generated from MFU-4*l*-formate (**1**), which was readily obtained from MFU-4*l* through chloride–formate ligand exchange (Figure 3, path a). Alternatively, postsynthetic metal metathesis, that is, the replacement of Zn^{II}–Cl units with Cu^{I} ions (Figure 3, path b), led to threefold-coordinated unsaturated Cu^{I} sites that showed reversible and remarkably strong chemisorption of small molecules (i.e. H_2, O_2, N_2, and C_2H_4) under ambient conditions.

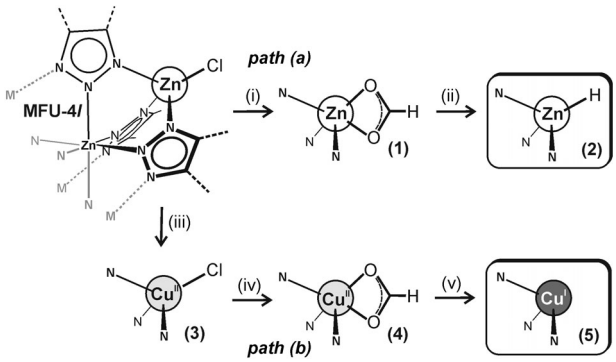

Figure 3. Reaction paths leading to MFU-4*l* derivatives **2** and **5** with active metal sites. Reaction conditions: i) HCOOLi/MeOH, room temperature; ii) 300 °C, 30 min, under vacuum; iii) $CuCl_2$, DMA, 60 °C; iv) HCOOLi/MeOH, room temperature; v) 180 °C, 1 h, under vacuum. DMA = *N*,*N*-dimethylacetamide.

Thermally activated decomposition of bulk metal formates has been reported previously. The decomposition of zinc formate, for example, leads to ZnO, whereas copper(II) formate yields the reduced products Cu_2O and Cu.[19] Our studies show that the thermally induced decomposition of coordinated formate ligands is a versatile approach for generating reactive metal sites in MFU-4*l*-type porous materials. Thus, the decomposition of **1** under flowing nitrogen gas took place in the temperature range of 190–280 °C, as shown by the curve derived from thermogravimetric analysis (TGA; see Figure S1 in the Supporting Information), whereby the crystalline order of the framework remained unchanged (see Figure S27). FTIR spectra showed clearly the formation of Zn–H species (i.e. **2**; Figure 3). Thus, a characteristic Zn–formate stretching vibration, which appeared as a shoulder in the FTIR spectrum at 1610 cm^{-1}, disappeared completely when compound **1** was heated at 300 °C (Figure 4).

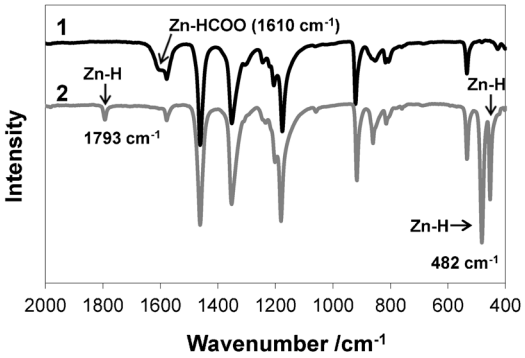

Figure 4. FTIR spectra of **1** and **2**.

Three new bands appeared upon heat treatment: at 1793, 482, and 453 cm^{-1}. On the basis of DFT calculations (using the PBE functional),[20] corrected for dispersive interactions,[21] we assign these bands to a Zn–H stretch mode and two Zn–H bending modes, respectively (see Figures S29 and S30).

Molecular hydride complexes of zinc scorpionates, prepared in a different way (either starting from ZnH_2 or by treatment of a Zn–F precursor with Et_3SiH), have been reported previously. These zinc hydride scorpionates were shown to react with various electrophiles, such as CO_2, CS_2, RNCS, RI, and CH_3COCl.[22] To demonstrate a comparable reactivity of the MFU-4*l* hydride derivative **2**, we added PhCOCl to a suspension of **2** in benzene at room temperature and obtained PhCHO as the main product, as determined by GC/MS analysis (see Figure S23). This test case indicates the potential of the hydride-containing MFU-4*l*-type framework **2** as a hydride-transfer and reducing agent.

We previously showed that all four peripheral Zn^{II} ions of each Kuratowski unit in MFU-4*l* could be substituted by Co^{II} upon heating with $CoCl_2$ in DMF.[16] An equivalent approach with $CuCl_2$ led to Cu^{II}-MFU-4*l* (**3**), in which, however, on average only two out of four tetrahedrally coordinated Zn centers per Kuratowski unit are replaced with Cu^{II} ions. Cu^{II}-MFU-4*l*-formate (**4**) could then be readily prepared by a subsequent ligand-exchange reaction, in analogy to the

synthesis of **1** (Figure 3). The TGA curve (see Figure S1) shows that **4** decomposes in two steps: The first weight loss at 120–180 °C corresponds to the decomposition of Cu^{II}-formate units, and the second weight loss at 190–280 °C corresponds to the transformation of Zn-formate units. Sorption and spectroscopic studies showed that thermal activation of **4** led finally to a MFU-4*l*-type framework with free Cu^{I} centers, termed Cu^{I}-MFU-4*l* (**5**; Figure 3). As proven by gas-sorption measurements, **5** formed very stable complexes with CO and C_2H_4.

The quantity of bound species (ca. 38 $cm^3 g^{-1}$; see Figures S13 and S14) was nearly identical for both gases and very close to the calculated value (37.8 $cm^3 g^{-1}$) based on the analytically determined Cu content, thus suggesting the formation of stable 1:1 Cu^{I}–CO and Cu^{I}–C_2H_4 coordination units. The corresponding stretch modes of coordinatively bound CO and C_2H_4 molecules were observed in the FTIR spectra at 2081 and 1541 cm^{-1}, respectively (Figure 6b), in good agreement with the DFT-calculated values (2056 and 1517 cm^{-1}, respectively). Both vibrational frequencies are shifted to lower wavenumbers, as compared to those of the free gas molecules (2143 cm^{-1} for CO and 1623 cm^{-1} for C_2H_4).[23] One of the most interesting properties of **5** is the unprecedented strong and reversible chemisorption of H_2. The amount of chemisorbed H_2 (38 $cm^3 g^{-1}$; Figure 5a; see also Figure S13) was the same as for CO and C_2H_4, which indicates a 1:1 stoichiometry of Cu^{I}–H_2 coordination units. The adsorption/desorption isotherm measured at 273 K demonstrates full reversibility of hydrogen binding. Under equilibrium conditions (1 bar H_2 pressure), approximately 80 % of all Cu^{I} centers formed a 1:1 hydrogen complex at this temperature (Figure 5b). The isosteric heat of hydrogen adsorption, as calculated by using the Clausius–Clapeyron equation, is 32 kJ mol^{-1}, again in very good agreement with the DFT-calculated value of 25 kJ mol^{-1} (Table 1). The Cu–H_2 bonding energy in Cu^{I}-MFU-4*l* (**5**) is thus significantly higher

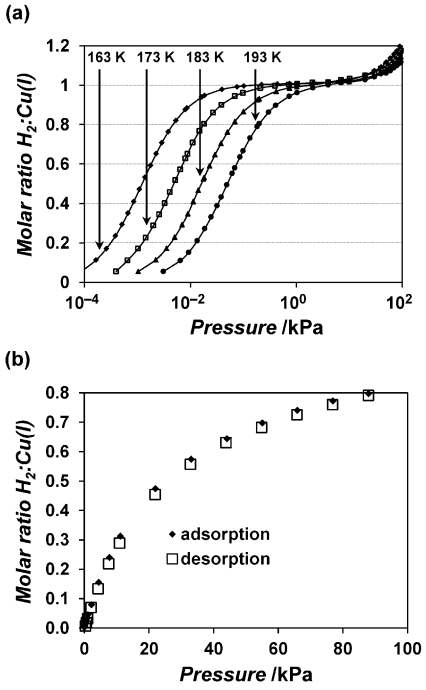

Figure 5. a) Hydrogen-adsorption isotherms on **5** at 163–193 K. b) Hydrogen-adsorption/desorption isotherm on **5** at 273 K.

Table 1: Experimental and DFT-calculated isosteric heats of adsorption in kJ mol^{-1} in Cu^{I}-MFU-4*l* (**5**).

	H_2	N_2	O_2	C_2H_4	CH_4
experiment	32.3 ± 0.4	41.6 ± 0.6	52.6 ± 0.6	88 ± 4	14.9 ± 0.4
DFT-B3LYP	25	44	46	84	15

than typical values for H_2 physisorption (5–10 kJ mol^{-1}),[24] but also significantly lower than in ionic metal hydrides or Kubas-type metal dihydrogen complexes, which normally require high desorption temperatures of 150–400 °C.[25] For example, an activation energy for hydrogen desorption of 156 kJ mol^{-1} has been measured for Mg_2NiH_4.[26] Intermetallic compounds, such as $LaNi_5$, show significantly lower desorption temperatures (as low as room temperature); however, they feature only low hydrogen-storage capacities.[25]

In fact, the hydrogen binding at the Cu^{I} centers matches well a suggested optimal binding energy of approximately 25 kJ mol^{-1} for hydrogen storage, thus enabling the accumulation and release of hydrogen at close to ambient temperature.[24] Although the amount of chemisorbed hydrogen in **5** is not high (0.34 wt %), owing to the low volumetric density of Cu^{I} centers, this degree of chemisorption is possible at close to ambient temperature and pressure, thus indicating the great potential of copper(I)-containing materials with a higher density of active metal sites for hydrogen storage. Higher storage capacities have only been observed either at low temperature or at high pressure.[27] For example, CPO-27-Ni showed less than 0.3 wt % H_2 uptake at 298 K and 65 bar.[28] Compound **5** also showed reversible chemisorption of N_2 and O_2 with the same 1:1 stoichiometry (see Figure S13) and isosteric heats of adsorption of 42 and 53 kJ mol^{-1}, respectively (Figure 6a). In contrast, methane showed only physisorption, as indicated by the low value of 15 kJ mol^{-1} determined for the isosteric heat of adsorption (Figure 6a; see also Figure S14). This value was also confirmed by DFT calculations (Table 1), which showed only dispersive interactions between Cu^{I} centers and CH_4 (see Figure S31). The fact that methane does not bind to Cu^{I} centers suggests **5** as a potential candidate for CH_4/N_2 separation with highly selective N_2 uptake. In the case of normal physisorption, most frequently observed in porous materials, CH_4 is adsorbed preferentially over N_2.[29] The exceptionally high difference of 73 kJ mol^{-1} between the heats of adsorption of C_2H_4 and CH_4 indicates that **5** is a very promising material for alkene/alkane separation or alkene capture. The isosteric heat of ethylene adsorption on CPO-27-Fe, for comparison, is about 45 kJ mol^{-1} and is the highest within the series of CPO-27 frameworks containing different metal ions (Mg^{2+}, Mn^{2+}, Fe^{2+}, Co^{2+}, Ni^{2+}, and Zn^{2+}), whereas the heat of CH_4 adsorption on CPO-27-Fe is 20 kJ mol^{-1}.[30] As summarized in Table 1, all isosteric heats of adsorption were very well reproduced in DFT calculations, thus confirming the picture

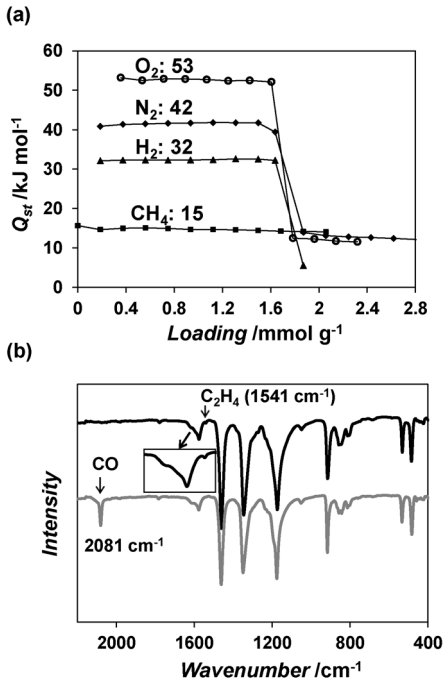

Figure 6. a) Dependence of isosteric heat of adsorption on loading for different gases on **5**. b) FTIR spectra of CO and C_2H_4 complexes of **5**.

of highly reactive and accessible Cu^I centers in Cu^I-MFU-4*l* (**5**).

We further note that **5** is air-stable (meaning that it is not oxidized irreversibly or destroyed in air like many copper(I)-containing compounds) and changes its color reversibly from slightly yellow (in a vacuum) to dark-gray (in air), which indicates the reversible binding of O_2 molecules at the Cu^I centers. Quantitative information about this process was gleaned by UV/Vis spectroscopy (see Figure S3). The binding of nitrogen was followed by diffuse reflectance infrared Fourier transform (DRIFT) spectroscopy. The experimental frequency for the IR-active N–N bond stretch (2242 cm^{-1}; see Figure S10) is typical for Cu^I–N_2 adducts, as previously described,[11] and close to the DFT-calculated value (2215 cm^{-1}). As observed for CO and C_2H_4, the N–N vibrational frequency was shifted to lower wavenumbers as compared to that of the free N_2 molecule (2331 cm^{-1}).[23]

The DFT-calculated geometries of the formed Cu^I–H_2, Cu^I–N_2, Cu^I–O_2, and Cu^I–C_2H_4 complexes in the Kuratowski unit are presented in Figure 7. H_2 binds in an η^2 (side-on) mode with a H–H bond distance of 0.83 Å and a Cu–H bond distance of 1.66 Å (Figure 7a). N_2 binds in an η^1 (end-on) mode with a N–N bond distance of 1.12 Å and a Cu–N bond distance of 1.83 Å; the Cu-N-N angle is 180° (Figure 7b). O_2 also binds in an η^1 (end-on) mode with an O–O bond distance of 1.29 Å, a Cu–O bond distance of 1.92 Å, and a Cu-O-O angle of 105.7° (Figure 7c). C_2H_4 forms an η^2 (side-on) complex with a C–C bond distance of 1.39 Å and a Cu–C bond distance of 2.03 Å (Figure 7d). All atomic distances within the bound species are longer than in the free molecules (0.74, 1.10, 1.21, and 1.34 Å for H_2, N_2, O_2, and C_2H_4, respectively),[23] in agreement with the experimentally observed red shifts of the stretch frequencies for N_2 and C_2H_4.

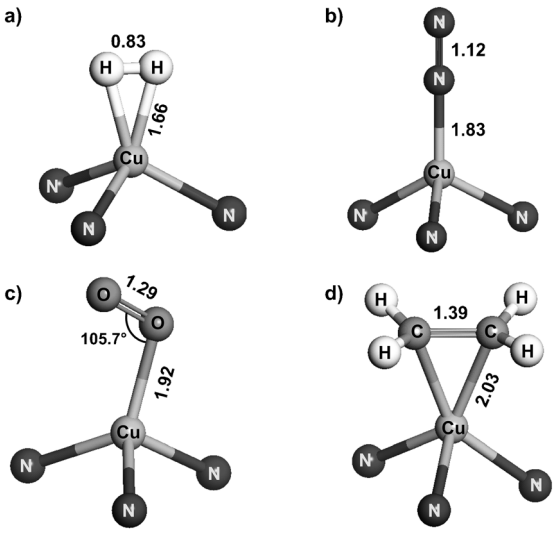

Figure 7. Binding geometries for a) H_2, b) N_2, c) O_2, and d) C_2H_4 at the Cu^I sites within the Kuratowski unit of MFU-4*l*, as determined by DFT calculations (interatomic distances in Å).

In summary, we have provided sound experimental and theoretical evidence for the synthesis, structure, and reactivity of robust metal–organic frameworks featuring open metal sites. The reactivity of these frameworks, which are derived from the MFU-4*l* structural family, towards small molecules was demonstrated by hydride transfer to electrophiles and by strong binding of small gas molecules. Since both processes are fundamental steps of catalytic transformation processes, further investigations in this direction should be highly rewarding. Selective chemisorption properties of Cu^I centers are of great interest for the storage, separation, and sensing of small gas molecules.

Experimental Section

Detailed synthetic procedures and characterization, TGA, XRPD, and GC/MS data, FTIR and UV/Vis/NIR spectra, gas-sorption isotherms, crystallographic data, and details of the DFT calculations are provided in the Supporting Information. CCDC 971404 (**1**), 971402 (**3**), and 971403 (**4**) contain the supplementary crystallographic data for this paper. These data can be obtained free of charge from The Cambridge Crystallographic Data Centre via www.ccdc.cam.ac.uk/data_request/cif.

Received: November 18, 2013
Revised: March 11, 2014
Published online: May 20, 2014

Keywords: chemisorption · copper · hydrides · hydrogen · metal–organic frameworks

[1] P. Valvekens, F. Vermoortele, D. De Vos, *Catal. Sci. Technol.* **2013**, *3*, 1435–1445.
[2] a) B. Chen, N. W. Ockwig, A. R. Millward, D. S. Contreras, O. M. Yaghi, *Angew. Chem.* **2005**, *117*, 4823–4827; *Angew. Chem. Int. Ed.* **2005**, *44*, 4745–4749; b) J. Park, H. Kim, S. S. Han, Y. Yung, *J. Phys. Chem. Lett.* **2012**, *3*, 826–829.

[3] a) P. D. C. Dietzel, V. Besikiotis, R. Blom, *J. Mater. Chem.* **2009**, *19*, 7362 – 7370; b) H. Oh, I. Savchenko, A. Mavrandonakis, T. Heine, M. Hirscher, *ACS Nano* **2014**, *8*, 761 – 770.
[4] B. Chen, Y. Yang, F. Zapata, G. Lin, G. Qian, E. B. Lobkovski, *Adv. Mater.* **2007**, *19*, 1693 – 1696.
[5] P. L. Holland, *Dalton Trans.* **2010**, *39*, 5415 – 5425.
[6] G. J. Kubas, *Metal Dihydrogen and σ-Bond Complexes*, Kluwer Academic Publishers, New York, **2001**.
[7] L. J. Murray, M. Dinca, J. Yano, S. Chavan, S. Bordiga, C. M. Brown, J. R. Long, *J. Am. Chem. Soc.* **2010**, *132*, 7856 – 7857.
[8] E. D. Bloch, L. J. Murray, W. L. Queen, S. Chavan, S. N. Maximoff, J. P. Bigi, R. Krishna, V. K. Peterson, F. Grandjean, G. J. Long, B. Smit, S. Bordiga, C. M. Brown, J. R. Long, *J. Am. Chem. Soc.* **2011**, *133*, 14814 – 14822.
[9] P. D. C. Dietzel, P. A. Georgiev, J. Eckert, R. Blom, T. Strässle, T. Unruh, *Chem. Commun.* **2010**, *46*, 4962 – 4964.
[10] H. S. Plitt, M. R. Bär, R. Ahlrichs, H. Schnöckel, *Angew. Chem.* **1991**, *103*, 848 – 850; *Angew. Chem. Int. Ed. Engl.* **1991**, *30*, 832 – 834.
[11] a) A. I. Serykh, M. D. Amiridis, *Microporous Mesoporous Mater.* **2006**, *94*, 320 – 324; b) Y. Kuroda, Y. Yoshikawa, S.-i. Konno, H. Hamano, H. Maeda, R. Kumashiro, M. Nagao, *J. Phys. Chem.* **1995**, *99*, 10621 – 10628; c) Y. Kuroda, Y. Yoshikawa, S. Emura, R. Kumashiro, M. Nagao, *J. Phys. Chem. B* **1999**, *103*, 2155 – 2164; d) Y. Kuroda, S.-i. Konno, K. Morimoto, Y. Yoshikawa, *J. Chem. Soc. Chem. Commun.* **1993**, 18 – 20; e) G. Spoto, S. Bordiga, G. Ricchiardi, D. Scarano, A. Zecchina, F. Geobaldo, *J. Chem. Soc. Faraday Trans.* **1995**, *91*, 3285 – 3290.
[12] a) A. I. Serykh, V. B. Kazansky, *Phys. Chem. Chem. Phys.* **2004**, *6*, 5250 – 5255; b) X. Solans-Monfort, V. Branchadell, M. Sodupe, C. M. Zicovich-Wilson, E. Gribov, G. Spoto, C. Busco, P. Ugliengo, *J. Phys. Chem. B* **2004**, *108*, 8278 – 8286; c) G. Spoto, E. Gribov, S. Bordiga, C. Lamberti, G. Ricchiardi, D. Scarano, A. Zecchina, *Chem. Commun.* **2004**, 2768 – 2769.
[13] D. Denysenko, M. Grzywa, M. Tonigold, B. Streppel, I. Krkljus, M. Hirscher, E. Mugnaioli, U. Kolb, J. Hanss, D. Volkmer, *Chem. Eur. J.* **2011**, *17*, 1837 – 1848.
[14] a) S. Biswas, M. Grzywa, H. P. Nayek, S. Dehnen, I. Senkovska, S. Kaskel, D. Volkmer, *Dalton Trans.* **2009**, 6487 – 6495; b) P. Schmieder, D. Denysenko, M. Grzywa, B. Baumgärtner, I. Senkovska, S. Kaskel, G. Sastre, L. van Wüllen, D. Volkmer, *Dalton Trans.* **2013**, *42*, 10786 – 10797.
[15] a) J. Teufel, H. Oh, M. Hirscher, M. Wahiduzzaman, L. Zhechkov, A. Kuc, T. Heine, D. Denysenko, D. Volkmer, *Adv. Mater.* **2013**, *25*, 635 – 639; b) A. Soleimani Dorcheh, D. Denysenko, D. Volkmer, W. Donner, M. Hirscher, *Microporous Mesoporous Mater.* **2012**, *162*, 64 – 68.
[16] D. Denysenko, T. Werner, M. Grzywa, A. Puls, V. Hagen, G. Eickerling, J. Jelic, K. Reuter, D. Volkmer, *Chem. Commun.* **2012**, *48*, 1236 – 1238.
[17] a) S. Biswas, M. Tonigold, D. Volkmer, *Z. Anorg. Allg. Chem.* **2008**, *634*, 2532 – 2538; b) S. Biswas, M. Tonigold, M. Speldrich, P. Kögerler, M. Weil, D. Volkmer, *Inorg. Chem.* **2010**, *49*, 7424 – 7434.
[18] S. Trofimenko, *Chem. Rev.* **1993**, *93*, 943 – 980.
[19] a) K. A. Buzdov, B. D. Antonov, *Russ. J. Inorg. Chem.* **2012**, *57*, 1599 – 1605; b) A. K. Galwey, D. M. Jamieson, M. E. Brown, *J. Phys. Chem.* **1974**, *78*, 2664 – 2670.
[20] a) V. Blum, R. Gehrke, F. Hanke, P. Havu, V. Havu, X. Ren, K. Reuter, M. Scheffler, *Comput. Phys. Commun.* **2009**, *180*, 2175 – 2196; b) X. Ren, P. Rinke, V. Blum, J. Wieferink, A. Tkatchenko, A. Sanfilippo, K. Reuter, M. Scheffler, *New J. Phys.* **2012**, *14*, 053020; c) J. P. Perdew, K. Burke, M. Ernzerhof, *Phys. Rev. Lett.* **1996**, *77*, 3865 – 3868.
[21] A. Tkatchenko, M. Scheffler, *Phys. Rev. Lett.* **2009**, *102*, 073005.
[22] a) R. Han, I. B. Gorrell, A. G. Looney, G. Parkin, *J. Chem. Soc. Chem. Commun.* **1991**, 717 – 719; b) A. Looney, R. Han, I. B. Gorrell, M. Cornebise, K. Yoon, G. Parkin, A. R. Rheingold, *Organometallics* **1995**, *14*, 274 – 278; c) M. Rombach, H. Brombacher, H. Vahrenkamp, *Eur. J. Inorg. Chem.* **2002**, 153 – 159.
[23] NIST Computational Chemistry Comparison and Benchmark Database, NIST Standard Reference Database Number 101, Release 16a, August 2013, Editor: Russell D. Johnson III, http://cccbdb.nist.gov.
[24] Y.-S. Bae, R. Q. Snurr, *Microporous Mesoporous Mater.* **2010**, *132*, 1121 – 1140.
[25] B. Sakintuna, F. Lamari-Darkrim, M. Hirscher, *Int. J. Hydrogen Energy* **2007**, *32*, 1121 – 1140.
[26] A. Zaluska, L. Zaluski, J. O. Ström-Olsen, *J. Alloys Compd.* **1999**, *289*, 197 – 206.
[27] D. J. Collins, H.-C. Zhou, *J. Mater. Chem.* **2007**, *17*, 3154 – 3160.
[28] P. D. C. Dietzel, B. Panella, M. Hirscher, R. Blom, H. Fjellvåg, *Chem. Commun.* **2006**, 959 – 961.
[29] B. Liu, B. Smit, *Langmuir* **2009**, *25*, 5918 – 5926.
[30] a) E. D. Bloch, W. L. Queen, R. Krishna, J. M. Zadrozny, C. M. Brown, J. R. Long, *Science* **2012**, *335*, 1606 – 1610; b) S. J. Geier, J. A. Mason, E. D. Bloch, W. L. Queen, M. R. Hudson, C. M. Brown, J. R. Long, *Chem. Sci.* **2013**, *4*, 2054 – 2061.

Angewandte Chemie
Eine Zeitschrift der Gesellschaft Deutscher Chemiker

Supporting Information

69451 Weinheim, Germany

Scorpionate-Type Coordination in MFU-4*l* Metal–Organic Frameworks: Small-Molecule Binding and Activation upon the Thermally Activated Formation of Open Metal Sites**

*Dmytro Denysenko, Maciej Grzywa, Jelena Jelic, Karsten Reuter, and Dirk Volkmer**

anie_201310004_sm_miscellaneous_information.pdf

Table of Contents

Materials and General Methods

All starting materials were of reagent grade and used as received from the commercial supplier. Fourier transform infrared (FTIR) spectra were recorded with an ATR unit in the range 4000–400 cm^{-1} on a Bruker Equinox 55 FT-IR spectrometer. Diffuse reflectance infrared Fourier-transformed (DRIFT) spectra were recorded with the same instrument equipped with a Harrick Praying Mantis I21012 reaction chamber. Diffuse reflectance UV-vis-NIR spectra were recorded in the range 2000–250 nm on a Perkin Elmer λ 750s spectrometer equipped with a Labsphere 60 mm RSA ASSY integrating sphere with 0°/d measuring geometry. Labsphere Spectralon SRS-99 was used as a white standard. In situ UV-vis-NIR spectra were recorded with the same instrument equipped with a Harrick Praying Mantis IRPQ623 reaction chamber. Thermogravimetric analysis (TGA) was performed with a TA Instruments Q500 analyzer in the temperature range of 25–900 °C in flowing nitrogen gas at the heating rate of 5 K min^{-1}. Energy-dispersive X-Ray spectroscopy (EDX) was performed with a Philips XL 30 scanning electron microscope. ICP-OES analyses were performed on a Varian VISTA MPX simultaneous spectrometer with a CCD detector. Elemental analyses were measured with a Vario EL III instrument from Elementar Analysensysteme GmbH. GC/MS measurements were performed on a Hewlett Packard GC System 6890 Series equipped with Rtx-5MS column and mass selective detector MSD 5973. N_2 adsorption isotherms for **1** and **2** at 77 K were measured with a Quantachrome NOVA 2000 Series instrument, approx. 10 mg of sample was used in both cases. Gas sorption isotherms for **3**, **4** and **5** were measured with a BELSORP-max instrument combined with a BELCryo system, approx. 100 mg of sample was used in all cases. Adsorbed amounts are given in $cm^3\ g^{-1}$ [STP], where STP = 101.3 kPa and 273.15 K. Prior to measurements, the samples were heated at 200 ˚C (**3**) or 70 °C (**1** and **4**) for 20 h in high vacuum to remove the occluded solvent molecules. **2** was prepared in situ by heating **1** under vacuum (10^{-1} mbar) up to 300 °C and keeping the sample at this temperature for 30 min. **5** was prepared in situ by heating **4** under vacuum (10^{-3} mbar) up to 180 °C (with a heating rate of 4 K min^{-1}) and keeping the sample at this temperature for 1 h.

Syntheses and Characterization

Preparation of lithium formate solution

Formic acid (4.6 g, 100 mmol) was added to a suspension of lithium carbonate (4.06 g, 55 mmol) in methanol (200 mL) and the mixture was stirred for 30 min at RT. Excess of Li_2CO_3 was filtered off and the resulted 0.5 M methanolic solution of HCOOLi was used for further transformations.

Synthesis of MFU-4*l*-formate (1)

MFU-4*l* (150 mg, 0.119 mmol) was stirred with 0.2 M solution of lithium formate in methanol (50 mL, 10 mmol) for 30 min at RT. The precipitate was filtered off, washed with methanol and CH_2Cl_2 and dried at 70 °C under vacuum. Yield 146 mg (0.113 mmol, 95 %). Zn:Cl atomic ratio, determined by EDX analysis, is 88:12, which corresponds to the substitution of 3.32 of 4 chloride ligands by formate. Anal. calcd. for $C_{39}H_{15}ClN_{18}O_{12}Zn_5$: C, 36.31; H, 1.24; N, 19.54. Found: C, 36.35; H, 0.75; N, 19.64 %. IR (ATR, cm^{-1}): 3096 (w), 1610 (sh), 1578 (m), 1461 (s), 1351 (m), 1244 (w), 1205 (m), 1176 (s), 921 (m), 853 (w), 817 (w), 534 (m), 427 (w).

Preparation of MFU-4*l*-hydride (2)

1 was heated under vacuum (0.1 mbar) up to 300 °C and kept at this temperature for 30 min. **2** was obtained as a slightly yellow powder. Anal. calcd. for $C_{36}H_{15}ClN_{18}O_6Zn_5$: C, 37.34; H, 1.31; N, 21.77. Found: C, 37.61; H, 0.97; N, 21.89 %. IR (ATR, cm^{-1}): 3083 (w), 1793 (w), 1578 (w), 1462 (s), 1355 (m), 1201 (m), 1180 (s), 917 (m), 861 (m), 815 (w), 533 (m), 482 (s), 453 (s).

Reaction of 2 with benzoyl chloride

Benzoyl chloride (2 mg, 0.014 mmol) was added to a suspension of **2** (5 mg, 0.0043 mmol, calculated hydride amount 0.013 mmol) in dry benzene (1 mL) and the mixture was stirred at room temperature. The reaction mixture was analyzed by GC/MS after 20 and 70 h (Figure S23).

Synthesis of Cu-MFU-4*l* (3)

Anhydrous copper (II) chloride (4.37 g, 32.5 mmol) was dissolved in N,N-dimethylacetamide (130 mL) and MFU-4*l* (0.8 g, 0.634 mmol) was added to the solution. The reaction mixture was heated for 20 h at 60 °C in a sealed tube. The green precipitate was filtered off, washed with N,N-dimethylacetamide, methanol and dichloromethane and dried at 150 °C under vacuum, giving a red-brown powder. Yield 0.76 g (0.604 mmol, 95 %). The number of Cu^{2+} ions in the formula unit, calculated from the Cu/Zn ratio determined by EDX and ICP-OES analyses, is 2.17 and 2.11, respectively. Anal. calcd. for $C_{36}H_{12}Cl_4N_{18}O_6Cu_2Zn_3$: C, 34.38; H, 0.96; N, 20.05. Found: C, 34.11; H, 0.98; N, 19.94 %. IR (ATR, cm^{-1}): 3080 (w), 2924 (w), 1575 (w), 1460 (s), 1351 (s), 1240 (w), 1206 (m), 1179 (s), 919 (m), 869 (m), 817 (w), 533 (m), 429 (w). UV-vis-NIR (λ_{max}, nm), with DMAc: 737; dry: 417, 523, 997.

Synthesis of Cu-MFU-4*l*-formate (4)

3 (150 mg, 0.119 mmol) was stirred with a 0.2 M solution of lithium formate in methanol (50 mL, 10 mmol) for 30 min at RT. The precipitate was filtered off, washed with methanol and CH_2Cl_2 and dried at 70 °C under vacuum. Yield 148 mg (0.114 mmol, 96 %). According to EDX analysis, 3.5 of 4 chloride ligands were replaced by formate. Anal. calcd. for $C_{40}H_{16}N_{18}O_{14}Cu_2Zn_3$: C, 37.07; H, 1.24; N, 19.46. Found: C, 36.43; H, 1.29; N, 19.08 %. IR (ATR, cm^{-1}): 3098 (w), 2924 (w), 2854 (w), 1577 (m), 1548 (w), 1461 (s), 1350 (s), 1298 (w), 1243 (w), 1179 (s), 921 (m), 857 (m), 817 (m), 534 (m), 424 (w). UV-vis-NIR (λ_{max}, nm): 782, 1174.

Preparation of Cu(I)-MFU-4*l* (5)

4 was heated under vacuum (10^{-3} mbar) up to 180 °C (with a heating rate of 4 K min^{-1}) and kept at this temperature for 1 h. **5** was obtained as a slightly grey powder, which becomes dark-grey immediately after exposure to air (due to binding of oxygen). Anal. calcd. for $C_{38}H_{14}N_{18}O_{14}Cu_2Zn_3$ (**5** • $2O_2$): C, 35.94; H, 1.11; N, 19.85. Found: C, 35.88; H, 1.44; N, 20.24 %.

Characterisation of **5** as CO complex: anal. calcd. for $C_{40}H_{14}N_{18}O_{12}Cu_2Zn_3$ (**5** • 2CO): C, 38.07; H, 1.12; N, 19.98. Found: C, 37.85; H, 1.21; N, 20.23 %. IR (ATR, cm^{-1}): 3083 (w),

2081 (m), 1577 (w), 1462 (s), 1350 (s), 1177 (s), 1052 (w), 917 (m), 844 (w), 814 (m), 534 (m), 483 (m).

Characterisation of **5** as C_2H_4 complex: IR (ATR, cm^{-1}): 1576 (m), 1541 (w), 1462 (s), 1347 (s), 1174 (s), 1049 (w), 915 (m), 858 (m), 813 (w), 532 (m), 485 (m).

TGA measurements

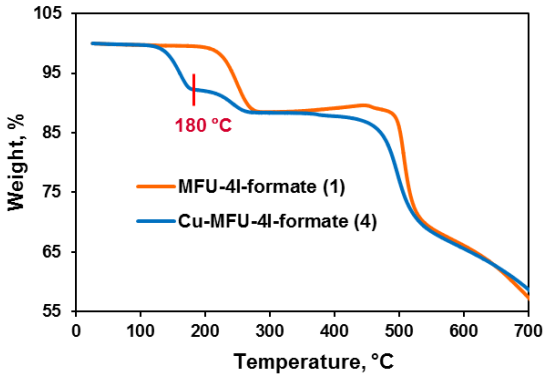

Figure S1. TGA curves for **1** and **4** showing the decomposition of Cu-formate (120–180 °C) and Zn-formate (200–280 °C) moieties.

UV-vis-NIR Spectroscopy

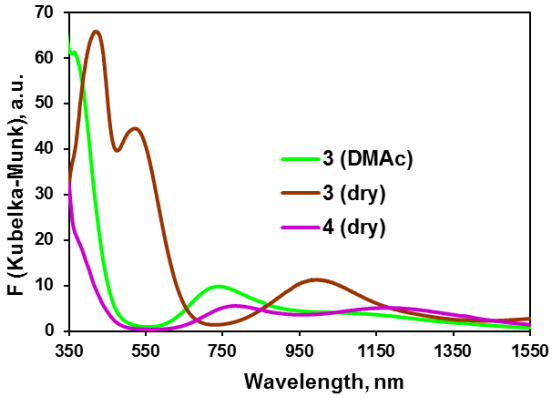

Figure S2. UV-vis-NIR spectra of **3** (filled with N,N-dimethylacetamide and dried in vacuum) and **4**.

In situ UV-vis-NIR spectra of **5** were recorded under argon and oxygen atmosphere. **5** was prepared in situ by heating **4** in a Harrick Praying Mantis reaction chamber up to 180 °C under Ar flow. After cooling down to RT, the spectrum was recorded under Ar flow. Then, the gas flow was switched to O_2 and the spectrum was recorded again after 10 min (Figure S3).

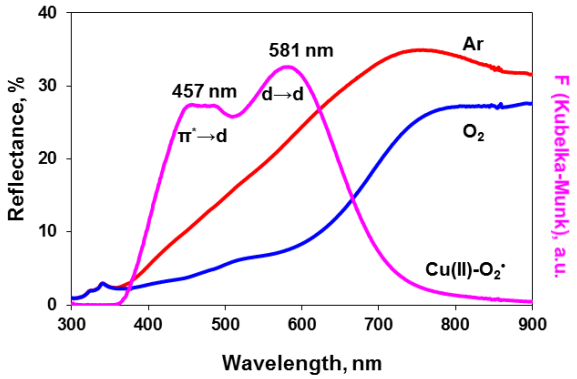

Figure S3. In situ UV-vis-NIR spectra of **5** under argon and oxygen flow and the difference spectrum, showing the absorbance of a Cu(I)-oxygen complex.

The difference spectrum shows clearly two absorption bands, typical for Cu(I)-O_2 complexes:[1] d→d transition of Cu^{2+} ions at 581 nm and π^*→d (LMCT) transition at 457 nm (since such species are normally Cu(II) superoxides Cu(II)–$O_2^{\bullet}$). However, due to very low reflectance of **5** under oxygen atmosphere at wavelength below 500 nm, the position of the CT band cannot be determined accurately. Owing to the same reason, the relative intensity of the CT band is underestimated. It has to be noted, that no changes of the spectrum under N_2 or H_2 flow, as compared to Ar, have been observed.

As well, we have performed calculations on Cu(II)–$O_2^{\bullet}$ system, in order to predict the UV-vis spectrum. Since calculations of the excited states are not available in FHI-aims code, we have used TURBOMOLE ab-initio quantum chemistry package code.[2] As a model, we have used a larger Kuratowski cluster. Since we have four Cu(II)–$O_2^{\bullet}$ centers there are eight unpaired electrons in the system. In the calculations we used GGA-PBE functional with TZVP basis set. Two characteristic peaks are predicted: at 384 nm, corresponding to the π_δ^*→d transition and at 584 nm, corresponding to the d→d transition (Figure S3A).

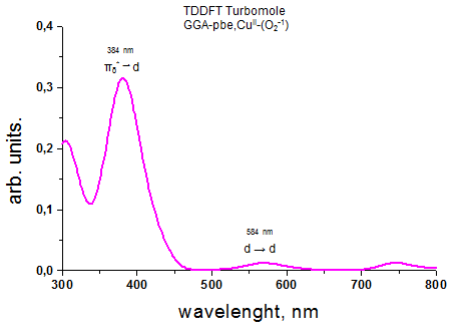

Figure S3A. Calculated UV-vis-NIR spectrum of Cu(II)–$O_2^{\bullet}$ moieties in a Kuratowski cluster.

[1] L.M. Mirica, X. Ottenwaelder, T.D.P. Stack, *Chem. Rev.* **2004**, *104*, 1013-1045.
[2] R. Ahlrichs *et al*., *Chem. Phys. Lett.* **1989**, *162*, 165-169.

FT-IR Spectra

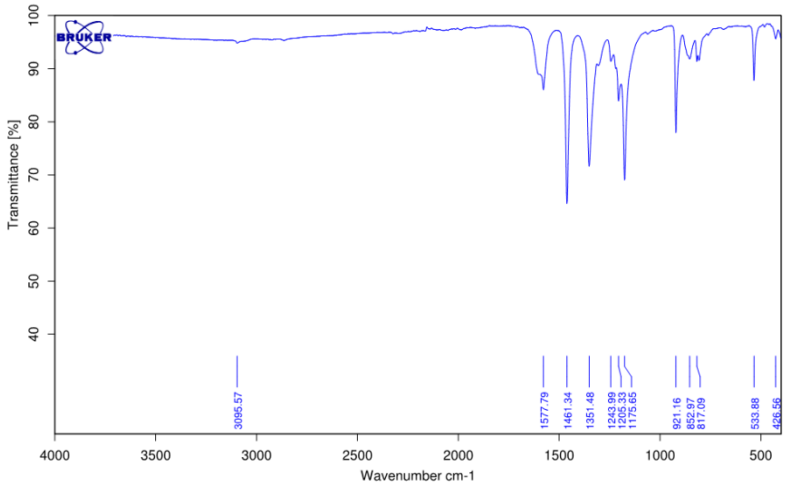

Figure S4. FT-IR spectrum of **1**.

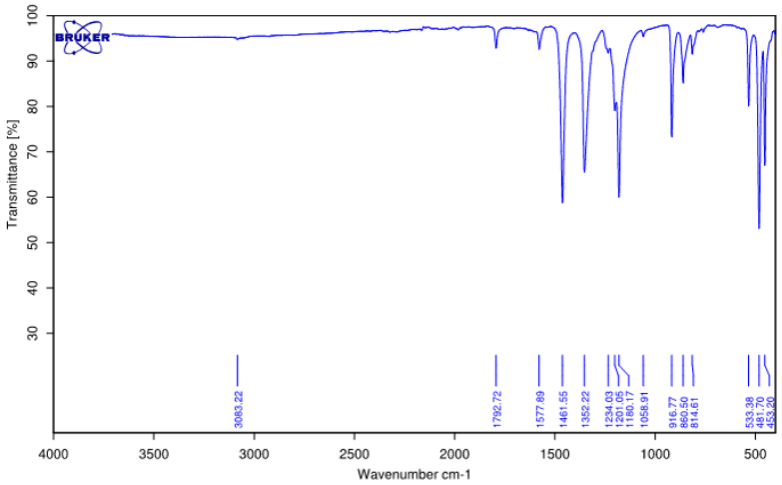

Figure S5. FT-IR spectrum of **2**.

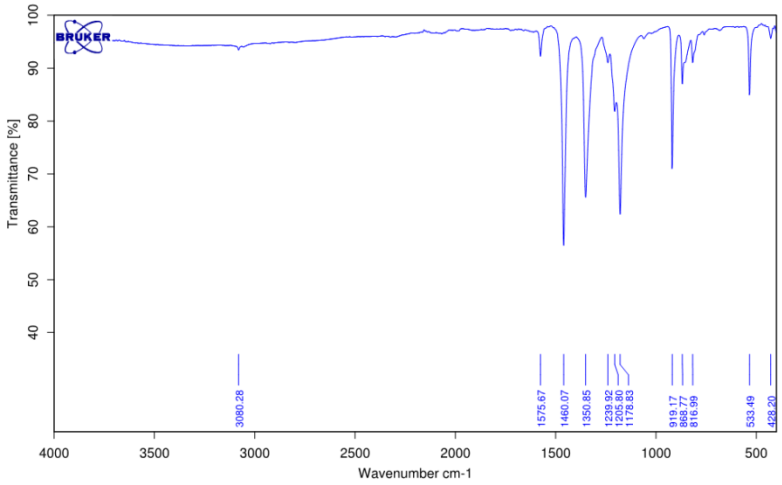

Figure S6. FT-IR spectrum of **3**.

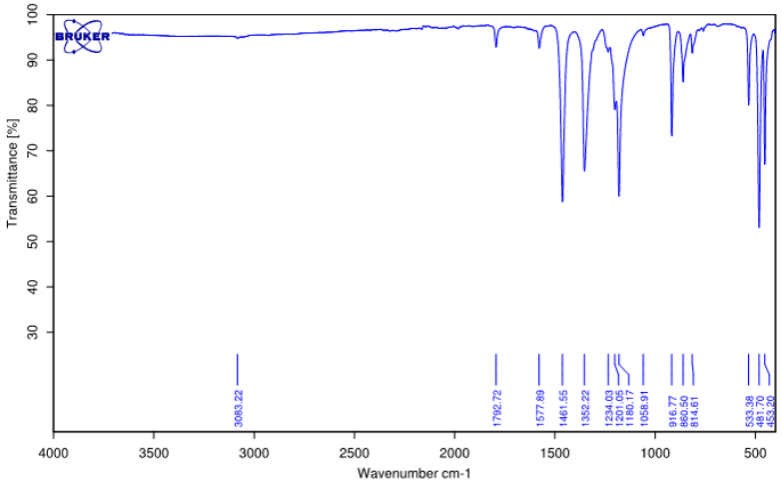

Figure S7. FT-IR spectrum of **4**.

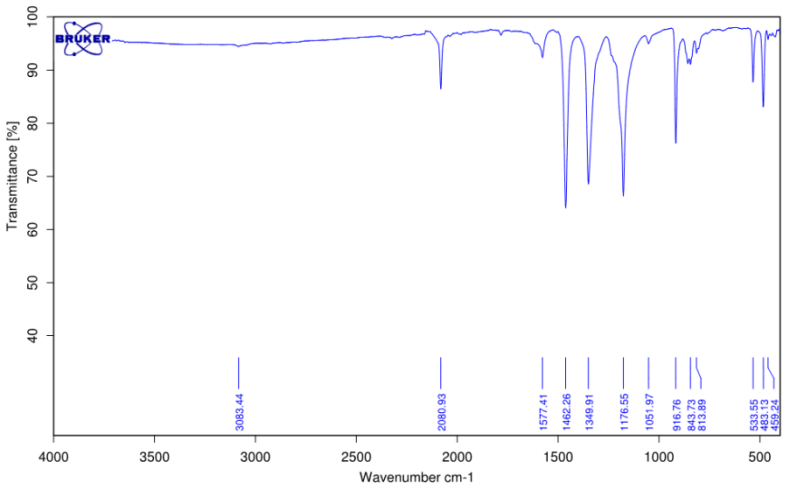

Figure S8. FT-IR spectrum of **5** • 2CO.

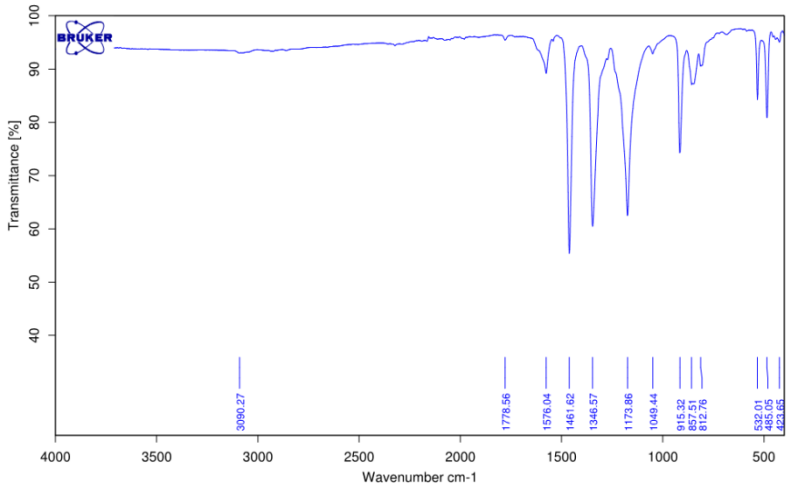

Figure S9. FT-IR spectrum of **5** • $2C_2H_4$.

DRIFT Spectroscopy

In situ DRIFT spectra of **5** were recorded under argon and nitrogen atmosphere. **5** was prepared in situ by heating **4** in a Harrick Praying Mantis reaction chamber up to 180 °C under Ar flow. After cooling down to RT, the spectrum was recorded under Ar flow. Then, the gas flow was switched to N_2 and the spectrum was collected again after 10 min (Figure S10). This sequence was repeated several times. It can be clearly seen, that the band at 2242 cm^{-1} becomes stronger under N_2 atmosphere and becomes weak again after changing to Ar. This band, assigned to N-N stretch of a Cu(I)-N_2 complex, can be more clearly seen in the difference spectrum (Figure S10, blue line).

No additional absorption bands could be detected under O_2 or H_2 flow.

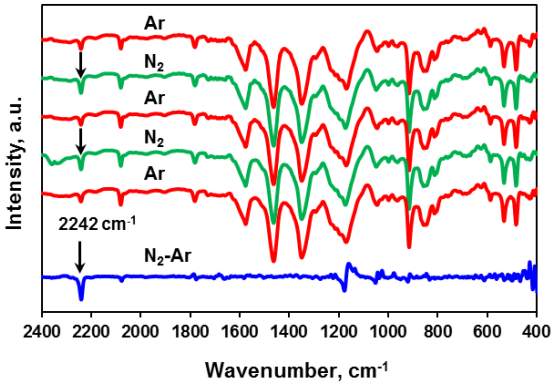

Figure S10. In situ DRIFT spectra of **5** under argon and nitrogen flow and the difference spectrum, showing the N-N stretch of Cu(I)-dinitrogen complex.

Gas sorption measurements

Nitrogen adsorption isotherms for the determination of the BET surface areas of **1** and **2** were measured at 77.3 K (Figure S11). The BET surface areas were determined in the pressure range $0.02 < p/p_0 < 0.07$. Argon adsorption isotherms for the determination of the BET surface areas of **3**,**4** and **5** were measured at 87.3 K (Figure S12). The BET surface areas were determined in the pressure range $0.06 < p/p_0 < 0.1$. The isosteric heats of adsorption were calculated from the measured isotherms (Figures S13-14) using the Clausius-Clapeyron equation (**I**). The slopes of linear plots lnP versus 1/RT for different loadings (Figures S15-18, 20) give the adsorption enthalpies, according to the equation (**II**).

$$Q_{st} = -R\left(\frac{\partial(\ln P)}{\partial(1/T)}\right)_{\theta}$$ (**I**), θ – surface coverage

$$\ln P = -\frac{Q_{st}}{R}\left(\frac{1}{T}\right) + C$$ (**II**), C – integration constant

In the case of CH_4, the isosteric heat of adsorption at zero limit surface coverage (initial heat of adsorption) has been determined. First, Henry's constants K_H were obtained as a slope from the linear ranges of isotherms at low pressure (Table S1 and Figure S21). In this range the dependence of amount adsorbed (n) on the pressure can be expressed with Henry's low (**III**). The isosteric heat of adsorption can be obtained in a similar way by using the Clausius-Clapeyron equation (**IV**).

$n = K_H \bullet P$ (**III**)

$$\lim_{n\to 0}(Q_{st}) = Q_{st}^0 = R\left(\frac{\partial(\ln K_H)}{\partial(1/T)}\right)$$ (**IV**)

Table S1. Henry's constants for CH_4 adsorption on **5**, $cm^3\ g^{-1}\ kPa^{-1}$

T, K	203	213	223	233
K_H	1.9023	1.2263	0.8193	0.5784

For other gases, the initial heat of adsorption could not be determined, since the initial linear range was not found in the isotherms.

In order to prove the reversibility of the chemisorption, adsorption and desorption isotherms were measured for O_2, N_2 and H_2 on **5** (Figure S22).

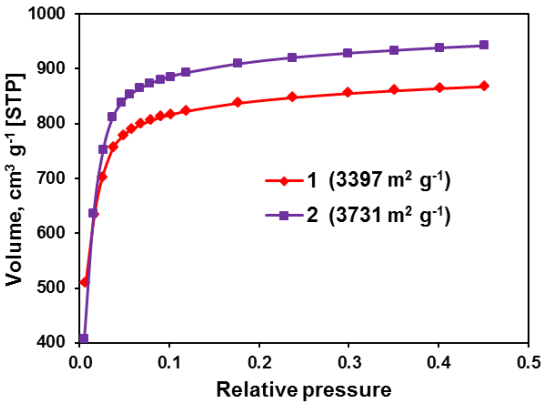

Figure S11. Nitrogen adsorption isotherms for compounds **1-2** and corresponding BET surface areas.

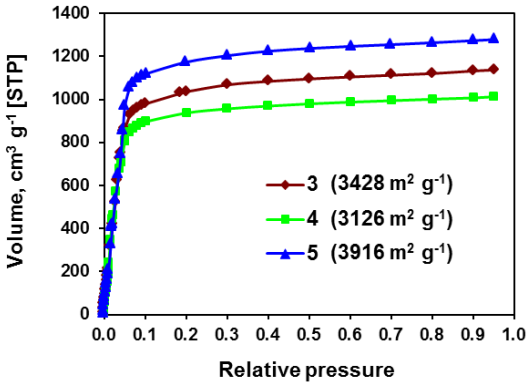

Figure S12. Argon adsorption isotherms for compounds **3-5** and corresponding BET surface areas.

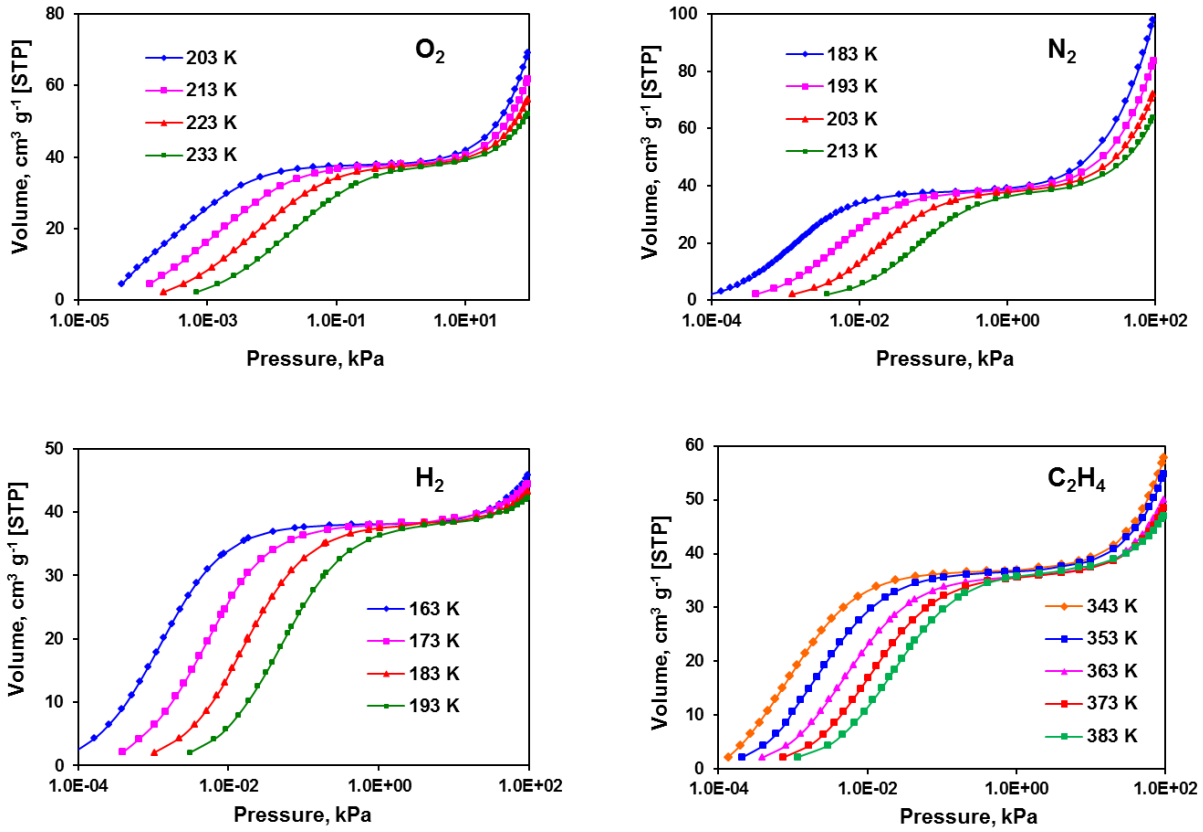

Figure S13. O_2, N_2, H_2 and C_2H_4 adsorption isotherms for **5** at different temperatures for the determination of the isosteric heats of adsorption.

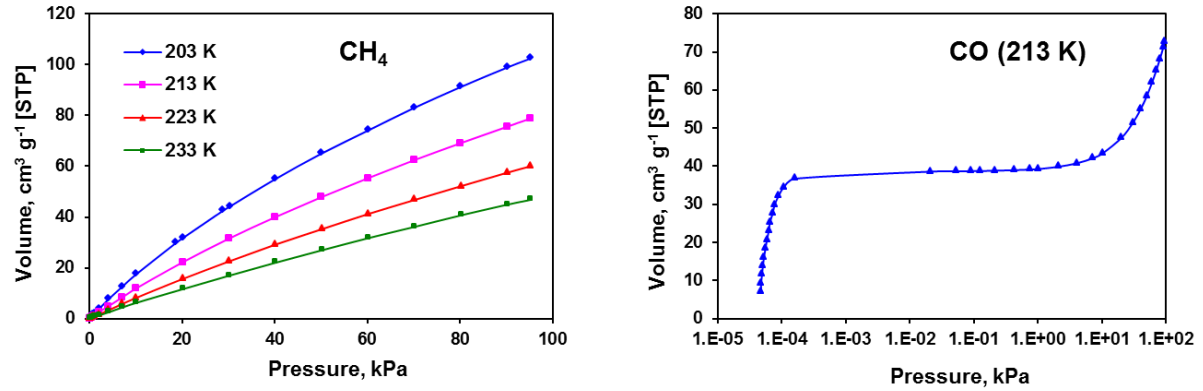

Figure S14. CH_4 adsorption isotherms for **5** at different temperatures for the determination of the isosteric heat of adsorption and CO adsorption isotherm for **5** at 213 K, showing strong chemisorption at low pressure.

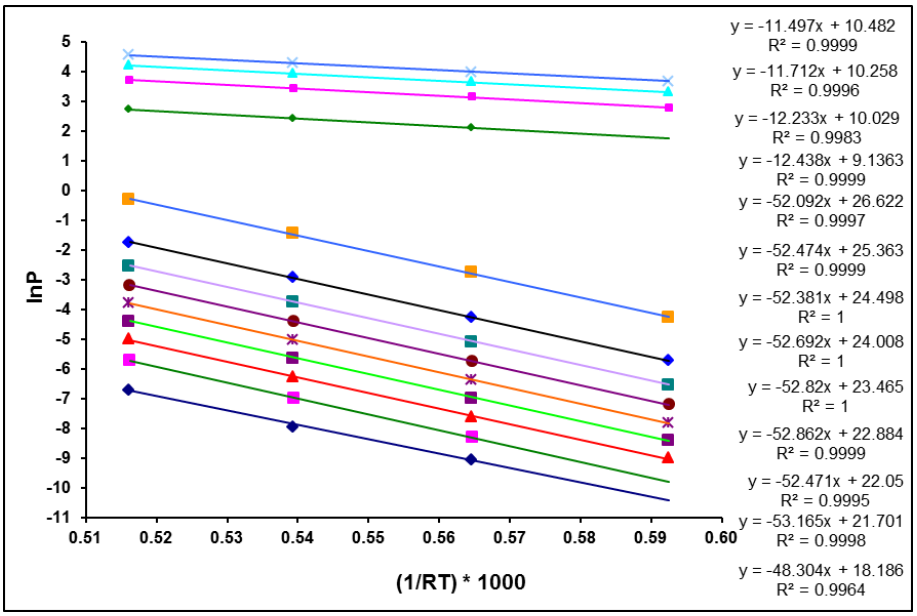

Figure S15. lnP versus 1/RT plots for different loadings for oxygen adsorption on **5**.

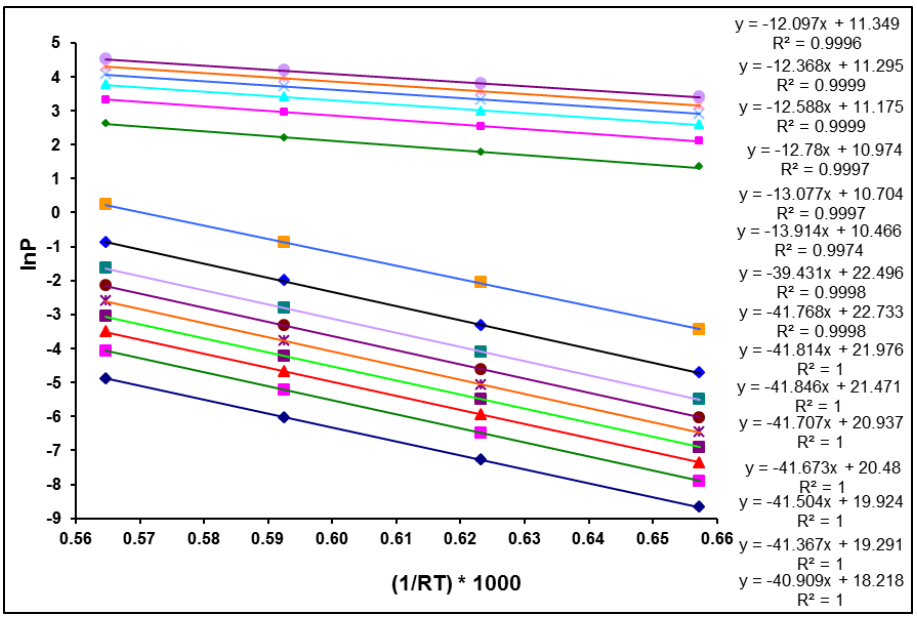

Figure S16. lnP versus 1/RT plots for different loadings for nitrogen adsorption on **5**.

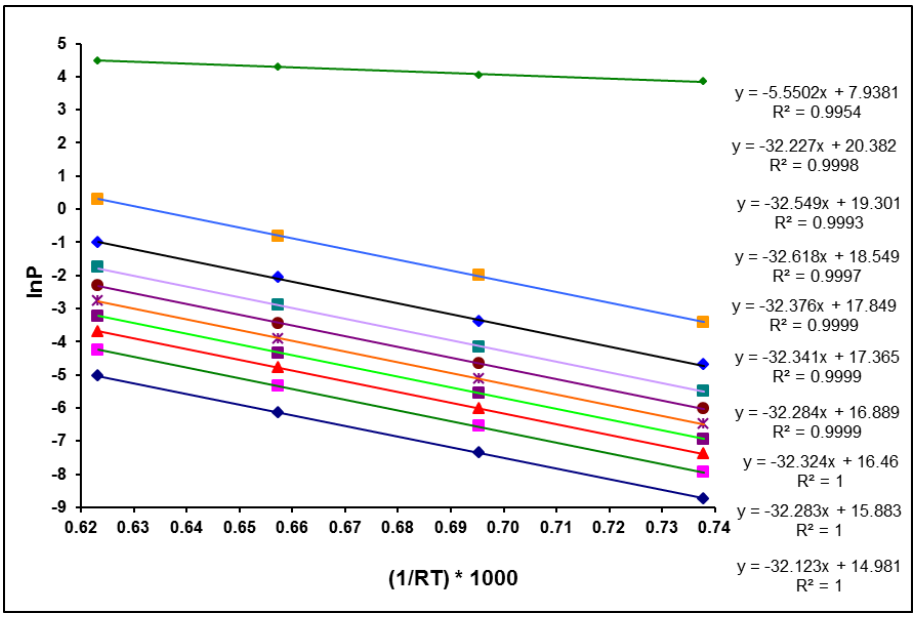

Figure S17. lnP versus 1/RT plots for different loadings for hydrogen adsorption on **5**.

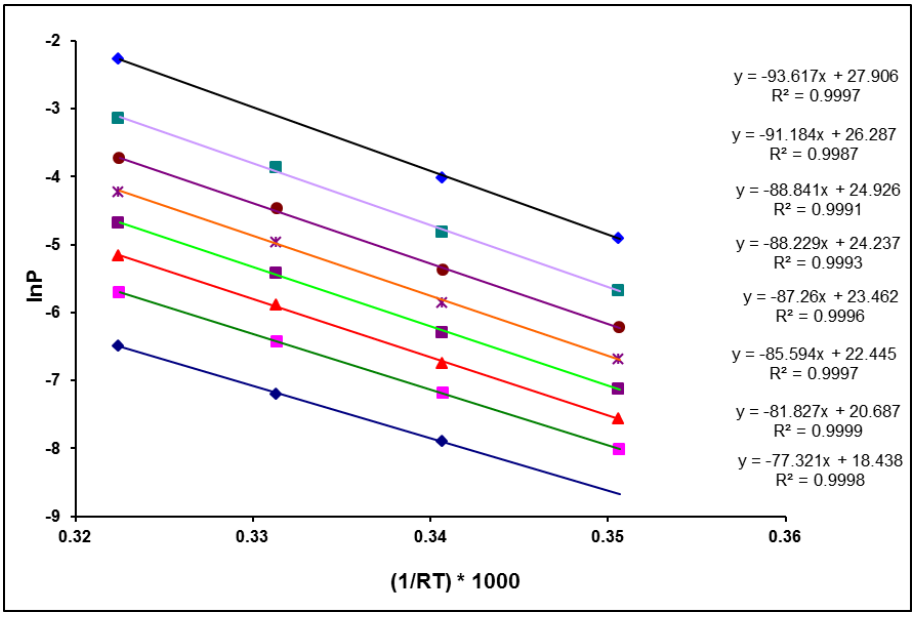

Figure S18. lnP versus 1/RT plots for different loadings for ethylene adsorption on **5**.

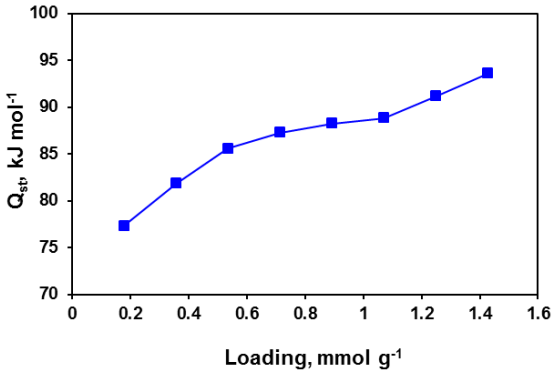

Figure S19. Dependence of the isosteric heat of adsorption on loading for ethylene adsorption on **5**.

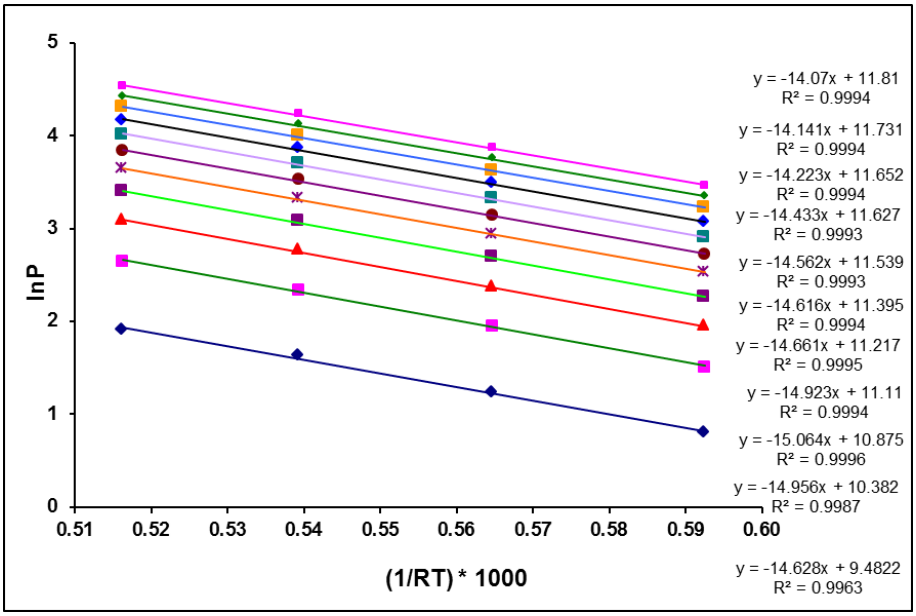

Figure S20. lnP versus 1/RT plots for different loadings for methane adsorption on **5**.

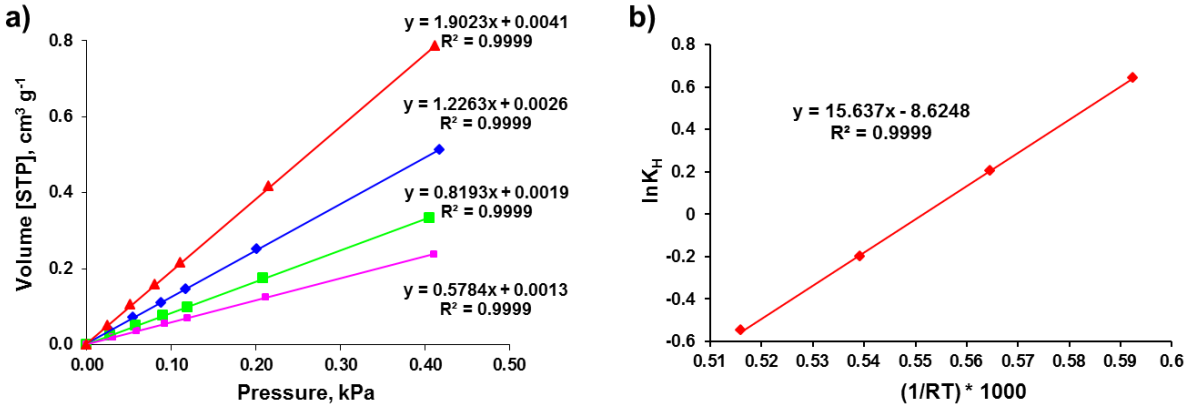

Figure S21. Determination of Henry's constants for methane adsorption on **5** and $\ln K_H$ versus 1/RT plot for the determination of the initial heat of adsorption.

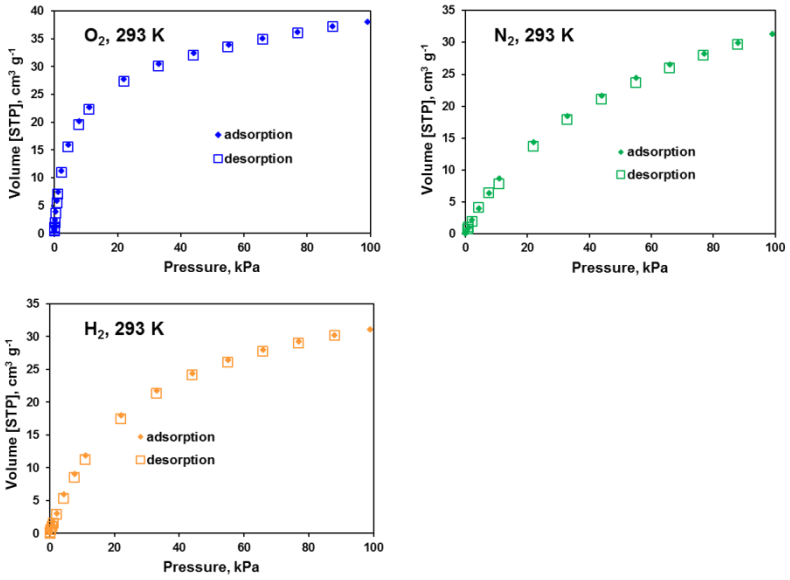

Figure S22. Adsorption and desorption isotherms for O_2, N_2 and H_2 on **5**.

GC/MS measurements

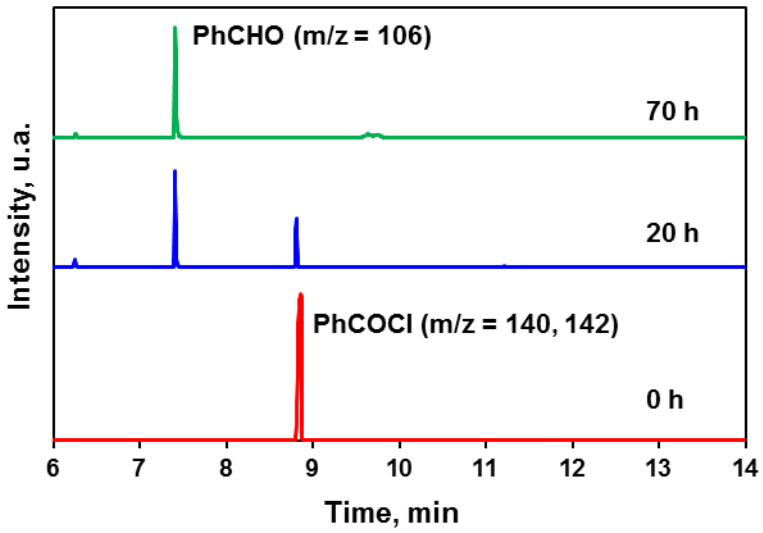

Figure S23. The reaction of **2** with benzoyl chloride followed by GC/MS.

Powder X-ray diffraction measurements and crystal structure determination of 1, 3 and 4

Crystalline samples of **1, 2, 3, 4** and **5** were ground using an agate mortar and pestle, and were deposited in the hollow of a zero-background sample holder. Diffraction data were collected in the 2θ range of 3–90° with 0.02° steps, with a time of 3000 s per step, using a Seifert XRD 3003 TT diffractometer equipped with Meteor 1D detector.

For the Rietveld refinement of **1, 3** and **4**, the crystal structure of MFU-4*l*[3] was used as a starting crystal model. After the profile refinement the Fourier map calculation was done, the position of HCOO ligand was detected on difference Fourier map. The Rietveld refinement was carried out using the Jana2006 program[4]. Weak geometric restrains on bond distances were used during the refinement process. Hydrogen atoms were placed at idealized positions using SHELXL program[5]. The experimental details and crystal data for **1** are listed in Tables S2-4. The final Rietveld refinement plots for **1** are presented in Figure S24. Experimental details and crystal data for **3** are listed in Tables S5-7. The final Rietveld refinement plots for **3** are presented in Figure S25. Experimental details and crystal data for **4** are listed in Tables S8-10. The final Rietveld refinement plots for **4** are presented in Figure S26.

The stability of the frameworks **2** and **5** was confirmed by the Le Bail fits. The fits were performed by Jana2006 Program.[4]. Le Bail fit plots for **2** and **5** are presented in Figures S27-28.

[3] D. Denysenko et al., *Chem. Commun*. **2012**, *48*, 1236–1238.
[4] V. Petricek, M. Dusek, L. Palatinus. 2006. Jana2006. Structure Determination Software Programs. Institute of Physics, Praha, Czech Republic.
[5] G. M. Sheldrick, SHELXL-97, Program for Refinement of Crystal Structures, University of Göttingen, Germany, 1997.

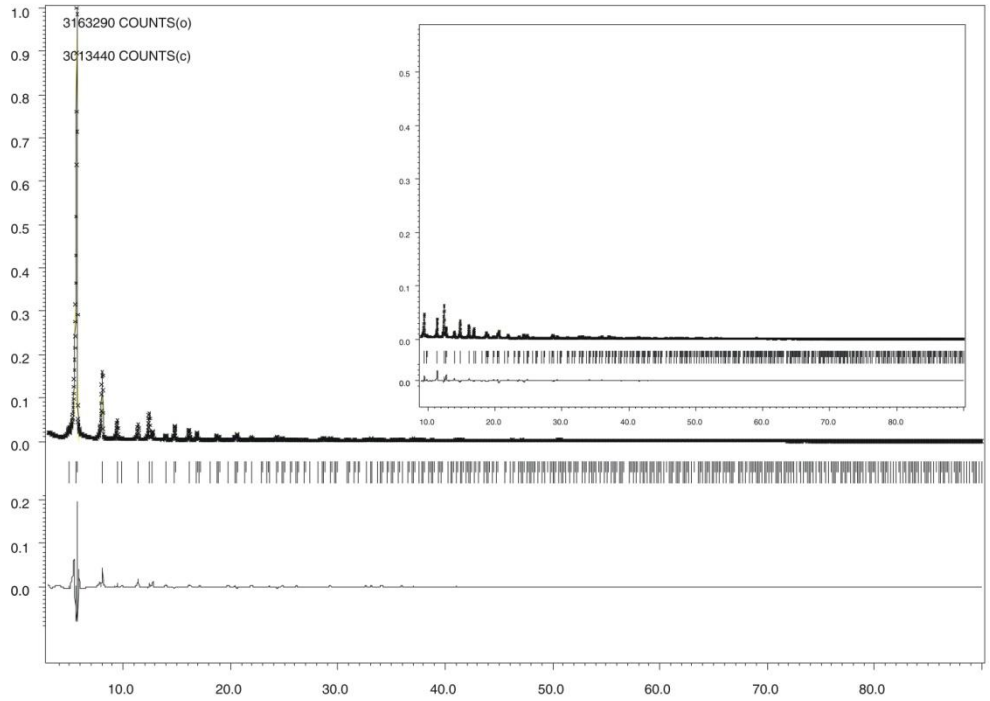

Figure S24. Rietveld refinement plots for **1**. Dotted and solid lines represent observed and calculated patterns, respectively with peak markers and the difference plot shown at the bottom. For clarity, the inset shows an expanded view in the range 9–90 2θ.

Table S2. Experimental details and crystal data for **1**.

Compound	MFU-4*l*-formate (**1**)
Diffractometer	Seifert XRD 3003 TT
X-ray source/wavelength/ Å	Cu, 1.5418
T/K	293(2)
Empirical formula	
Formula	$C_{40}H_{16}N_{18}O_{14}Zn_5$
M_r	1299.6
Crystal system	cubic
Space group (no)	$Fd\bar{3}m$ (no. 227)
a/Å	31.025(3)
V/Å^3	29862(3)
Z	8
D_c/g cm^{-3}	0.5779
F(000)	5152
2θ Range/°	3-90
Refls. Obs.	671
Number of observation	4350
R_P	14.11
R_{Fobs}	9.95
R_B	14.14

Table S3. Atomic coordinates for **1**.

Atom	x	y	z	U_{iso}
N1	0.3376(4)	0.27432(10)	0.2257	0.026(10)
C1	0.3808(2)	0.2663(4)	0.2337	0.027(10)
N2	0.3126(6)	0.25	0.25	0.026(10)

C2	0.4205(2)	0.2791(4)	0.2209	0.027(10)
C3	0.4617(3)	0.2660(3)	0.234	0.027(10)
O1	0.5	0.2826(4)	0.2174	0.027(10)
Zn1	0.25	0.25	0.25	0.03(2)
O2	0.35610(10)	0.35610(10)	0.1985(3)	0.027(10)
Zn2	0.3151(2)	0.3151(2)	0.1849	0.03(2)
C4	0.3523(3)	0.3523(3)	0.1477	0.027(10)
H2	0.4205	0.3002	0.1998	0.037995
H4	0.3706	0.3706	0.1294	0.037995

Table S4. Bond lengths [Å] and angles [°] for **1**.

N1-C1;1.386(14)
N1-N2;1.319(13)
N1-Zn2;1.920(7)
C1-C1^i^;1.431(12)
C1-C2;1.353(9)
N2-Zn1;1.942(19)
C2-C3;1.398(11)
C3-C3^i^;1.407(9)
C3-O1;1.394(10)
O2-Zn2;1.849(7)
Zn2-C4;2.002(9)
C1-N1-N2;111.3(8)
C1-N1-Zn2;126.1(6)
N2-N1-Zn2;122.6(10)
N1-C1-C1^i^;104.7(6)
N1-C1-C2;140.9(8)
C1^i^-C1-C2;114.4(7)
N1-N2-N1^i^;108.0(14)
N1-N2-Zn1;126.0(8)
N1^i^-N2-Zn1;126.0(8)
C1-C2-C3;131.5(8)
C2-C3-C3^i^;114.1(8)
C2-C3-O1;124.4(7)
C3^i^-C3-O1;121.5(8)
C3-O1-C3^ii^;117.0(8)
N2-Zn1-N2^iii^;180.0(5)
N2-Zn1-N2^iv^;90
N2-Zn1-N2^v^;90
N2-Zn1-N2^vi^;90
N2-Zn1-N2^vii^;90
N2^iii^-Zn1-N2^iv^;90
N2^iii^-Zn1-N2^v^;90
N2^iii^-Zn1-N2^vi^;90
N2^iii^-Zn1-N2^vii^;90
N2^iv^-Zn1-N2^v^;180.0(5)
N2^iv^-Zn1-N2^vi^;90
N2^iv^-Zn1-N2^vii^;90
N2^v^-Zn1-N2^vi^;90
N2^v^-Zn1-N2^vii^;90
N2^vi^-Zn1-N2^vii^;180.0(5)
N1-Zn2-N1^viii^;92.7(4)
N1-Zn2-N1^ix^;92.7(4)
N1-Zn2-O2;93.0(4)
N1-Zn2-O2^viii^;171.8(6)

N1-Zn2-O2^ix^;93.0(4)
N1-Zn2-C4;123.4(5)
N1^viii^-Zn2-N1^ix^;92.7(4)
N1^viii^-Zn2-O2;93.0(4)
N1^viii^-Zn2-O2^viii^;93.0(4)
N1^viii^-Zn2-O2^ix^;171.8(6)
N1^viii^-Zn2-C4;123.4(5)
N1^ix^-Zn2-O2;171.8(5)
N1^ix^-Zn2-O2^viii^;93.0(4)
N1^ix^-Zn2-O2^ix^;93.0(4)
N1^ix^-Zn2-C4;123.4(4)
O2-Zn2-O2^viii^;80.8(4)
O2-Zn2-O2^ix^;80.8(4)
O2-Zn2-C4;48.4(4)
O2^viii^-Zn2-O2^ix^;80.8(3)
O2^viii^-Zn2-C4;48.4(4)
O2^ix^-Zn2-C4;48.4(4)

(i) x,-y+1/2,-z+1/2
(ii) -x+1,-z+1/2,-y+1/2
(iii) -x+1/2,-y+1/2,z
(iv) z,x,y
(v) z,-x+1/2,-y+1/2
(vi) y,z,x
(vii) -y+1/2,z,-x+1/2
(viii) -z+1/2,x,-y+1/2
(ix) y,-z+1/2,-x+1/2

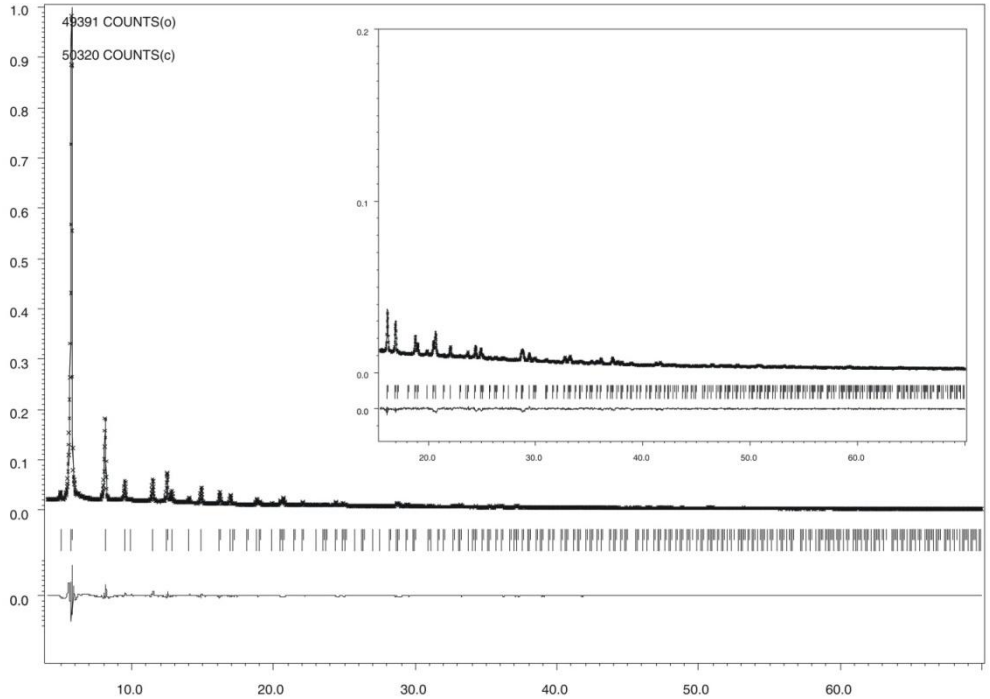

Figure S25. Rietveld refinement plots for **3**. Dotted and solid lines represent observed and calculated patterns, respectively with peak markers and the difference plot shown at the bottom. For clarity, the inset shows an expanded view in the range 18–90 2θ.

Table S5. Experimental details and crystal data for **3**.

Compound	Cu-MFU-4*l* (**3**)
Diffractometer	Seifert XRD 3003 TT
X-ray source/wavelength/ Å	Cu, 1.5418
T/K	293(2)
Empirical formula	
Formula	$C_{36}H_{12}Cl_4Cu_{1.66}N_{18}O_6Zn_{3.34}$
M_r	1258.3
Crystal system	cubic
Space group (no)	$Fd\bar{3}m$ (no. 227)
a/Å	31.0196(9)
V/Å^3	29847.5(9)
Z	8
D_c/g cm^{-3}	0.5599
F(000)	4947
2θ Range/°	4-70
Number of observation	3300
R_P	5.37
R_{Fobs}	6.99
R_B	10.28

Table S6. Atomic coordinates for **3**.

Atom	x	y	z	U_{iso}
Zn1	0.31726(10)	0.31726(10)	0.1827	0.055(3)
Cl1	0.3554(2)	0.3554(2)	0.1446	0.0576(10)
Zn2	0.25	0.25	0.25	0.055(3)
N1	0.3405(3)	0.2750(2)	0.225	0.056(10)
C1	0.3823(2)	0.2668(4)	0.2332	0.061(10)
N2	0.3157(3)	0.25	0.25	0.056(10)
C2	0.4210(3)	0.2829(3)	0.2171	0.061(10)
C3	0.4609(3)	0.2666(3)	0.2334	0.061(10)
O1	0.5	0.2828(4)	0.2172	0.061(10)
Cu1	0.31726(10)	0.31726(10)	0.1827	0.055(3)
H1	0.4209	0.3041	0.1959	0.037995

Table S7. Bond lengths [Å] and angles [°] for **3**.

Zn1-Cl1;2.047(6)
Zn1-N1;1.988(6)
Zn1-N1^i^;1.988(6)
Zn1-N1^ii^;1.988(6)
Cl1-Cu1;2.047(6)
Zn2-N2;2.036(9)
Zn2-N2^iii^;2.036(9)
Zn2-N2^iv^;2.036(9)
Zn2-N2^v^;2.036(9)
Zn2-N2^vi^;2.036(9)
Zn2-N2^vii^;2.036(9)
N1-C1;1.345(11)
N1-N2;1.341(8)
N1-Cu1;1.988(6)
C1-C1^viii^;1.472(12)
C1-C2;1.396(11)

C2-C3;1.430(12)
C3-C3^viii^;1.454(9)
C3-O1;1.406(10)
Cl1-Zn1-N1;123.5(3)
Cl1-Zn1-N1^i^;123.5(3)
Cl1-Zn1-N1^ii^;123.5(3)
N1-Zn1-N1^i^;92.5(3)
N1-Zn1-N1^ii^;92.5(3)
N1^i^-Zn1-N1^ii^;92.5(3)
N2-Zn2-N2^iii^;180.0(5)
N2-Zn2-N2^iv^;90
N2-Zn2-N2^v^;90
N2-Zn2-N2^vi^;90
N2-Zn2-N2^vii^;90
N2^iii^-Zn2-N2^iv^;90
N2^iii^-Zn2-N2^v^;90
N2^iii^-Zn2-N2^vi^;90
N2^iii^-Zn2-N2^vii^;90
N2^iv^-Zn2-N2^v^;180.0(5)
N2^iv^-Zn2-N2^vi^;90
N2^iv^-Zn2-N2^vii^;90
N2^v^-Zn2-N2^vi^;90
N2^v^-Zn2-N2^vii^;90
N2^vi^-Zn2-N2^vii^;180.0(5)
Zn1-N1-C1;126.9(6)
Zn1-N1-N2;123.7(7)
C1-N1-N2;109.5(6)
C1-N1-Cu1;126.9(6)
N2-N1-Cu1;123.7(7)
N1-C1-C1^viii^;105.6(6)
N1-C1-C2;133.9(8)
C1^viii^-C1-C2;120.5(6)
Zn2-N2-N1;125.1(5)
Zn2-N2-N1^viii^;125.1(5)
N1-N2-N1^viii^;109.9(8)
C1-C2-C3;119.4(6)
C1-C2-H1;120.3(9)
C3-C2-H1;120.3(8)
C2-C3-C3^viii^;120.1(8)
C2-C3-O1;119.4(6)
C3^viii^-C3-O1;120.5(8)
C3-O1-C3^ix^;119.0(7)
Cl1-Cu1-N1;123.5(3)
Cl1-Cu1-N1^i^;123.5(3)
Cl1-Cu1-N1^ii^;123.5(3)
N1-Cu1-N1^i^;92.5(3)
N1-Cu1-N1^ii^;92.5(3)
N1^i^-Cu1-N1^ii^;92.5(3)
(i) -z+1/2,x,-y+1/2
(ii) y,-z+1/2,-x+1/2
(iii) -x+1/2,-y+1/2,z
(iv) z,x,y
(v) z,-x+1/2,-y+1/2
(vi) y,z,x
(vii) -y+1/2,z,-x+1/2

(viii) x,-y+1/2,-z+1/2
(ix) -x+1,-z+1/2,-y+1/2

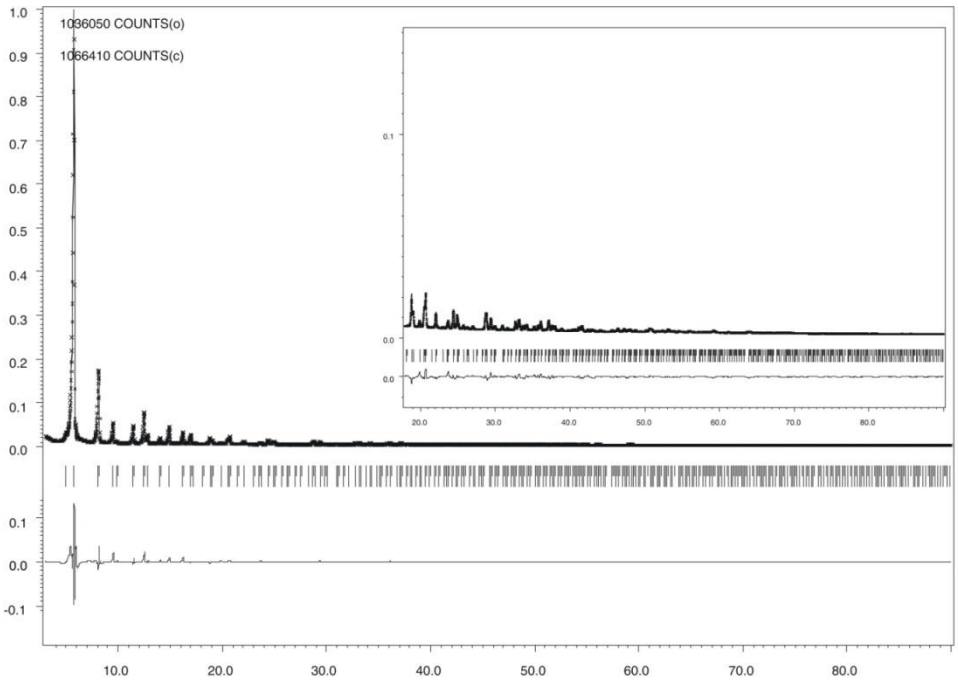

Figure S26. Rietveld refinement plots for **4**. Dotted and solid lines represent observed and calculated patterns, respectively with peak markers and the difference plot shown at the bottom. For clarity, the inset shows an expanded view in the range 18–90 2θ.

Table S8. Experimental details and crystal data for **4**.

Compound	Cu-MFU-4*l*-formate (**4**)
Diffractometer	Seifert XRD 3003 TT
X-ray source/wavelength/ Å	Cu, 1.5418
T/K	293(2)
Empirical formula	
Formula	$C_{40}H_{16}Cu_{1.92}N_{18}O_{14}Zn_{3.08}$
M_r	1296.1
Crystal system	cubic
Space group (no)	$Fd\bar{3}m$ (no. 227)
a/Å	30.922(3)
V/Å^3	29566(3)
Z	8
D_c/g cm^{-3}	0.5822
F(000)	5137
2θ Range/°	3-90
Refls. Obs.	665
Number of observation	4350
R_P	9.78
R_{Fobs}	8.30
R_B	14.15

Table S9. Atomic coordinates for **4**.

Atom	x	y	z	U_{iso}
Cu1	0.3146(2)	0.3146(2)	0.1854;	0.035(3)
N1	0.3393(3)	0.2746(3)	0.2254;	0.022(10)

C1	0.3820(3)	0.2662(4)	0.2338;	0.019(10)
N2	0.3141(3)	0.25	0.25;	0.022(10)
C2	0.4207(3)	0.2809(3)	0.2191	0.019(10)
C3	0.4614(3)	0.2661(3)	0.2339	0.019(10)
O1	0.5	0.2820(4)	0.218	0.019(10)
Zn1	0.25	0.25	0.25	0.035(3)
O2	0.3566(2)	0.3566(2)	0.1967(4)	0.019(10)
Zn2	0.3146(2)	0.3146(2)	0.1854	0.035(3)
C4	0.1434(4)	0.1434(4)	0.1434(4)	0.019(10)
H1	0.4205	0.3022	0.1978	0.037995
H2	0.1251	0.1251	0.1251	0.037995

Table S10. Bond lengths [Å] and angles [°] for **4**.

Cu1-N1;1.909(8)
Cu1-N1^i^;1.909(8)
Cu1-N1^ii^;1.909(9)
Cu1-O2;1.868(9)
Cu1-O2^i^;1.868(8)
Cu1-O2^ii^;1.868(8)
N1-C1;1.370(13)
N1-N2;1.327(9)
N1-Zn2;1.909(8)
C1-C1^iii^;1.418(12)
C1-C2;1.359(13)
N2-Zn1;1.983(9)
C2-C3;1.415(12)
C3-C3^iii^;1.407(9)
C3-O1;1.381(10)
O2-Zn2;1.868(9)
N1-Cu1-N1^i^;95.6(3)
N1-Cu1-N1^ii^;95.6(4)
N1-Cu1-O2;93.0(5)
N1-Cu1-O2^i^;167.2(6)
N1-Cu1-O2^ii^;93.0(4)
N1^i^-Cu1-N1^ii^;95.6(4)
N1^i^-Cu1-O2;93.0(4)
N1^i^-Cu1-O2^i^;93.0(5)
N1^i^-Cu1-O2^ii^;167.2(6)
N1^ii^-Cu1-O2;167.2(5)
N1^ii^-Cu1-O2^i^;93.0(4)
N1^ii^-Cu1-O2^ii^;93.0(4)
O2-Cu1-O2^i^;77.1(5)
O2-Cu1-O2^ii^;77.1(5)
O2^i^-Cu1-O2^ii^;77.1(5)
Cu1-N1-C1;129.1(6)
Cu1-N1-N2;120.6(7)
C1-N1-N2;110.3(7)
C1-N1-Zn2;129.1(6)
N2-N1-Zn2;120.6(7)
N1-C1-C1^iii^;105.5(8)
N1-C1-C2;136.3(8)
C1^iii^-C1-C2;118.2(8)
N1-N2-N1^iii^;108.3(8)
N1-N2-Zn1;125.9(5)
N1^iii^-N2-Zn1;125.9(5)

C1-C2-C3;124.5(7)
C1-C2-H1;117.7(9)
C3-C2-H1;117.7(8)
C2-C3-C3^iii^;117.2(8)
C2-C3-O1;122.6(6)
C3^iii^-C3-O1;120.2(8)
C3-O1-C3^iv^;119.7(8)
N2-Zn1-N2^v^;180.0(5)
N2-Zn1-N2^vi^;90
N2-Zn1-N2^vii^;90
N2-Zn1-N2^viii^;90
N2-Zn1-N2^ix^;90
N2^v^-Zn1-N2^vi^;90
N2^v^-Zn1-N2^vii^;90
N2^v^-Zn1-N2^viii^;90
N2^v^-Zn1-N2^ix^;90
N2^vi^-Zn1-N2^vii^;180.0(5)
N2^vi^-Zn1-N2^viii^;90
N2^vi^-Zn1-N2^ix^;90
N2^vii^-Zn1-N2^viii^;90
N2^vii^-Zn1-N2^ix^;90
N2^viii^-Zn1-N2^ix^;180.0(5)
N1-Zn2-N1^i^;95.6(3)
N1-Zn2-N1^ii^;95.6(4)
N1-Zn2-O2;93.0(5)
N1-Zn2-O2^i^;167.2(6)
N1-Zn2-O2^ii^;93.0(4)
N1^i^-Zn2-N1^ii^;95.6(4)
N1^i^-Zn2-O2;93.0(4)
N1^i^-Zn2-O2^i^;93.0(5)
N1^i^-Zn2-O2^ii^;167.2(6)
N1^ii^-Zn2-O2;167.2(5)
N1^ii^-Zn2-O2^i^;93.0(4)
N1^ii^-Zn2-O2^ii^;93.0(4)
O2-Zn2-O2^i^;77.1(5)
O2-Zn2-O2^ii^;77.1(5)
O2^i^-Zn2-O2^ii^;77.1(5)

(i)	-z+1/2,x,-y+1/2
(ii)	y,-z+1/2,-x+1/2
(iii)	x,-y+1/2,-z+1/2
(iv)	-x+1,-z+1/2,-y+1/2
(v)	-x+1/2,-y+1/2,z
(vi)	z,x,y
(vii)	z,-x+1/2,-y+1/2
(viii)	y,z,x
(ix)	-y+1/2,z,-x+1/2

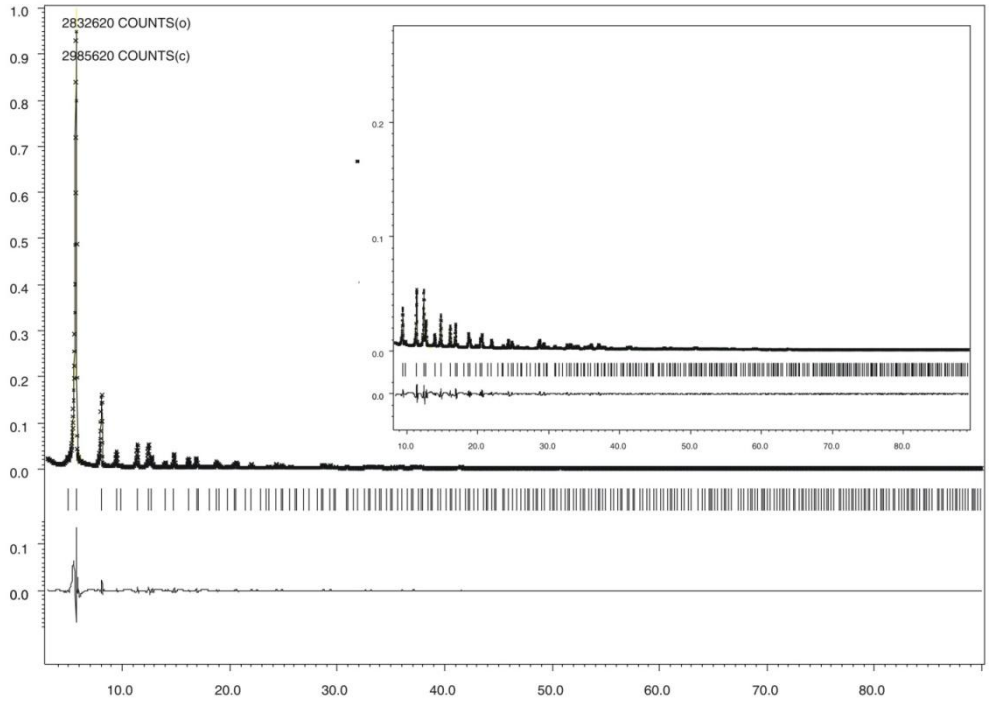

Figure S27. Le Bail fit plots for **2**: Dotted and solid lines represent observed and calculated patterns, respectively with peak markers and the difference plot shown at the bottom. For clarity, the inset shows an expanded view in the range 9–90 2θ.

a = b = c = 31.071(4) A, V = 29996(4); $Fd\bar{3}m$ (no. 227)
R_P = 12.10 w_{RP} = 16.23, number of observations: 4350

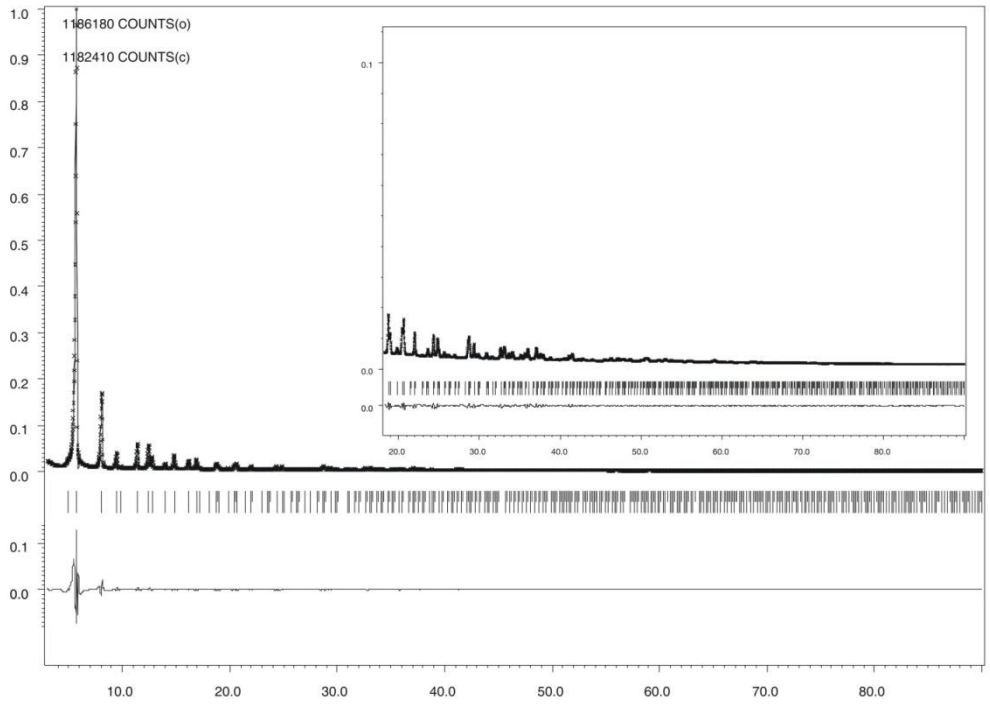

Figure S28. Le Bail fit plots for **5** • $2O_2$: Dotted and solid lines represent observed and calculated patterns, respectively with peak markers and the difference plot shown at the bottom. For clarity, the inset shows an expanded view in the range 18–90 2θ.

a = b = c = 30.972(1) A, V = 29709(1); $Fd\bar{3}m$ (no. 227)
R_P = 8.62 w_{RP} = 14.35, number of observations: 4350

Theory Section

Density-Functional Theory calculations of vibrational frequencies and heats of adsorption

All DFT calculations of vibrational frequencies and isosteric heats of adsorption have been performed with the all-electron full-potential code FHI-aims.[6] Electronic exchange and correlation was treated on the level of the generalized gradient approximation (GGA) PBE functional[7] or on the level of the hybrid B3LYP functional.[8] Dispersive interactions lacking at these levels of theory were considered through the dispersion-correction scheme due to Tkatchenko and Scheffler.[9] The calculations were performed on a metal-modified scorpionate model complex, in which the HB unit of a typical scorpionate (Figure 2, main text) is replaced by a Zn(II) metal ion. Detailed test calculations[10] confirmed the reliability of this model in describing Lewis-acidic metal centers in MFU-4*l* frameworks typically possessing low coordination numbers. Geometry optimization was generally performed at the PBE level until residual forces fell below 10^{-4} eV/Å. Hybrid B3LYP energetics was subsequently obtained through single-point calculations on these optimized geometries, as test calculations showed insignificant geometry changes upon full geometry optimization at B3LYP level. Similar findings were obtained in the frequency calculations, which is why the zero point energy and internal thermal correction enthalpies entering the isosteric heats of adsorption have also been computed at the PBE level. Systematic tests demonstrate a numerical convergence of these isosteric heats of adsorption within 5 kJ mol^{-1} at the employed "tier2" NAO basis set and when using tight integration grids. No scaling has been applied to the vibrational frequencies.

A comparison of the DFT-calculated and experimentally measured IR spectra of **1** and **2** is shown in Figures S29 and S30. In Figure S29 band "a" (1610 cm^{-1} experiment, 1626 cm^{-1} DFT) is assigned to the C-O stretching mode of the $HCOO^-$ species. In Figure S30 the band "b" (1793 cm^{-1}experiment, 1865 cm^{-1} DFT) is assigned to Zn – H stretching mode. Bands "c" (482 cm^{-1} experiment, 488 cm^{-1} DFT) and "d" (453 cm^{-1} experiment, 462 cm^{-1} DFT) are assigned to Zn – H bending modes. The two latter modes differ in their bending orientation.

---

[6] a) V. Blum, R. Gehrke, F. Hanke, P. Havu, V. Havu, X. Ren, K. Reuter, M. Scheffler, *Comp. Phys. Commun*. **2009**, *180*, 2175-2196; b) X. Ren, P. Rinke, V. Blum, J. Wieferink, A. Tkatchenko, A. Sanfilippo, K. Reuter, M. Scheffler, *New J. Phys*. **2012**, *14*, 053020.

[7] J.P. Perdew, K. Burke, M. Ernzerhof, *Phys. Rev. Lett*. **1996**, *77*, 3865-3868.

[8] a) A.D. Becke, *J. Chem. Phys*. **1993**, *98*, 5648-5652; b) P.J. Stephens, J.F. Devlin, C.F. Chabalowski, M.J. Frisch, *J. Chem. Phys*. **1993**, *98*, 11623-11627.

[9] A. Tkatchenko, M. Scheffler, *Phys. Rev. Lett*. **2009**, *102*, 073005.

[10] J. Jelic, D. Denysenko, D. Volkmer, K. Reuter, *New J. Phys*. **2013**, *15*, 115004.

In mode ”c” the H atom is bending along the ligand, and in mode “d” it bends between the two ligands.

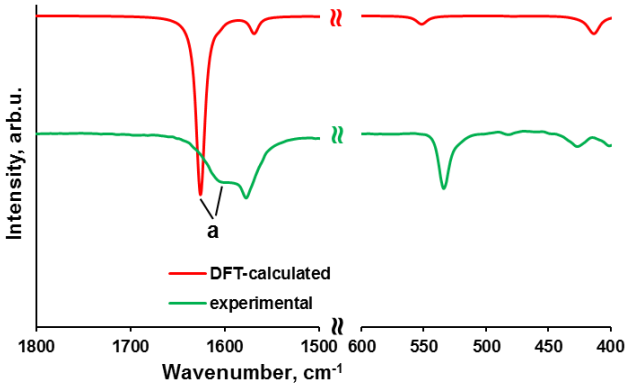

Figure S29. Comparison of DFT-calculated and experimentally measured IR spectra of **1** in selected wavenumber ranges.

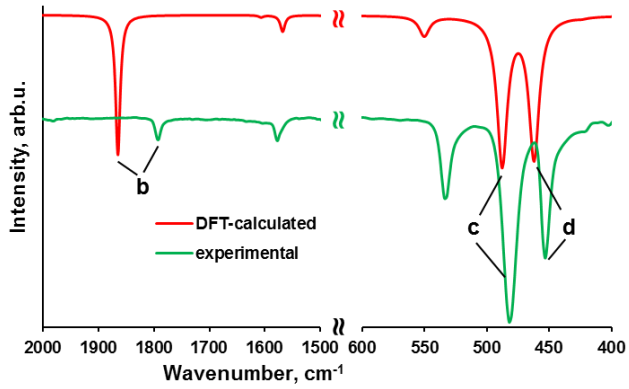

Figure S30. Comparison of DFT-calculated and experimentally measured IR spectra of **2** in selected wavenumber ranges.

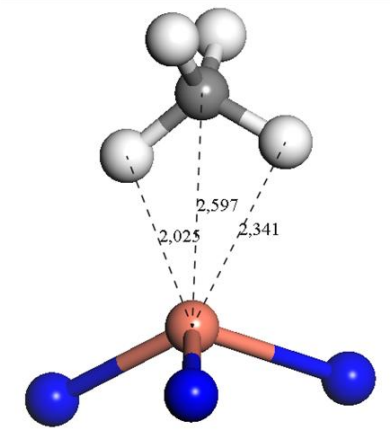

Figure S31. DFT-calculated optimized binding geometry of CH_4 on Cu(I) centers within the Kuratowski unit of MFU-4*l*. The large bond distances indicate a predominantly dispersive interaction (all atomic distances in Å).

ChemPubSoc Europe

DOI: 10.1002/chem.201406564

CHEMISTRY
A European Journal
Full Paper

Metal–Organic Frameworks

Postsynthetic Metal and Ligand Exchange in MFU-4*l*: A Screening Approach toward Functional Metal–Organic Frameworks Comprising Single-Site Active Centers

Dmytro Denysenko,[a] Jelena Jelic,[b] Karsten Reuter,[b] and Dirk Volkmer*[a]

Abstract: The isomorphous partial substitution of Zn^{2+} ions in the secondary building unit (SBU) of MFU-4*l* leads to frameworks with the general formula $[M_xZn_{(5-x)}Cl_4(BTDD)_3]$, in which $x \approx 2$, M = Mn^{II}, Fe^{II}, Co^{II}, Ni^{II}, or Cu^{II}, and BTDD = bis(1,2,3-triazolato-[4,5-b],[4′,5′-i])dibenzo-[1,4]-dioxin. Subsequent exchange of chloride ligands by nitrite, nitrate, triflate, azide, isocyanate, formate, acetate, or fluoride leads to a variety of MFU-4*l* derivatives, which have been characterized by using XRPD, EDX, IR, UV/Vis-NIR, TGA, and gas sorption measurements. Several MFU-4*l* derivatives show high catalytic activity in a liquid-phase oxidation of ethylbenzene to acetophenone with air under mild conditions, among which Co- and Cu derivatives with chloride side-ligands are the most active catalysts. Upon thermal treatment, several side-ligands can be transformed selectively into reactive intermediates without destroying the framework. Thus, at 300 °C, Co^{II}-azide units in the SBU of Co-MFU-4*l* are converted into Co^{II}-isocyanate under continuous CO gas flow, involving the formation of a nitrene intermediate. The reaction of Cu^{II}-fluoride units with H_2 at 240 °C leads to Cu^{I} and proceeds through the heterolytic cleavage of the H_2 molecule.

Introduction

Metal–organic frameworks (MOFs) are coordination polymers featuring an open framework containing potential voids. MOFs represent an exponentially growing research field[1] and have been tested for many different applications such as capture of gases and vapors,[2] gas separation and storage,[3] catalysis,[4] sensing,[5] as luminescent[6] or ferroelectric[7] materials, and as materials for non-linear optics[8] or biomedicine.[9] For each kind of application, the framework properties have to be adjusted according to the specific requirements. However, it is often difficult to synthesize a MOF with desired properties directly. For this reason, post-synthetic modification has been developed as a powerful approach towards functional metal–organic frameworks. The most frequently practiced way for post-synthetic framework modification includes covalent modification(s) of the organic linkers, such as the reaction sequence of nitration or bromination of aromatic moieties, condensation reactions of amines with aldehydes, carboxylic acid derivatives or isocyanates, post-synthetic deprotection and click reactions (cycloaddition to azides).[10] These methods allow the introduction of the desired functional groups into the framework, adjustment of the pore structure, tuning of the breathing properties, and so on. Another common approach towards modified frameworks is represented by the post-synthetic metalation (coordination of metal ions to the functional groups or free coordination sites of organic linkers), which is used for introducing catalytically active or luminescent metal ions into the framework or for improving the sorption properties of the MOF.[11] A post-synthetic linker exchange has been realized for several MOF structures.[12] Finally, post-synthetic metal exchange in secondary building units (SBUs) has been described for different MOF families, whereas in many cases only partial substitution was achieved.[13] We have previously described the post-synthetic exchange of the peripheral (tetrahedrally coordinated) Zn^{II} ions by Co^{II}[14] and Cu^{II}[15] in MFU-4*l*.[16] In addition, the solvent-dependent Zn/Co exchange in MFU-4*l* has been investigated in detail.[17] MFU-4*l*, constructed from deprotonated bis(1*H*-1,2,3-triazolo-[4,5-b],[4′,5′-i])dibenzo-[1,4]-dioxin (BTDD) ligands and $\{Zn_5Cl_4\}^{6+}$ building units, is a large-pore member of the MFU-4 structure family of cubic frameworks featuring exceptionally high thermal and solvolytic stability.[18] A close structural relative to this family, CFA-1, has been shown to undergo Zn/Co exchange under similar reaction conditions.[19] The SBU of these frameworks (and in structurally related molecular Kuratowski-type coordination compounds)[20] includes one octahedrally coordinated (central) metal ion and four tetrahedrally coordinated (peripheral) metal ions. The tetrahedrally coordinated metal ions are structurally related to well-known scorpionate complexes.[21] This coordination principle allows for the stepwise exchange of peripheral metal ions, whereas the central octahedrally coordinated Zn^{2+} ion remains unchanged and the SBU

[a] D. Denysenko, Prof. Dr. D. Volkmer
Institute of Physics, Chair of Solid State and Materials Chemistry
University of Augsburg, Universitätsstrasse 1, 86159 Augsburg (Germany)
E-mail: dirk.volkmer@physik.uni-augsburg.de

[b] Dr. J. Jelic, Prof. Dr. K. Reuter
Chair of Theoretical Chemistry and Catalysis Research Center
Technische Universität München, Lichtenbergstr. 4
85747 Garching (Germany)

Supporting information for this article is available on the WWW under http://dx.doi.org/10.1002/chem.201406564.

remains intact (Figure 1). This approach allows us to obtain heterometallic derivatives of MFU-4*l*, which were so far unavailable through direct synthesis. We have previously also shown that chloride side-ligands in MFU-4*l* and Cu-MFU-4*l* can be easily substituted by formate ligands.[15] Thermal activation of thus obtained formate MFU-4*l* derivatives led to Zn–H or Cu^{I} species, the latter showing unique chemisorption properties for several simple gas molecules (e.g., H_2, N_2 and O_2).[15] In addition, Co-MFU-4*l* was found to be catalytically active in the heterogeneous oxidation of carbon monoxide.[14] Lastly, MFU-4 and MFU-4*l* frameworks have been studied in technically demanding gas separations such as Xe/Kr[22] or H_2/D_2.[23] Introducing other metal ions into MFU-4*l* structure therefore seems a rewarding research goal in terms of developing functional frameworks. Subsequent ligand exchange allows us to tune the reactivity of metal centers and to perform further transformations including the in situ generation of active metal sites. Additionally, the pore geometry can be optimized for applications such as gas storage and separation. In this manuscript we present the synthesis and characterization of a variety of MFU-4*l* derivatives obtained through post-synthetic metal and ligand exchange leading to a screening approach towards functional metal–organic frameworks comprising open metal sites. Mn-, Fe- and Ni derivatives of MFU-4*l* are presented, which were not considered in our earlier works. The possibilities and limitations of side-ligand exchange reactions are discussed in detail.

Results and Discussion

Post-synthetic modifications of MFU-4*l*

We have previously reported on the complete exchange of peripheral Zn^{2+} ions in MFU-4*l* by Co^{2+} at 140 °C in DMF.[14] Metal exchange with Cu^{2+}, however, can only be conducted at 60 °C (due to the formation of amorphous impurities at higher temperatures) and leads to a partial (≈50%) substitution.[15] Similarly, other 3d transition-metal ions (Mn^{2+}, Fe^{2+}, and Ni^{2+}) can be introduced into the SBU by dispersing MFU-4*l* crystals into a solution containing a large excess of metal(II) chloride in DMF or DMA at 60 °C. Under these conditions, approximately 40 to 60% of the peripheral Zn^{2+} ions are substituted leading to frameworks with the general formula $[M_xZn_{(5-x)}Cl_4(BTDD)_3]$, in which $x \approx 2$ and BTDD = bis(1,2,3-triazolato-[4,5-b],[4′,5′-i])dibenzo-[1,4]-dioxin (Scheme 1).

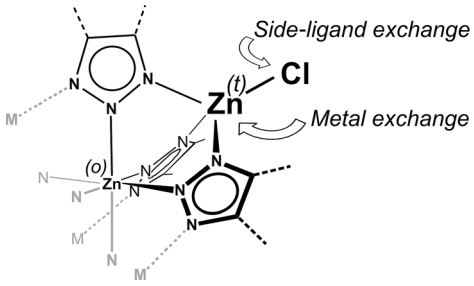

Figure 1. Metal- and side-ligand exchange on the peripheral position in the SBU of MFU-4-type frameworks (a part of the SBU is shown; *t*-tetrahedral, *o*-octahedral; only one out of four tetrahedrally coordinated (= peripheral) Zn centers is shown).

Only in the case of Co^{II} are approximately 3 of 4 Zn^{2+} ions substituted under these conditions, indicating that substitution by Co^{II} is more favorable than that of other 3d transition-metal ions. This is probably due to the highest ligand field stabilization energy (12 D_q^{tet} for tetrahedrally coordinated d^7 metal ions) among the applied metal ions. For Mn^{II}, Fe^{II}, and Cu^{II}, metal exchange at temperatures above 60 °C leads to impure products, as verified by XRPD, IR spectroscopy, and gas sorption measurements. Only in the case of Ni^{II} is metal exchange also possible at 80 °C, leading to almost complete substitution of peripheral Zn centers (Figure 2). However, analytically pure products, as determined by elemental analyses, were only obtained at 60 °C. Figure 2 shows that 50% of the peripheral Zn^{2+} ions are substituted easily when an approximately equimolar M/Zn starting ratio is used. Further increase of the initial M/Zn ratio then results only in a moderate enhancement of the metal substitution degree. For this reason, we have used

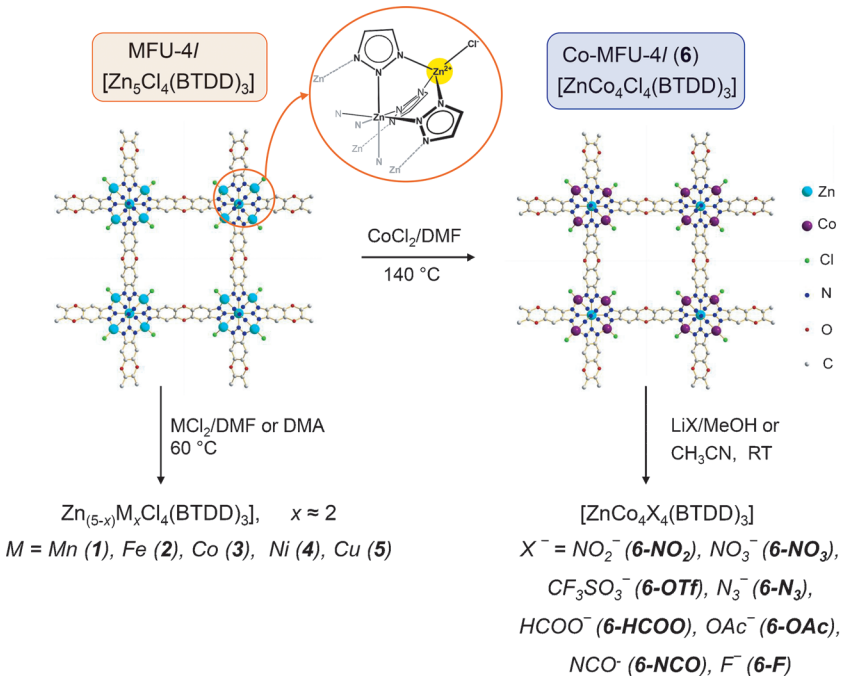

Scheme 1. Post-synthetic modifications of MFU-4*l* described in this study (DMF = *N*,*N*-dimethylformamide, DMA = *N*,*N*-dimethylacetamide).

a 13-fold excess of metal(II) chloride in 0.25 M DMA or DMF solution in preparative scale metal exchange procedures. Higher metal salt concentrations result in the precipitation of metal salts and should be avoided. To improve the metal substitution degree, samples of metal-exchanged MFU-4*l* have been subjected to a second exchange step employing identical starting conditions. However, according to analytical results, this second exchange did not improve the substitution degree significantly. For instance, in the case of Cu, the Zn/Cu exchange degree increased from 55 to 60% upon repeating the procedure. All MFU-4*l* hetero-metal derivatives thus prepared possess a thermal stability similar to the original MFU-4*l* framework (up to 400 °C according to TGA data, see the Supporting Information, Figure S1). XRPD data show that all derivatives are phase-pure and have the same structure as the parent framework MFU-4*l* (the Supporting Information, Figure S78). Also, the IR spectra are nearly identical to that of MFU-4*l* (the Supporting Information, Figures S10–S13). All frameworks are highly porous, as confirmed by argon sorption at 87.3 K (the Supporting Information, Figure S33). Our attempts to introduce other metal ions such as Ag^{+}, Pd^{2+}, or VO^{2+} into MFU-4*l* by using a similar procedure were unsuccessful up to now. Post-synthetic metal exchange in MFU-4*l* can be augmented by the side-ligand exchange reaction as exemplified for chloride exchange in Co-MFU-4*l* (Scheme 1). Hence, the chloride side-ligand can be substituted by a number of different anions such as NO_2^-, NO_3^-, N_3^-, $CF_3SO_3^-$, NCO^-, $HCOO^-$, CH_3COO^-, or F^-. Lithium salts well-soluble in methanol or acetonitrile were used in all cases except fluoride, in which case CsF soluble in methanol was applied. For weakly coordinating ligands (formate, acetate, nitrate, and triflate) a 20-fold excess of lithium salt in methanol was employed. In the case of triflate, the exchange with this procedure is incomplete. However, nearly 90% of chloride ligands can be substituted when the procedure is repeated twice. The success of ligand exchange was controlled mainly by EDX analysis and in several cases by FIR spectroscopy. Thus, a characteristic band at 383 cm^{-1} assigned to the Co–Cl stretch mode,[14] disappears almost completely upon side-ligand exchange (the Supporting Information, Figure S21). In the case of stronger coordinating ligands (nitrite, azide, and isocyanate), such large excess of lithium salt leads to discernible leaching of Co^{2+} ions from Co-MFU-4*l* (**6**) and to decomposition of the framework. For this reason, only a moderate excess of the corresponding lithium salt ($\approx$25%) was used. Acetonitrile approved to be a better choice for these ligands leading to products with higher crystallinity. All attempts to introduce cyanide into Co-MFU-4*l* (**6**) failed completely due to immediate decomposition of the framework. Also, treatment with hydroxide led to decomposition of the framework, as verified by XRPD measurements. Fluoride exchange proceeds smoothly on all 3d transition-metal centers studied except zinc. Treatment of MFU-4*l* with CsF in methanol does not lead to the Cl/F exchange, as verified by EDX and IR measurements. EDX analyses show that partially substituted fluoride derivatives of Mn-, Fe-, Ni-, and Cu-MFU-4*l* (**1-F**, **2-F**, **4-F**, and **5-F**, respectively) contain a considerable amount of chloride, which corresponds well to a number of peripheral Zn^{2+} ions in the SBU and indicates that chloride side-ligands at Zn^{II} centers are not substituted by fluoride. Co-MFU-4*l*-fluoride (**6-F**) is, in contrast, almost chloride-free, since all four peripheral zinc ions in each SBU are replaced by Co^{II} centers in peripheral positions. According to the TGA data, all derivatives obtained after the side-ligand exchange are quite stable (at least up to 150 °C, see the Supporting Information, Figures S2, S3, and S6). XRPD measurements confirm phase purity and intact structure of the frameworks (the Supporting Information, Figures S79–81). The high porosity typical for MFU-4*l* frameworks is also retained (the Supporting Information, Figures S33 and S34).

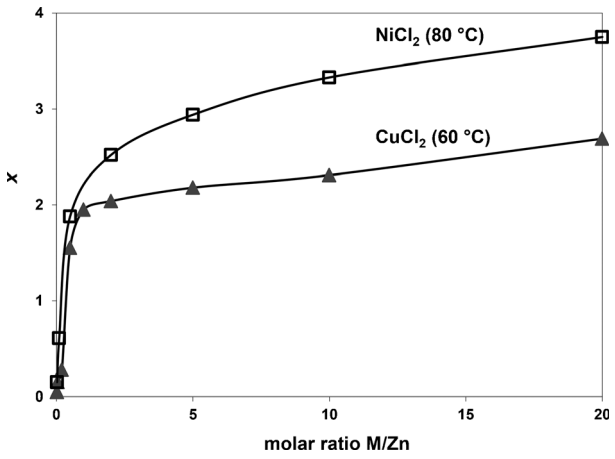

Figure 2. Total number, *x*, of Ni^{II} or Cu^{II} ions per $\{M_xZn_{5-x}Cl_4\}^{6+}$ unit as a function of (M/Zn) molar ratio in the starting reaction mixture (DMA, 20 h).

UV/Vis-NIR spectra

All derivatives except Mn-MFU-4*l* (**1**) show several absorption bands in the UV/Vis-NIR spectrum relating to d–d metal-centered valence electron transitions. Fe-MFU-4*l* (**2**) does not show any bands in the visible range, but it shows a strong charge-transfer (CT) band at 335 nm and other bands in the NIR range at 1385 and approximately 1660 nm (Figure 3).

The bands in the NIR range correspond to a split $^5T_2 \rightarrow {}^5E$ transition.[24] The tetrahedral complex $[FeQ_2Cl_2]$ (Q = quinuclidine) shows the same split band with two maxima at approximately 1400 and 1950 nm. The shift towards lower energy is caused by a weaker ligand field.[25] Ni-MFU-4*l* (**4**), when filled with DMA, is green-colored and shows bands at 630 and 1039 nm, which are typical for octahedral Ni^{II} ions and correspond to the $^3A_{2g} \rightarrow {}^3T_{1g}$ and $^3A_{2g} \rightarrow {}^3T_{2g}$ transitions, respectively.[24] The third spin-allowed transition, $^3A_{2g} \rightarrow {}^3T_{1g}(P)$, which normally appears at 370–520 nm, is overlapped by the strong ligand absorption and can hardly be seen as a shoulder at approximately 420 nm (Figure 4).

After solvent removal, compound **4** becomes red-colored. The tetrahedrally coordinated Ni^{II} ions with C_{3v}-symmetric ligand surrounding in **4** show a much more complicated spectrum (Figure 4), which has previously been observed for a similar scorpionate complex [Tp*NiCl] (Tp* = hydrotris(3,5-dimethyl-1-pyrazolyl)borate).[26] Thus, based on ligand-field calculations performed for [Tp*NiCl], the observed absorption bands

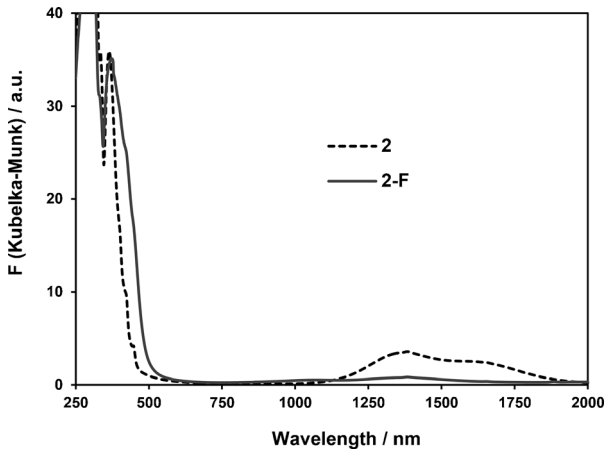

Figure 3. Diffuse reflectance UV/Vis-NIR spectra of **2** and **2-F**.

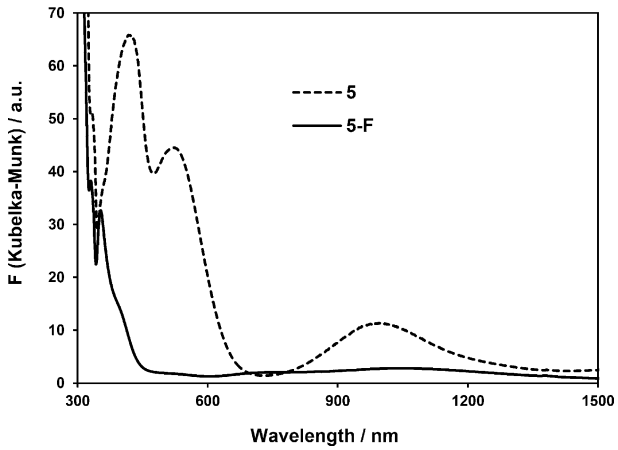

Figure 5. Diffuse reflectance UV/Vis-NIR spectra of **5** and **5-F**.

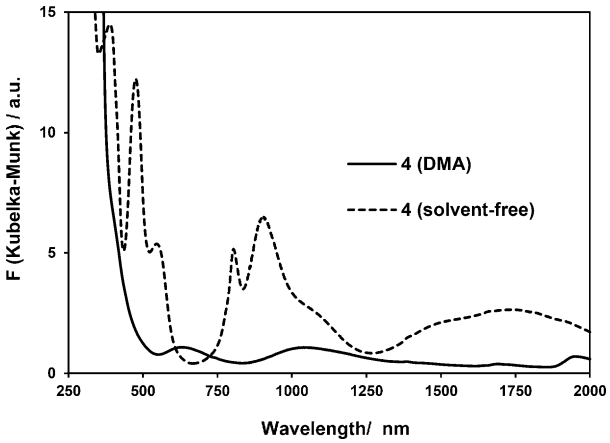

Figure 4. Diffuse reflectance UV/Vis-NIR spectra of **4** (filled with DMA and solvent-free).

can be assigned as the following transitions: 386 nm: CT, 475 nm: $^3A_2(^3T_1, F)\rightarrow{}^3A_2(^3A_2, F)$, 547 nm: $^3A_2(^3T_1, F)\rightarrow{}^3E(^3T_1, P)$, 804 nm: $^3A_2(^3T_1, F)\rightarrow{}^3A_2(^3T_1, P)$, 905 nm: $^3A_2(^3T_1, F)\rightarrow{}^3E(^3T_2, F)$, 1743 nm: $^3A_2(^3T_1, F)\rightarrow{}^3E(^3T_1, F)$. The same behavior was observed in case of Cu^{II}-MFU-4*l* (**5**): When filled with DMA, the compound is green and shows absorption bands typical for sixfold coordinated Cu^{II}. Solvent-free **5** is red–brown and shows very intensive absorption bands at 417, 523, and 997 nm (Figure 5).[15]

These spectral features are very similar to previously described scorpionate complexes [$Tp^{tBu,Me}$CuCl] and [Cu(L)Cl]-(CLO_4), in which $Tp^{tBu,Me}$ = hydrotris(3-*tert*-butyl-5-methyl-1-pyrazolyl)borate and L = tris(3-*tert*-butyl-5-methyl-1-pyrazolyl)methane.[27] Thus, the first two bands at 417 and 523 nm can be assigned to the Cl^- to Cu^{II} CT transitions, the third one at 997 nm to the d–d transition at the Cu^{II} centers. In **5-F**, the CT absorption bands disappear almost completely, which remains in agreement with the much higher electronegativity of fluorine. At the same time, also the intensities of d–d transitions become much lower (Figure 5). The same behavior is observed for **4-F** (the Supporting information, Figure S9). In **2-F**, only the intensity of the d–d transitions is reduced, whereas the intensity of the CT band remains unchanged (Figure 3). This can be explained by the nature of the transition, which is in this case most probably metal-to-ligand charge-transfer involving a triazolate moiety. In contrast, such a hypochromic effect is not observed for **6-F** (the Supporting Information, Figure S8). These phenomena are well known in coordination chemistry, but have no simple explanation. Qualitatively, the intensity of a d–d transition grows with increasing covalency of a metal–ligand bond and respective mixing between metal and ligand orbitals.[24] The fluoride ligand has a much higher ionic character compared with chloride, and thus leads to low intensities of d–d transitions. The spectral properties of Co-MFU-4*l* (**6**) described previously[14] undergo strong changes upon substitution of chloride ligands. UV/Vis-NIR spectra of selected derivatives of **6** are shown on Figure 6. Substitution of the chloride ligand by azide leads to a very intensive CT absorption band at 389 nm. The strong absorption band centered at 612 nm, typical for tetrahedral Co^{II} ions, is more intense and shows a much stronger split compared with **6**. Framework **6-HCOO** contains fivefold coordinated Co^{II} ions, which results in a significant shift and much lower intensity of the absorption bands. Figure S8 (the Supporting information) shows that nitrite, nitrate, and triflate derivatives of **6** also contain fivefold coordinated Co^{II}, as confirmed by comparison to the literature-known complex [Tp*Co(OAc)].[28] Nitrite is an interesting case since it is known to coordinate either in monodentate (nitro-, by the N-atom) or bidentate (nitrito-, by two oxygen atoms) fashion. The nitrito-to-nitro linkage isomerization has been extensively studied for Co^{III}[29] and it has been found that the nitro-form is more stable.[30] However, in the case of scorpionate-type coordination of Co^{II}, the nitrito-form seems to be more stable. Thus, [$Tp^{tBu,Me}Co(NO_2)$] contains fivefold coordinated Co^{II} with the nitrite ligand coordinated by two oxygen atoms.[31] [$Tp^{Ph_2}Co(NO_2)$] (Tp^{Ph_2} = hydrotris(3,5-diphenyl-1-pyrazolyl)borate) shows complex solution behavior being blue (tetrahedrally coordinated) in CH_2Cl_2 and pink-red (fivefold coordinated) in THF.[32]

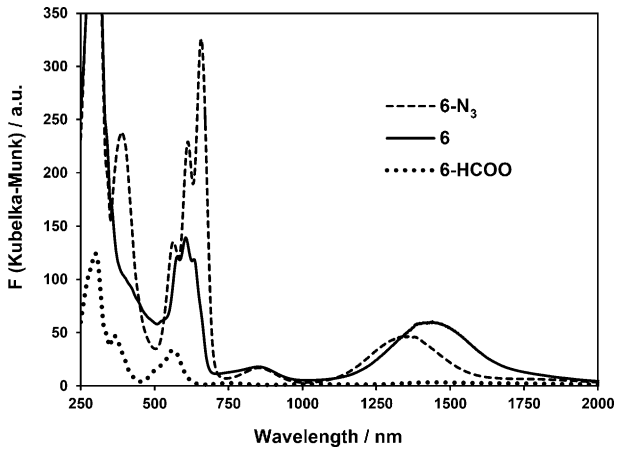

Figure 6. Diffuse reflectance UV/Vis-NIR spectra of selected derivatives of **6**.

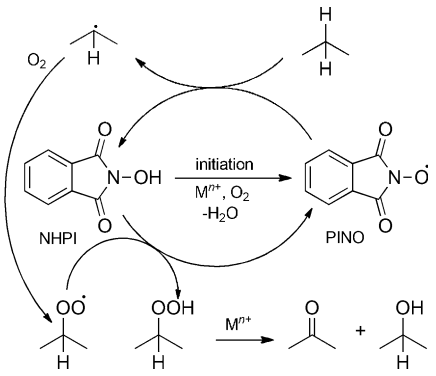

Scheme 2. Schematic representation of the aerobic oxidation of hydrocarbons catalyzed by the NHPI/PINO system in the presence of transition-metal ions.

Liquid-phase aerobic oxidation

MFU-4*l* frameworks featuring coordinatively unsaturated metal sites, large pores, and high thermal stability are promising candidates for catalytic applications. Binding of the O_2 molecule at the active metal site is a crucial step for the gas-phase oxidation under mild conditions. Searching for MOFs that could be utilized for heterogeneously catalyzed reactions employing molecular oxygen, we have systematically studied heterometallic MFU-4*l* derivatives. Since physisorption enthalpies for argon and oxygen are very similar,[33] a comparison of the isosteric heats of Ar and O_2 adsorption will show whether chemisorptive oxygen binding at the unsaturated metal site takes place or not. Unfortunately, in all tested cases, the heats of Ar and O_2 adsorption determined from the adsorption isotherms measured in the temperature range 183–213 K (as described in the Supporting information, pp. S13–S31), are very similar (Table S1). Density-functional theory (DFT) calculations of O_2 binding energies on metal centers in scorpionate-type coordination, which was used as a model environment for metal sites in MFU-4*l*, confirm these results and show that strongly basic ligands such as hydroxide, hydride, or amide would enable oxygen binding.[34] Only in these cases was sufficient charge transfer from the metal center to the oxygen identified through Hirshfeld charge analyses. Unfortunately, up to now, we were not able to prepare these derivatives. It seems that tetrahedral and fivefold coordination of divalent metal centers in MFU-4*l* frameworks comprising one additional side ligand is less favorable for binding small molecules if compared with Cu^{I}-MFU-4*l* featuring trigonal-pyramidal Cu^{I} sites and showing quite strong O_2 binding.[15] Although MFU-4*l* derivatives seem rather inactive in terms of dioxygen binding from the gas phase, they show catalytic activity in liquid-phase oxidation reactions. Selective oxidation of hydrocarbons is an important process for fine chemical synthesis. MOFs have been extensively tested as catalysts for this kind of application. In most cases, different peroxides such as H_2O_2 or *t*BuOOH were applied as oxidizing agents.[4d] Molecular oxygen is the most attractive oxidant due to its unlimited availability. However, due to its low reactivity at low temperatures, oxygen activation still remains a challenge. One effective strategy for oxygen activation is the use of *N*-hydroxyphthalimide (NHPI) as co-catalyst, which is easily oxidized to phthalimide *N*-oxyl radical (PINO) with air in the presence of transition-metal ions. PINO acts then as initiator for the radical oxidation of C–H bonds (Scheme 2).[35]

This strategy has been successfully applied with homogeneous catalysts such as acetates or acetylacetonates of V^{IV}, Mo^{VI}, Mn^{III}, Fe^{III}, Co^{II}, Co^{III}, and Cu^{II}.[36] Several MOFs have been tested as catalysts for this reaction. Thus, MFU-1 was found to be catalytically active in the PINO-mediated oxidation of cyclohexanol, cyclohexane, cyclohexene, and ethylbenzene.[37] Solution impregnation of MFU-1 with NHPI led to a heterogeneous catalyst NHPI@MFU-1 suitable for solvent-free oxidation of hydrocarbons. Similar catalytic model reactions have been reported subsequently for Fe-BTC[38] and Co-BTT.[39] Continuing our work on MFU-1 derivatives we have tested different MFU-4*l* derivatives as catalysts in the aerobic oxidation of ethylbenzene under mild reaction conditions (Scheme 3).

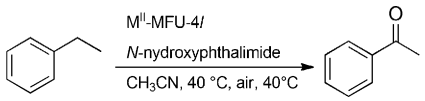

Scheme 3. Liquid-phase oxidation of ethylbenzene. Reaction conditions: catalyst (1 mol% based on Mn-, Fe-, Co-, Ni- or Cu centers), NHPI (10 mol%).

The results are summarized in Table 1. The highest conversion is achieved with **5**, **6**, and **6-OAc** (within the experimental error). Even though **5** remains highly crystalline (the Supporting information, Figure S82) and porous (BET surface area 3232 $m^2 g^{-1}$, as determined by N_2 sorption at 77.3 K) after the reaction, the hot filtration test, performed after 24 h reaction time, shows probable leaching of Cu^{2+} ions.

The conversion in filtered solution increases with time in a similar way as in the unfiltered reaction mixture (Figure 7, △). A prolonged induction period indicates the slow formation of PINO radicals in the beginning and could also indicate the leaching of Cu^{2+} ions. However, the amount of leached Cu^{2+} ions must be very low since EDX analysis of **5** recovered after catalysis shows an unchanged Zn/Cu ratio (see the Experimen-

Table 1. Conversions and selectivities for the liquid-phase oxidation of ethylbenzene catalyzed by MFU-4*l* derivatives after a reaction time of 48 h.

Compound	Metal ion	Side ligand	Conversion of ethylbenzene [%]	Selectivity ketone/alcohol[a]
6	Co^{2+}	Cl^-	27±3	97
6-OAc	Co^{2+}	CH_3COO^-	26±3	95
6-NO_3	Co^{2+}	NO_3^-	8±1	95
6-OTf	Co^{2+}	$CF_3SO_3^-$	3±0.5	–
1	Mn^{2+}	Cl^-	0	–
2	Fe^{2+}	Cl^-	0	–
4	Ni^{2+}	Cl^-	9±1	–
5	Cu^{2+}	Cl^-	28±3	95

[a] The selectivity for **4** and **6-OTf** could not be estimated due to very low content of alcohol

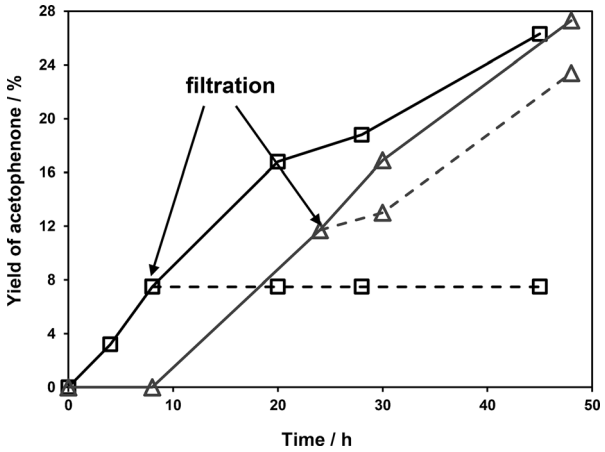

Figure 7. Time-dependent formation of acetophenone in the PINO-mediated oxidation of ethylbenzene catalyzed by **5** (△) and **6** (□). Dashed lines show the reaction progress after hot filtration.

tal Section). In contrast, framework **6**, having nearly the same activity, does not show such an induction period. The heterogeneous character of catalysis is confirmed by the hot filtration test performed after 8 h reaction time (Figure 7, □). Framework **6** also remains stable after the reaction, but the crystallinity (the Supporting information, Figure S83) and porosity (BET surface area 2172 m^2g^{-1}, as determined by N_2 sorption at 77.3 K) become slightly decreased. The EDX analysis of **6** recovered after catalysis shows, similarly to **5**, an unchanged Zn/Co ratio (see the Experimental Section). Framework **6-OAc** shows almost the same activity, whereas **6-NO_3** and **6-OTf** are much less active. Framework **4** shows low activity, as compared with that of **5** and **6**. Frameworks **1** and **2** are not stable under reaction conditions: A fast oxidation of Mn^{2+} or Fe^{2+} ions and no conversion of ethylbenzene were observed. GC/MS analysis shows the formation of 1-phenylethanol as a byproduct in all cases (the Supporting information, Figure S76). However, the ketone/alcohol selectivity is very high (≥95%) in all cases. In general, framework **6** shows similar activity and selectivity as MFU-1. Interestingly, only traces of benzoic acid (<0.1%) were found in the reaction mixture as revealed by ESI-MS analysis (for details see the Supporting information, pp. S33–S34). The recyclability test shows that **6** recovered after catalysis has almost unchanged activity and gives 25.7% conversion in the second run, which is 94% of the value listed in Table 1.

Thermal transformations of MFU-4*l*-formates and azides

As shown by us in a recent report, the thermal decomposition of formate moieties at peripheral Zn^{II} centers in MFU-4*l*-HCOO leads to the formation of Zn–H species, whereas decomposition of Cu^{II}-HCOO moieties gives Cu^{I} species.[15] Thus, thermal decomposition of formate ligands can be considered as a method for the in situ generation of reactive or low-valent metal sites. TGA measurements show that formate side-ligands at the peripheral 3d transition-metal sites in heterometallic derivatives of MFU-4*l* can be selectively decomposed, as can be seen by the stability range without weight loss, before the decomposition of the framework starts (the Supporting information, Figure S3). Only in the case of **6-HCOO** is the stability range less well pronounced. Table 2 shows decomposition ranges of formate ligands at different metal(II) centers in hetero-metal derivatives of MFU-4*l* determined by TGA.

Table 2. Temperatures for thermal transformations of formate side-ligands in heterometallic derivatives of MFU-4*l*.[a]

Compound	Metal ion	Start [°C]	End [°C]
MFU-4*l*-HCOO	Zn^{2+}	195	280
1-HCOO	Mn^{2+}	330	370
2-HCOO	Fe^{2+}	195	325
6-HCOO	Co^{2+}	195	325
4-HCOO	Ni^{2+}	180	280
5-HCOO	Cu^{2+}	120	180

[a] Determined by TGA under N_2 flow with a heating rate of 5 $K min^{-1}$.

It has to be noted that only Zn- and Co-MFU-4*l*-formates contain only one type of peripheral metal ions; the other derivatives are mixed with zinc. In the case of Mn^{II} and Cu^{II}, the decomposition steps are well separated, since Cu-HCOO moieties decompose at considerably lower, and Mn-HCOO at considerably higher temperature, than Zn-HCOO. XRPD measurements show that the crystallinity of **2-HCOO** and **4-HCOO** is completely retained after decomposition of formate side-ligands (the Supporting information Figure S84). The crystallinity of **6-HCOO** becomes lower and **1-HCOO** shows only main X-ray reflexes after thermal treatment. Treatment of **6-HCOO** under CO gas flow at 325 °C gives a proof for the formation of low-valent cobalt sites (Scheme 4). Thus, a band appearing at 1971 cm^{-1} (the Supporting information, Figure S30) is very similar to a CO stretch in Co^{I}-containing scorpionate [$Tp^{iPr,Me}Co(CO)$] (1940 cm^{-1}, $Tp^{iPr,Me}$ = hydrotris(3-isopropyl-5-methyl-1-pyrazolyl)borate).[40]

The DFT-calculated CO stretching frequency for the scorpionate Co^{I}-CO cluster is 1966 cm^{-1}. Further detailed studies on thermal transformations of formate side-ligands in heterometallic derivatives of MFU-4*l* have to be performed to explore the potential of this strategy for the generation of highly

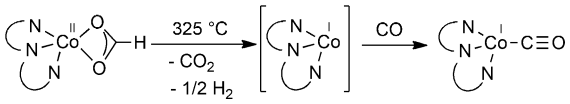

Scheme 4. Schematic representation for the formation of Co^{I}–CO species after thermal treatment of **6-HCOO** under CO gas flow.

active metal sites. Another interesting reaction is a thermal transformation of azide to isocyanate under CO gas in **6**. The reaction is very clean, as confirmed by IR spectroscopy (Figure 8) and most likely involves a nitrene as an intermediate. The crystallinity of the product is somewhat lower, compared with that of **6-N_3** and **6-NCO** prepared through the side-ligand exchange, but all X-ray reflexes are retained and no impurities can be seen (the Supporting Information, Figure S85).

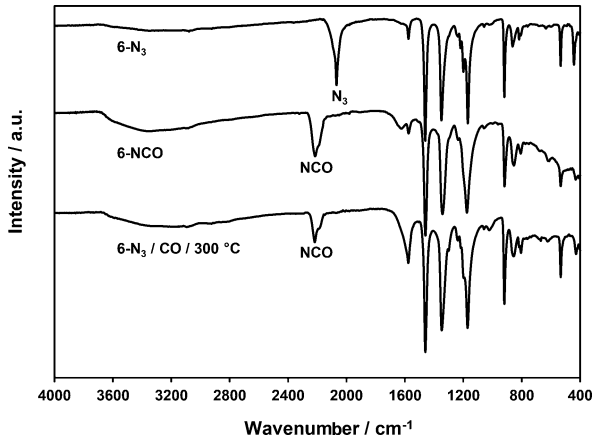

Figure 8. IR spectra of **6-N_3**, **6-NCO** (prepared form **6** by ligand exchange), and of the product obtained from **6-N_3** after heating under CO flow at 300 °C.

Transition-metal nitrene (nitrido- or imido-) complexes[41] have attracted much attention due to their supposed role in biological nitrogen fixation[42] and potential as N-atom transfer reagents.[43] Aryl-substituted bis(imino)pyridine cobalt azide complexes (^{iPr}BPDI)CoN_3 and (^{Mes}BPDI)CoN_3 have been shown to generate a nitrene intermediate under photolytic or thermal (215 °C) conditions, which then undergoes an intramolecular insertion into the C–H bond.[44] (^{Mes}BPDI)CoN_3 reacts with CO in toluene at 23 °C to give (^{Mes}BPDI)CoNCO. These mild conditions for the reaction with CO, in contrast to the intramolecular insertion into the C–H bond, indicate that the latter transformation proceeds more likely through the direct insertion of the CO molecule into azide. The solvent-assisted conversion of coordinated azide anions to isocyanate ligands under mild conditions has also been described in several other cases.[45] The conversion of **6-N_3** to **6-NCO** does not occur at RT and thus most probably involves the formation of a nitrene intermediate representing heterogeneous single-site reaction (Scheme 5). According to DFT calculations, the formation of a nitrene in the first step is endothermic (127 kJ mol^{-1}) with an activation energy of 217 kJ mol^{-1}. The barrier occurs at the Co–N···N_2 distance of 1.7 Å. Subsequent reaction with CO to isocyanate

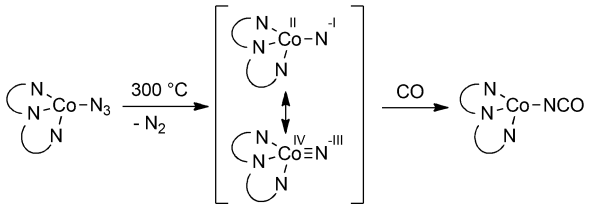

Scheme 5. Schematic representation of the conversion of **6-N_3** to **6-NCO** through the nitrene intermediate.

takes place spontaneously without any barrier and is highly exothermic (−380 kJ mol^{-1}).

Preparation of Cu^{I}-MFU-4*l* in different ways

Previously, we have described the preparation of Cu^{I}-MFU-4*l* through the thermolysis of **5-HCOO** (path **d** in Scheme 6).[15] Using the possibilities for the postsynthetic modification of MFU-4*l*, Cu^{I} centers can be generated also in alternative ways. Thus, heating a suspension of **5** in DMF at 140 °C leads to a colorless product (path **a** in Scheme 6). The presence of Cu^{I} centers in this product is confirmed by oxygen adsorption isotherms showing clear chemisorption (the Supporting Information, Figure S46, left). The heat of oxygen chemisorption (50 kJ mol^{-1}, the Supporting Information, Figure S75) is very close to the one previously described for Cu^{I}-MFU-4*l* (52 kJ mol^{-1}).[15] Additionally, the formation of Cu^{I} centers is supported by the IR spectrum after CO adsorption (the Supporting Information, Figure S31): A characteristic CO stretch at 2090 cm^{-1} is observed (2081 cm^{-1} in a previously described Cu^{I}-MFU-4*l* prepared through path **d**). However, the amount of chemisorbed oxygen (≈10 cm^3 g^{-1}, as seen from the adsorption isotherms) is much lower as described previously (38 cm^3 g^{-1}). Also, a small deviation in the heat of oxygen adsorption and position of the CO stretch as well as significantly reduced BET surface area (2615 m^2 g^{-1}) indicate that the reaction is not clean. The mechanism probably includes the formation and further decomposition of Cu-formate moieties (formate is produced by the hydrolysis of DMF). Path **b** on Scheme 6 shows a direct substitution of Zn^{2+} centers by Cu^{I} in MFU-4*l*. Since CuCl is not soluble in common solvents (except strongly coordinating solvents such as pyridine), we added lithium chloride, which leads to the formation of a mixture of soluble chloro cuprates(I). The product obtained in this way shows the same oxygen chemisorption with the heat of 52 kJ mol^{-1} (the Supporting Information, Figures S46 and S75), which matches exactly the value described previously. However, the amount of chemisorbed oxygen (≈12 cm^3 g^{-1}) is also very low, due to much lower exchange degree. Both products, prepared through the pathways **a** and **b** (Scheme 6), show the same high crystallinity as **5** (the Supporting Information, Figure S86). Finally, Cu^{I} centers in MFU-4*l* can be generated by the gas-phase reaction of **5-F** with H_2 at 240 °C (path **c** on Scheme 6).

Thus, the TGA curve of **5-F** under H_2/Ar flow shows a weight loss in the range 120–220 °C, which is not observed under N_2

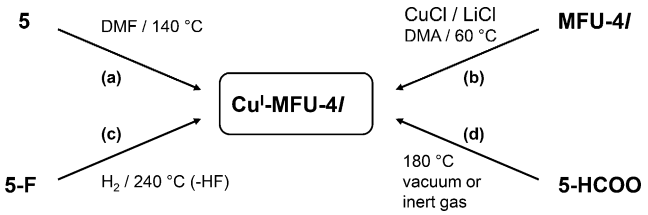

Scheme 6. Different ways for the preparation of Cu^{I}-MFU-4*l*.

(Figure 9). The weight loss of 2.8% corresponds well to the loss of fluoride ligands connected to Cu^{II} centers (calcd 3.1%). The product obtained in this way shows typical oxygen chemisorption with the heat of adsorption of 52 kJ mol^{-1} (the Supporting Information, Figures S47 and S75). The chemisorbed amount of approximately 34 cm^3 g^{-1}, high porosity (BET surface area 3682 m^2 g^{-1}), crystallinity (the Supporting Information, Figure S87) and the results of the elemental analysis confirm the purity of the obtained product with the formula $[Cu_2Zn_3Cl_2(BTDD)_3]$. Interestingly, framework **5** exhibits a similar weight loss of 4.9% in the range 250–350 °C under H_2/Ar flow, as indicated by the TGA curve (the Supporting Information, Figure S4). This weight loss corresponds quite well to the loss of two chloride ligands at the Cu^{II} centers (calcd 5.6%) and could be assumed as a formation of Cu^{I} centers. Formation of HCl in the gas phase was confirmed by TG/MS measurement (the Supporting Information, Figure S5). The loss of halide seems to occur at higher temperature even under nitrogen. Thus, both frameworks **5** and **5-F** show a weight loss in the range 350–400 °C (Figure 9 and the Supporting Information, Figure S4) before the decomposition of the framework starts.

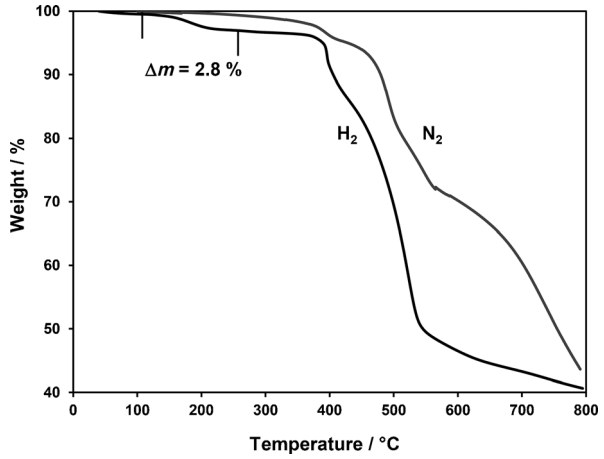

Figure 9. TGA curves for **5-F** under N_2 and H_2/Ar (1:9) flow.

Oxygen adsorption isotherms for products, obtained from **5** by heating at 350 °C under H_2/Ar flow or 400 °C under N_2 flow, show clearly that no chemisorption occurs and thus both products do not contain active Cu^{I} sites (the Supporting Information, Figure S47, right). Although the crystallinity in both cases is retained (only two small additional reflexes at 6.8 and 7.4° 2θ are observed, the Supporting Information, Figure S87), the porosity is strongly reduced to 2078 and 2054 m^2 g^{-1}, respectively. The results of the elemental analysis are similar in both cases and give C/N ratios of 36:16.6 and 36:16.1, respectively, whereas an ideal ratio for an unchanged MFU-4*l* framework must be 36:18. This indicates clearly that the triazolate moieties lose some nitrogen atoms and partial decomposition of the framework occurs under these conditions. Thus, only the reduction of **5-F** with hydrogen under milder conditions represents an alternative way for the preparation of pure Cu^{I}-MFU-4*l*. TGA studies on other fluoride derivatives of MFU-4*l* show that no reaction with H_2 takes place before the framework starts to decompose (the Supporting Information, Figure S6). The mechanism of the reaction of Cu^{II}-fluoride units in **5-F** with hydrogen probably proceeds through a heterolytic cleavage of the H_2 molecule followed by the decomposition of a Cu^{II}-hydride intermediate (Scheme 7).

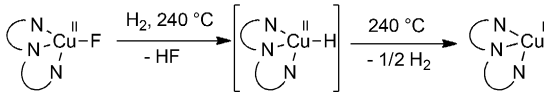

Scheme 7. Schematic representation of the conversion of Cu^{II}-F units to Cu^{I} in **5-F** through the Cu^{II}–H intermediate.

Fluoride ligands serve as basic anions forming very stable H–F bonds and thus driving the reaction. According to our DFT calculations, the formation of Cu^{II}–H species in the first step is endothermic (44 kJ mol^{-1}) with an activation energy of 80 kJ mol^{-1}. The barrier occurs at a Cu–F···H_2 distance of 1.2 Å and at that distance the H···H bond is elongated to 1.02 Å (normal bond length for H_2 molecule is 0.74 Å). Subsequent dissociation of Cu^{II}-hydride species to Cu^{I} and H radicals (which then recombine to H_2 molecules) has a calculated activation energy of 145 kJ mol^{-1} and the full free radical split takes place at a Cu···H distance of approximately 3 Å. Heterolysis of the H_2 molecule by Cu^{I} *tert*-butoxide in the presence of phosphine ligands in a THF solution leading to a hexameric Cu^{I}-hydride complex has been described.[46] This complex was shown to reduce α,β-unsaturated carbonyl compounds with high yields and selectivities.[47] Heterolytic cleavage of hydrogen was also observed, for instance, for a Fe^{II} complex that served as a model for the hydrogenase enzyme,[48] as well as for some other transition-metal ions such as Co^{II}, Mn^{I}, Mo^{III}, Re^{I}, Ru^{I}, Ir^{II}, Pd^{II}, and Pt^{II}.[49] To the best of our knowledge, the heterogeneous reaction of **5-F** with hydrogen represents the first example for the heterolytic cleavage of a H_2 molecule on single-site active centers within a metal–organic framework.

Conclusion

Post-synthetic metal and side-ligand exchange reactions enable the preparation of a large variety of MFU-4*l* derivatives with the general formula $[M_xZn_{(5-x)}(L)_yCl_{(4-y)}(BTDD)_3]$, in which M = Mn^{II}, Fe^{II}, Co^{II}, Ni^{II}, Cu^{II}, and L = NO_2^-, NO_3^-, $CF_3SO_3^-$, N_3^-, NCO^-, $HCOO^-$, CH_3COO^-, and F^-. The possibilities and limitations of this approach are shown in the manuscript. Several of

thus-prepared MFU-4*l* derivatives show high catalytic activity in a liquid-phase oxidation of ethylbenzene to acetophenone with air under mild conditions, among which Co- and Cu derivatives with chloride side-ligands are the most active. Further thermal transformations of the side ligands in the gas phase, such as the decomposition of formate, conversion of azide to isocyanate, and removal of fluoride can be performed selectively without destroying the framework. Thermal conversion of Co^{II}-azide units in the SBU of Co-MFU-4*l* involves the formation of a nitrene intermediate, which is potentially interesting as an N-atom transfer reagent. Treatment of Cu^{II}-fluoride units with H_2 at 240 °C leads to Cu^{I} and proceeds through the heterolytic cleavage of the H_2 molecule, showing the potential of Cu^{II}-MFU-4*l*-fluoride as a catalyst for hydrogenation reactions. Thus, combined with its robustness, the MFU-4*l* family represents a modular "construction kit", which allows fine adjustments of the framework properties and can be suggested for different applications such as catalysis, sensing, gas capture, storage, and separation. Further studies on MFU-4*l* derivatives should be highly rewarding in terms of searching for new functional porous materials.

Experimental Section

General procedures

All starting materials were of reagent grade and used as received from the commercial supplier. [Tp*Co(OAc)] was prepared according to the literature procedure.[28] Fourier transform infrared (FTIR) spectra were recorded with an ATR unit in the range 4000–180 cm^{-1} on a Bruker Equinox 55 FTIR spectrometer. Diffuse reflectance UV/Vis-NIR spectra were recorded in the range 2000–250 nm on a PerkinElmer λ 750 s spectrometer equipped with a Labsphere 60 mm RSA ASSY integrating sphere with 0°/d measuring geometry. Labsphere Spectralon SRS-99 was used as a white standard. Thermogravimetric analyses (TGA) were performed with a TA Instruments Q500 analyzer in the temperature range of 25–900 °C in flowing nitrogen gas at the heating rate of 5 K min^{-1}. TG/MS measurements were performed with the same instrument combined with the Hiden QIC-20 gas analysis system. Energy-dispersive X-ray spectroscopy (EDX) was performed with a Philips XL 30 scanning electron microscope. An area of at least 10×10 μm including at least 10 MOF crystals was scanned. Elemental analyses were measured with a Vario EL III instrument from Elementar Analysensysteme GmbH. GC/MS measurements were performed on a Hewlett Packard GC System 6890 Series equipped with Rtx-5MS column and mass selective detector MSD 5973. N_2 adsorption isotherms for the determination of BET surface areas were measured at 77 K in the relative pressure range 0.01–0.45 with a Quantachrome NOVA 2000 Series instrument. O_2 and Ar adsorption isotherms were measured with a BELSORP-max instrument combined with a BELCryo system. Adsorbed amounts are given in $cm^3 g^{-1}$ [STP], in which STP = 101.3 kPa and 273.15 K. Powder X-ray diffraction data were collected in the 2θ range of 4–70° with 0.02° steps, with a time of 200 s per step, by using a Seifert XRD 3003 TT diffractometer equipped with Meteor 1D detector. All DFT calculations have been performed with the all-electron full-potential code FHI-aims.[50] Electronic exchange and correlation was treated on the level of the generalized gradient approximation (GGA) PBE functional[51] for the geometry optimizations and on the level of the hybrid B3LYP functional[52] for consecutive single-point calculations on these optimized geometries. Dispersive interactions lacking at these levels of theory were considered through the dispersion-correction scheme according to Tkatchenko and Scheffler.[53] Geometry optimization was performed using tight, tier1 basis sets until residual forces fell below 10^{-4} eV $Å^{-1}$. Hybrid B3LYP + TS energetics are the finally presented numbers in the paper. Reaction barriers presented in the paper were obtained through calculations of the potential energy of the system going from initial to final state by having one constraint-fixed distance along the main reaction coordinate.

Syntheses

Preparation of lithium salts: A lithium formate solution in MeOH was prepared as described previously.[15] Methanolic solutions of $LiNO_2$, LiN_3, and LiNCO were prepared by the following general procedure: LiCl (4.24 g, 100 mmol) and $NaNO_2$, NaN_3 or NaNCO (115 mmol) were stirred under reflux in methanol (100 mL) for 16 h. After cooling to RT, the precipitate was filtered off and the resulting approximately 1 M methanolic solution of $LiNO_2$, LiN_3, or LiNCO was used for further transformations.

General procedure for the metal exchange in MFU-4*l*: Metal(II) chloride ($MnCl_2{\cdot}4H_2O$, $FeCl_2{\cdot}4H_2O$, $NiCl_2{\cdot}6H_2O$, $CoCl_2$ or $CuCl_2$, 32.5 mmol) was dissolved in *N*,*N*-dimethylformamide (for $FeCl_2$) or *N*,*N*-dimethylacetamide (130 mL) and MFU-4*l* (0.8 g, 0.634 mmol) was added to the solution. The reaction mixture was heated for 20 h at 60 °C in a sealed tube. In the case of $FeCl_2$, the reaction was performed at 50 °C under an Ar atmosphere. The precipitate was filtered off, washed with DMF or DMA, methanol and dichloromethane and dried at 150 °C under vacuum. The yield is close to quantitative. The number of M^{2+} ions in the formula unit was calculated from the M/Zn ratio determined by EDX analysis. All products are hygroscopic and may contain variable amounts of adsorbed water.

Mn_2-MFU-4*l* (1): Pale-yellow powder. Number of Mn^{2+} ions in the formula unit: 1.86; IR (ATR): $\tilde{\nu}$ = 3076 (w), 1577 (w), 1460 (s), 1349 (s), 1239 (w), 1218 (m), 1198 (m), 1170 (s), 919 (m), 869 (m), 816 (w), 531 (m), 428 cm^{-1} (w); BET surface area (Ar, 87.3 K): 3512 $m^2 g^{-1}$; elemental analysis calcd (%) for $C_{36}H_{12}Cl_4N_{18}O_6Mn_2Zn_3$: C 34.86, H 0.98, N 20.33; found: C 34.59, H 1.23, N 20.12.

Fe_2-MFU-4*l* (2): Yellow powder. Number of Fe^{2+} ions in the formula unit: 1.50; IR (ATR): $\tilde{\nu}$ = 3078 (w), 1577 (w), 1461 (s), 1351 (s), 1239 (w), 1219 (m), 1203 (m), 1174 (s), 920 (m), 869 (m), 817 (w), 532 (m), 429 cm^{-1} (w); UV/Vis-NIR: λ_{max} = 335, 1385 nm; BET surface area (Ar, 87.3 K): 3470 $m^2 g^{-1}$; elemental analysis calcd (%) for $C_{36}H_{12}Cl_4N_{18}O_6Fe_{1.5}Zn_{3.5}$: C 34.67; H 0.97; N 20.22; found: C 34.25; H 1.49; N 20.06.

Co_3-MFU-4*l* (3): Green-blue powder. Number of Co^{2+} ions in the formula unit: 3.13. IR (ATR): $\tilde{\nu}$ = 3078 (w), 1576 (w), 1460 (s), 1351 (s), 1239 (w), 1220 (m), 1204 (m), 1173 (s), 919 (m), 869 (m), 818 (w), 533 (m), 429 cm^{-1} (w); BET surface area (N_2, 77.3 K): 3639 $m^2 g^{-1}$; elemental analysis calcd (%) for $C_{36}H_{12}Cl_4N_{18}O_6Co_3Zn_2$: C 34.81, H 0.97, N 20.30; found: C 34.74, H 1.23, N 20.09.

Ni_2-MFU-4*l* (4): Red powder. Number of Ni^{2+} ions in the formula unit: 2.13. IR (ATR): $\tilde{\nu}$ = 3079 (w), 1576 (w), 1460 (s), 1350 (s), 1242 (w), 1212 (m), 1187 (s), 1062 (w), 920 (m), 869 (m), 808 (w), 535 (m), 429 cm^{-1} (w); UV/Vis-NIR, with DMA: λ_{max} = 630, 1039, 1952 nm; dry: λ_{max} = 386, 475, 547, 804, 905, 1743 nm; BET surface area (Ar, 87.3 K): 3290 $m^2 g^{-1}$; elemental analysis calcd (%) for $C_{36}H_{12}Cl_4N_{18}O_6Ni_2Zn_3{\cdot}2H_2O$: C 33.68, H 1.26, N 19.64; found: C 33.52, H 1.33, N 19.45.

General procedures for the side-ligand exchange in heterometallic MFU-4*l* derivatives: a) *Formates, acetates, nitrates, and tri-*

flates: MFU-4*l* derivative (150 mg, approx. 0.12 mmol) was stirred with 0.2 M solution of lithium salt (HCOOLi, LiOAc, $LiNO_3$, or LiOTf) in methanol (50 mL, 10 mmol) for 30 min at RT. The precipitate was filtered off, washed with methanol and CH_2Cl_2 and dried at 80 °C under vacuum. In the case of triflate, the exchange procedure was repeated twice. b) *Nitrites, azides and isocyanates*: 1 M solution of lithium salt ($LiNO_2$, LiN_3, or LiNCO) in methanol (0.6 mL, 0.6 mmol) was added to a suspension of MFU-4*l* derivative (150 mg, approx. 0.12 mmol) in acetonitrile (30 mL) and the mixture was stirred for 30 min at RT. The precipitate was filtered off, washed with methanol and CH_2Cl_2, and dried at 80 °C under vacuum. *c) Fluorides*: MFU-4*l* derivative (150 mg, approx. 0.12 mmol) was added to a solution of CsF (91 mg, 0.6 mmol) in methanol (30 mL) and the mixture was stirred for 30 min at RT. The precipitate was filtered off, washed with methanol and CH_2Cl_2, and dried at 150 °C under vacuum. The yield is in all cases close to quantitative. The substitution degree of chloride ligands was calculated from the Zn/M/Cl atomic ratio, determined by EDX analysis.

Co-MFU-4*l*-nitrite (6-NO_2): Purple powder. Zn/Co/Cl ratio: 1.33:3.67:0.48. IR (ATR): $\tilde{\nu}$ = 3095 (w), 1576 (m), 1462 (s), 1348 (s), 1171 (s), 1131 (m), 921 (m), 853 (w), 817 (w), 533 (m), 425 (w), 326 (w), 301 (m), 224 cm^{-1} (s); UV/Vis-NIR: λ_{max} = 371, 575, 745, 975, 1460 nm; BET surface area (Ar, 87.3 K): 3066 $m^2 g^{-1}$.

Co-MFU-4*l*-nitrate (6-NO_3): Purple powder. Zn/Co/Cl ratio: 1.12:3.88:0.19. IR (ATR): $\tilde{\nu}$ = 1568 (m), 1461 (s), 1348 (s), 1240 (w), 1171 (s), 989 (w), 921 (m), 852 (w), 805 (w), 533 (m), 428 (w), 352 (w), 301 (m), 278 (m), 246 (m), 226 cm^{-1} (s); UV/Vis-NIR: λ_{max} = 366, 566, 721, 954, 1441 nm; BET surface area (Ar, 87.3 K): 3049 $m^2 g^{-1}$.

Co-MFU-4*l*-triflate (6-OTf): Purple powder. Zn/Co/Cl ratio: 1.19:3.81:0.51. IR (ATR): $\tilde{\nu}$ = 1577 (m), 1461 (s), 1348 (s), 1235 (m), 1174 (s), 1028 (m), 921 (m), 854 (w), 805 (w), 764 (w), 639 (m), 576 (w), 532 (m), 429 (w), 353 (w), 302 (m), 280 (m), 228 cm^{-1} (s); UV/Vis-NIR: λ_{max} = 354, 574, 754, 1391 nm; BET surface area (Ar, 87.3 K): 2603 $m^2 g^{-1}$.

Co-MFU-4*l*-formate (6-HCOO): Purple powder. Zn/Co/Cl ratio: 0.88:4.12:0.05; IR (ATR): $\tilde{\nu}$ = 3098 (w), 1577 (s), 1460 (s), 1348 (s), 1299 (m), 1242 (m), 1171 (s), 921 (m), 851 (w), 803 (w), 532 cm^{-1} (m); UV/Vis-NIR: λ_{max} = 363, 561, 756, 1051, 1448 nm; BET surface area (Ar, 87.3 K): 2805 $m^2 g^{-1}$.

Co-MFU-4*l*-azide (6-N_3): Blue powder. Zn/Co/Cl ratio: 1.01:3.99:0.23. IR (ATR): $\tilde{\nu}$ = 3078 (w), 2068 (s), 1575 (m), 1461 (s), 1349 (s), 1219 (w), 1199 (m), 1169 (s), 919 (m), 862 (w), 818 (w), 533 (m), 442 (m), 353 (w), 304 (m), 280 (m), 246 (m), 226 cm^{-1} (s); UV/Vis-NIR: λ_{max} = 389, 563, 612, 659, 854, 1347 nm; BET surface area (Ar, 77.3 K): 2252 $m^2 g^{-1}$.

Co-MFU-4*l*-acetate (6-OAc): Purple powder. Zn/Co/Cl ratio: 0.89:4.11:0.04. IR (ATR): $\tilde{\nu}$ = 3095 (w), 1575 (s), 1460 (s), 1347 (s), 1240 (w), 1173 (s), 920 (m), 851 (w), 815 (w), 688 (m), 619 (w), 532 cm^{-1} (m); BET surface area (N_2, 77.3 K): 2601 $m^2 g^{-1}$.

Co-MFU-4*l*-isocyanate (6-NCO): Blue powder. Zn/Co/Cl ratio: 0.96:4.04:2.28. IR (ATR): $\tilde{\nu}$ = 3095 (w), 2217 (m), 1576 (s), 1460 (s), 1347 (s), 1170 (s), 919 (m), 855 (w), 805 (w), 532 (m), 427 (m), 384 (w), 303 (m), 225 cm^{-1} (s); UV/Vis-NIR: λ_{max} = 602, 856, 1383 nm; BET surface area (N_2, 77.3 K): 1649 $m^2 g^{-1}$.

Mn_2-MFU-4*l*-formate (1-HCOO): Pale-yellow powder. Zn/Mn/Cl ratio: 2.78:2.22:0.74. IR (ATR): $\tilde{\nu}$ = 3093 (w), 1577 (s), 1461 (s), 1348 (s), 1216 (m), 1195 (m), 1168 (s), 921 (m), 854 (m), 807 (w), 531 (m), 427 cm^{-1} (w); BET surface area (N_2, 77.3 K): 3352 $m^2 g^{-1}$.

Fe_2-MFU-4*l*-formate (2-HCOO): Yellow powder. Zn/Fe/Cl ratio: 3.54:1.46:0.87. IR (ATR): $\tilde{\nu}$ = 3095 (w), 1577 (s), 1461 (s), 1349 (s), 1200 (m), 1173 (s), 921 (m), 854 (w), 805 (w), 532 (m), 426 cm^{-1} (w); UV/Vis-NIR: λ_{max} = 968, 1728 nm; BET surface area (N_2, 77.3 K): 3306 $m^2 g^{-1}$.

Ni_2-MFU-4*l*-formate (4-HCOO): Green powder. Zn/Ni/Cl ratio: 2.84:2.16:0.72. IR (ATR): $\tilde{\nu}$ = 3099 (w), 1577 (s), 1461 (s), 1351 (s), 1303 (w), 1244 (w), 1182 (s), 922 (m), 865 (w), 816 (w), 535 cm^{-1} (m); UV/Vis-NIR: λ_{max} = 417, 523, 997 nm; BET surface area (N_2, 77.3 K): 3246 $m^2 g^{-1}$.

Mn_2-MFU-4*l*-fluoride (1-F): Pale-yellow powder. Zn/Mn/Cl ratio: 3.20:1.80:1.26. IR (ATR): $\tilde{\nu}$ = 3078 (w), 1577 (w), 1460 (s), 1349 (s), 1171 (s), 919 (m), 868 (w), 815 (w), 578 (w), 530 (m), 478 (w), 428 cm^{-1} (w); BET surface area (N_2, 77.3 K): 3148 $m^2 g^{-1}$.

Fe_2-MFU-4*l*-fluoride (2-F): Orange-grey powder. Zn/Fe/Cl ratio: 3.59:1.41:2.46. IR (ATR): $\tilde{\nu}$ = 3079 (w), 1577 (w), 1460 (s), 1350 (s), 1239 (m), 1204 (m), 1177 (s), 920 (m), 868 (m), 817 (w), 532 (m), 429 cm^{-1} (w); UV/Vis-NIR: λ_{max} = 372 nm; BET surface area (Ar, 87.3 K): 3505 $m^2 g^{-1}$.

Ni_2-MFU-4*l*-fluoride (4-F): Pale-red powder, turns quickly to pale green in air. Zn/Ni/Cl ratio: 2.86:2.14:1.93. IR (ATR): $\tilde{\nu}$ = 3079 (w), 1576 (w), 1461 (s), 1351 (s), 1240 (w), 1183 (s), 1061 (w), 920 (m), 868 (w), 808 (w), 534 cm^{-1} (m); UV/Vis-NIR: λ_{max} = 697, 868 nm; BET surface area (N_2, 77.3 K): 2977 $m^2 g^{-1}$.

Cu_2-MFU-4*l*-fluoride (5-F): Green-grey powder. Zn/Cu/Cl ratio: 2.84:2.16:1.72. IR (ATR): $\tilde{\nu}$ = 3080 (w), 1576 (w), 1460 (s), 1349 (s), 1179 (s), 919 (s), 868 (m), 808 (m), 533 (m), 428 cm^{-1} (w); UV/Vis-NIR: λ_{max} = 353, 763, 1054 nm; BET surface area (N_2, 77.3 K): 3480 $m^2 g^{-1}$.

Co-MFU-4*l*-fluoride (6-F): Blue-violet powder. Zn/Co/Cl ratio: 1.04:3.96:0.34. IR (ATR): $\tilde{\nu}$ = 3078 (w), 1576 (w), 1460 (s), 1348 (s), 1171 (s), 917 (s), 867 (m), 805 (w), 594 (m), 532 (m), 429 cm^{-1} (w); UV/Vis-NIR: λ_{max} = 359, 547, 645, 834, 1361 nm; BET surface area (N_2, 77.3 K): 2524 $m^2 g^{-1}$.

General procedure for the catalytic oxidation of ethylbenzene: MFU-4*l* derivative (0.1 mmol, based on Mn, Fe, Co, Ni or Cu centers) was added to a solution of ethylbenzene (1.06 g, 10 mmol), *N*-hydroxyphthalimide (163 mg, 1 mmol) and 1,2,4-trichlorobenzene (907 mg, 5 mmol, used as a standard) in acetonitrile/water (98:2) mixture (30 mL) and the mixture was stirred at 40 °C. The conversion was followed by GC/MS. For analysis, 0.1 mL of mixture was filtered through a short pad of neutral Al_2O_3, which was then eluted with Et_2O/CH_2Cl_2/MeOH (10:10:1) mixture. Each analysis was repeated three times. In the case of **5** and **6**, the catalyst was filtered off after the reaction, washed with acetonitrile, DMF, methanol, and CH_2Cl_2, and dried in vacuum. EDX analysis of **5**: Zn/Cu/Cl ratio: 2.81:2.19:2.78. EDX analysis of **6**: Zn/Co/Cl ratio: 0.99:4.01:1.95.

Thermal transformations of MFU-4*l*-formates under N_2: MFU-4*l*-formates (approx. 10 mg) were heated under N_2 gas flow (90 mL min^{-1}) up to 300–350 °C with a heating rate 5 K min^{-1} using a TA Instruments Q500 analyzer and kept at this temperature for 15 min.

Thermal transformations of 6-HCOO and 6-N_3 under CO: Framework **6-HCOO** or **6-N_3** (approx. 5 mg) was heated under CO/Ar (1/9) gas flow (50 mL min^{-1}) up to 325 or 300 °C, respectively, with a heating rate 5 K min^{-1} using a Netzsch STA 409 simultaneous thermal analyzer and kept at this temperature for 15 min.

Preparation of Cu^I-MFU-4*l* through the solvothermal reduction of 5 in DMF: Framework **5** (150 mg) was heated in DMF (25 mL) for 10 h at 140 °C in a sealed tube (until the green color of a solid has disappeared completely). The yellow precipitate was filtered off, washed with DMF, methanol, and dichloromethane and dried at 150 °C under vacuum. Yield 140 mg. Zn/Cu/Cl ratio: 2.43:2.57:2.17. IR (ATR): $\tilde{\nu}$ = 3079 (w), 1577 (w), 1462 (s), 1351 (s),

1204 (m), 1176 (s), 918 (m), 869 (w), 838 (w), 817 (w), 534 (m), 427 cm^{-1} (w); BET surface area (Ar, 87.3 K): 2615 $m^2 g^{-1}$.

Preparation of Cu^I-MFU-4*l* from MFU-4*l* through metal exchange: Copper (I) chloride (149 mg, 1.5 mmol) and lithium chloride (191 mg, 4.5 mmol)) were stirred under nitrogen in *N*,*N*-dimethylacetamide (30 mL) for 1 h at RT. Undissolved CuCl was filtered off through a syringe filter and MFU-4*l* (100 mg, 0.08 mmol) was added to the solution. The reaction mixture was heated for 20 h at 60 °C in a sealed tube. The pale-brown precipitate was filtered off, washed with *N*,*N*-dimethylacetamide, methanol and dichloromethane and dried at 150 °C under vacuum. Zn/Cu/Cl ratio: 3.96:1.04:3.08. IR (ATR): $\tilde{\nu}$ = 3080 (w), 1576 (w), 1461 (s), 1350 (s), 1174 (s), 917 (m), 867 (w), 813 (w), 534 (m), 427 cm^{-1} (w); BET surface area (Ar, 87.3 K): 3944 $m^2 g^{-1}$.

Preparation of Cu^I-MFU-4*l* through the heterogeneous reaction of 5-F with H_2: Framework **5-F** (approx. 10 mg) was heated under H_2/Ar (1:9) gas flow (90 mL min^{-1}) up to 240 °C with a heating rate 5 K min^{-1} using a TA Instruments Q500 analyzer and kept at this temperature for 15 min. A dark-grey powder was obtained. IR (ATR): $\tilde{\nu}$ = 3081 (w), 1577 (w), 1461 (s), 1350 (s), 1175 (s), 1051 (w), 918 (m), 868 (w), 816 (w), 534 (m), 426 cm^{-1} (w); BET surface area (Ar, 87.3 K): 3682 $m^2 g^{-1}$; elemental analysis calcd (%) for $C_{36}H_{12}Cl_2N_{18}O_{10}Cu_2Zn_3$ (Cu^I-MFU-4*l*·2 O_2): C 34.57, H 0.97, N 20.16; found: C 34.68, H 1.19, N 20.35.

Heterogeneous reaction of 5 with H_2: Framework **5** (approx. 10 mg) was heated under H_2/Ar (1:9) gas flow (90 mL min^{-1}) up to 350 °C with a heating rate 5 K min^{-1} using a TA Instruments Q500 analyzer and kept at this temperature for 15 min. A dark-grey powder was obtained. BET surface area (Ar, 87.3 K): 2078 $m^2 g^{-1}$; elemental analysis calcd (%) for $C_{36}H_{12}Cl_2N_{18}O_{10}Cu_2Zn_3$ (Cu^I-MFU-4*l*·2 O_2): C 34.57, H 0.97, N 20.16; found: C 35.26; H 1.20; N 18.95.

Thermal decomposition of 5 under N_2: Framework **5** (approx. 10 mg) was heated under N_2 gas flow (90 mL min^{-1}) up to 400 °C with a heating rate 5 K min^{-1} using a TA Instruments Q500 analyzer and kept at this temperature for 15 min. A dark-grey powder was obtained. BET surface area (Ar, 87.3 K): 2054 $m^2 g^{-1}$; elemental analysis calcd (%) for $C_{36}H_{12}Cl_2N_{18}O_{10}Cu_2Zn_3$ (Cu^I-MFU-4*l*·2 O_2): C 34.57, H 0.97, N 20.16; found: C 35.05, H 1.13, N 18.30.

Acknowledgements

We gratefully acknowledge funding by the priority program 1362 "Porous Metal-Organic Frameworks (MOFs)" of the Deutsche Forschungsgemeinschaft (DFG).

Keywords: heterogeneous catalysis · hydrogen · ligands · metal–organic frameworks · transition metals

[1] H. Furukawa, K. E. Cordova, M. O'Keeffe, O. M. Yaghi, *Science* **2013**, *341*, 1230444.
[2] a) K. Sumida, D. L. Rogow, J. A. Mason, T. M. McDonald, E. D. Bloch, Z. R. Herm, T.-H. Bae, J. R. Long, *Chem. Rev.* **2012**, *112*, 724–781; b) E. Barea, C. Montoro, J. A. R. Navarro, *Chem. Soc. Rev.* **2014**, *43*, 5419–5430.
[3] a) J.-R. Li, J. Sculley, H.-C. Zhou, *Chem. Rev.* **2012**, *112*, 869–932; b) M. P. Suh, H. J. Park, T. K. Prasad, D.-W. Lim, *Chem. Rev.* **2012**, *112*, 782–835; c) Y. Peng, V. Krungleviciute, I. Eryazici, J. T. Hupp, O. K. Farha, T. Yildirim, *J. Am. Chem. Soc.* **2013**, *135*, 11887–11894.
[4] a) J. Gascon, A. Korma, F. Kapteijn, F. X. L. i. Xamena, *ACS Catal.* **2014**, *4*, 361–378; b) J. Liu, L. Chen, H. Cui, J. Zhang, L. Zhang, C.-Y. Su, *Chem. Soc. Rev.* **2014**, *43*, 6011–6061; c) Z.-Y. Gu, J. Park, A. Raiff, Z. Wei, H.-C. Zhou, *ChemCatChem* **2014**, *6*, 67–75; d) K. Leus, Y.-Y. Liu, P. Van Der Voort, *Catal. Rev.* **2014**, *56*, 1–56; e) P. García-García, M. Müller, A. Corma, *Chem. Sci.* **2014**, *5*, 2979–3007.
[5] L. E. Kreno, K. Leong, O. K. Farha, M. Allendorf, R. P. Van Duyne, J. T. Hupp, *Chem. Rev.* **2012**, *112*, 1105–1125.
[6] Y. Cui, Y. Yue, G. Qian, B. Chen, *Chem. Rev.* **2012**, *112*, 1126–1162.
[7] W. Zhang, R.-G. Xiong, *Chem. Rev.* **2012**, *112*, 1163–1195.
[8] C. Wang, T. Zhang, W. Lin, *Chem. Rev.* **2012**, *112*, 1084–1104.
[9] P. Horcajada, R. Gref, T. Baati, P. K. Allan, G. Maurin, P. Couvreur, G. Férey, R. E. Morris, C. Serre, *Chem. Rev.* **2012**, *112*, 1232–1268.
[10] S. M. Cohen, *Chem. Rev.* **2012**, *112*, 970–1000.
[11] J. D. Evans, C. J. Sumby, C. J. Doonan, *Chem. Soc. Rev.* **2014**, *43*, 5933–5951.
[12] a) Y. Han, J.-R. Li, Y. Xie, G. Guo, *Chem. Soc. Rev.* **2014**, *43*, 5952–5981; b) P. Deria, J. E. Mondloch, O. Karagiaridi, W. Bury, J. T. Hupp, O. K. Farha, *Chem. Soc. Rev.* **2014**, *43*, 5896–5912.
[13] C. K. Brozek, M. Dincâ, *Chem. Soc. Rev.* **2014**, *43*, 5456–5467.
[14] D. Denysenko, T. Werner, M. Grzywa, A. Puls, V. Hagen, G. Eickerling, J. Jelic, K. Reuter, D. Volkmer, *Chem. Commun.* **2012**, *48*, 1236–1238.
[15] D. Denysenko, M. Grzywa, J. Jelic, K. Reuter, D. Volkmer, *Angew. Chem. Int. Ed.* **2014**, *53*, 5832–5836.
[16] D. Denysenko, M. Grzywa, M. Tonigold, B. Streppel, I. Krkljus, M. Hirscher, E. Mugnaioli, U. Kolb, J. Hanss, D. Volkmer, *Chem. Eur. J.* **2011**, *17*, 1837–1848.
[17] C. K. Brozek, L. Bellarosa, T. Soejima, T. V. Klark, N. López, M. Dincâ, *Chem. Eur. J.* **2014**, *20*, 6871–6874.
[18] S. Biswas, M. Grzywa, H. P. Nayek, S. Dehnen, I. Senkovska, S. Kaskel, D. Volkmer, *Dalton Trans.* **2009**, 6487–6495.
[19] P. Schmieder, D. Denysenko, M. Grzywa, B. Baumgärtner, I. Senkovska, S. Kaskel, G. Sastre, L. van Wüllen, D. Volkmer, *Dalton Trans.* **2013**, *42*, 10786–10797.
[20] a) S. Biswas, M. Tonigold, D. Volkmer, *Z. Anorg. Allg. Chem.* **2008**, *634*, 2532–2538; b) S. Biswas, M. Tonigold, M. Speldrich, P. Kögerler, M. Weil, D. Volkmer, *Inorg. Chem.* **2010**, *49*, 7424–7434; c) Y.-Y. Liu, M. Grzywa, M. Tonigold, G. Sastre, T. Schüttrigkeit, N. S. Leeson, D. Volkmer, *Dalton Trans.* **2011**, *40*, 5926–5938.
[21] S. Trofimenko, *Chem. Rev.* **1993**, *93*, 943–980.
[22] a) A. Soleimani Dorcheh, D. Denysenko, D. Volkmer, W. Donner, M. Hirscher, *Microporous Mesoporous Mater.* **2012**, *162*, 64–68; b) A. Soleimani-Dorcheh, R. E. Dinnebier, A. Kuc, O. Magdysyuk, F. Adams, D. Denysenko, T. Heine, D. Volkmer, W. Donner, M. Hirscher, *Phys. Chem. Chem. Phys.* **2012**, *14*, 12892–12897; c) O. V. Magdysyuk, D. Denysenko, I. Weinrauch, D. Volkmer, M. Hirscher, R. E. Dinnebier, *Chem. Commun.* **2014**, *51*, 714–717.
[23] J. Teufel, H. Oh, M. Hirscher, M. Wahiduzzaman, L. Zhechkov, A. Kuc, T. Heine, D. Denysenko, D. Volkmer, *Adv. Mater.* **2013**, *25*, 635–639.
[24] A. B. P. Lever, in *Inorganic Electronic Spectroscopy*, 2nd ed., Elsevier, Amsterdam, **1984**.
[25] J. V. Quagliano, A. K. Banerjee, V. L. Goedken, L. M. Vallarino, *J. Am. Chem. Soc.* **1970**, *92*, 482–488.
[26] P. J. Desrochers, J. Telser, S. A. Zvyagin, A. Ozarowski, J. Krzystek, D. A. Vicic, *Inorg. Chem.* **2006**, *45*, 8930–8941.
[27] K. Fujisawa, H. Iwamoto, K. Tobita, Y. Miyashita, K.-i. Okamoto, *Inorg. Chim. Acta* **2009**, *362*, 4500–4509.
[28] S. Hikichi, Y. Sasakura, M. Yoshizawa, Y. Ohzu, Y. Moro-oka, M. Akita, *Bull. Chem. Soc. Jpn.* **2002**, *75*, 1255–1262.
[29] W. G. Jackson, A. M. Sargeson, in *Rearrangements in Ground and Excited States* (Ed.: P. de Mayo), Vol. 2, Academic Press, New York, **1980**, pp. 273–378.
[30] I. R. Beattie, D. P. N. Satchell, *Trans. Faraday Soc.* **1956**, *52*, 1590–1593.
[31] S. Thyagarajan, C. D. Incarvito, A. L. Rheingold, K. H. Theopold, *Inorg. Chim. Acta* **2003**, *345*, 333–339.
[32] D. J. Harding, P. Harding, R. Daengngern, S. Yimklan, H. Adams, *Dalton Trans.* **2009**, 1314–1320.
[33] J. A. Dunne, R. Mariwala, M. Rao, S. Sircar, R. J. Gorte, A. L. Myers, *Langmuir* **1996**, *12*, 5888–5895.
[34] J. Jelic, D. Denysenko, D. Volkmer, K. Reuter, *New J. Phys.* **2013**, *15*, 115004 .
[35] I. Hermans, L. Vereecken, P. A. Jacobs, J. Peeters, *Chem. Commun.* **2004**, 1140–1141.
[36] Y. Ishii, S. Sakaguchi, T. Iwahama, *Adv. Synth. Catal.* **2001**, *343*, 393–427.

[37] M. Tonigold, Y. Lu, A. Mavrandonakis, A. Puls, R. Staudt, J. Möllmer, J. Sauer, D. Volkmer, *Chem. Eur. J.* **2011**, *17*, 8671 – 8695.
[38] A. Dhakshinamoorthy, M. Alvaro, H. Garcia, *Chem. Eur. J.* **2011**, *17*, 6256 – 6262.
[39] S. Biswas, M. Maes, A. Dhakshinamoorthy, M. Feyand, D. E. De Vos, H. Garcia, N. Stock, *J. Mater. Chem.* **2012**, *22*, 10200 – 10209.
[40] O. M. Reinaud, K. H. Theopold, *J. Am. Chem. Soc.* **1994**, *116*, 6979 – 6980.
[41] R. A. Eikey, M. M. Abu-Omar, *Coord. Chem. Rev.* **2003**, *243*, 83 – 124.
[42] a) B. Hinnemann, J. K. Nørskov, *Top. Catal.* **2006**, *37*, 55 – 70; b) L. C. Seefeldt, B. M. Hoffman, D. R. Dean, *Annu. Rev. Biochem.* **2009**, *78*, 701 – 722.
[43] J. du Bois, C. S. Tomooka, J. Hong, E. M. Carreira, *Acc. Chem. Res.* **1997**, *30*, 364 – 372.
[44] C. C. Hojilla Atienza, A. C. Bowman, E. Lobkovsky, P. J. Chirik, *J. Am. Chem. Soc.* **2010**, *132*, 16343 – 16345.
[45] a) Y.-J. Kim, Y.-S. Kwak, S.-W. Lee, *J. Organomet. Chem.* **2000**, *603*, 152 – 160; b) D. Sellmann, F. Geipel, F. W. Heinemann, *Chem. Eur. J.* **2000**, *6*, 4279 – 4284.
[46] G. V. Goeden, K. G. Kaulton, *J. Am. Chem. Soc.* **1981**, *103*, 7354 – 7355.
[47] W. S. Mahoney, D. M. Brestensky, J. M. Stryker, *J. Am. Chem. Soc.* **1988**, *110*, 291 – 293.
[48] T. Liu, X. Wang, C. Hoffmann, D. L. DuBois, R. M. Bullock, *Angew. Chem. Int. Ed.* **2014**, *53*, 5300 – 5304; *Angew. Chem.* **2014**, *126*, 5404 – 5408.
[49] a) M. B. Mooiman, J. M. Pratt, *J. Chem. Soc. Chem. Commun.* **1981**, 33 – 34; b) E. B. Hulley, K. D. Welch, A. M. Appel, D. L. DuBois, R. M. Bullock, *J. Am. Chem. Soc.* **2013**, *135*, 11736 – 11739; c) R. A. Kinney, D. G. H. Hetterscheid, B. S. Hanna, R. R. Schrock, B. M. Hoffman, *Inorg. Chem.* **2010**, *49*, 704 – 713; d) G. J. Kubas, *Adv. Inorg. Chem.* **2004**, *56*, 127 – 177; e) K. Q. A. Leñero, Y. Guari, P. C. J. Kamer, P. W. N. M. van Leeuwen, B. Donnadieu, S. Sabo-Etienne, B. Chaudret, M. Lutz, A. L. Spek, *Dalton Trans.* **2013**, *42*, 6495 – 6512.
[50] a) V. Blum, R. Gehrke, F. Hanke, P. Havu, V. Havu, X, Ren, K. Reuter, M. Scheffler, *Comput. Phys. Commun.* **2009**, *180*, 2175 – 2196; b) X. Ren, P. Rinke, V. Blum, J. Wieferink, A. Tkatchenko, A. Sanfilippo, K. Reuter, M. Scheffler, *New J. Phys.* **2012**, *14*, 053020.
[51] J. P. Perdew, K. Burke, M. Ernzerhof, *Phys. Rev. Lett.* **1996**, *77*, 3865 – 3868.
[52] a) A. D. Becke, *J. Chem. Phys.* **1993**, *98*, 5648 – 5652; b) P. J. Stephens, J. F. Devlin, C. F. Chabalowski, M. J. Frisch, *J. Chem. Phys.* **1994**, *98*, 11623 – 11627.
[53] A. Tkatchenko, M. Scheffler, *Phys. Rev. Lett.* **2009**, *102*, 073005.

Received: December 19, 2014
Revised: March 11, 2015
Published online on April 16, 2015

CHEMISTRY
A European Journal

Supporting Information

Postsynthetic Metal and Ligand Exchange in MFU-4*l*: A Screening Approach toward Functional Metal–Organic Frameworks Comprising Single-Site Active Centers

Dmytro Denysenko,[a] Jelena Jelic,[b] Karsten Reuter,[b] and Dirk Volkmer*[a]

chem_201406564_sm_miscellaneous_information.pdf

Table of Contents

TGA and TG/MS measurements

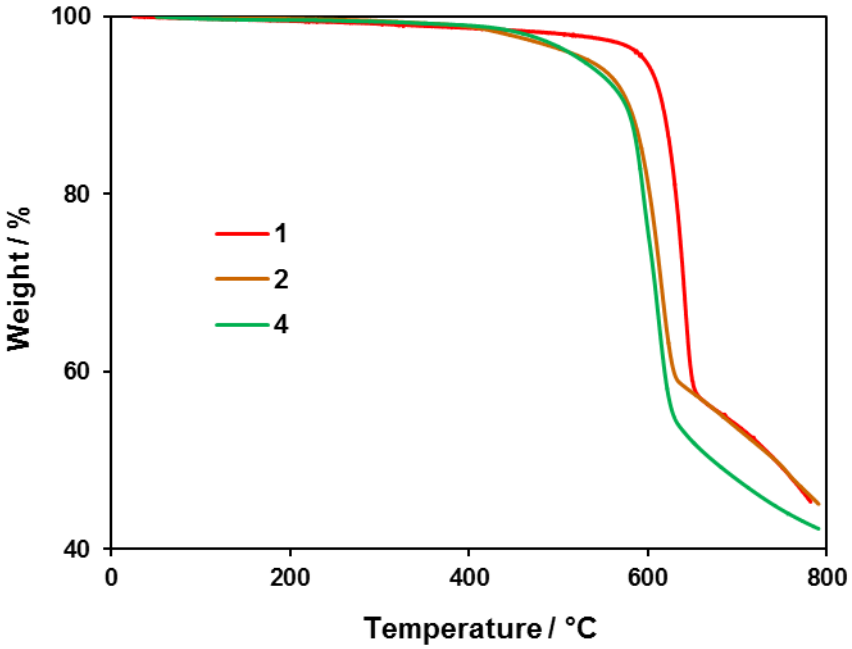

Figure S1. TGA curves for **1**, **2** and **4** under N_2 flow.

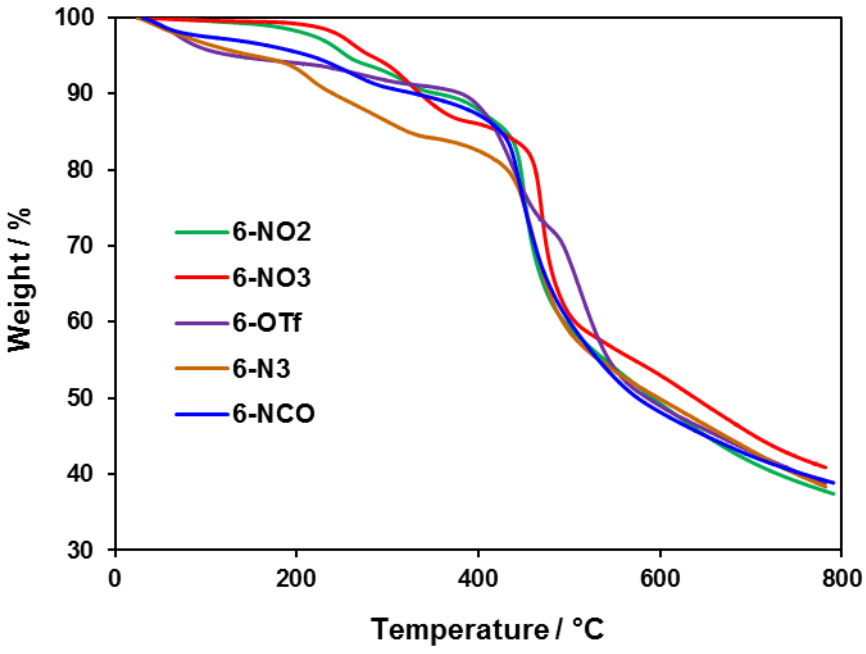

Figure S2. TGA curves for **6-NO_2**, **6-NO_3**, **6-OTf**, **6-N_3** and **6-NCO** under N_2 flow.

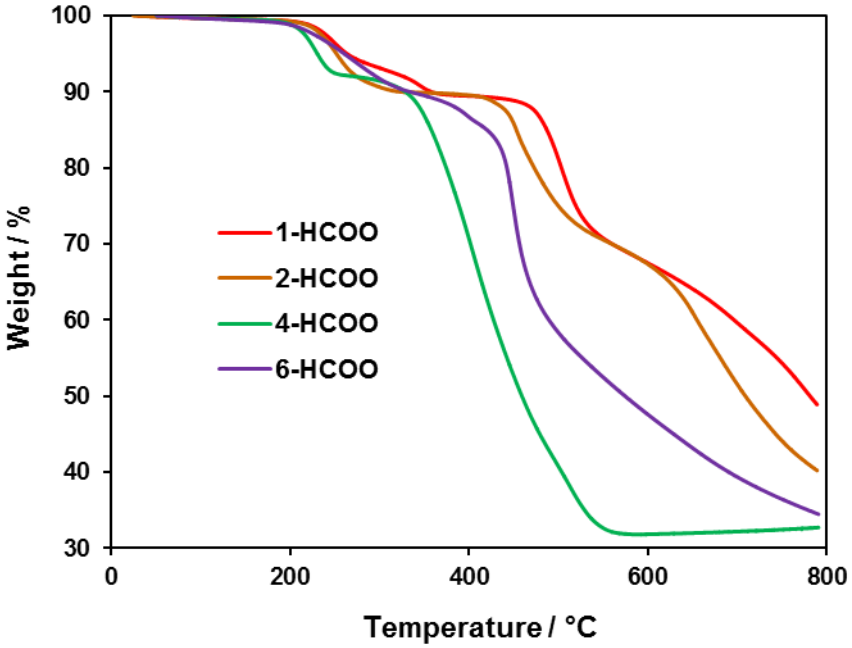

Figure S3. TGA curves for Mn-, Fe-, Ni- and Co-MFU-4*l*-formates under N_2 flow.

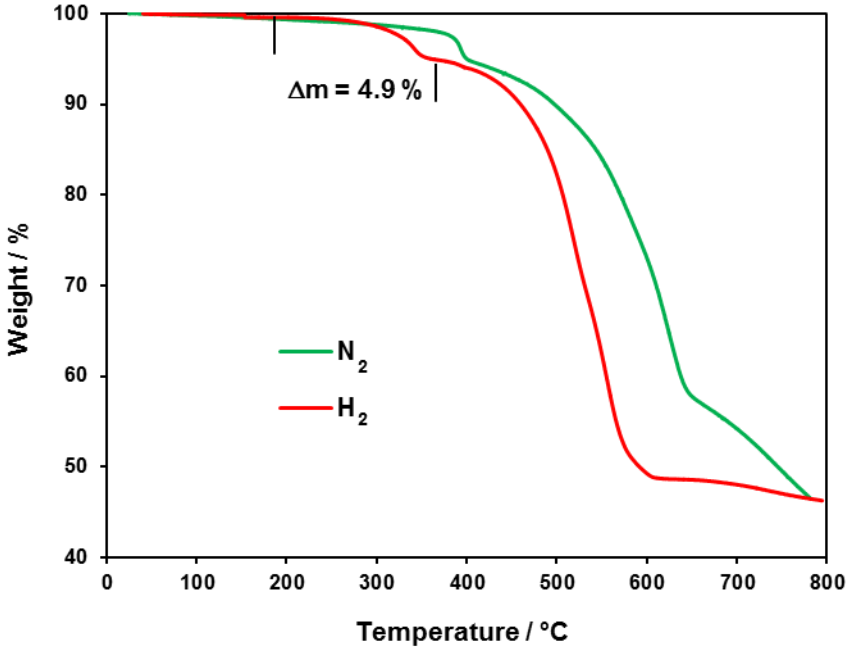

Figure S4. TGA curves for **5** under N_2 and H_2/Ar (1/9) flow.

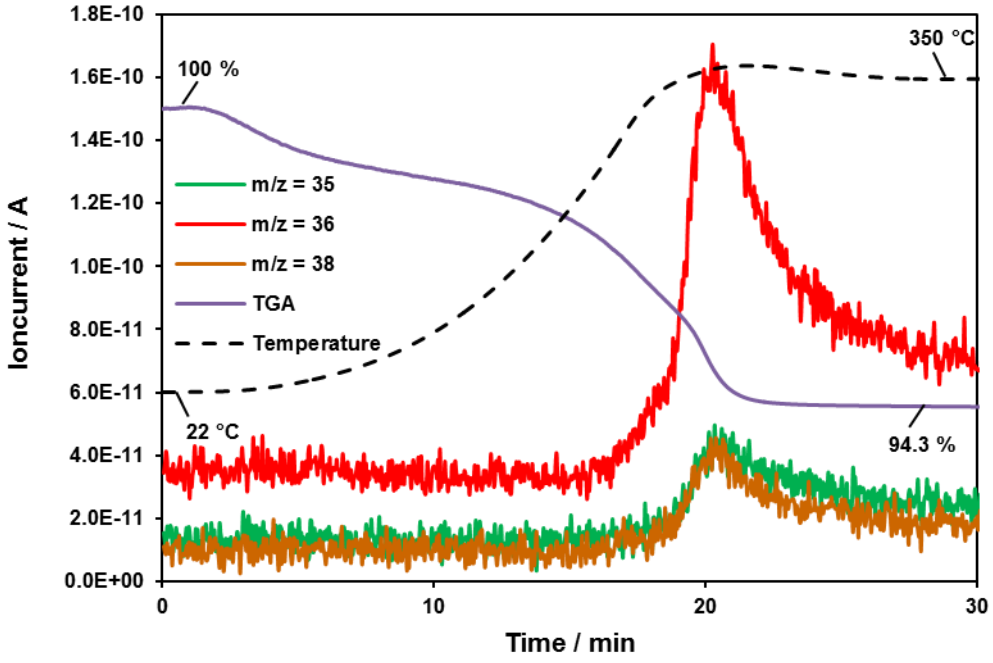

Figure S5. TG/MS curves for **5** under H_2/Ar (1/9) flow.

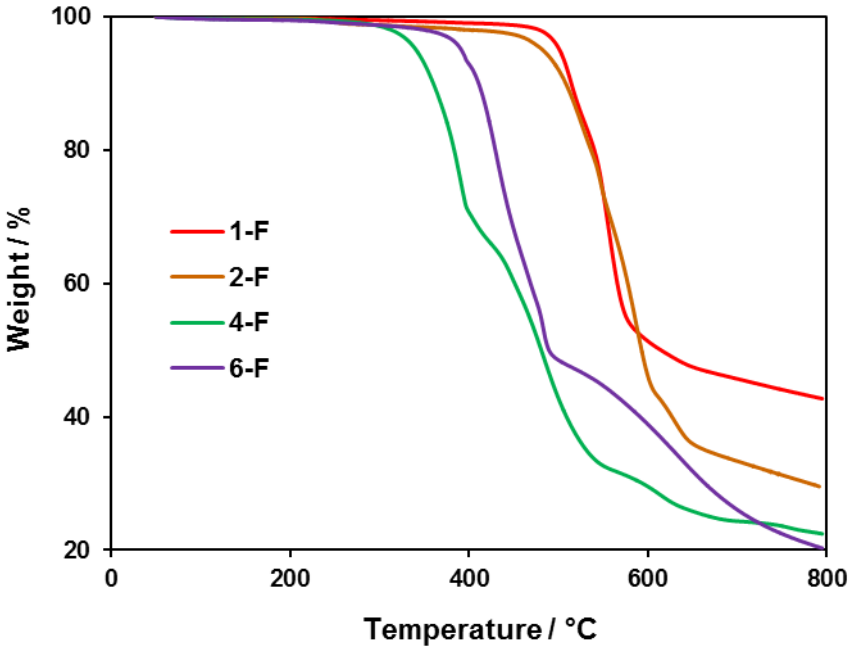

Figure S6. TGA curves for Mn-, Fe-, Ni- and Co-MFU-4*l*-fluorides under H_2/Ar (1/9) flow.

UV-vis-NIR Spectroscopy

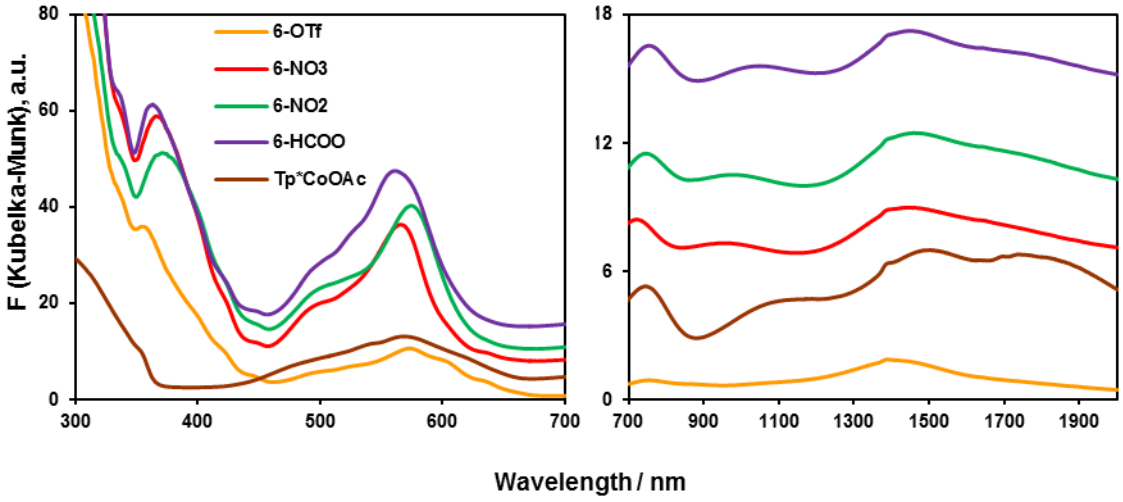

Figure S7. UV-vis-NIR spectra of different derivatives of **6** and of Tp*CoOAc as a reference compound.

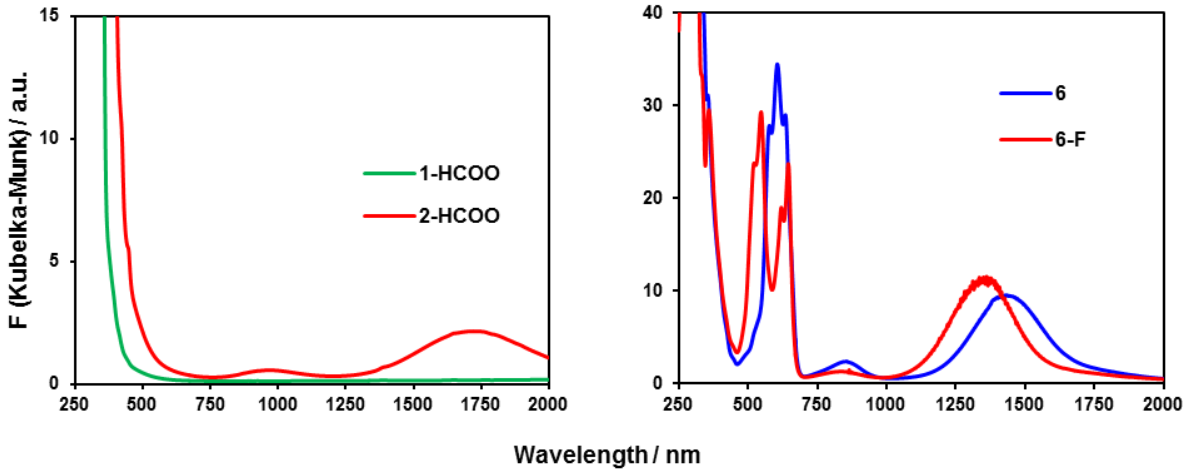

Figure S8. UV-vis-NIR spectra of Mn- and Fe-MFU-4*l*-formates (left) and Co-MFU-4*l* and Co-MFU-4*l*-fluoride (right).

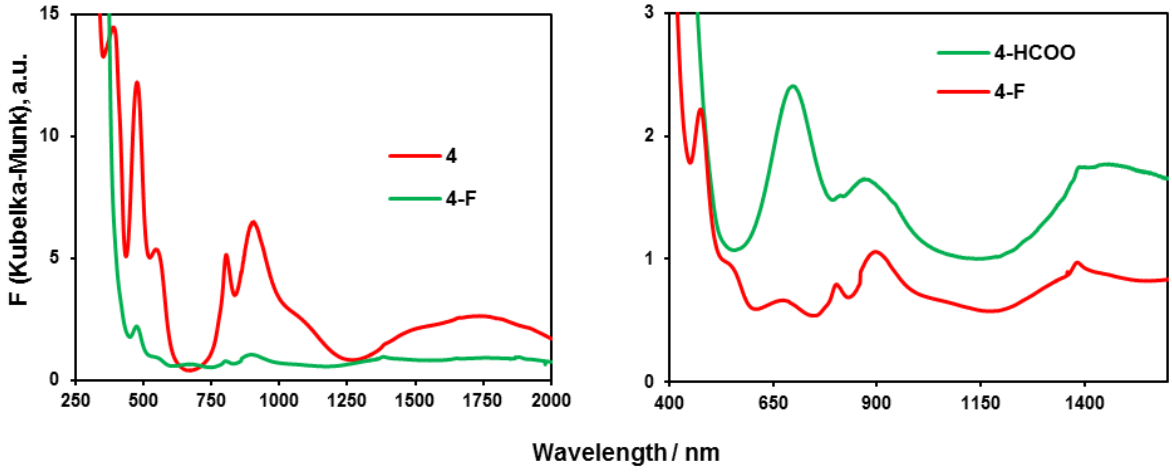

Figure S9. UV-vis-NIR spectra of Ni-MFU-4*l* and its fluoride- and formate-derivatives in comparison.

FT-IR Spectra

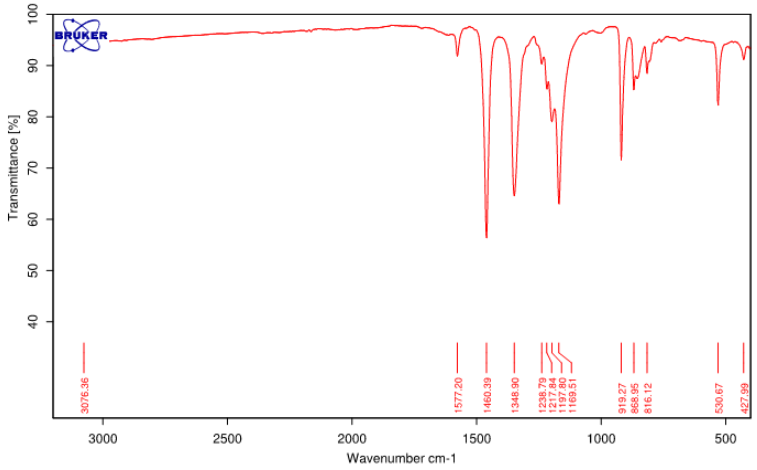

Figure S10. FT-IR spectrum of **1**.

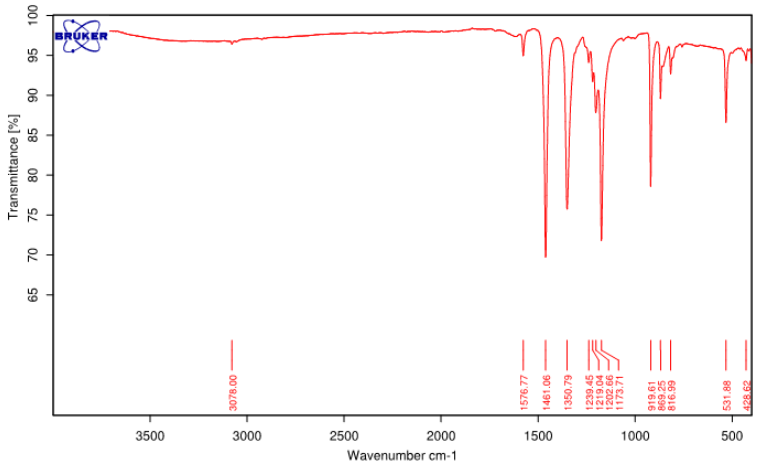

Figure S11. FT-IR spectrum of **2**.

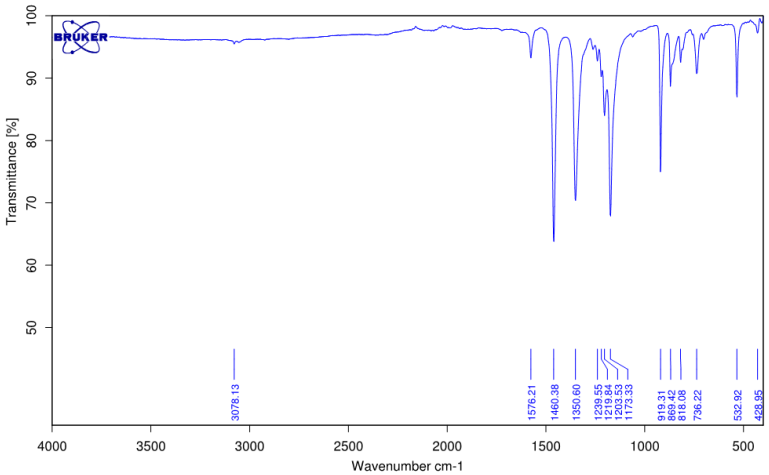

Figure S12. FT-IR spectrum of **3**.

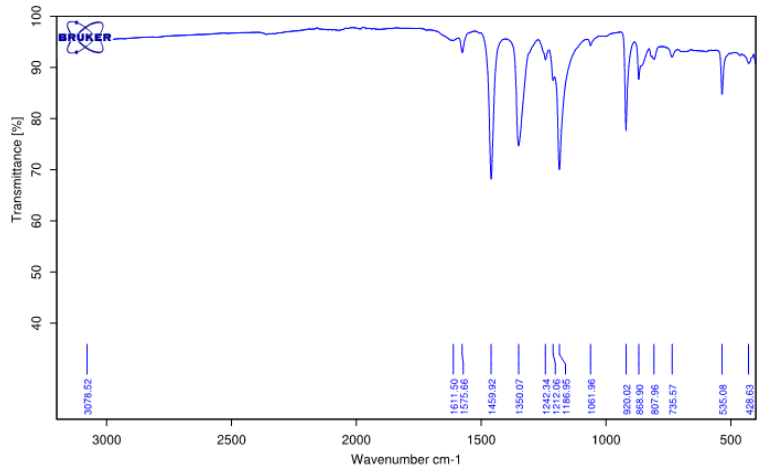

Figure S13. FT-IR spectrum of **4**.

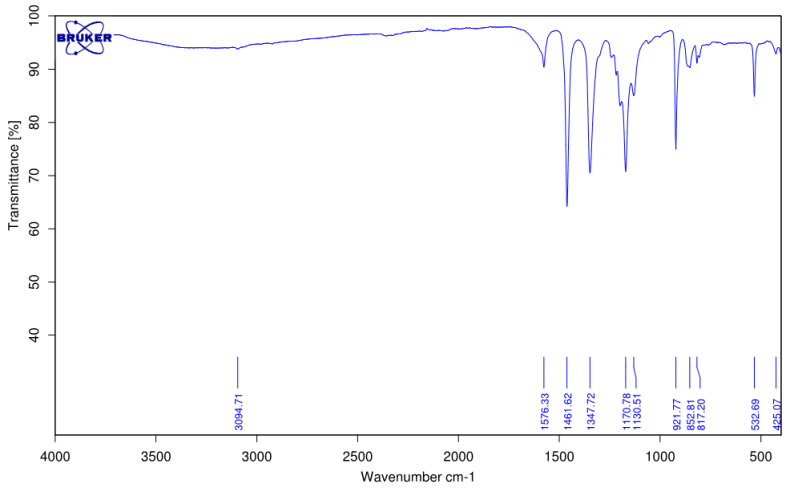

Figure S14. FT-IR spectrum of **6-NO_2**.

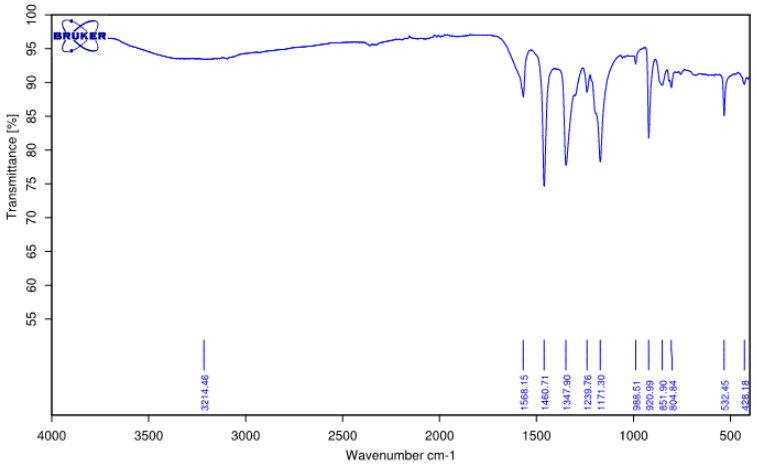

Figure S15. FT-IR spectrum of **6-NO_3**.

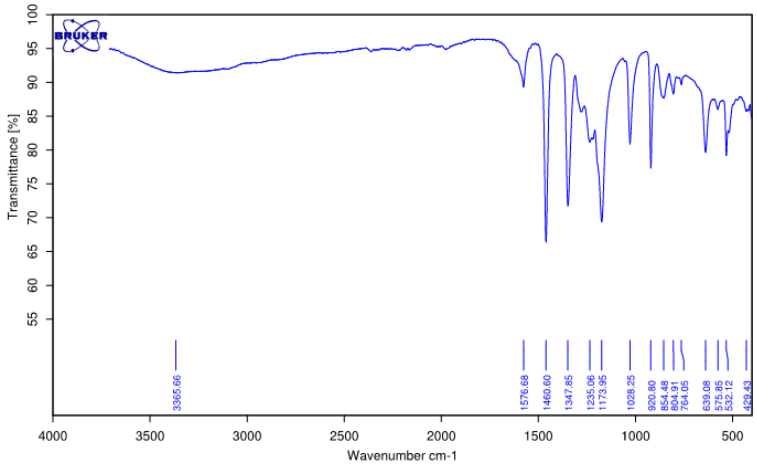

Figure S16. FT-IR spectrum of **6-OTf**.

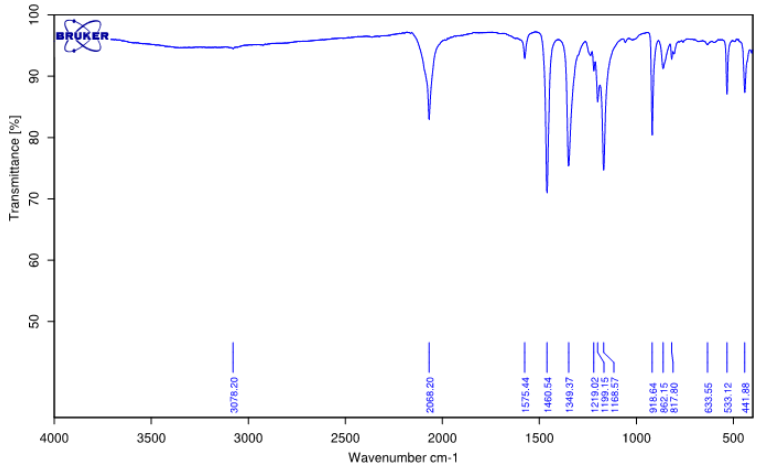

Figure S17. FT-IR spectrum of **6-N_3**.

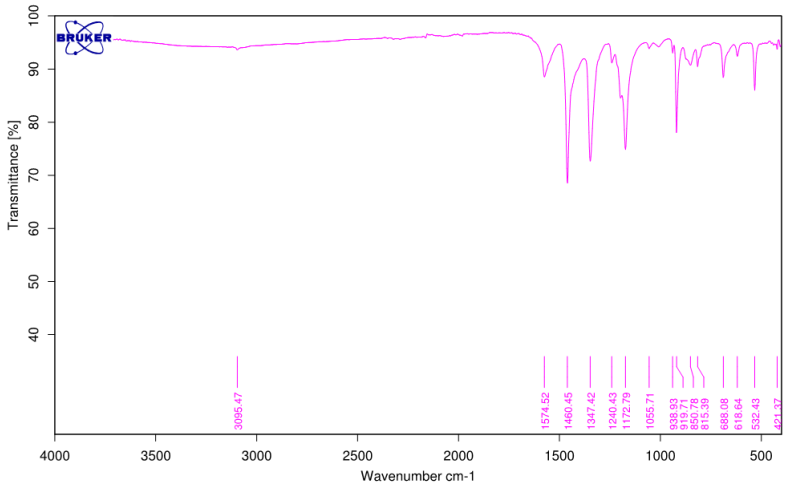

Figure S18. FT-IR spectrum of **6-OAc**.

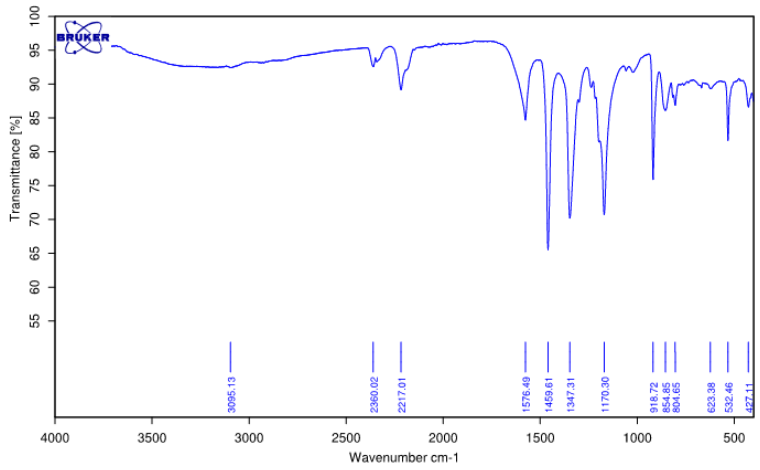

Figure S19. FT-IR spectrum of **6-NCO**.

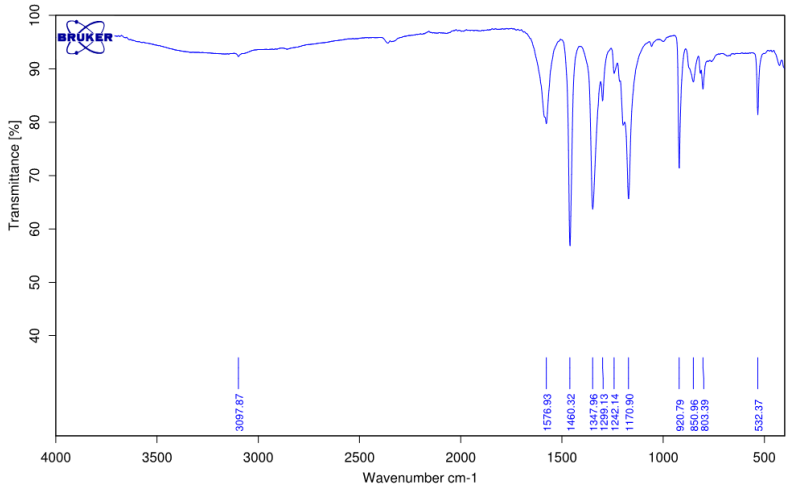

Figure S20. FT-IR spectrum of **6-HCOO**.

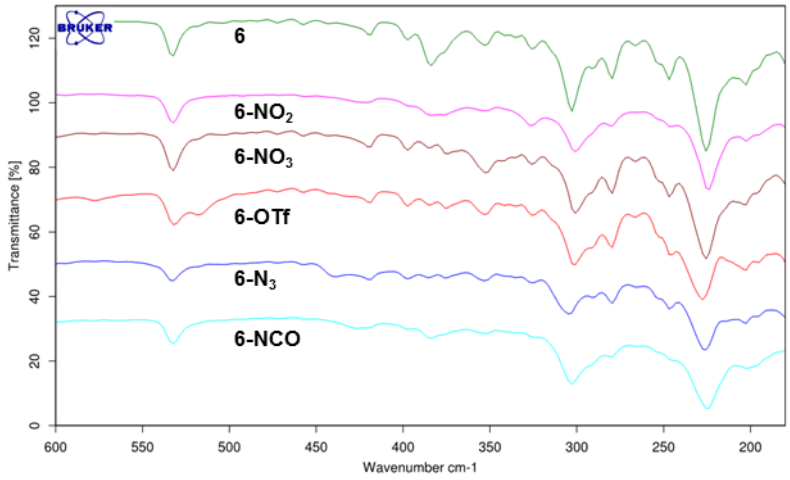

Figure S21. FIR spectra of different derivatives of **6**.

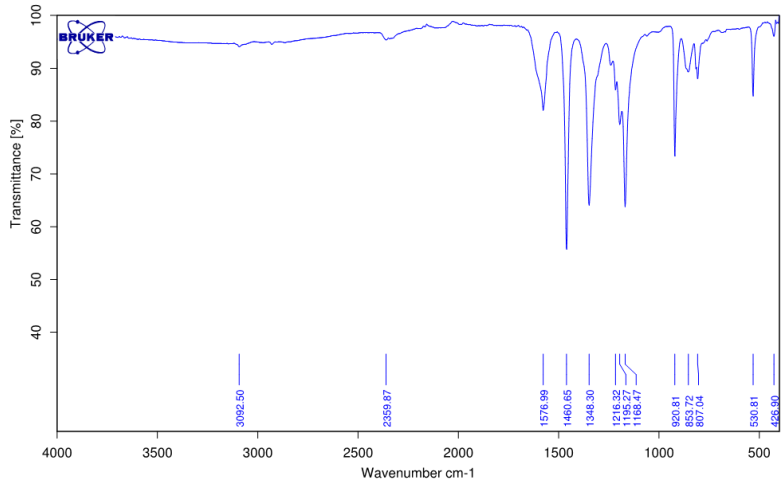

Figure S22. FT-IR spectrum of **1-HCOO**.

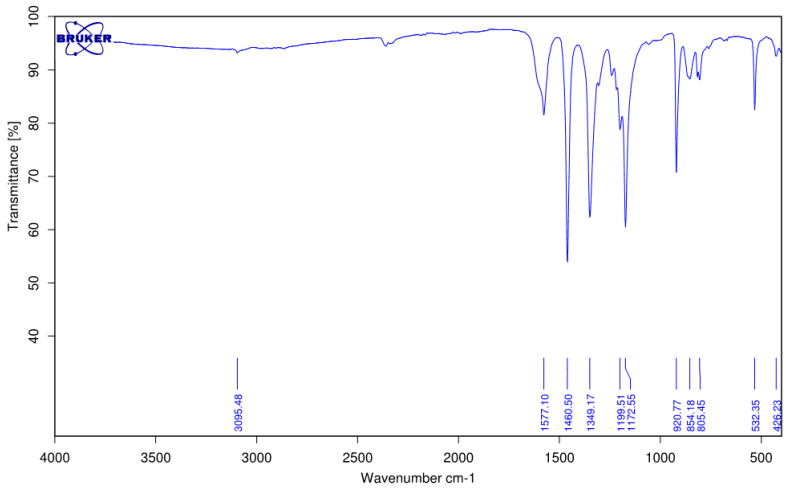

Figure S23. FT-IR spectrum of **2-HCOO**.

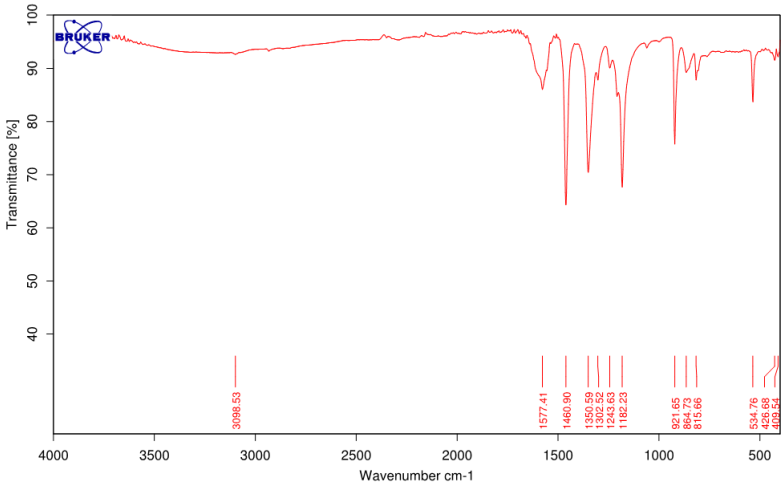

Figure S24. FT-IR spectrum of **4-HCOO**.

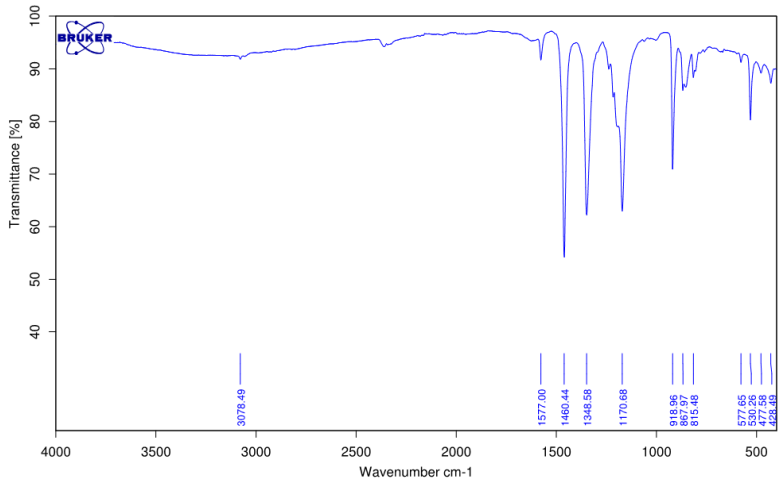

Figure S25. FT-IR spectrum of **1-F**.

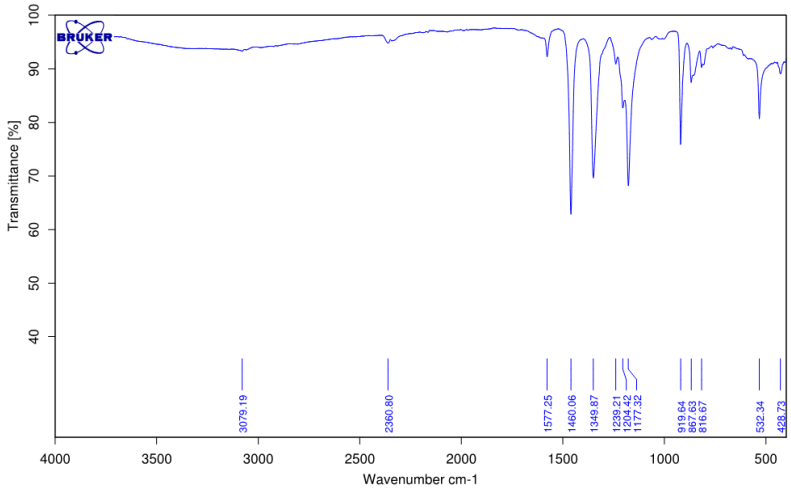

Figure S26. FT-IR spectrum of **2-F**.

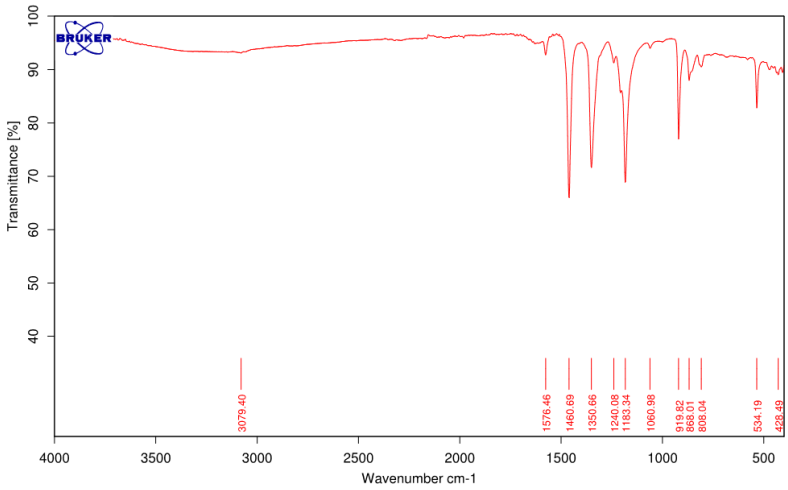

Figure S27. FT-IR spectrum of **4-F**.

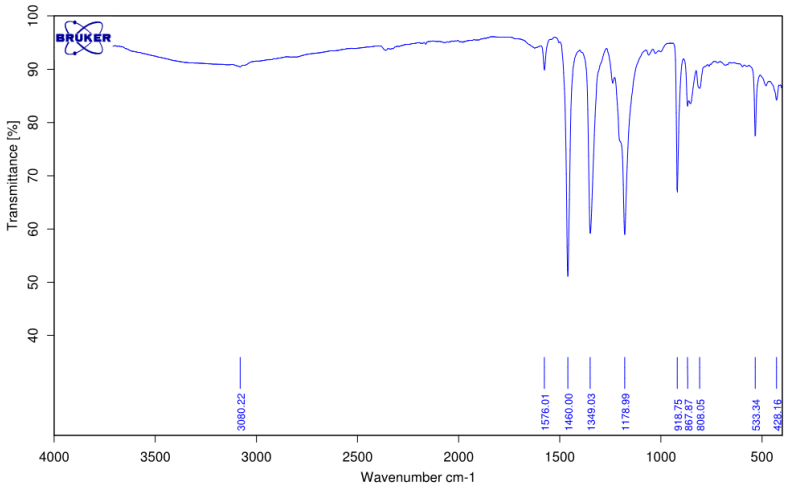

Figure S28. FT-IR spectrum of **5-F**.

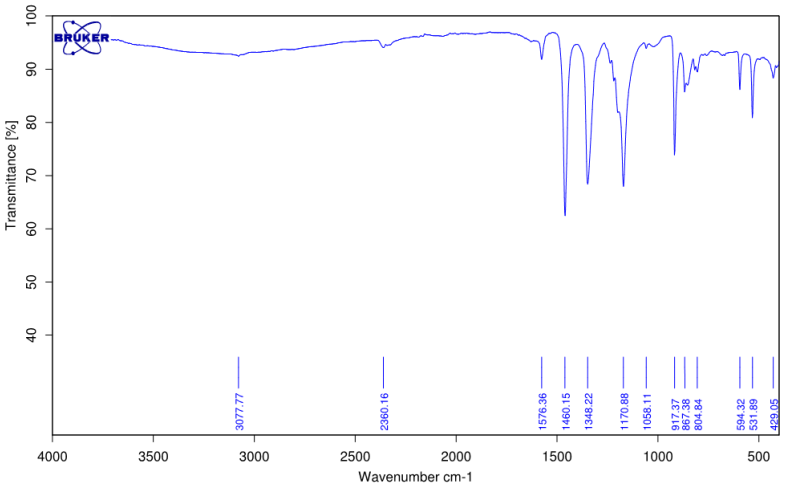

Figure S29. FT-IR spectrum of **6-F**.

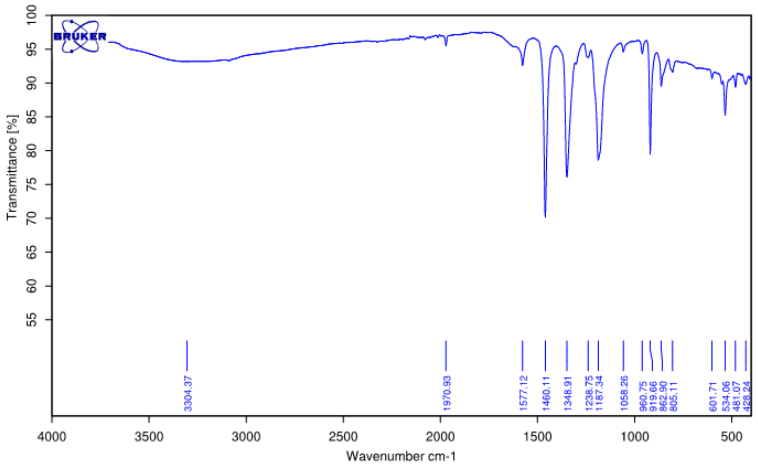

Figure S30. FT-IR spectrum of **6-HCOO** heated at 325 °C under CO (5 % in He) flow.

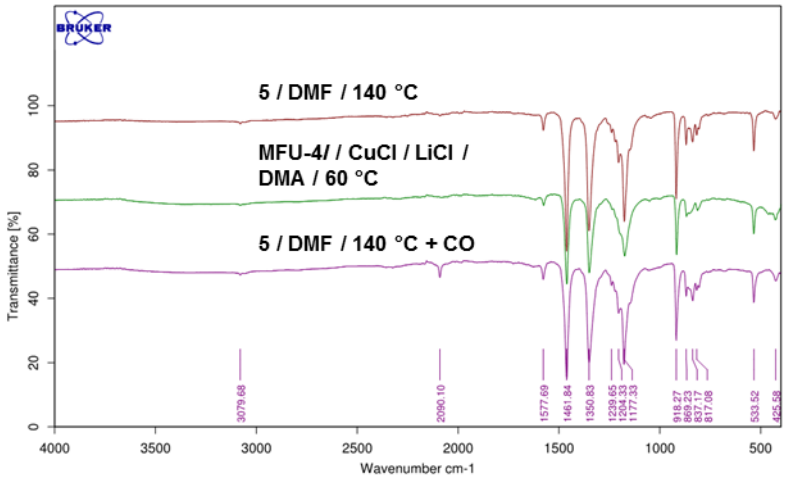

Figure S31. FT-IR spectra of Cu(I)-MFU-4*l* prepared in different ways and of the CO adduct of Cu(I)-MFU-4*l*.

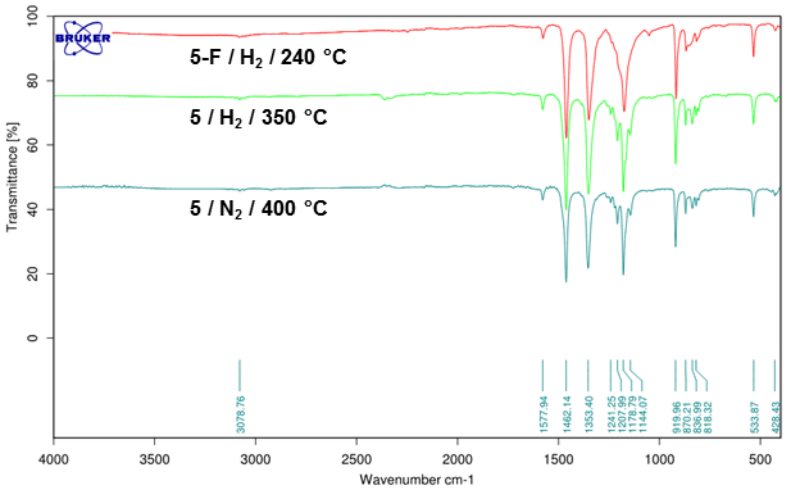

Figure S32. FT-IR spectra of products obtained from **5** and **5-F**.

Gas sorption measurements

The isosteric heats of adsorption were calculated from the measured isotherms (Figures S40-52) using the Clausius-Clapeyron equation (**I**). The slopes of linear plots lnP versus 1/RT for different loadings (Figures S53-77) give the adsorption enthalpies, according to the equation (**II**).

$$Q_{st} = -R\left(\frac{\partial(\ln P)}{\partial(1/T)}\right)_{\theta}$$ (**I**), θ – surface coverage

$$\ln P = -\frac{Q_{st}}{R}\left(\frac{1}{T}\right) + C$$ (**II**), C – integration constant

The values for the isosteric heats of argon and oxygen adsorption are listed in Table S1.

Table S1. Isosteric heats of argon and oxygen adsorption and calculated O_2 binding energies for MFU-4*l* derivatives

Compound	Metal ion	Side ligand	Q_{st} (Ar) / kJ mol^{-1}[a]	Q_{st} (O_2) / kJ mol^{-1}[a]	Calculated O_2 binding energy / kJ mol^{-1}[b]
MFU-4*l*	Zn^{2+}	Cl^-	11.7±0.2	11.8±0.2	12.3
6	Co^{2+}	Cl^-	12.2±0.2	14.0±0.2	12.4
6-NO_2	Co^{2+}	NO_2^-	13.0±0.2	12.9±0.2	11.5
6-NO_3	Co^{2+}	NO_3^-	12.3±0.2	12.6±0.2	11.6
6-OTf	Co^{2+}	$CF_3SO_3^-$	12.0±0.2	12.5±0.2	11.5
1	Mn^{2+}	Cl^-	11.6±0.2	11.6±0.2	12.5
2	Fe^{2+}	Cl^-	-	11.4±0.2	10.5
2-F	Fe^{2+}	F^-	-	12.3±0.2	20.0
4	Ni^{2+}	Cl^-	12.1±0.2	13.3±0.2	12.7
4-F	Ni^{2+}	F^-	-	13.1±0.2	12.1
5	Cu^{2+}	Cl^-	12.4±0.2	11.8±0.2	12.7

[a] at 0.35 mmol g^{-1} loading.

[b] in all cases except Fe-F binding energies for the physisorbed state are given since they are higher as for the chemisorbed state.

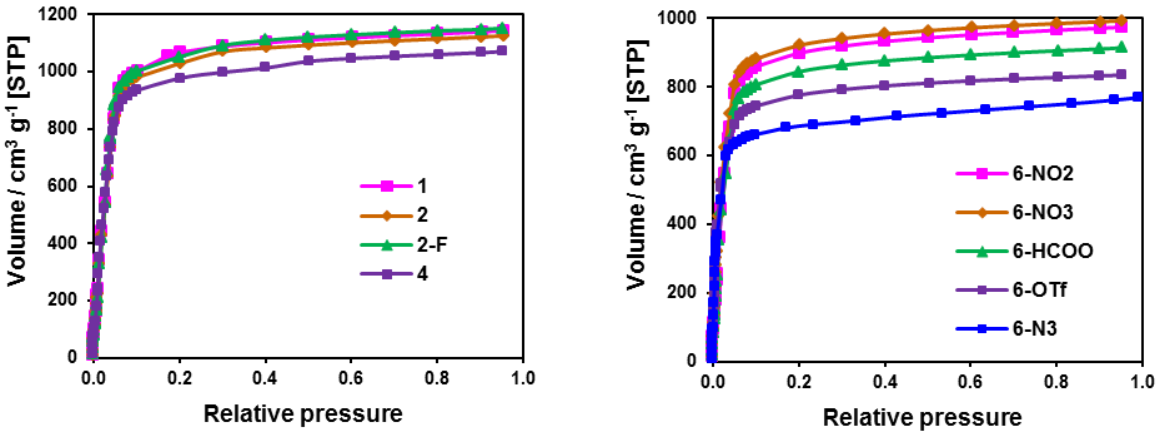

Figure S33. Argon adsorption isotherms at 87.3 K for compounds **1, 2, 2-F**, **4** and derivatives of **6**.

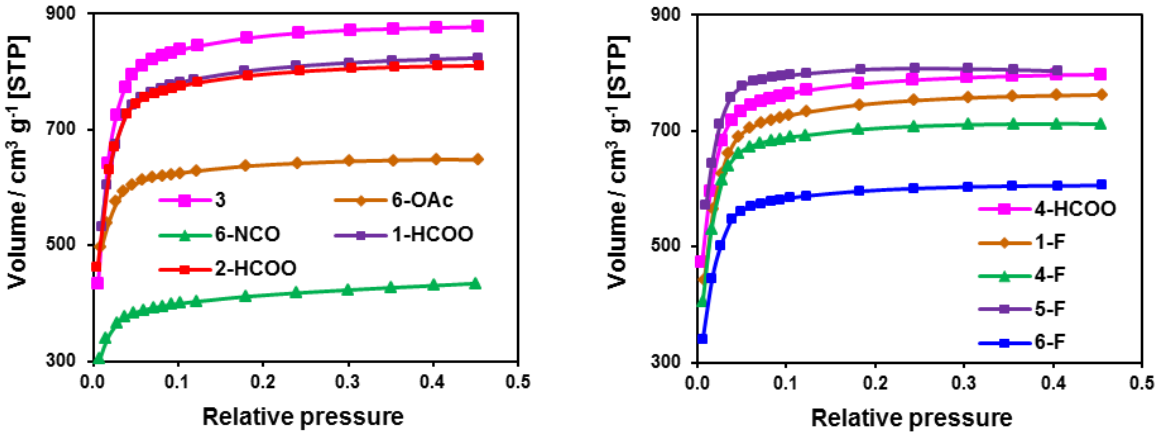

Figure S34. Nitrogen adsorption isotherms at 77.3 K.

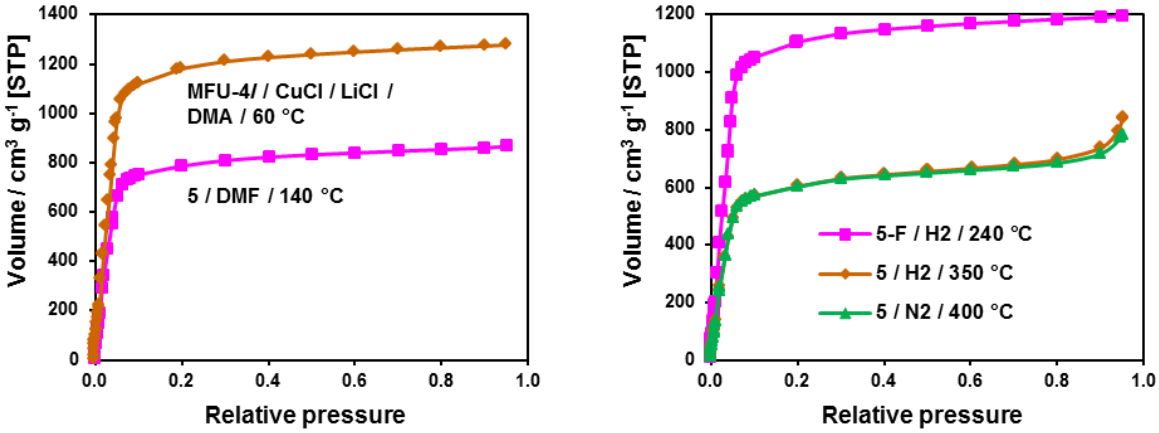

Figure S35. Argon adsorption isotherms at 87.3 K for Cu(I)-MFU-4*l* prepared in different ways (left) and for the products of the gas-phase reactions of **5** and **5-F** (right).

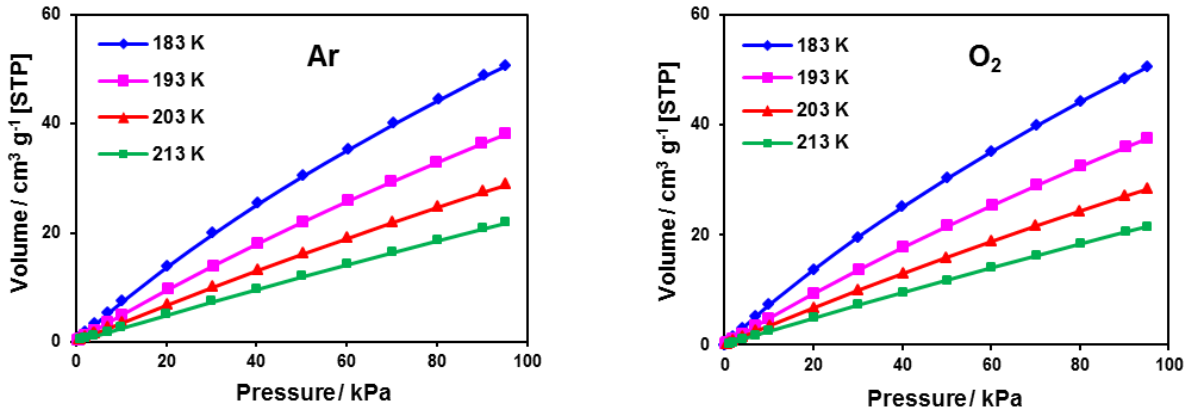

Figure S36. Ar and O_2 adsorption isotherms for **MFU-4*l*** at different temperatures for the determination of the isosteric heats of adsorption.

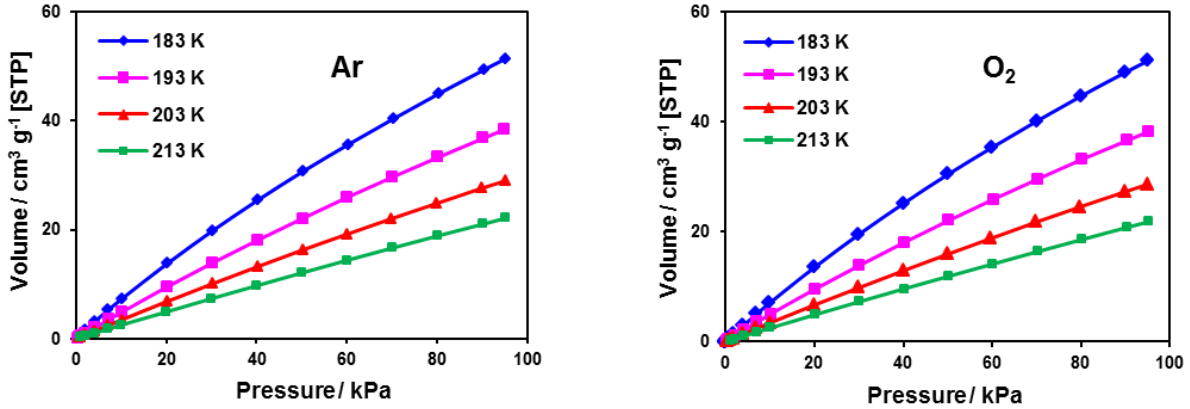

Figure S37. Ar and O_2 adsorption isotherms for **1** at different temperatures for the determination of the isosteric heats of adsorption.

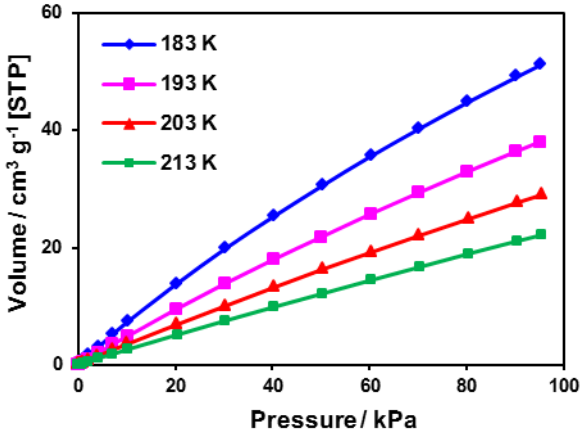

Figure S38. O_2 adsorption isotherms for **2** at different temperatures for the determination of the isosteric heats of adsorption.

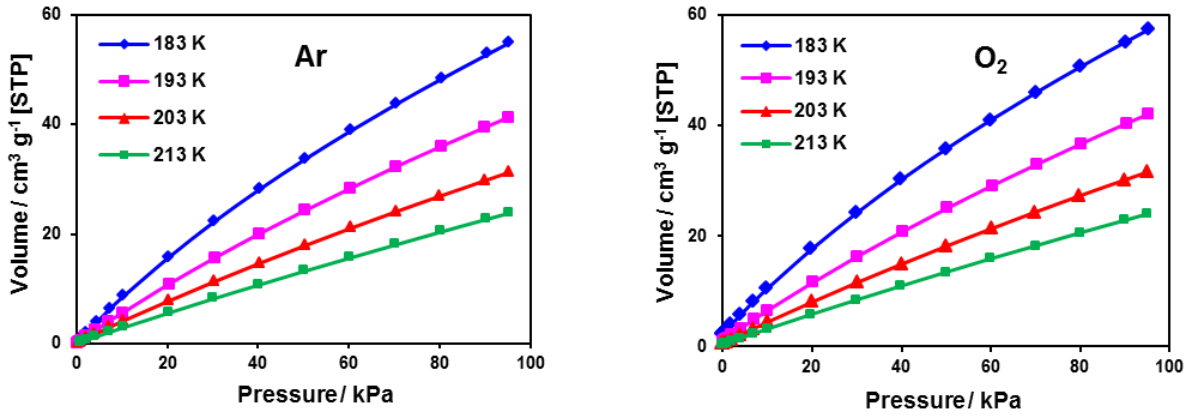

Figure S39. Ar and O_2 adsorption isotherms for **4** at different temperatures for the determination of the isosteric heats of adsorption.

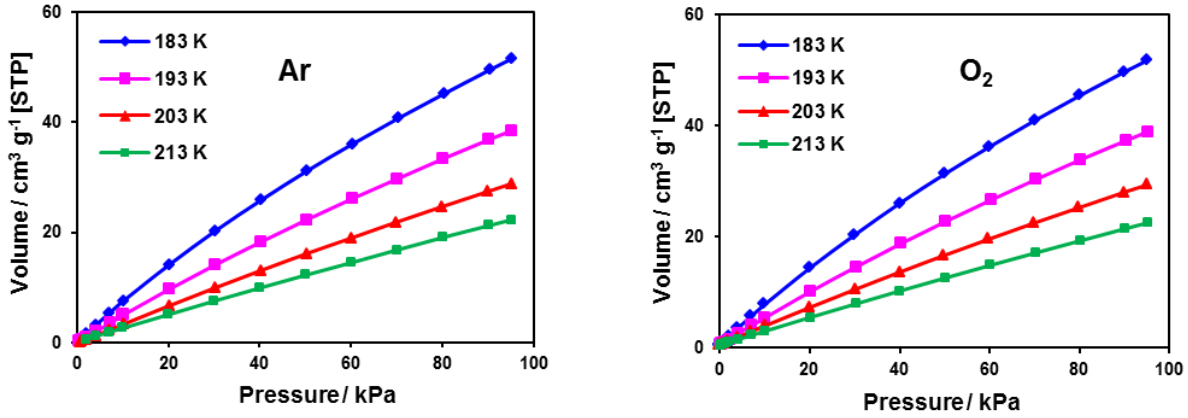

Figure S40. Ar and O_2 adsorption isotherms for **5** at different temperatures for the determination of the isosteric heats of adsorption.

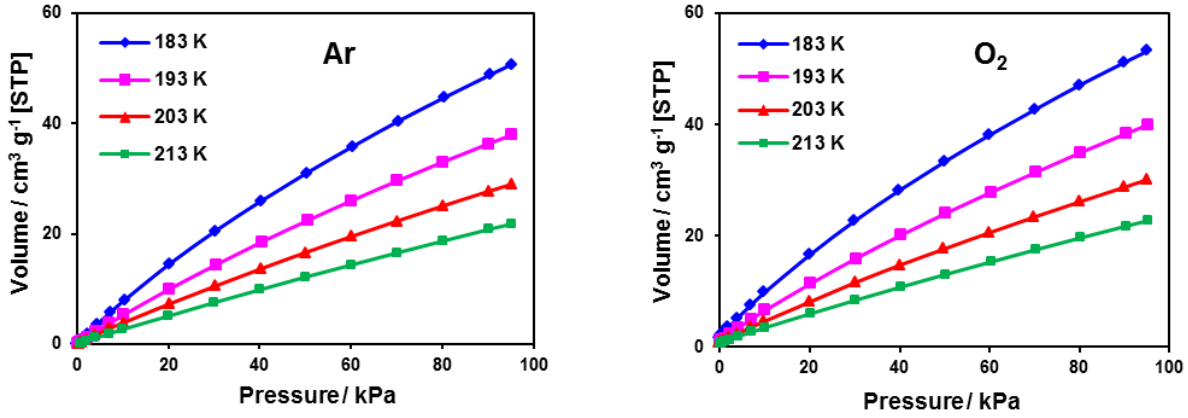

Figure S41. Ar and O_2 adsorption isotherms for **6** at different temperatures for the determination of the isosteric heats of adsorption.

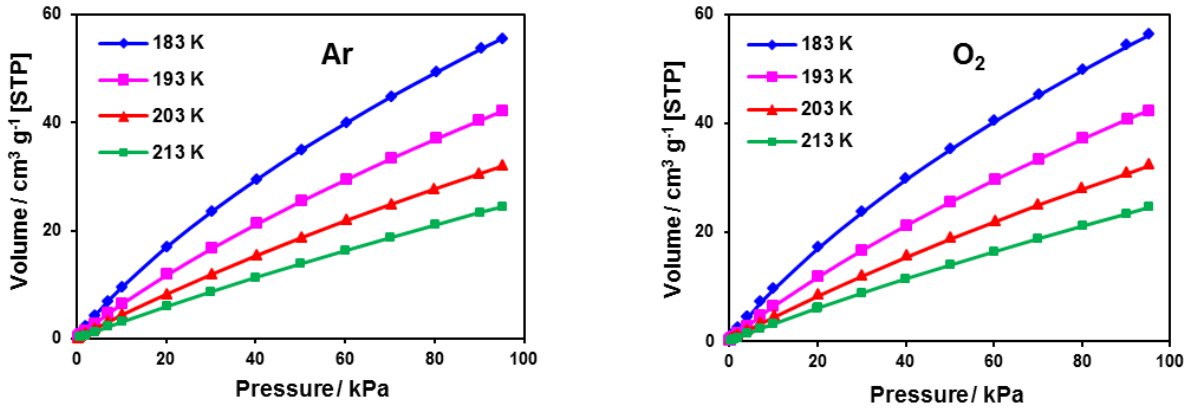

Figure S42. Ar and O_2 adsorption isotherms for **6-NO_2** at different temperatures for the determination of the isosteric heats of adsorption.

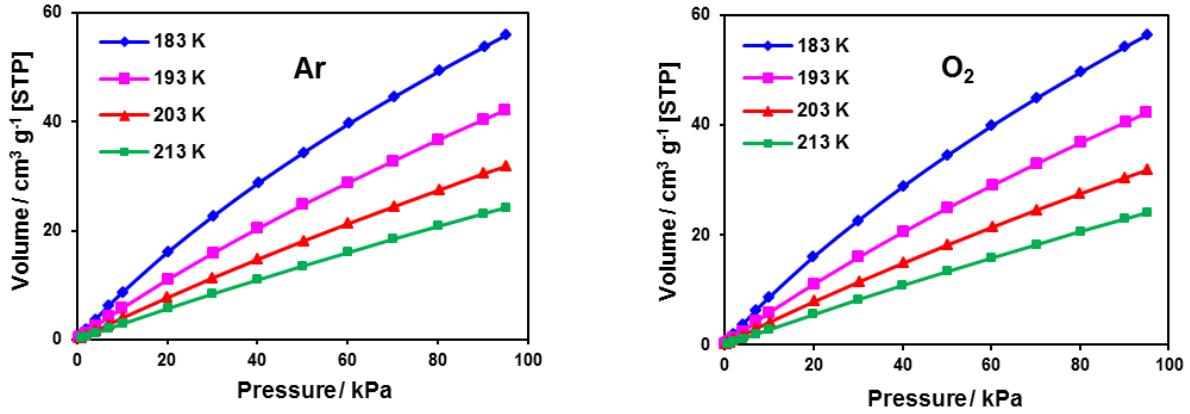

Figure S43. Ar and O_2 adsorption isotherms for **6-NO_3** at different temperatures for the determination of the isosteric heats of adsorption.

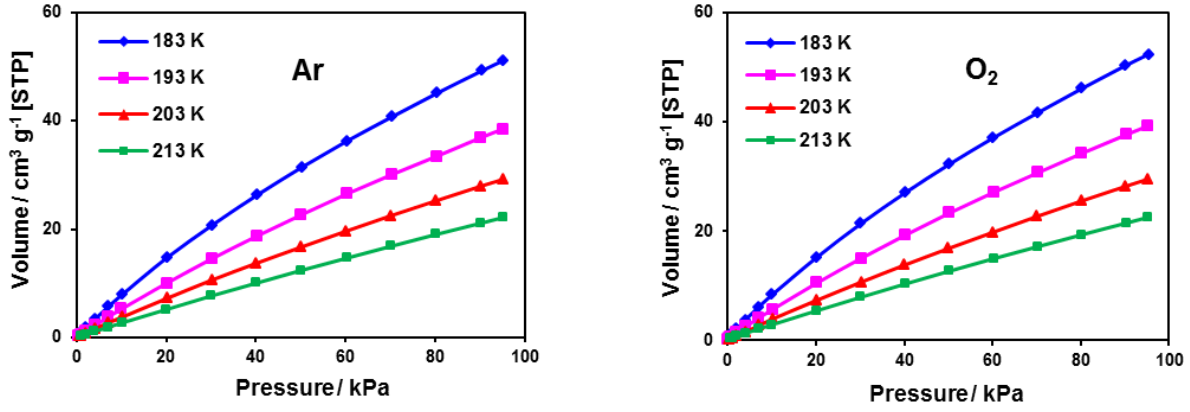

Figure S44. Ar and O_2 adsorption isotherms for **6-OTf** at different temperatures for the determination of the isosteric heats of adsorption.

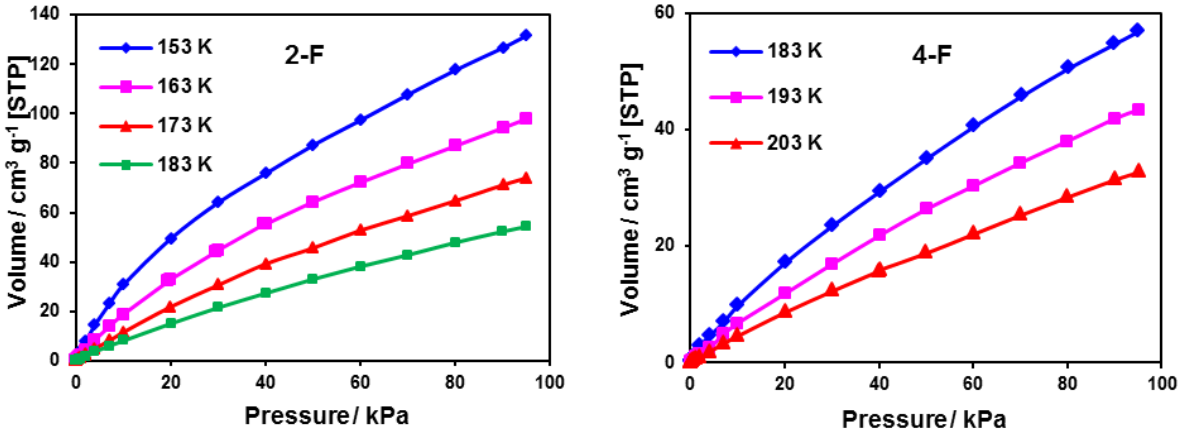

Figure S45. O_2 adsorption isotherms for **2-F** and **4-F** at different temperatures for the determination of the isosteric heats of adsorption.

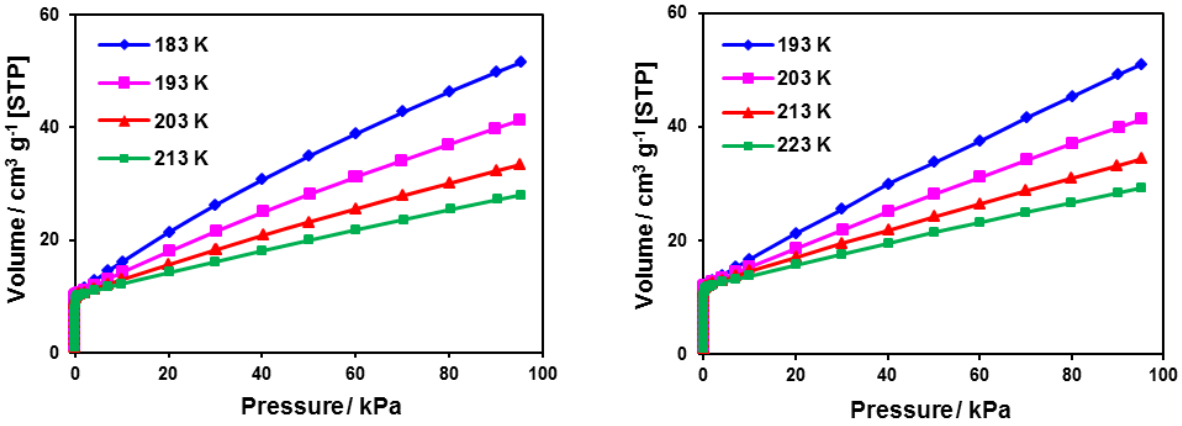

Figure S46. O_2 adsorption isotherms for Cu(I)-MFU-4*l* prepared *via* solvothermal reduction of **5** in DMF (left) and *via* metal exchange in MFU-4*l* with CuCl/LiCl in DMA (right).

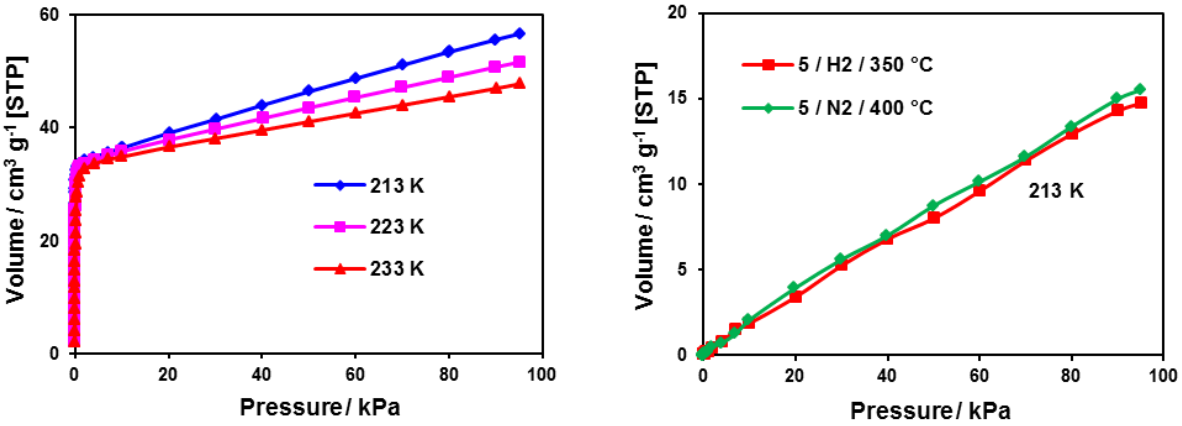

Figure S47. O_2 adsorption isotherms for Cu(I)-MFU-4*l* prepared *via* the gas-phase reduction of **5-F** with H_2 (left) and for the products of the gas-phase reactions of **5** (right).

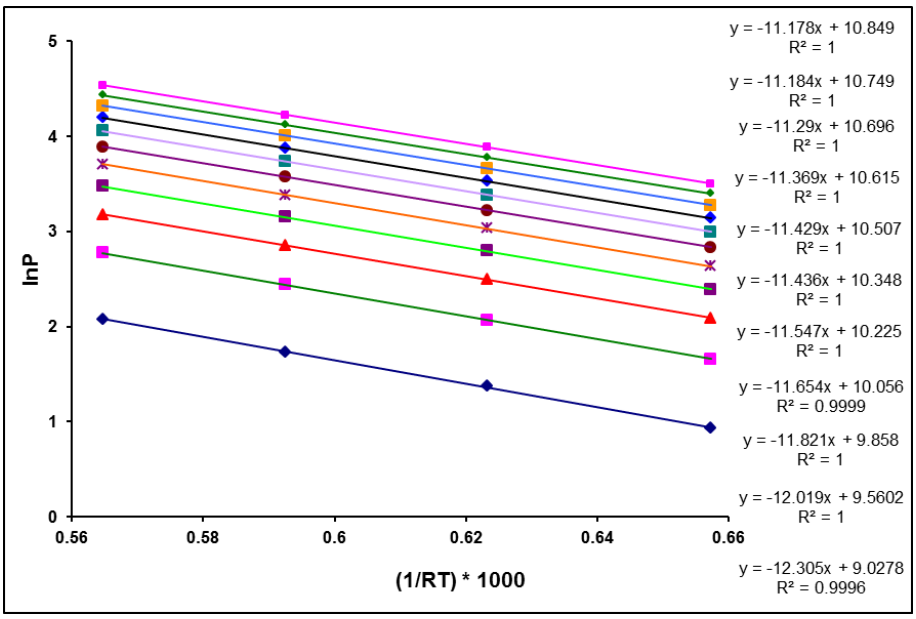

Figure S48. lnP versus 1/RT plots for different loadings for Ar adsorption on **MFU-4*l***.

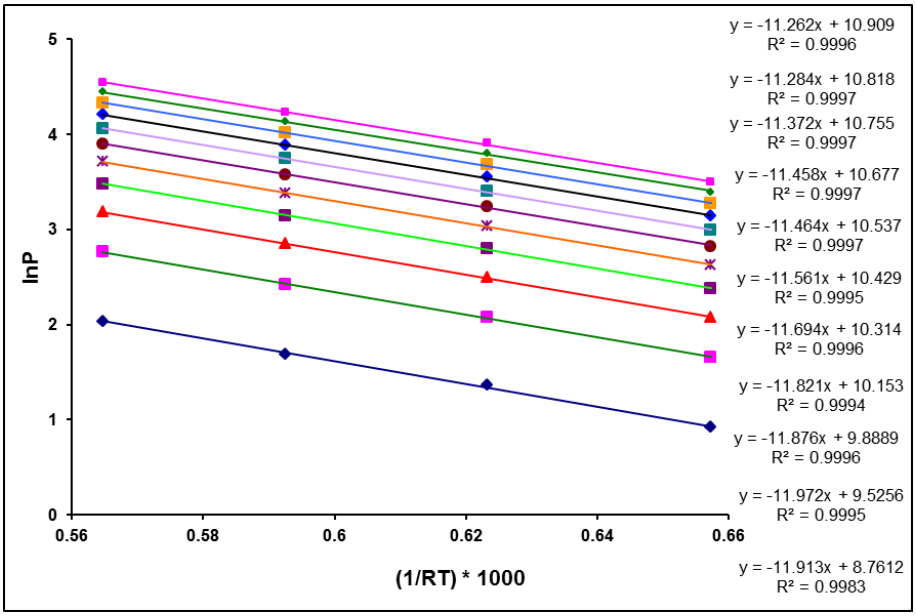

Figure S49. lnP versus 1/RT plots for different loadings for O_2 adsorption on **MFU-4*l***.

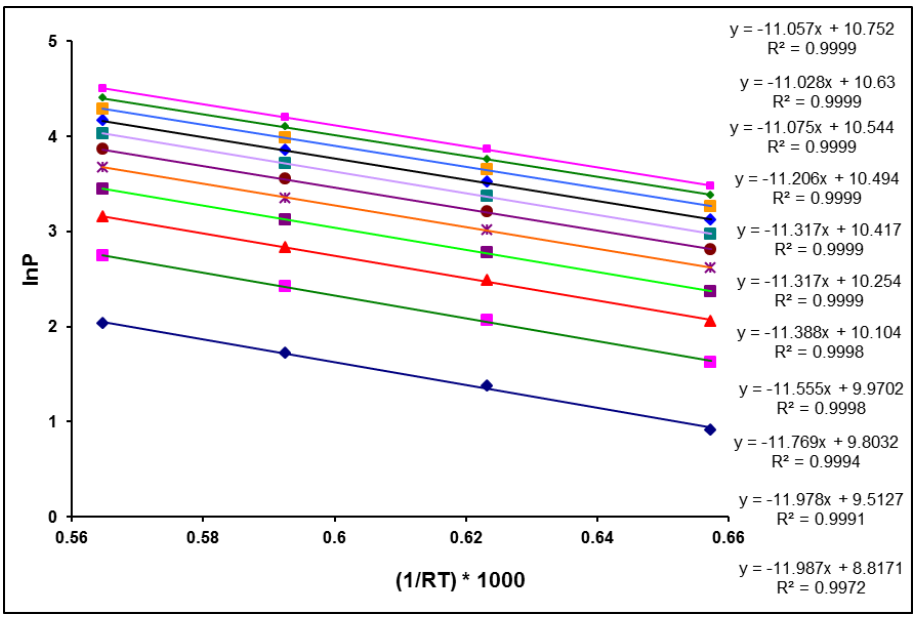

Figure S50. lnP versus 1/RT plots for different loadings for Ar adsorption on **1**.

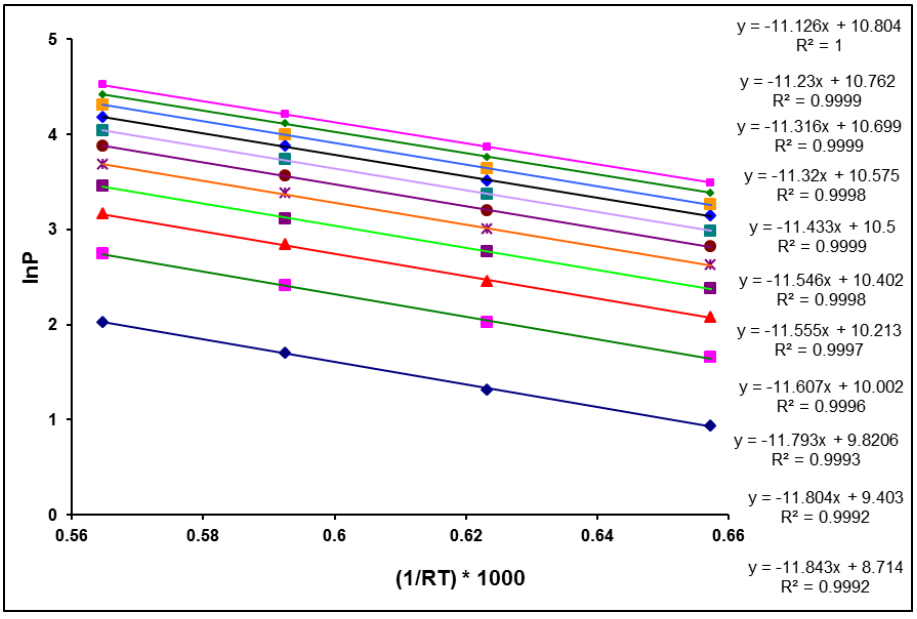

Figure S51. lnP versus 1/RT plots for different loadings for O_2 adsorption on **1**.

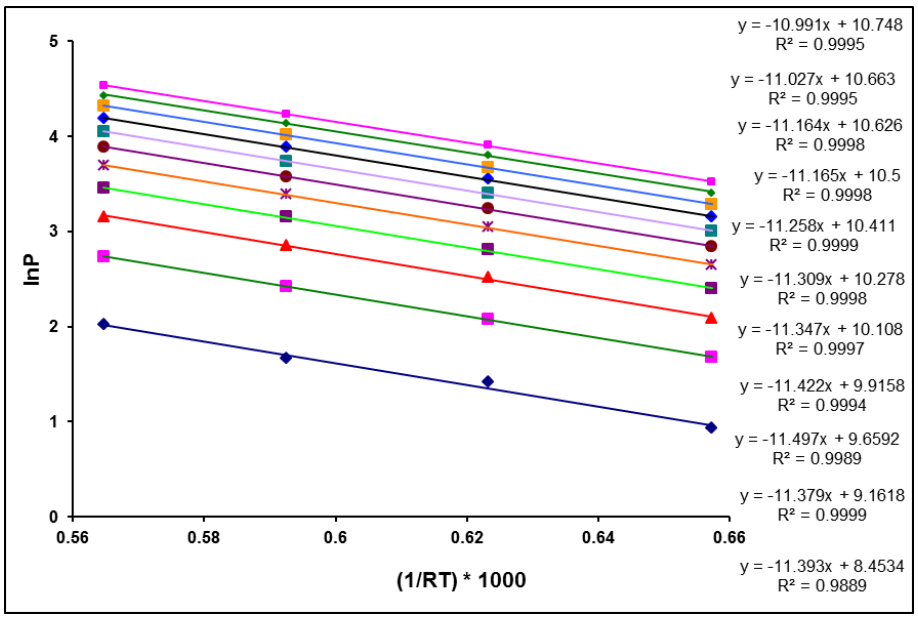

Figure S52. lnP versus 1/RT plots for different loadings for O_2 adsorption on **2**.

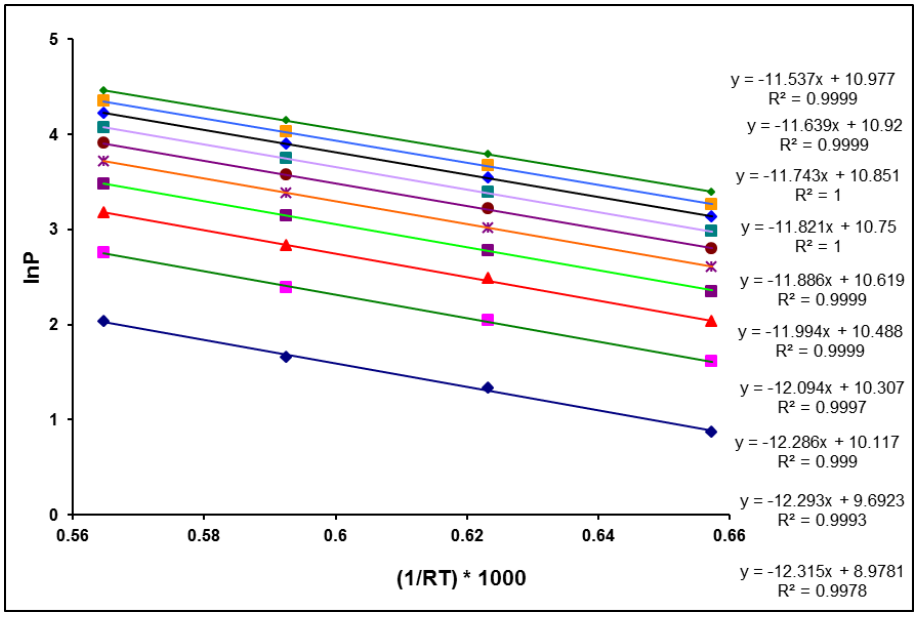

Figure S53. lnP versus 1/RT plots for different loadings for Ar adsorption on **4**.

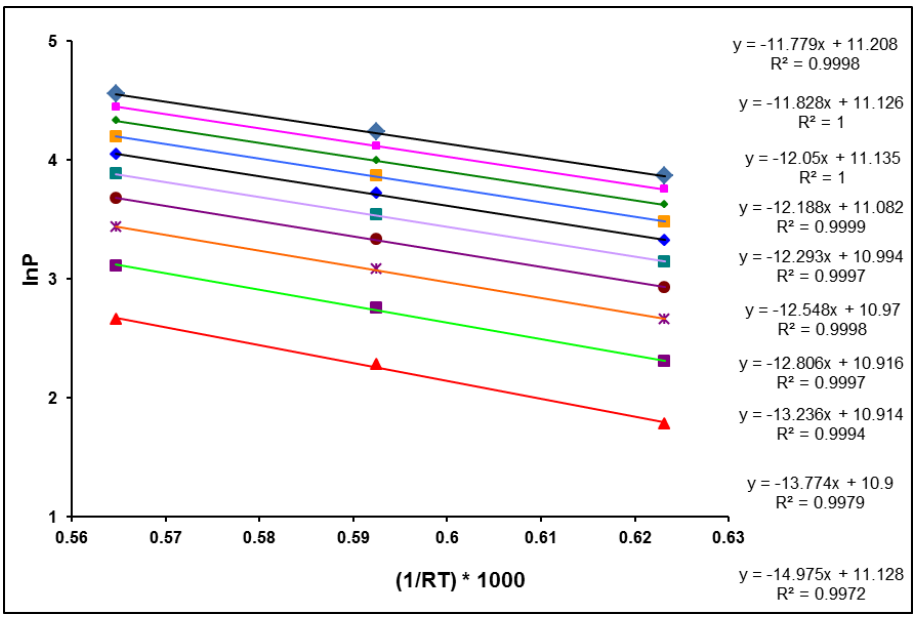

Figure S54. lnP versus 1/RT plots for different loadings for O_2 adsorption on **4**.

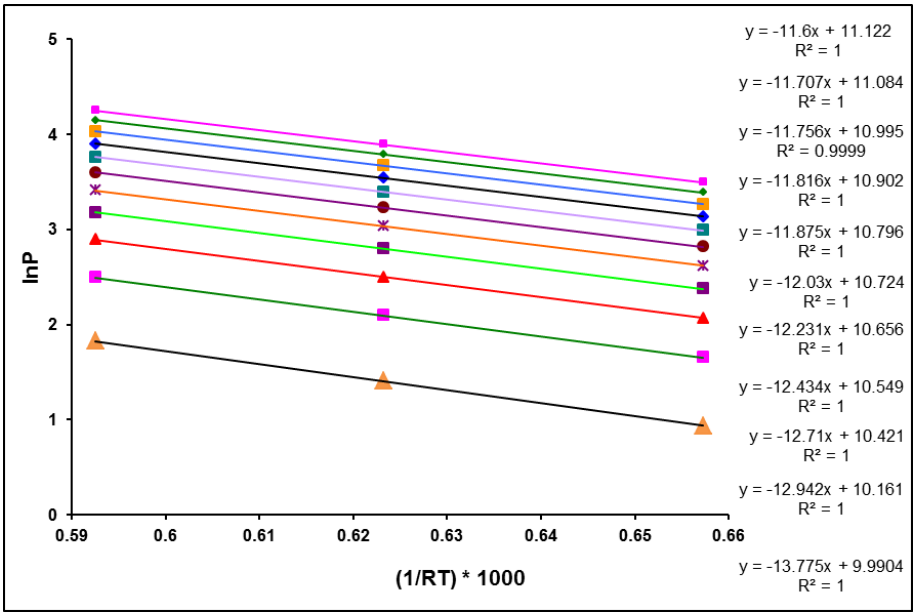

Figure S55. lnP versus 1/RT plots for different loadings for Ar adsorption on **5**.

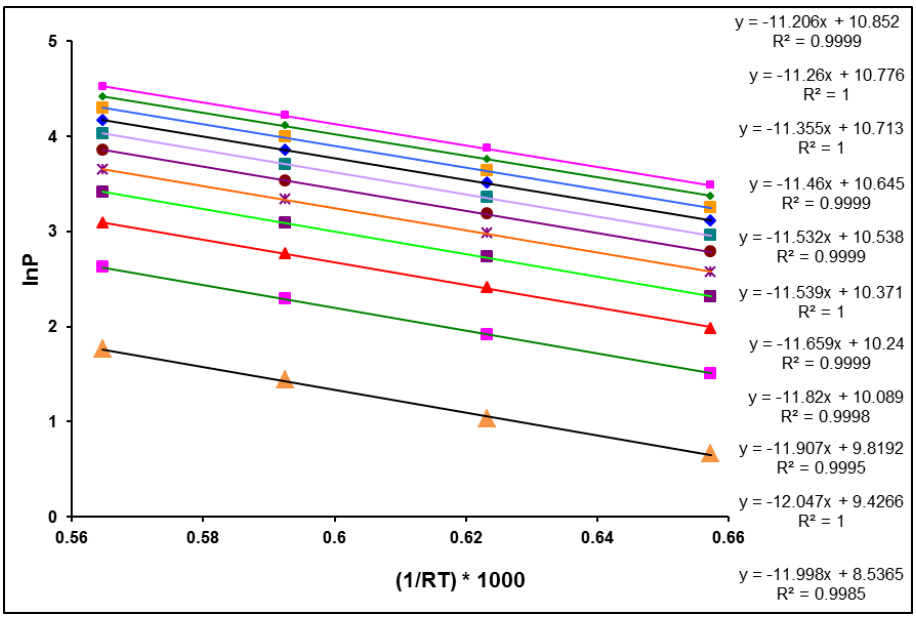

Figure S56. lnP versus 1/RT plots for different loadings for O_2 adsorption on **5**.

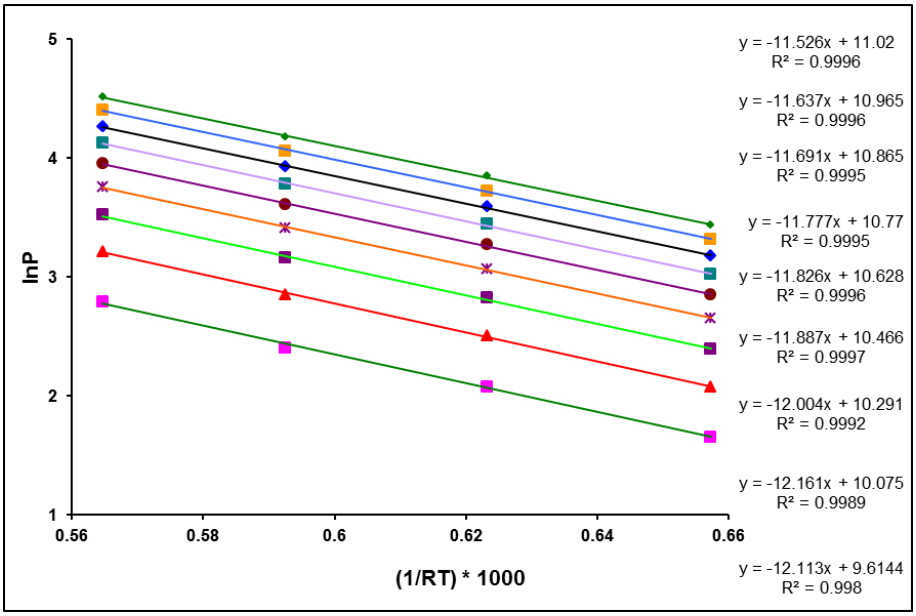

Figure S57. lnP versus 1/RT plots for different loadings for Ar adsorption on **6**.

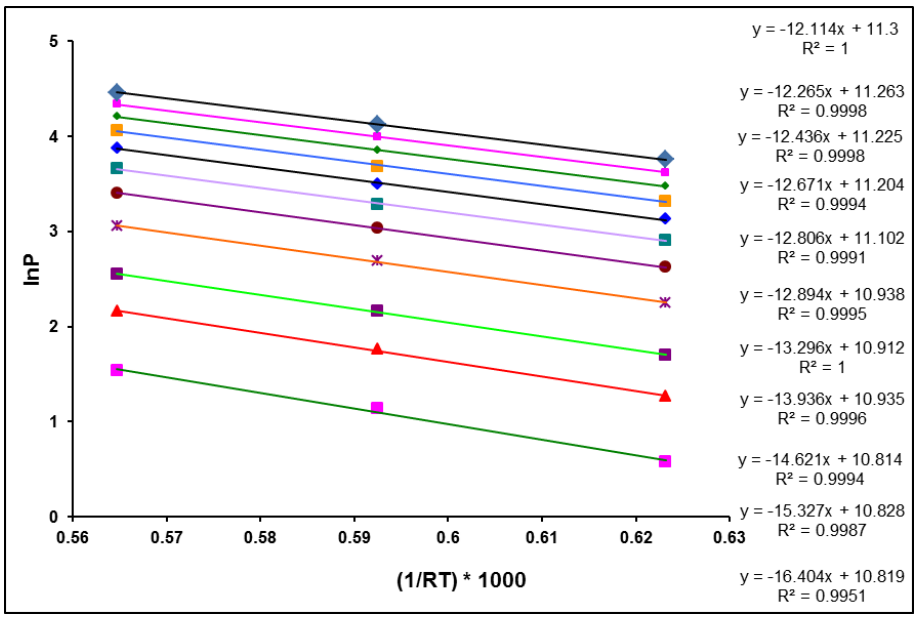

Figure S58. lnP versus 1/RT plots for different loadings for O_2 adsorption on **6**.

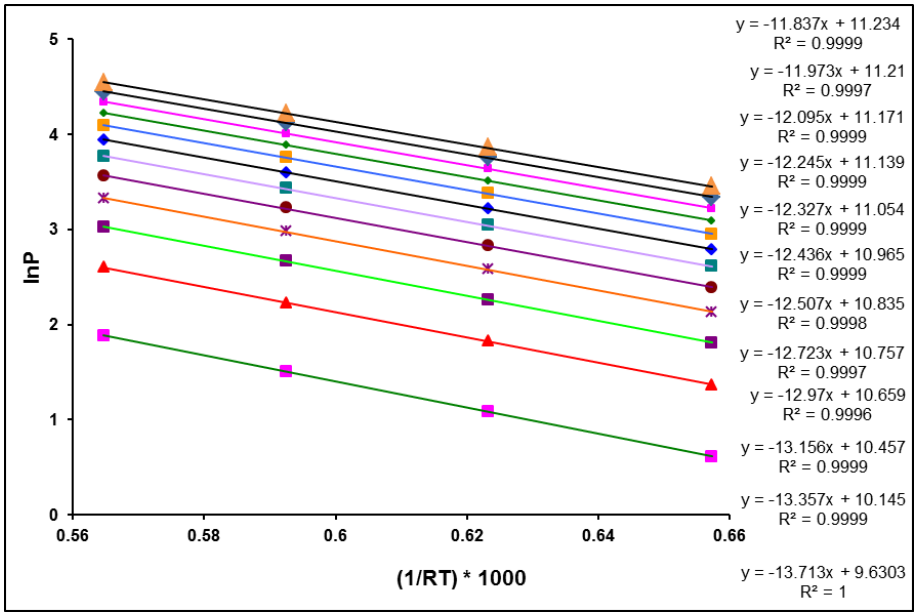

Figure S59. lnP versus 1/RT plots for different loadings for Ar adsorption on **6-NO_2**.

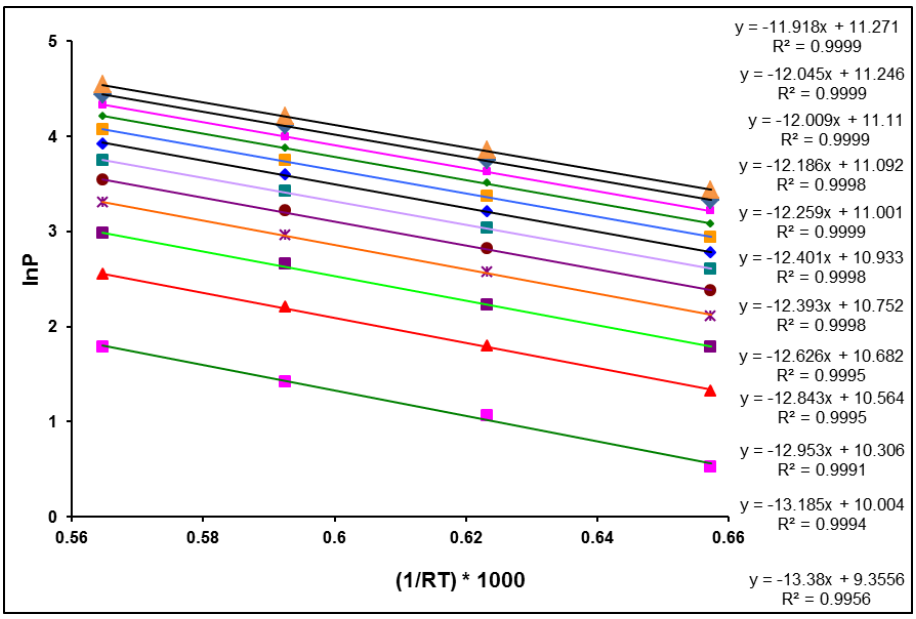

Figure S60. lnP versus 1/RT plots for different loadings for O_2 adsorption on **6-NO_2**.

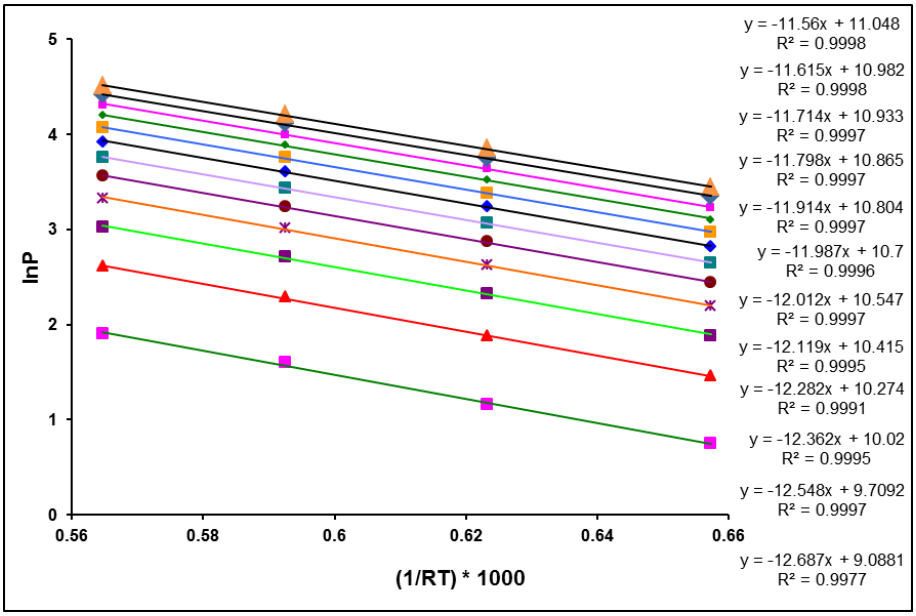

Figure S61. lnP versus 1/RT plots for different loadings for Ar adsorption on **6-NO_3**.

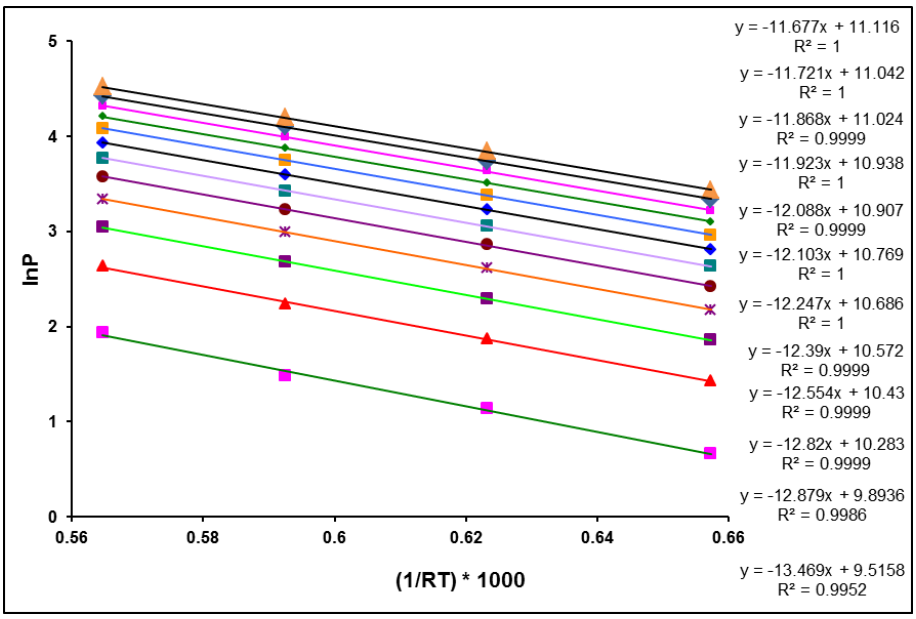

Figure S62. lnP versus 1/RT plots for different loadings for O_2 adsorption on **6-NO$_3$**.

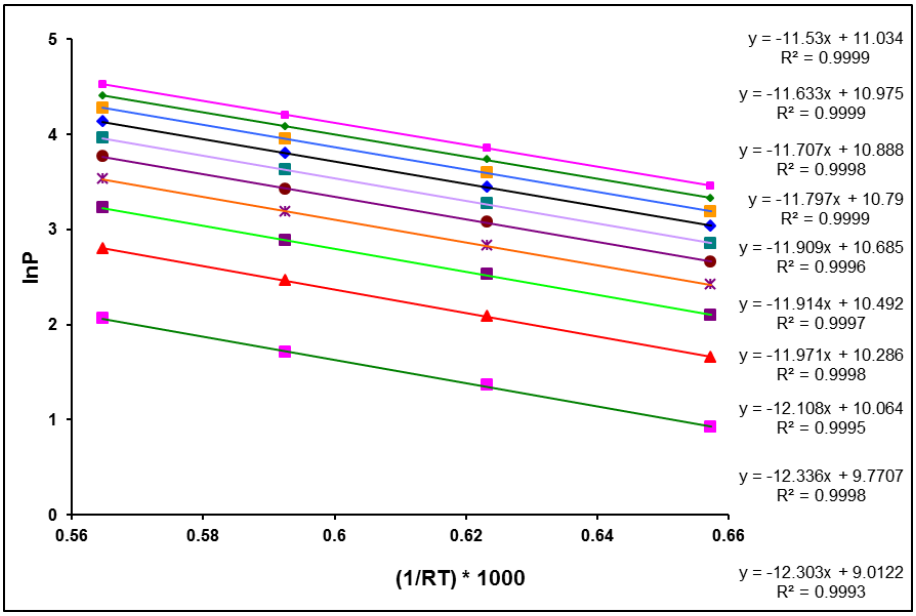

Figure S63. lnP versus 1/RT plots for different loadings for Ar adsorption on **6-OTf**.

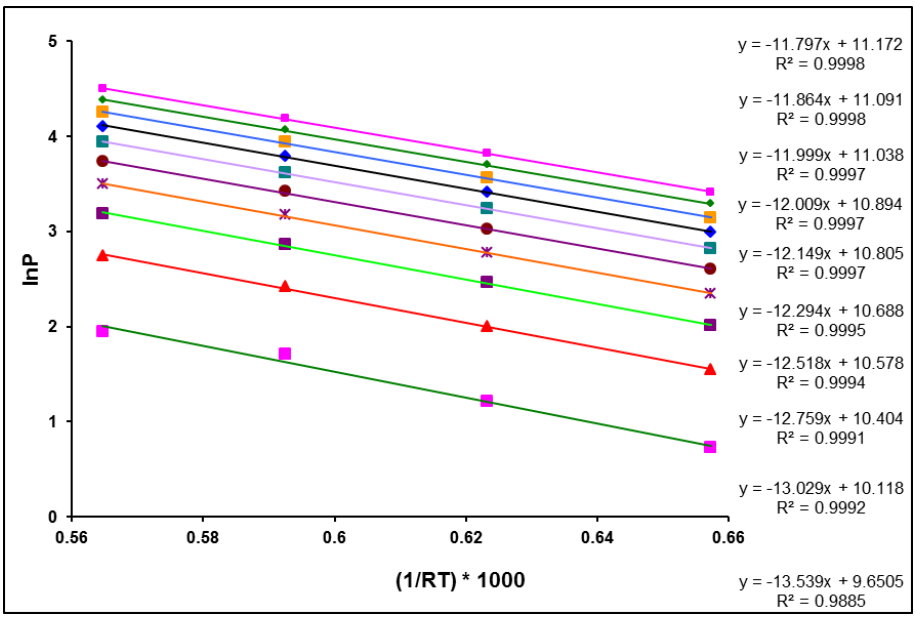

Figure S64. lnP versus 1/RT plots for different loadings for O_2 adsorption on **6-OTf**.

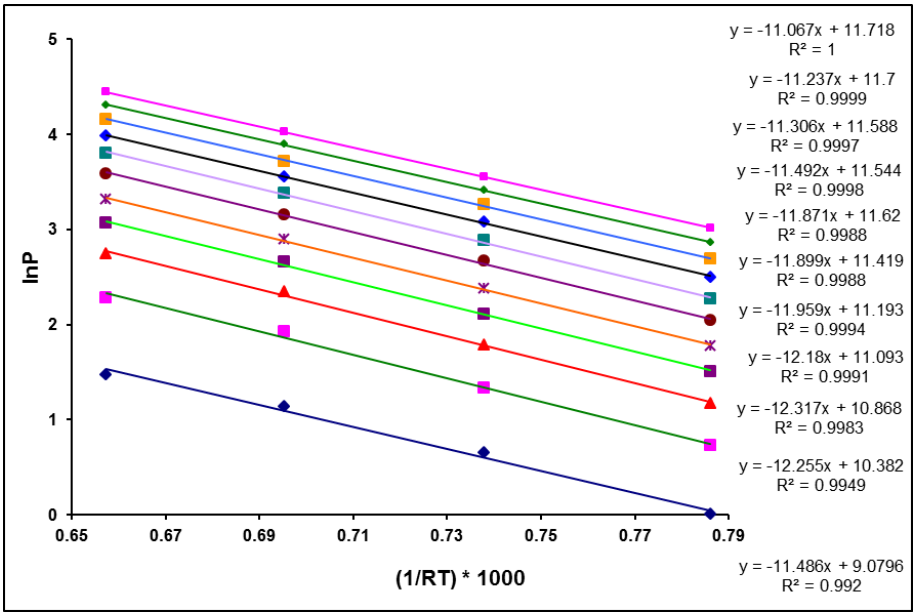

Figure S65. lnP versus 1/RT plots for different loadings for O_2 adsorption on **2-F**.

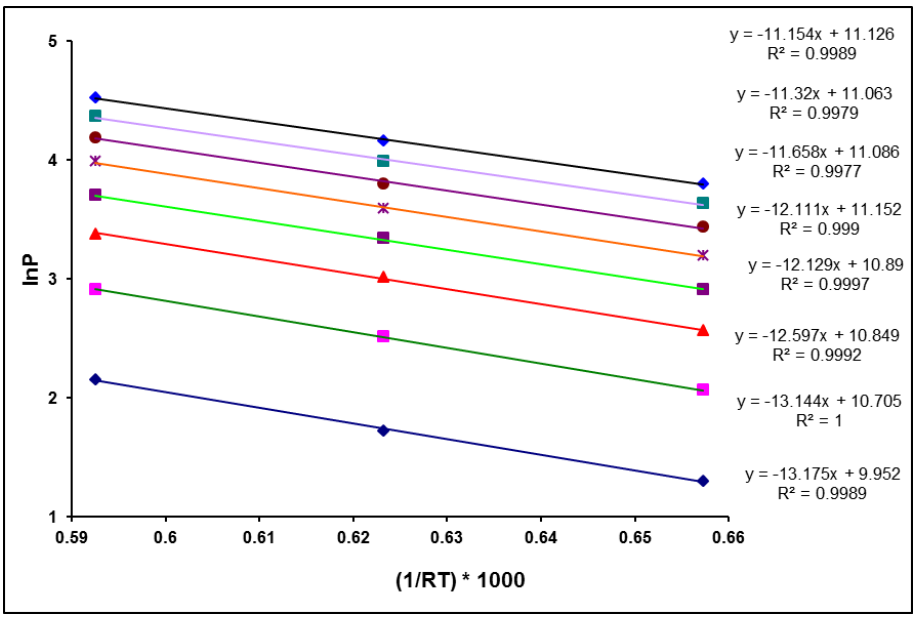

Figure S66. lnP versus 1/RT plots for different loadings for O_2 adsorption on **4-F**.

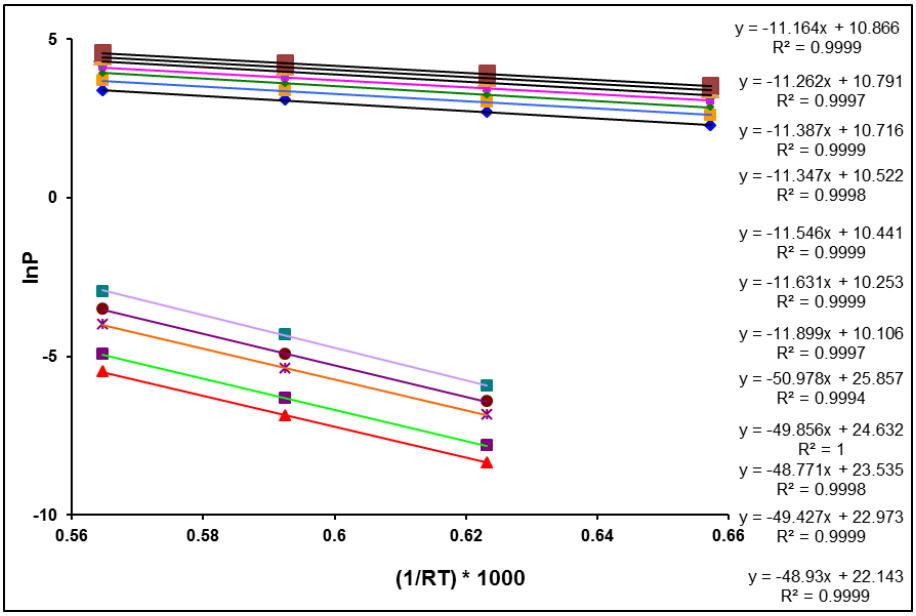

Figure S67. lnP versus 1/RT plots for different loadings for O_2 adsorption on Cu(I)-MFU-4*l* prepared *via* solvothermal reduction of **5** in DMF.

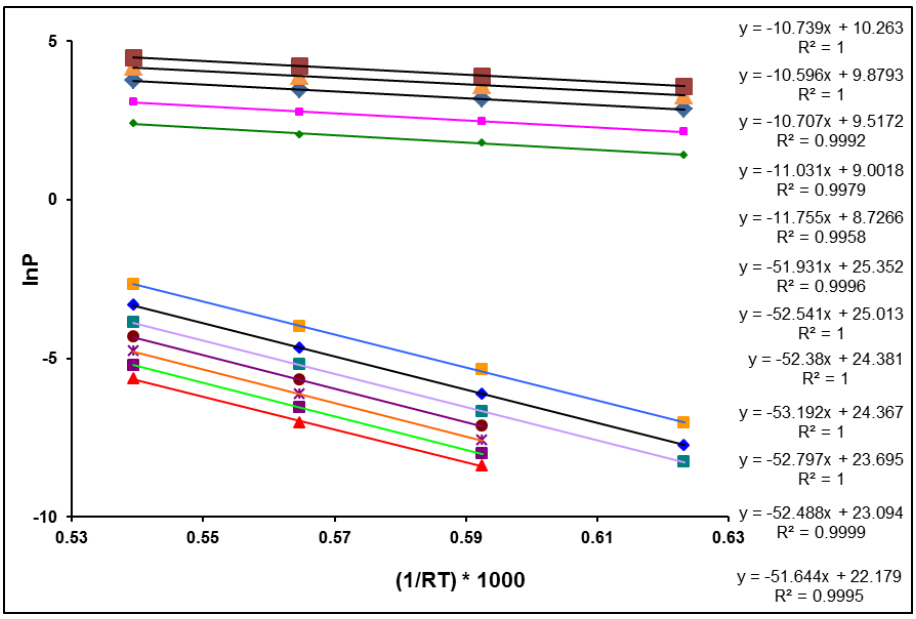

Figure S68. lnP versus 1/RT plots for different loadings for O_2 adsorption on Cu(I)-MFU-4*l* prepared *via* metal exchange in MFU-4*l* with CuCl/LiCl in DMA.

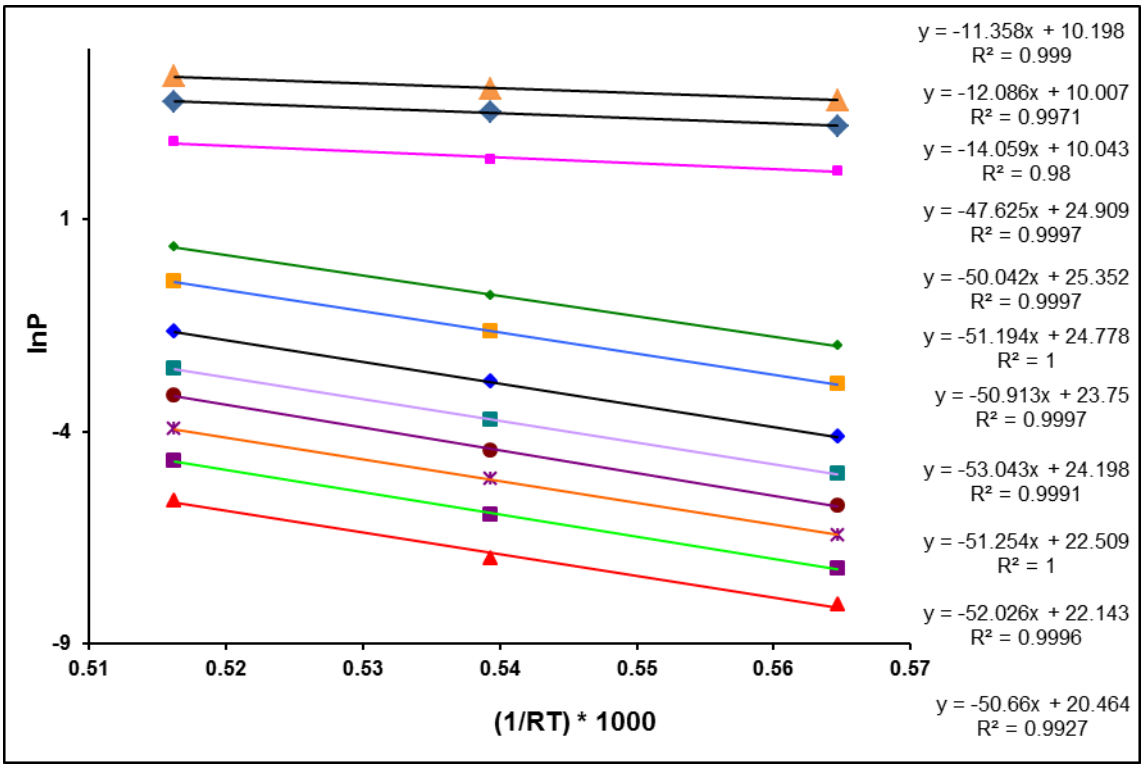

Figure S69. lnP versus 1/RT plots for different loadings for O_2 adsorption on Cu(I)-MFU-4*l* prepared *via* the gas-phase reduction of **5-F** with H_2.

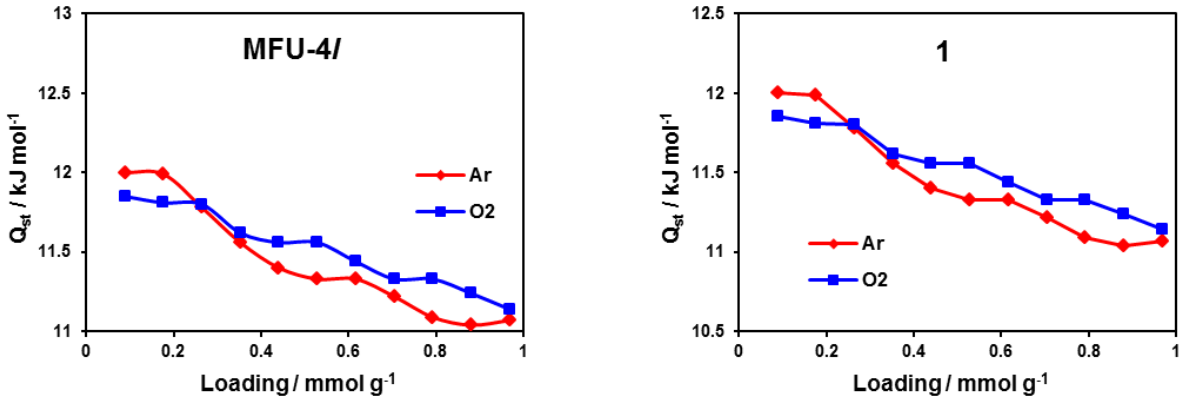

Figure S70. Dependence of isosteric heats of Ar and O_2 adsorption on loading for **MFU-4/** (left) and **1** (right).

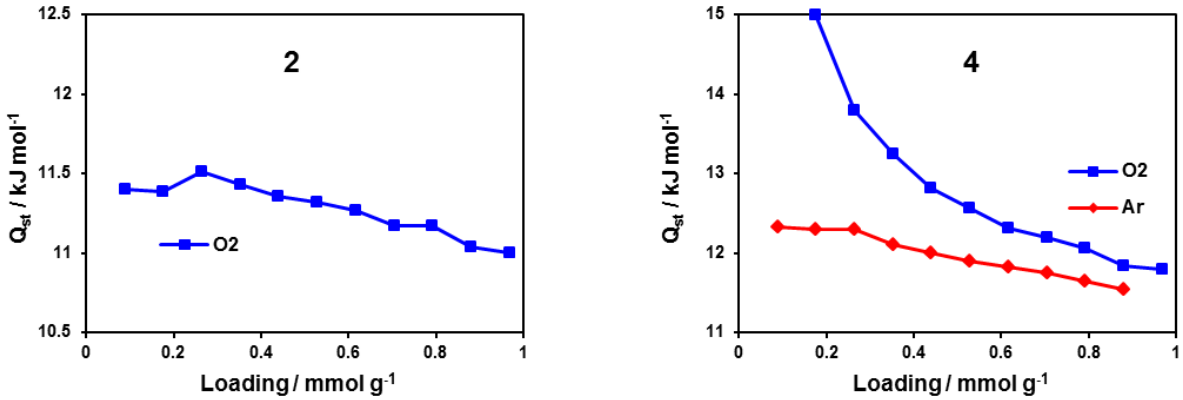

Figure S71. Dependence of isosteric heats of Ar and O_2 adsorption on loading for **2** (left) and **4** (right).

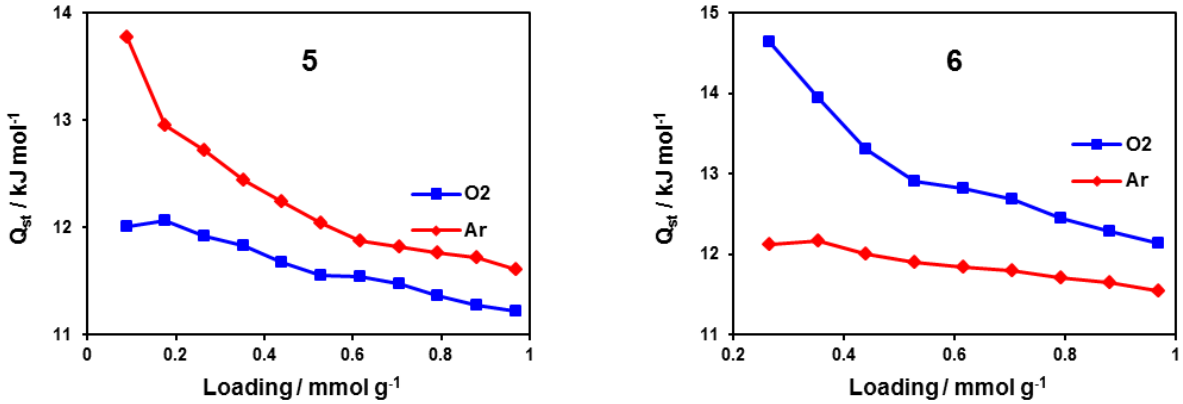

Figure S72. Dependence of isosteric heats of Ar and O_2 adsorption on loading for **5** (left) and **6** (right).

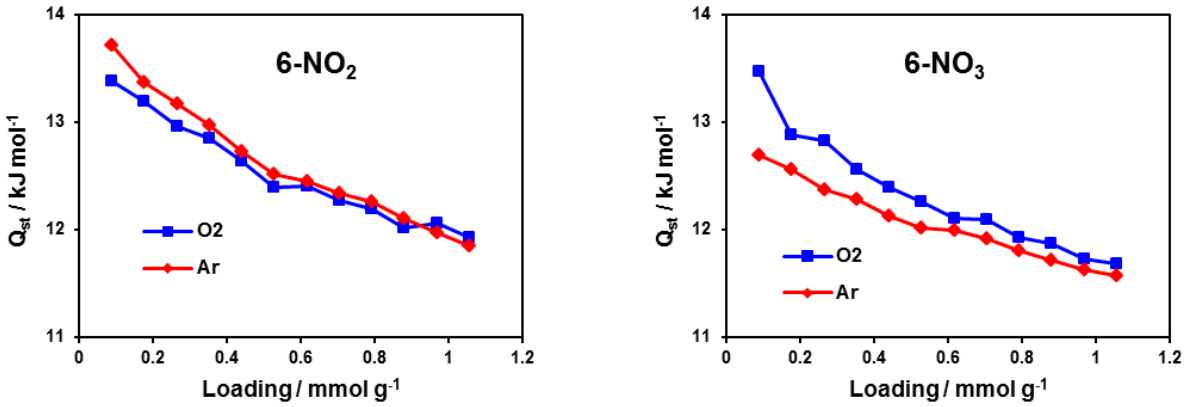

Figure S73. Dependence of isosteric heats of Ar and O_2 adsorption on loading for **6-NO$_2$** and **6-NO$_3$**.

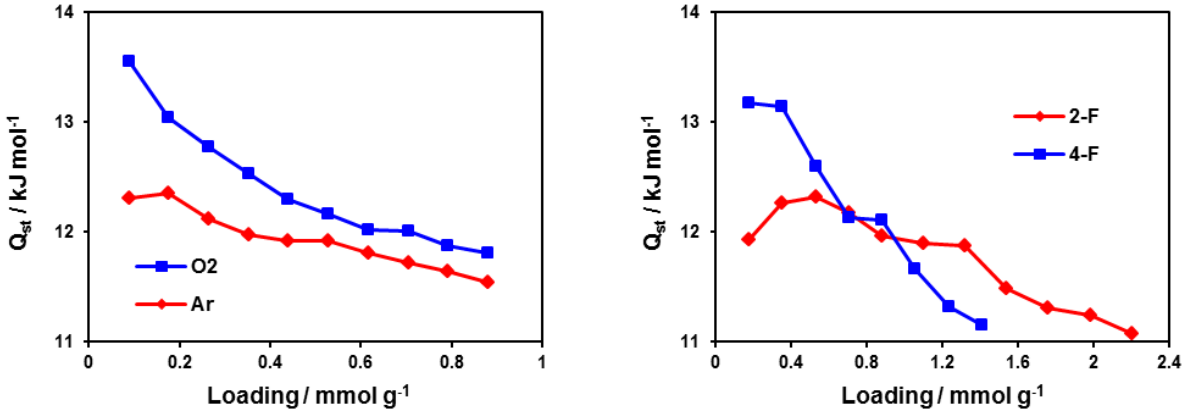

Figure S74. Dependence of isosteric heats of Ar and O_2 adsorption on loading for **6-OTf** and of O_2 adsorption for **2-F** and **4-F**.

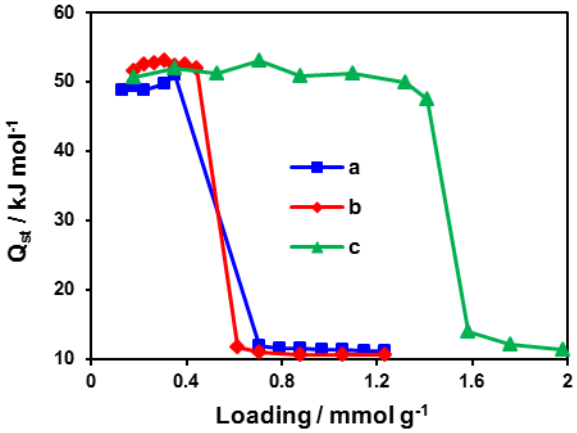

Figure S75. Dependence of isosteric heats of O_2 adsorption on Cu^{I}-MFU-4*l* prepared in different ways: *via* the solvothermal reduction of **5** in DMF (a), from MFU-4*l* *via* metal exchange (b) and *via* the gas-phase reaction of **5-F** with H_2 (c).

GC/MS measurements

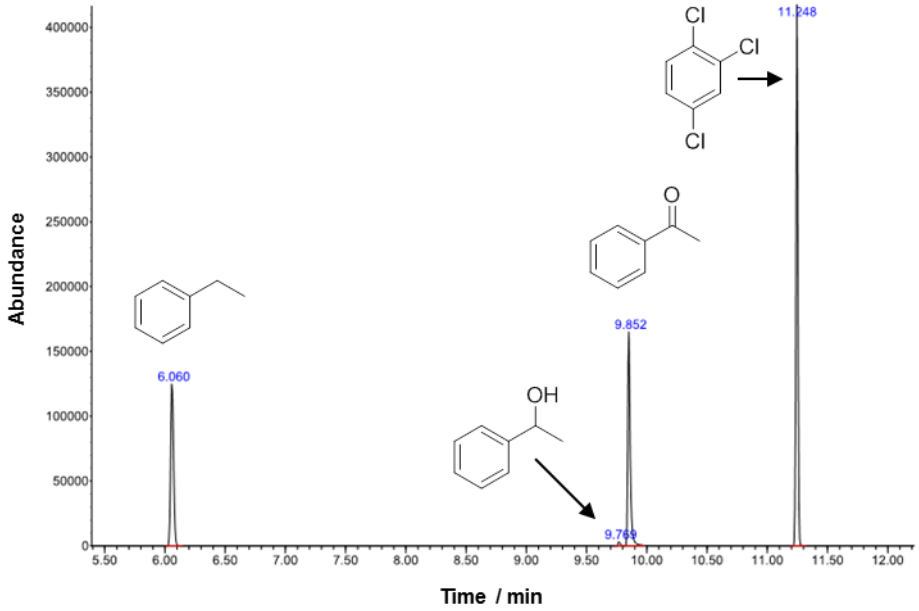

Figure S76. Representative GC/MS of the reaction mixture after catalytic oxidation of ethylbenzene.

ESI-MS measurements

The mass spectrometric experiments were performed with a Q-Tof Ultima mass spectrometer (Micromass) equipped with an ESI source. All samples were measured at the same conditions. Samples were injected into the ESI source with a flow rate of 10 μL min^{-1} and measured in an ESI negative mode. The ion-source voltage was 3.00 kV for capillary and 40 V for cone voltage. The collision energy was set to 8.0 eV. Each spectrum is an average of spectra collected within 2 min and was externally calibrated using phosphoric acid. The reaction mixture obtained after aerobic oxidation of ethylbenzene catalyzed by **6** was filtered through a syringe filter. 100 μL of the filtrate was mixed with known amounts of benzoic acid (0 μg, 0.92 μg, 1.84 μg and 4.6 μg - added as a solution in methanol) and diluted with methanol to a total volume of 1 mL. The concentration of benzoic acid in the reaction mixture calculated from the measured peak areas of benzoic acid (m/z = 121.06, $PhCOO^-$, Table S2) is 29±4 μg mL^{-1} which corresponds to 0.07 % yield.

Table S2. Peak areas for m/z = 121.06 ($PhCOO^-$) found in the reaction mixture after aerobic oxidation of ethylbenzene catalyzed by **6**.

Amount of benzoic acid added	0	0.92	1.84	4.6
Peak area	346	461	638	849

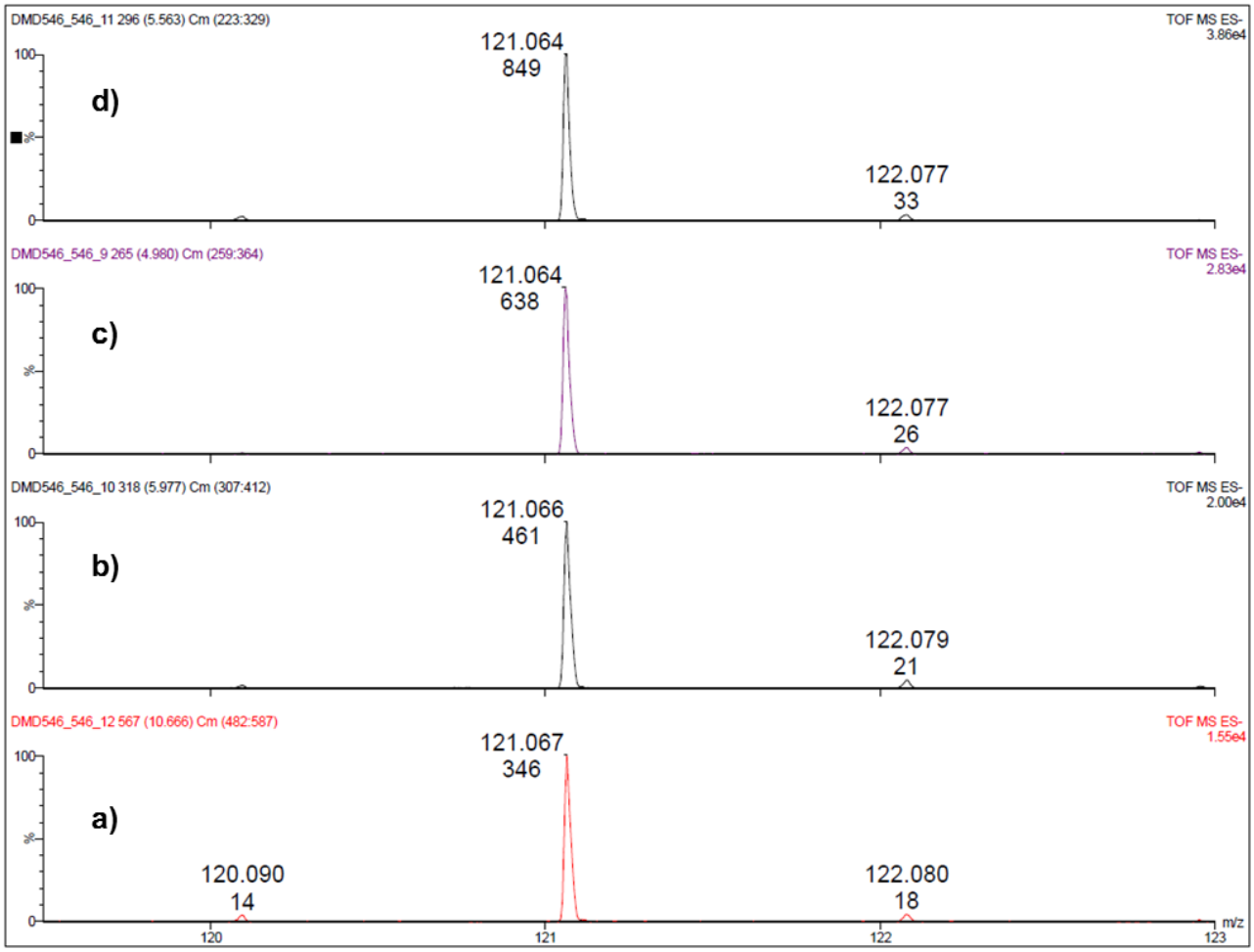

Figure S77. ESI-MS spectra showing benzoic acid peak (m/z = 121.06, $PhCOO^-$) in the reaction mixture after catalytic oxidation of ethylbenzene catalyzed by **6** after filtration and addition of different amounts of benzoic acid: 0 μg mL^{-1} (a), 9.2 μg mL^{-1} (b), 18.4 μg mL^{-1} (c), 46 μg mL^{-1} (d). The numbers below the mass are peak areas.

Powder X-ray diffraction measurements

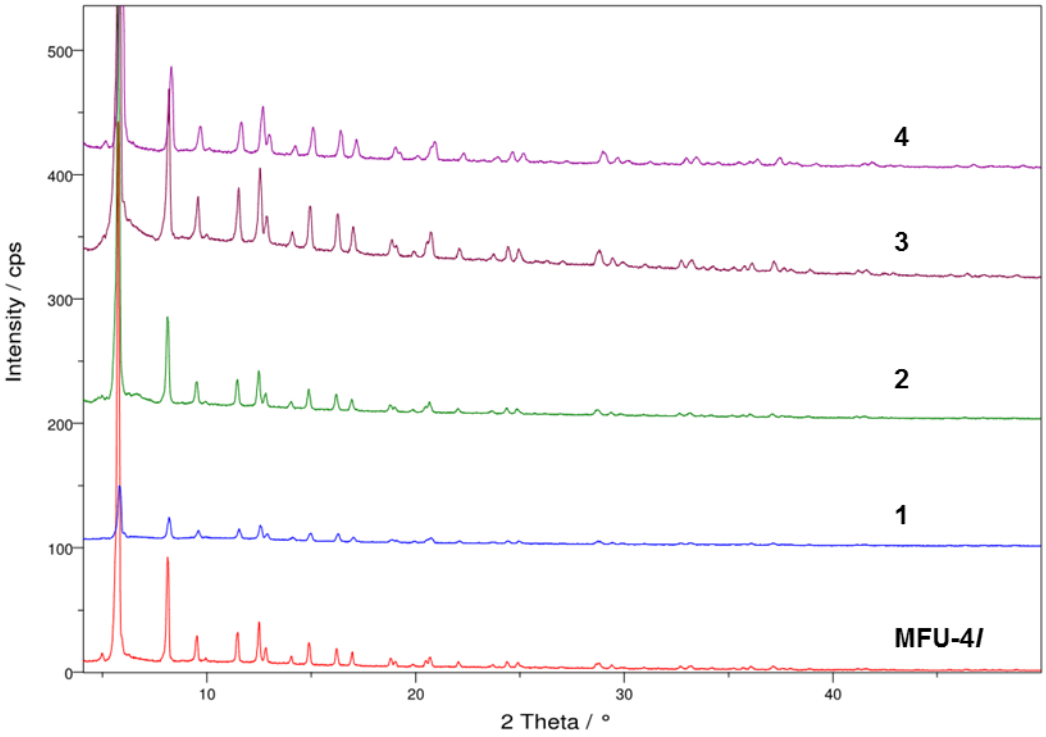

Figure S78. XRPD patterns of **1-4**.

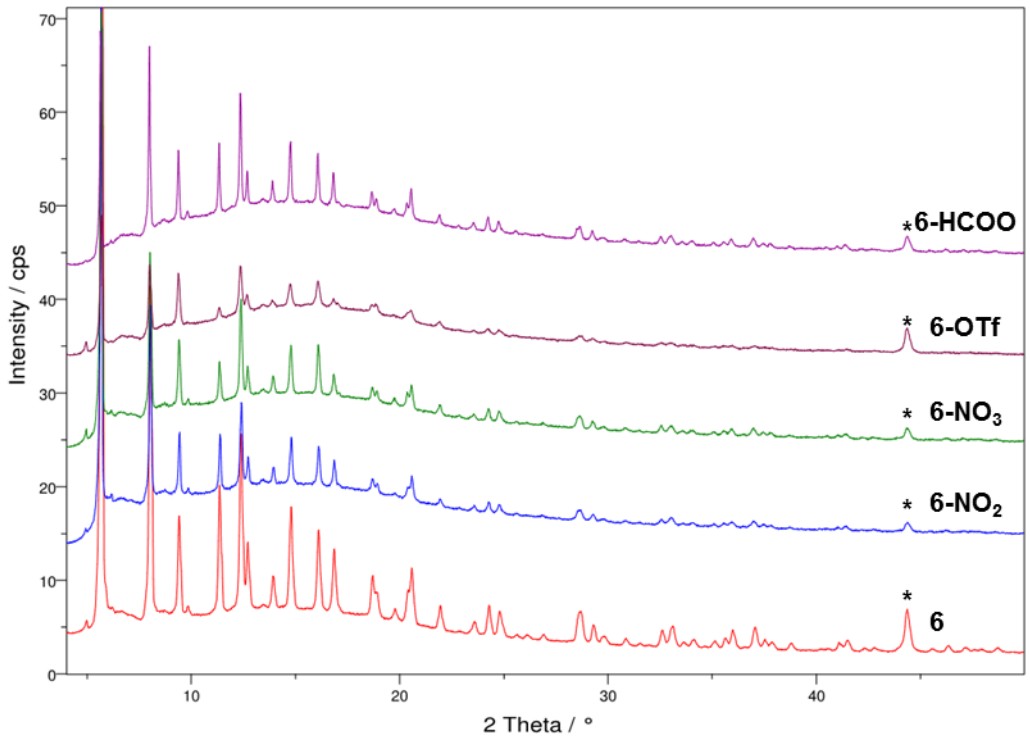

Figure S79. XRPD patterns of different derivatives of **6** (* - reflex from the sample holder).

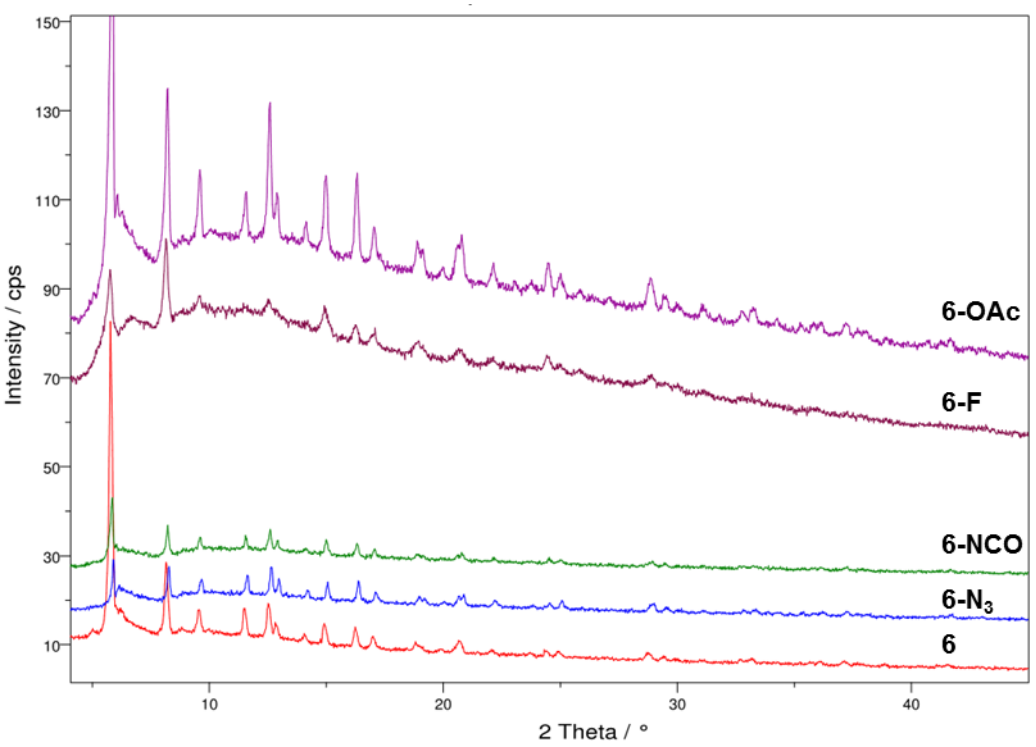

Figure S80. XRPD patterns of different derivatives of **6**.

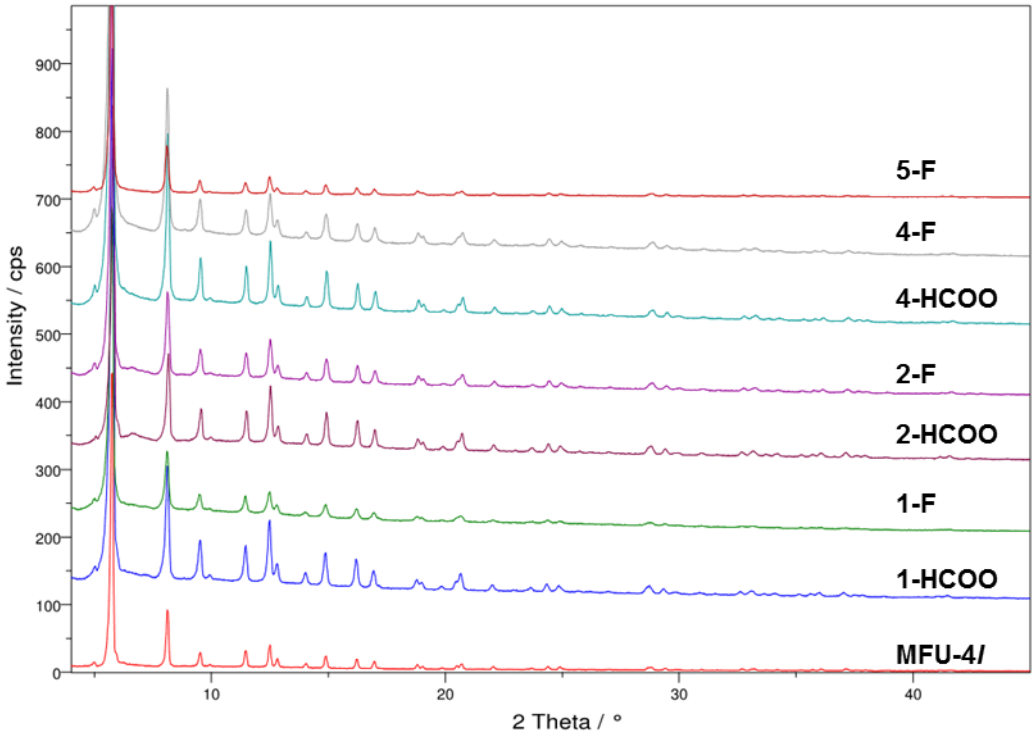

Figure S81. XRPD patterns of formate- and fluoride-substituted MFU-4*l* derivatives.

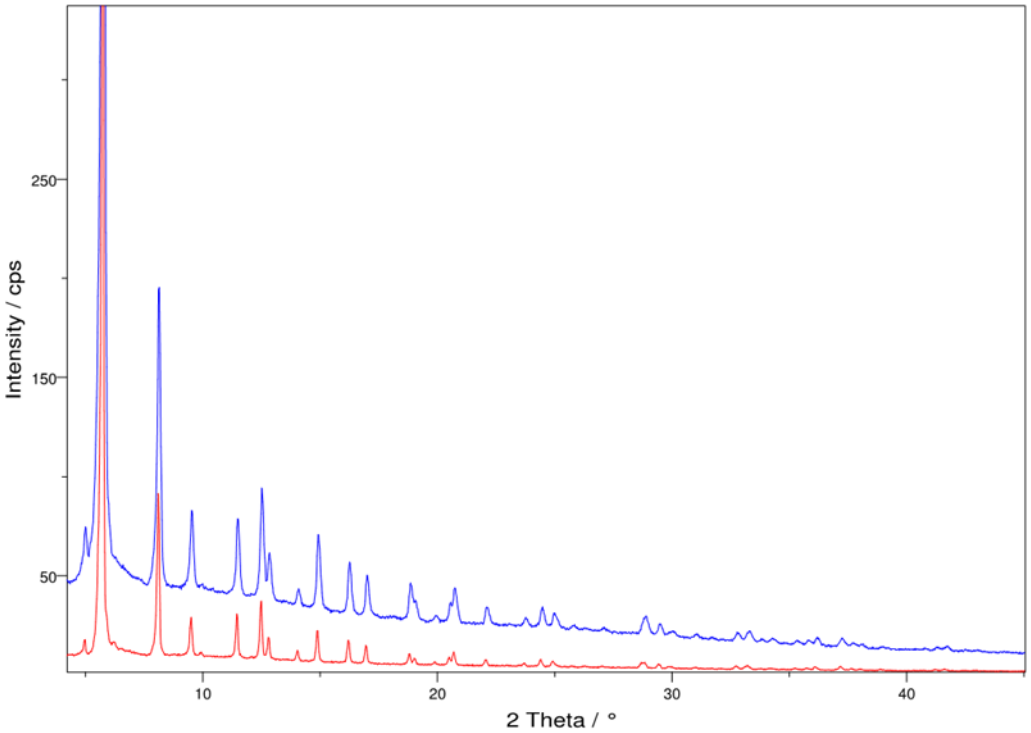

Figure S82. XRPD patterns of **5** before (red) and after (blue) use as a catalyst.

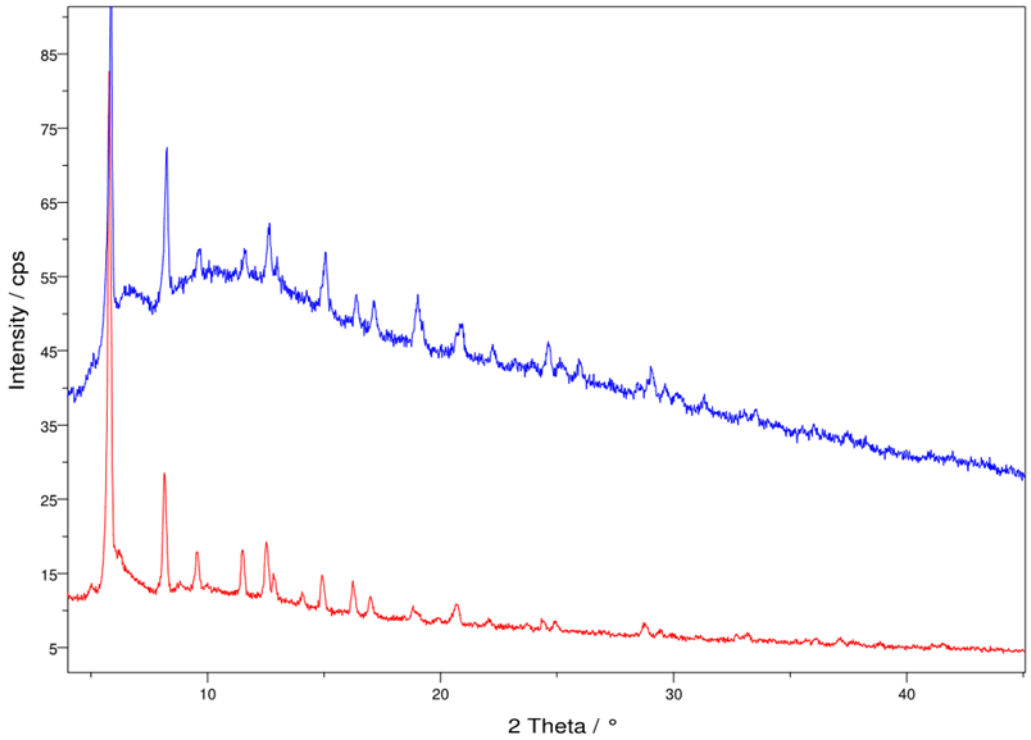

Figure S83. XRPD patterns of **6** before (red) and after (blue) use as a catalyst.

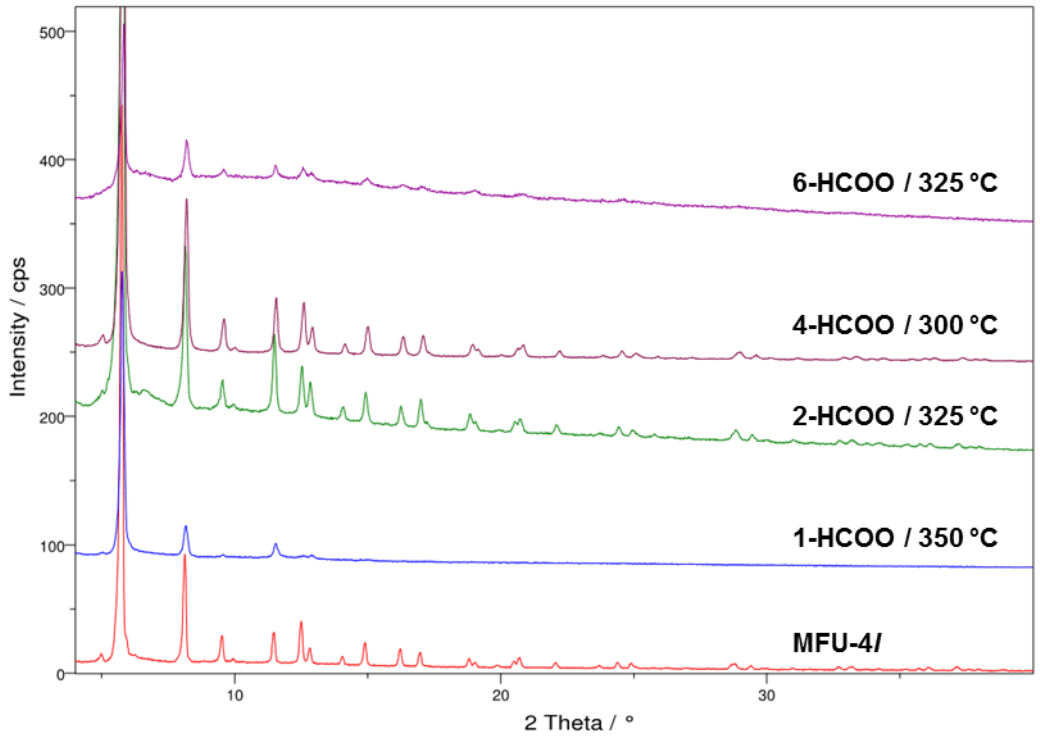

Figure S84. XRPD patterns of formate-substituted MFU-4*l* derivatives heated under N_2 flow.

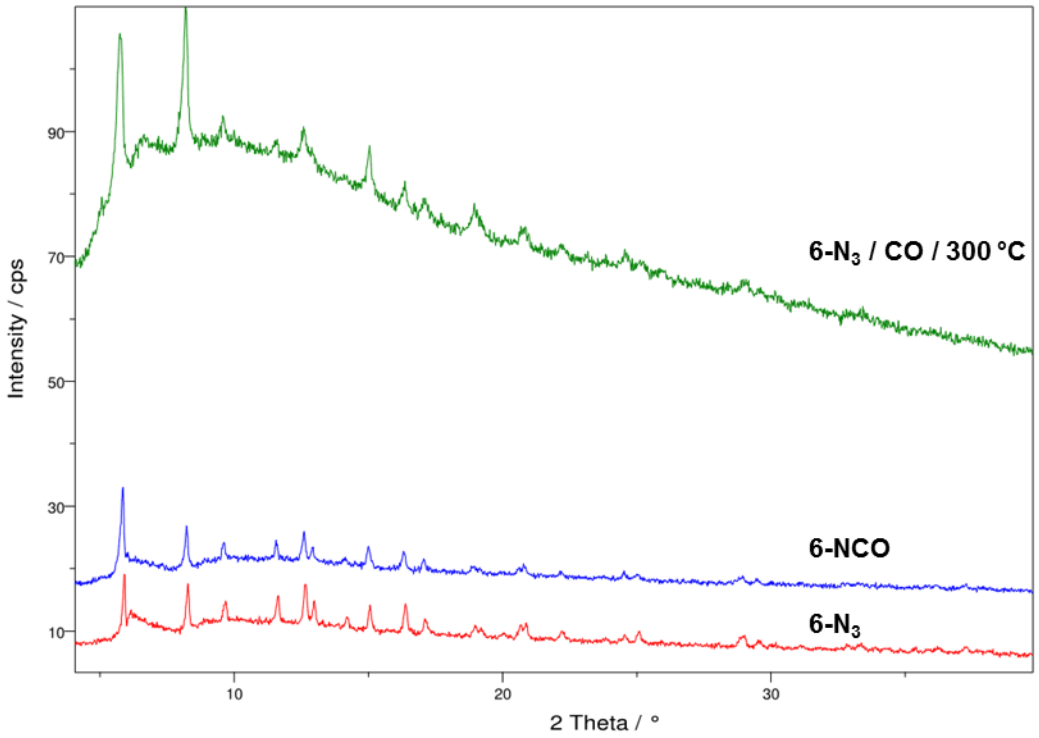

Figure S85. XRPD patterns of **6-N_3**, **6-NCO** and **6-N_3** heated at 300 °C under CO flow.

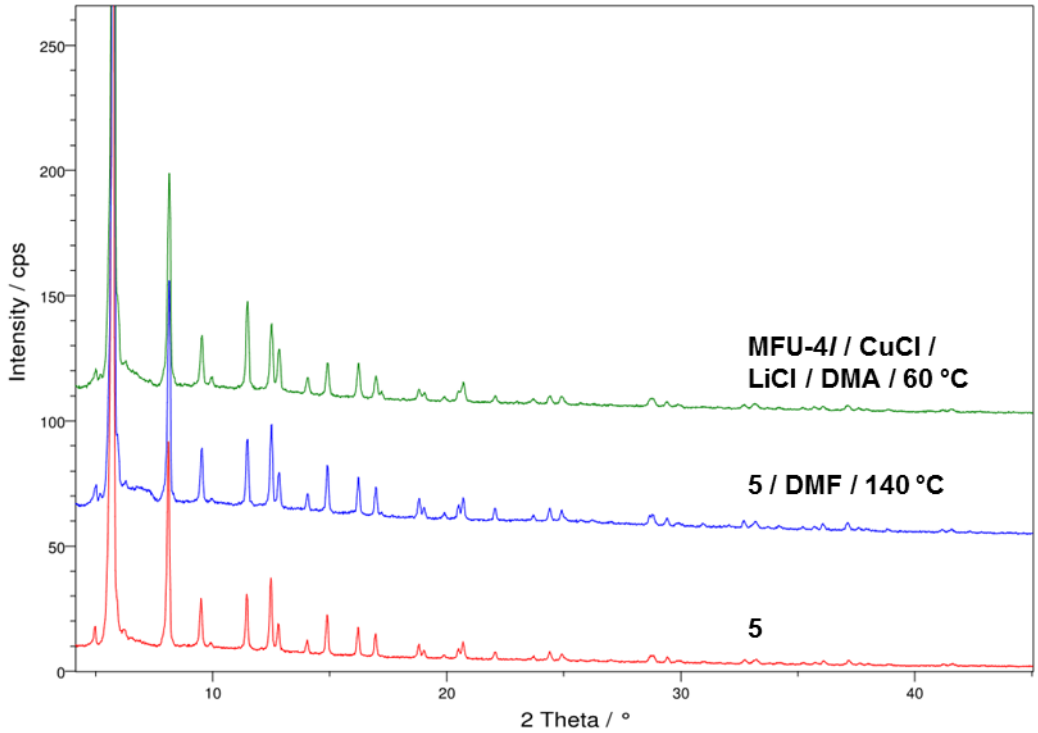

Figure S86. XRPD patterns of **Cu(I)-MFU-4*l*** obtained in different ways.

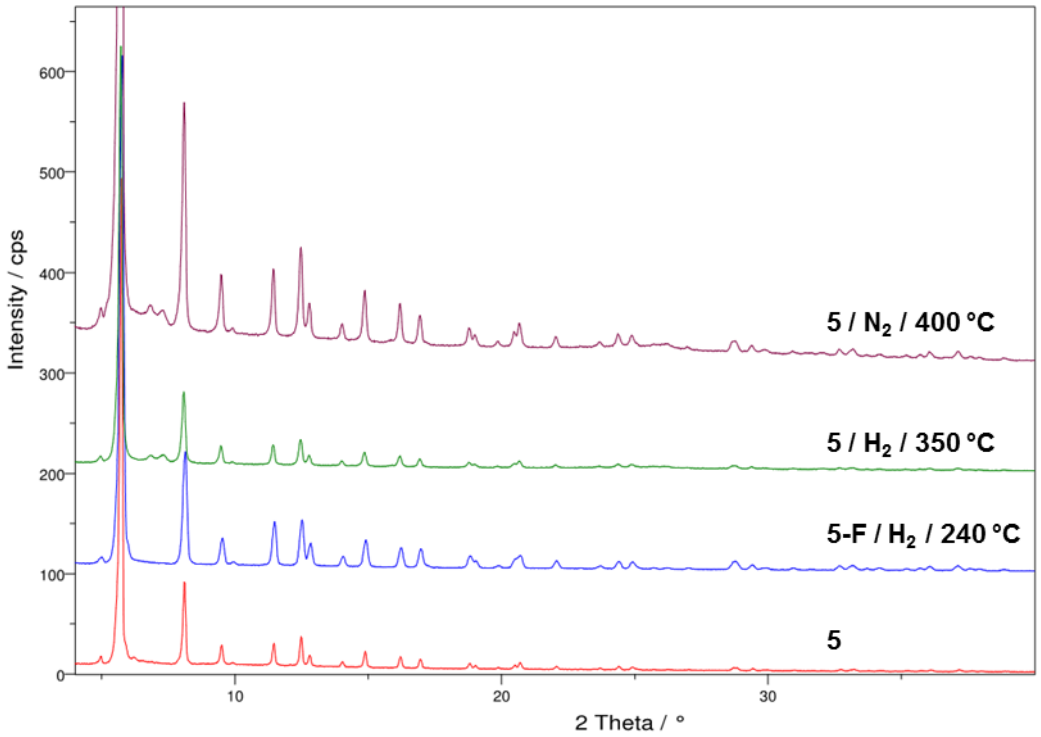

Figure S87. XRPD patterns of products obtained from **5** and **5-F**.

ESEM Micrographs

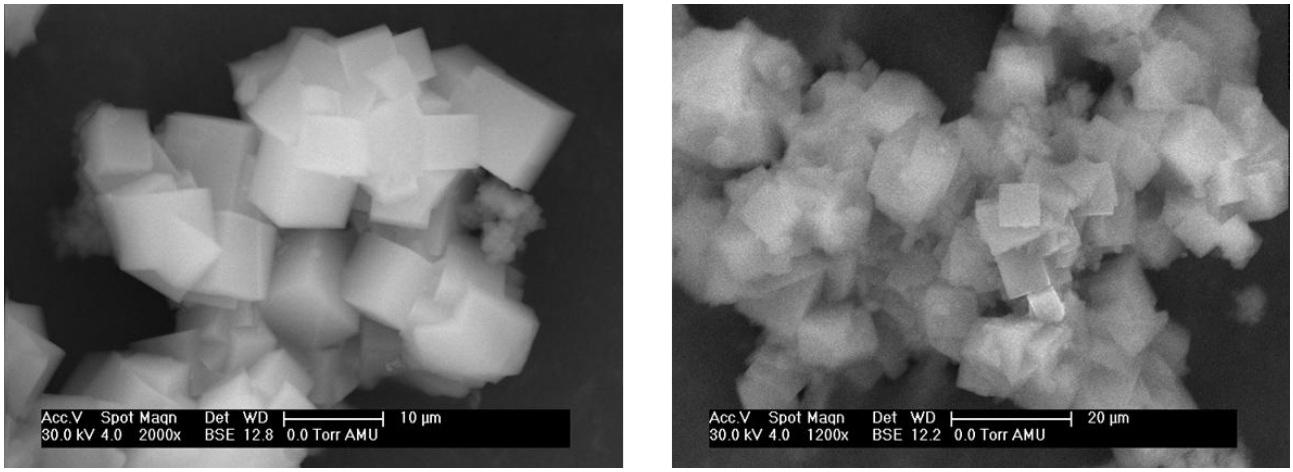

Figure S88. ESEM micrographs of **1** (left) and **2** (right).

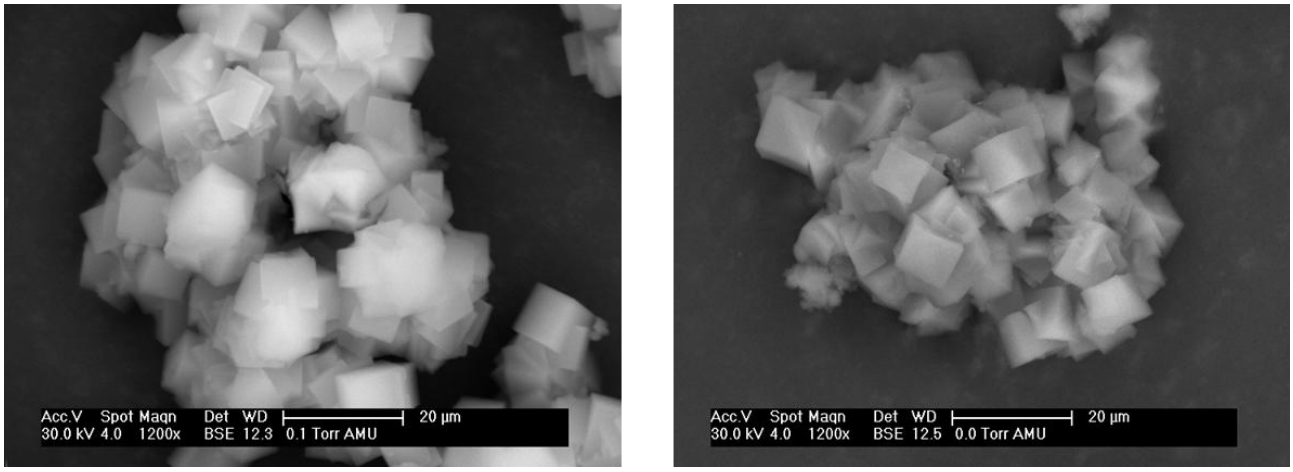

Figure S89. ESEM micrographs of **3** (left) and **4** (right).

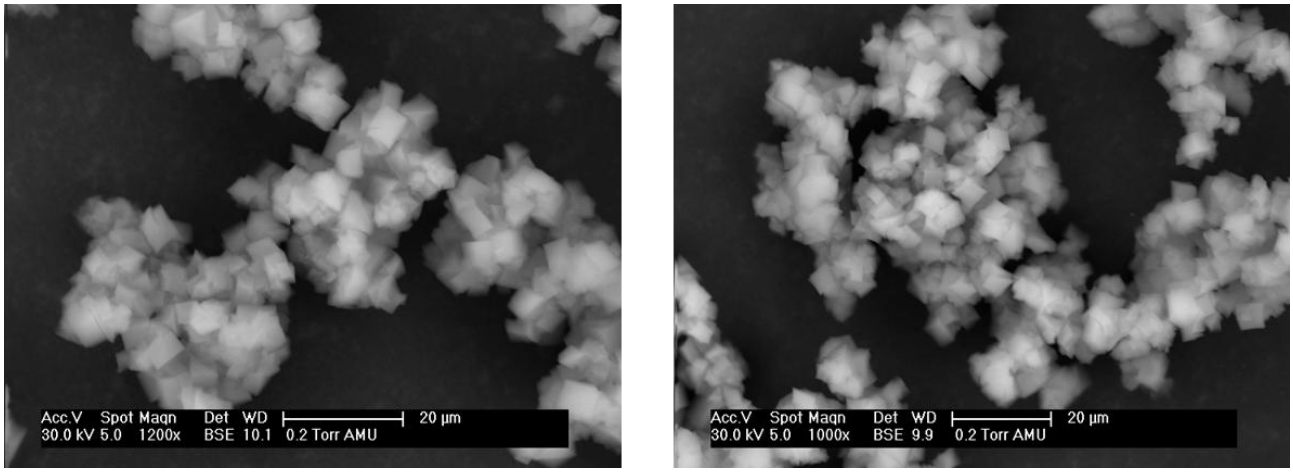

Figure S90. ESEM micrographs of **6-NO_2** (left) and **6-NO_3** (right).

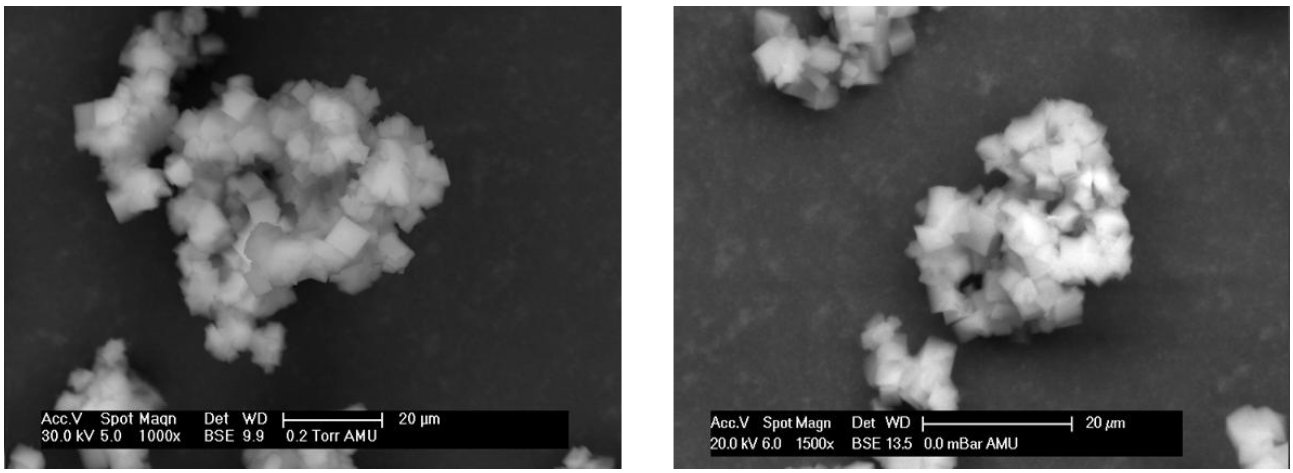

Figure S91. ESEM micrographs of **6-OTf** (left) and **6-HCOO** (right).

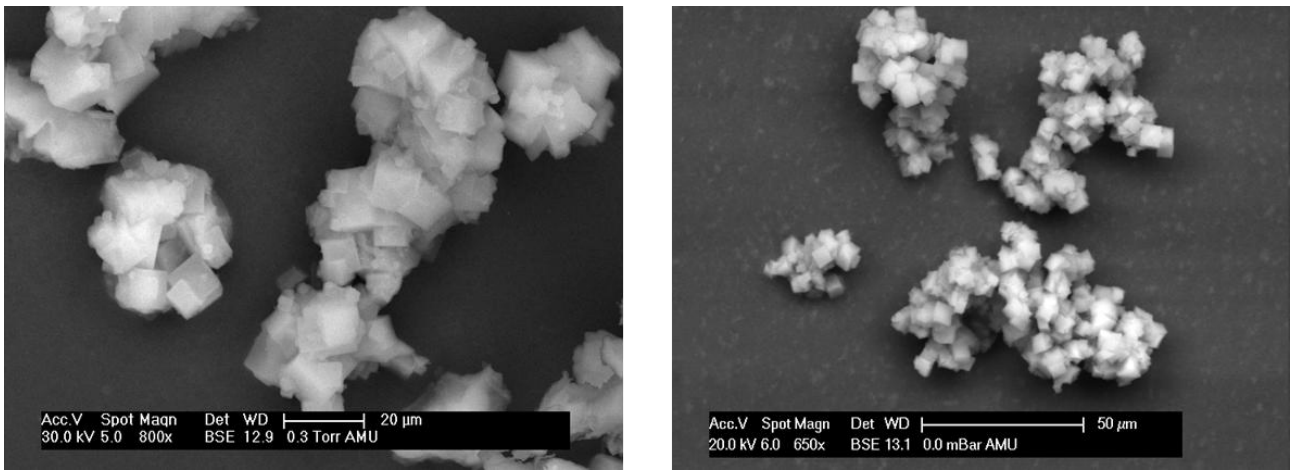

Figure S92. ESEM micrographs of **6-N_3** (left) and **6-OAc** (right).

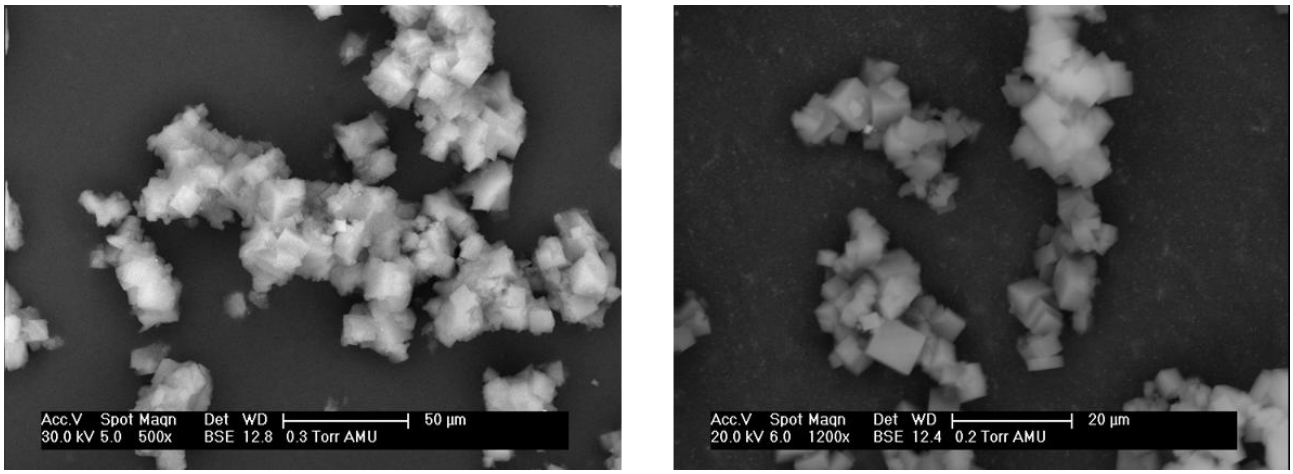

Figure S93. ESEM micrographs of **6-NCO** (left) and **1-HCOO** (right).

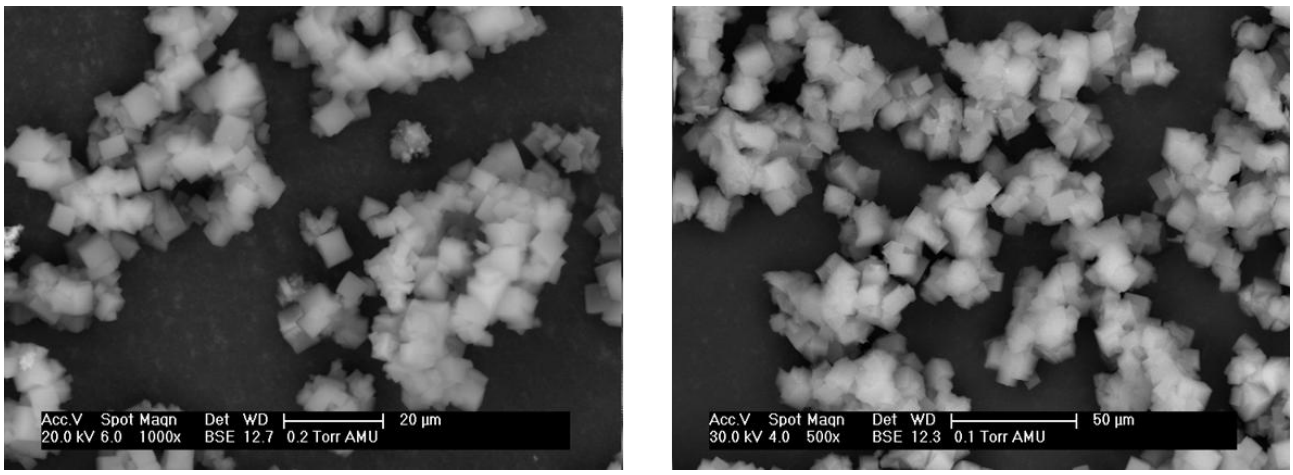

Figure S94. ESEM micrographs of **2-HCOO** (left) and **4-HCOO** (right).

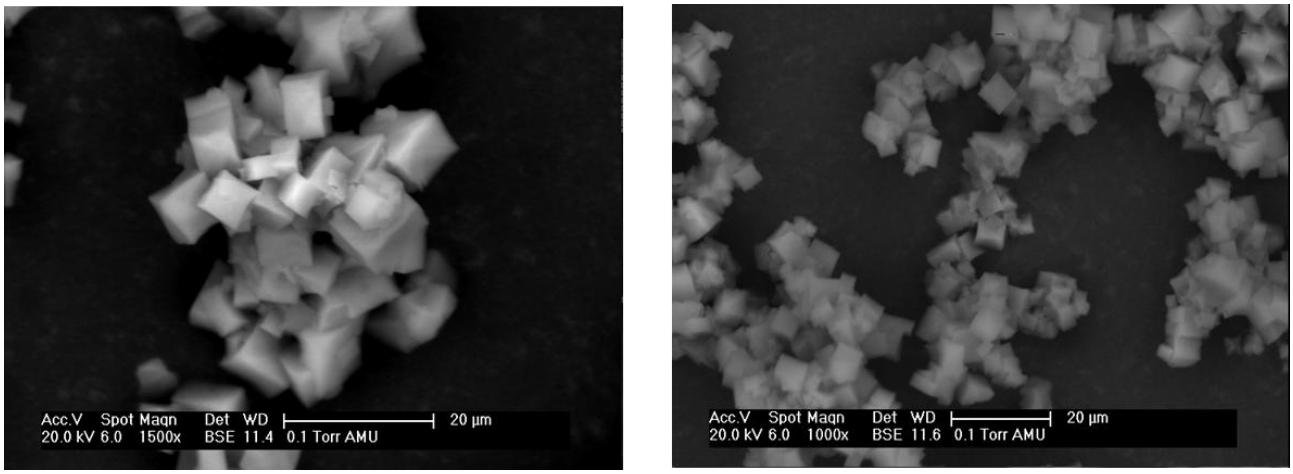

Figure S95. ESEM micrographs of **1-F** (left) and **2-F** (right).

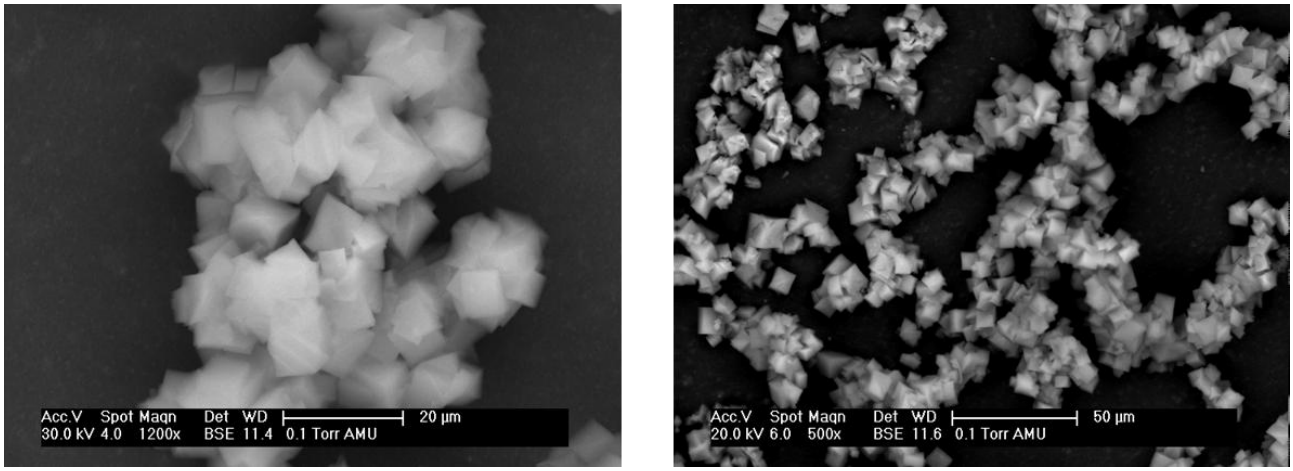

Figure S96. ESEM micrographs of **4-F** (left) and **5-F** (right).

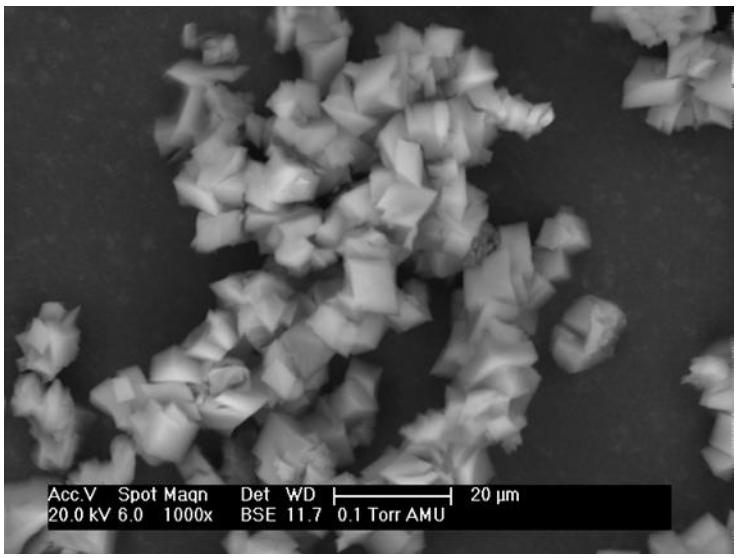

Figure S97. ESEM micrograph of **6-F**.

Microporous and Mesoporous Materials 216 (2015) 146–150

Contents lists available at ScienceDirect

Microporous and Mesoporous Materials

journal homepage: www.elsevier.com/locate/micromeso

Elucidating Lewis acidity of metal sites in MFU-4*l* metal-organic frameworks: N_2O and CO_2 adsorption in MFU-4*l*, Cu^I-MFU-4*l* and Li-MFU-4*l*

Dmytro Denysenko [a], Jelena Jelic [b], Oxana V. Magdysyuk [c], Karsten Reuter [b], Dirk Volkmer [a, *]

[a] Institute of Physics, Chair of Solid State and Materials Chemistry, University of Augsburg, Universitätsstrasse 1, D-86159 Augsburg, Germany
[b] Chair of Theoretical Chemistry and Catalysis Research Center, Technische Universität München, Lichtenbergstr. 4, D-85747 Garching, Germany
[c] Diamond Light Source Ltd., Harwell Science and Innovation Campus, OX11 0DE Didcot, United Kingdom

ARTICLE INFO

Article history:
Received 16 January 2015
Received in revised form
17 March 2015
Accepted 18 March 2015
Available online 25 March 2015

Keywords:
Metal-organic frameworks
Nitrous oxide
Adsorption
Copper

ABSTRACT

The interaction strength of N_2O and CO_2 molecules with different Lewis-acidic sites within MFU-4*l*–type metal-organic frameworks was studied *via* gas sorption measurements and density-functional theory calculations. MFU-4*l* comprising Zn–Cl units shows only physisorption of both gases. Introduction of Li into the parent MFU-4*l* framework leads to a remarkable increase of binding strength of both N_2O and CO_2 showing considerable Lewis acidity of Li^I centers. Cu^I-MFU-4*l* shows even stronger binding of N_2O, as compared to Li-MFU-4*l*, whereas CO_2 doesn't bind to Cu^I centers. Preferential binding of N_2O to Cu^I centers was also confirmed by *in situ* synchrotron X-ray powder diffraction measurements. These results show that Cu^I-MFU-4*l* can be considered as a material for selective N_2O adsorption.

1. Introduction

Metal-organic frameworks (MOFs) represent an exponentially growing class of functional porous materials featuring well defined pore structures, high internal surface areas, high thermal and chemical stability as well as possibility to vary pore size and chemical or physical properties [1]. MOFs have been extensively studied as materials for the capture of gases and vapors [2,3] and for gas separation and storage [4–6]. Despite of the huge number of publications on gas sorption, adsorption of nitrous oxide (N_2O) has only rarely been studied. Thus, to the best of our knowledge, it was only once described for MOFs (MOF-5 and MOF-177) [7] and only a few times for other porous materials such as active carbons [8–10] and zeolites [7,11–15]. Dissociative N_2O chemisorption is a widely used method for the characterization of metal-containing (especially copper-containing) catalysts [16,17]. N_2O is among the most powerful greenhouse [18] and ozone-depleting [19] gases and thus its removal from industrial waste gases is an important task [20]. Catalytic decomposition is a normally used approach for N_2O removal [21]. Adsorptive removal of N_2O by using metal-exchanged zeolites has been proposed for the cases where catalytic decomposition is not feasible economically due to very low N_2O concentration [22,23]. In this manuscript we describe N_2O adsorption on MFU-4*l* [24] and its Li- and Cu^I-derivatives. MFU-4*l*, constructed from deprotonated bis(1*H*-1,2,3-triazolo-[4,5-b],[4′,5′-i])dibenzo-[1,4]-dioxin $BTDD^{2-}$ ligands and $\{Zn_5Cl_4\}^{6+}$ building units, is a large-pore member of the MFU-4 structure family of cubic frameworks featuring exceptionally high thermal and solvolytic stability [25]. MFU-4 was studied for specific gas separation processes, i.e. separation of isotopologues H_2 and D_2 by quantum sieving [26] and kinetic CO_2/N_2 separation [27]. MFU-4*l* was suggested for technically demanding separation of Kr and Xe [28,29]. The SBUs (secondary building units) of this framework contain Kuratowski-type coordination units [30–32] that include one octahedrally coordinated (central) metal ion and four tetrahedrally coordinated (peripheral) metal ions, the latter structurally related to well-known scorpionate complexes [33]. Postsynthetic metal and ligand exchange allows to prepare a large variety of MFU-4*l* frameworks containing Mn^{II}, Fe^{II}, Co^{II}, Ni^{II}, Cu^{II} and Cu^I ions in peripheral positions [34–36]. Cu^I-MFU-4*l* was shown to chemisorb reversibly several simple gas molecules (e.g. H_2, N_2 and O_2) [35]. Besides

* Corresponding author.
E-mail address: dirk.volkmer@physik.uni-augsburg.de (D. Volkmer).

http://dx.doi.org/10.1016/j.micromeso.2015.03.014
1387-1811/

technically relevant applications, studying the adsorption of small gas molecules in MOFs possessing well defined single-site active centers (in contrast to structurally fluctuating species in solutions, zeolites or non-porous solids) might help to understand the role of active sites and to design an optimized framework for gas capture, purification or separation. Detailed studies on metal-exchanged zeolites have shown that the metal ion plays an important role for N_2O sorption properties. Thus, Ba-ZSM-5 was found to be the most efficient material for N_2O adsorption [23]. The enhanced properties of Ba-ZSM-5 in the N_2O adsorption are not related to a specific chemisorption but rather to a strong electrostatic field generated by naked Ba^{2+} ions within the zeolite cavities [23]. A weak binding of the N_2O molecule to Cu^{I} sites in Cu^{I}-ZSM-5 has been observed with IR spectroscopy at 110–120 K [37]. Herein, we study the influence of Lewis-acidic metal sites in MFU-4*l* on N_2O adsorption properties. Since N_2O, possessing only weak dipole moment (0.161 D), is isoelectronic with CO_2 and has very similar physical and physisorption properties [22], comparing the interaction strength for these two molecules will help to find an optimized framework for selective N_2O adsorption.

2. Experimental

All starting materials were of reagent grade and used as received from the commercial supplier. Fourier transform infrared (FTIR) spectra were recorded with an ATR unit in the range 4000–400 cm^{-1} on a Bruker Equinox 55 FT-IR spectrometer. Thermogravimetric analysis (TGA) was performed with a TA Instruments Q500 analyzer in the temperature range of 25–800 °C in flowing nitrogen gas at the heating rate of 5 K min^{-1}. ICP-OES analyses were performed on a Varian VISTA MPX simultaneous spectrometer with a CCD detector. Elemental analyses were measured with a Vario EL III instrument from Elementar Analysensysteme GmbH. Gas sorption isotherms were measured with a BELSORP-max instrument combined with a BELCryo system. Adsorbed amounts are given in cm^3 g^{-1} [STP], where STP = 101.3 kPa and 273.15 K. Prior to measurements, the samples of MFU-4*l* and Li-MFU-4*l* were heated at 200 °C for 20 h in high vacuum to remove the occluded solvent molecules. Cu^{I}-MFU-4*l* was prepared *in situ* by heating Cu^{II}-MFU-4*l*–formate under vacuum (10^{-3} mbar) up to 180 °C (with a heating rate of 4 K min^{-1}) and keeping the sample at this temperature for 1 h (as described previously [35]). X-ray powder diffraction measurements of N_2O adsorption at different temperatures and pressures in Cu^{I}-MFU-4*l* were performed at the diffractometer I12 at Diamond (UK). All DFT calculations have been performed with the all-electron full-potential code FHI-aims [38,39]. Electronic exchange and correlation was treated on the level of the generalized gradient approximation (GGA) PBE functional [40] for the geometry optimizations and on the level of the hybrid B3LYP functional [41,42] for consecutive single point calculations on these optimized geometries. Dispersive interactions lacking at these levels of theory were considered through the dispersion-correction scheme due to Tkatchenko and Scheffler [43]. Geometry optimization was performed using tight, tier1 basis sets until residual forces fell below 10^{-4} eV/Å. Hybrid B3LYP + TS energetics, corrected for the zero point energy, are the finally presented numbers in the paper. MFU-4*l* systems are represented by a Scorpionate-type unit with Zn substituting the B–H unit. For N_2O adsorption, both coordination modes, *via* the N- or O-atom, were considered. The final binding geometry discussed here represents the energetically most favorable state.

2.1. Preparation of Li-MFU-4l

LiCl (1.38 g, 32.5 mmol) was dissolved in N,N-dimethylformamide (130 mL) and MFU-4*l* (0.8 g, 0.634 mmol) was added to the solution. The reaction mixture was heated for 20 h at 60 °C in a sealed tube. The precipitate was filtered off, washed with DMF, methanol and dichloromethane and dried at 150 °C under vacuum. The yield is close to quantitative. The number of Li^+ ions in the formula unit was calculated from the Li/Zn ratio determined by ICP-OES analysis. The slightly yellow product is hygroscopic and may contain variable amount of adsorbed water. Number of Li^+ ions in the formula unit: 1.91. Anal. calcd. for $C_{36}H_{12}Cl_2N_{18}O_6Li_2Zn_3 \cdot 2H_2O$: C, 38.97; H, 1.45; N, 22.72. Found: C, 39.17; H, 2.11; N, 22.73%. IR (ATR, cm^{-1}): 3079 (w), 1615 (w), 1575 (w), 1461 (s), 1348 (s), 1172 (s), 916 (m), 850 (m), 809 (w), 533 (m), 425 (w). BET surface area (Ar, 87.3 K): 3356 m^2 g^{-1}.

3. Results and discussion

Li-MFU-4*l* was prepared *via* postsynthetic metal exchange from MFU-4*l* and LiCl in DMF at 60 °C (Fig. 1). Similarly to a previously described metal exchange with $MnCl_2$, $FeCl_2$, $NiCl_2$ and $CuCl_2$ [35,36], approx. 2 of 4 Zn^{2+} ions in the SBU are substituted at these conditions leading to a framework with the composition $[Li_2Zn_3Cl_2(BTDD)_3]$. Performing the reaction at 140 °C, as described previously for $CoCl_2$ [34], leads to a complete dissolution of MFU-4*l*. According to the TGA data, which show a weight loss of 3.0% below 100 °C, and furthermore confirmed by elemental analysis, the framework obtained upon drying in vacuum and subsequent exposure to air has a net composition formulated as $[Li_2Zn_3Cl_2(BTDD)_3] \cdot 2H_2O$, which corresponds to one bound water molecule per lithium ion. This observation shows immediately that Li^+ ions in the SBU of MFU-4*l* represent centers of much stronger Lewis-acidy as Zn^{II}–Cl units which do not bind water molecules at the same conditions. The isosteric heats of CO_2 and N_2O adsorption in MFU-4*l* determined from the adsorption isotherms (as described in Supplementary Information) are very similar (16.4 and 17.9 kJ mol^{-1} at 0.35 mmol g^{-1} loading, respectively, see Table 1) and decrease only slightly with increasing loading (Figs. 2 and 3). These values stay in agreement with the DFT-calculated binding energies (Table 1) and correspond to a physisorbed state. Although the Lewis acidity of Zn^{II} is well-documented in the literature [44], Zn^{II}–Cl units within the MFU-4*l* framework do not coordinate CO_2

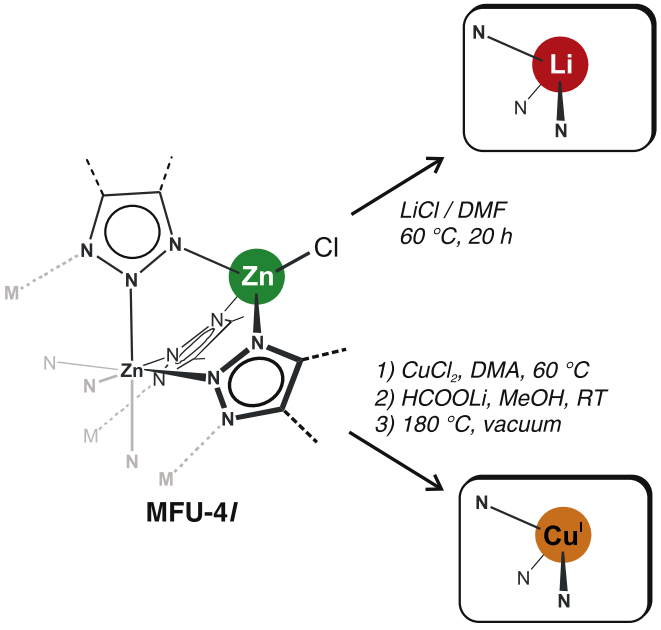

Fig. 1. Preparation of Cu^{I}- and Li-derivatives of MFU-4*l* *via* postsynthetic modification.

Table 1
Experimental and DFT-calculated binding energies for CO_2 and N_2O in MFU-4*l* derivatives.

Compound	Peripheral unit in the SBU	CO_2 binding energy/kJ mol^{-1}		N_2O binding energy/kJ mol^{-1}	
		Experimental[a]	DFT-calculated	Experimental[a]	DFT-calculated
MFU-4*l*	Zn^{II}–Cl	16.4 ± 0.1	17	17.9 ± 0.3	18
Li-MFU-4*l*	Li^{I}	22.7 ± 0.9	25	23.6 ± 0.2	25
Cu^{I}-MFU-4*l*	Cu^{I}	15.3 ± 0.5	18	30.8 ± 1.4	33

[a] Isosteric heat of adsorption at 0.35 mmol g^{-1} loading. Errors are the standard deviations calculated for the linear regression.

or N_2O molecules since this would require an energetically unfavorable distortion of the tetrahedral coordination of the Zn^{II} centers. Li^+ ions in the trigonal-pyramidal coordination within the SBU of MFU-4*l*, in contrast, possess at least one free coordination site which can be filled without any energetic barrier leading to the tetrahedral coordination. A tetrahedral configuration, common for non-transition metal ions, has very often been observed for Li^+ [45]. In accordance with this, Li-MFU-4*l* shows considerably higher isosteric heats of CO_2 and N_2O adsorption (22.7 and 23.6 kJ mol^{-1} at 0.35 mmol g^{-1} loading, respectively, see Table 1) which decrease slowly with increasing loading (Figs. 2 and 3). The values are very similar for both gases as also predicted by our DFT calculations (Table 1) and correspond to a weak interaction of the adsorbed gas molecules with the Li^+ ions. The weak binding is also confirmed by quite long atomic distances (2.25 Å Li–O distance for CO_2 and 2.35 Å Li–N distance for N_2O) as can be seen from the binding geometries obtained from the DFT calculations (Fig. 4). These results can be well explained within the HSAB (hard and soft (Lewis) acids and bases) concept [46]. Due to this concept, Li^+ ions are hard Lewis acids with high charge density (chemical hardness $\eta = 35.12$ eV), whereas CO_2 and N_2O possess quite similar moderate chemical hardness as Lewis bases (8.8 and 7.6 eV, respectively) [47]. This results in a similar moderate binding of CO_2 and N_2O to Li^+ ions. The situation is completely different in the case of Cu^I. Thus, Cu^I-MFU-4*l* shows only physisorption of CO_2 (isosteric heat of adsorption 15.3 kJ mol^{-1} at 0.35 mmol g^{-1} loading, see Table 1). DFT calculations predict low interaction energy (Table 1) and large Cu^I–CO_2 distance as well (Fig. 5a). N_2O, in contrast, shows quite strong binding to Cu^I centers (isosteric heat of adsorption in Cu^I-MFU-4*l* is 30.8 kJ mol^{-1} at 0.35 mmol g^{-1} loading, see Table 1). The high binding energy for N_2O on Cu^I centers is also confirmed by DFT (Table 1). The calculated binding geometry reveals an almost linear orientation of the N_2O molecule (with respect to the Cu–N bond) and a Cu–N distance of 1.94 Å (Fig. 5b). Both speak for a chemical binding between Cu^I and N_2O. In terms of the HSAB concept, Cu^I is a soft Lewis acid with low charge density (chemical hardness $\eta = 6.28$ eV [47]) and thus it is not surprising that CO_2 doesn't bind to Cu^I. However, a relatively strong binding of N_2O to Cu^I centers cannot be explained easily within the HSAB concept unless N_2O is a slightly softer Lewis base as compared to CO_2. This fact underscores the specific character of the Cu^I–N_2O interaction. Looking at the results of the Hirshfeld charge analysis for Li–N_2O and Cu^I–N_2O adducts within the Kuratowski unit (Table 2) we can see that Li^+ ions change their charge from +0.301 to +0.2096 upon N_2O binding. This behavior corresponds to a typical coordinative binding – Li^+ acts as a Lewis acid (electron accepting) whereas N_2O serves as a Lewis base (electron donating). Coordination of N_2O molecule to Cu^I center, in contrast, do not lead to a considerable changes of atomic charges (Cu^+ changes its charge from +0.22851 to +0.2149) unless even stronger binding is observed. These results might speak for the partial charge transfer from Cu^I to N_2O compensating the coordinative donation of electron density from N_2O to Cu^+. Thus, binding of N_2O to Cu^I might be related to the charge-donating properties of Cu^I as well as electron accepting properties of N_2O

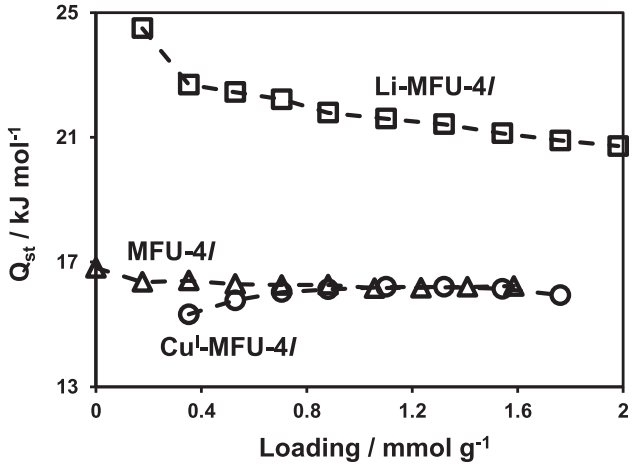

Fig. 2. Dependence of isosteric heats of CO_2 adsorption on loading for MFU-4*l* (triangles), Cu^I-MFU-4*l* (circles) and Li-MFU-4*l* (squares).

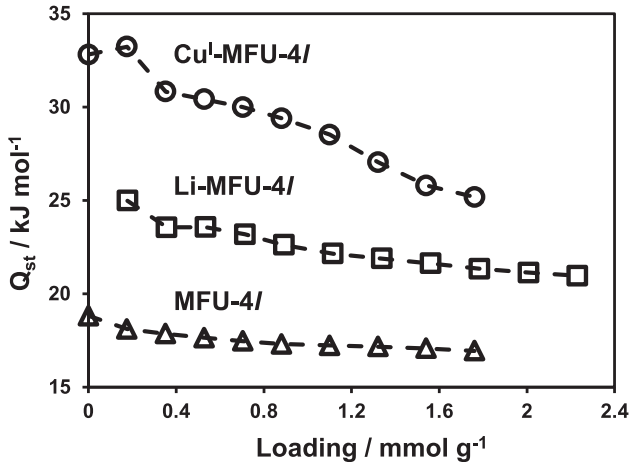

Fig. 3. Dependence of isosteric heats of N_2O adsorption on loading for MFU-4*l*, Cu^I-MFU-4*l* and Li-MFU-4*l*.

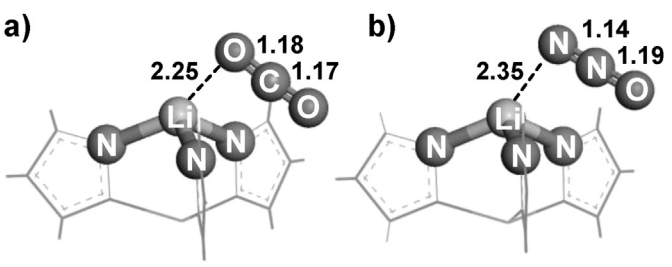

Fig. 4. Binding geometries for CO_2 (a) and N_2O (b) at the Li^I sites within the Kuratowski unit of MFU-4*l* as obtained from DFT calculations (atomic distances in Å).

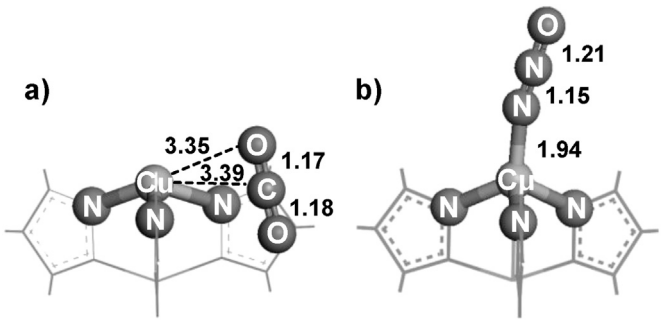

Fig. 5. Binding geometries for CO_2 (a) and N_2O (b) at the Cu^I sites within the Kuratowski unit of MFU-4*l* as obtained from DFT calculations (atomic distances in Å).

Table 2
Hirshfeld charge analysis for Li–N_2O and Cu^I–N_2O adducts within the Kuratowski unit.

Compound/atom[a]	Li-MFU-4*l*		Cu^I-MFU-4*l*	
	Plain[b]	Adduct	Plain[b]	Adduct
M(I)	+0.301	+0.2096	+0.22851	+0.2149
N1	−0.0718	−0.0464	−0.0718	−0.0385
N2	+0.2078	+0.2379	+0.2078	+0.2135
O	−0.1359	−0.0841	−0.1359	−0.1284

[a] M(I) – Li or Cu^I atom of the Kuratowski unit. N1 – terminal N-atom of the N_2O molecule, N2 – the central one.
[b] Plain refers to the Li- or Cu^I–Kuratowski unit and N_2O molecule in the gas phase.

which are reflected in its considerably higher electron affinity as compared to CO_2 [47]. Due to its poor ligand characteristics (low dipole moment and weak σ-donor and π-acceptor properties [48]), N_2O complexes are very rare and have so far only been described for Ru^{II} and V^{III} [49–51].

The preferential binding of N_2O to Cu^I centers is also confirmed by *in situ* synchrotron X-ray powder diffraction measurements. The quality of the data as well as the high temperature of the measurements did not allow the determination of the orientation of the linear N_2O molecule, so that only the approximate position of the center of rotation for the N_2O molecule could be determined. The rotationally (and possibly positionally) disordered N_2O molecule was modeled as a large sphere with a center, coinciding with the center of mass of the molecule. This approximation allows correct determination of positions, but analysis of the N_2O–framework distances is complicated. In total, six adsorption sites were localized. Four of them form a first adsorption layer in the large cavity, one forms a second adsorption layer in the large cavity and one fills the small cavity. The main adsorption positions for the N_2O molecule are the open metal sites, which are located in the small cavity (Fig. 6I, I). The second adsorption site is located in the center of three faces of the Cu^IN_3 unit and close to centers of three triazolate rings coordinating metal ions in the SBU (Fig. 6, II, large cavity). The adsorption site III is located near the center of the 1,4-dioxane ring of the organic linker (Fig. 6, III, large cavity). The N_2O molecule is strongly disordered when placed close to this position, and it was refined as occupying a single position, due to the difficulties in the correct description of disorder. The fourth position of the N_2O

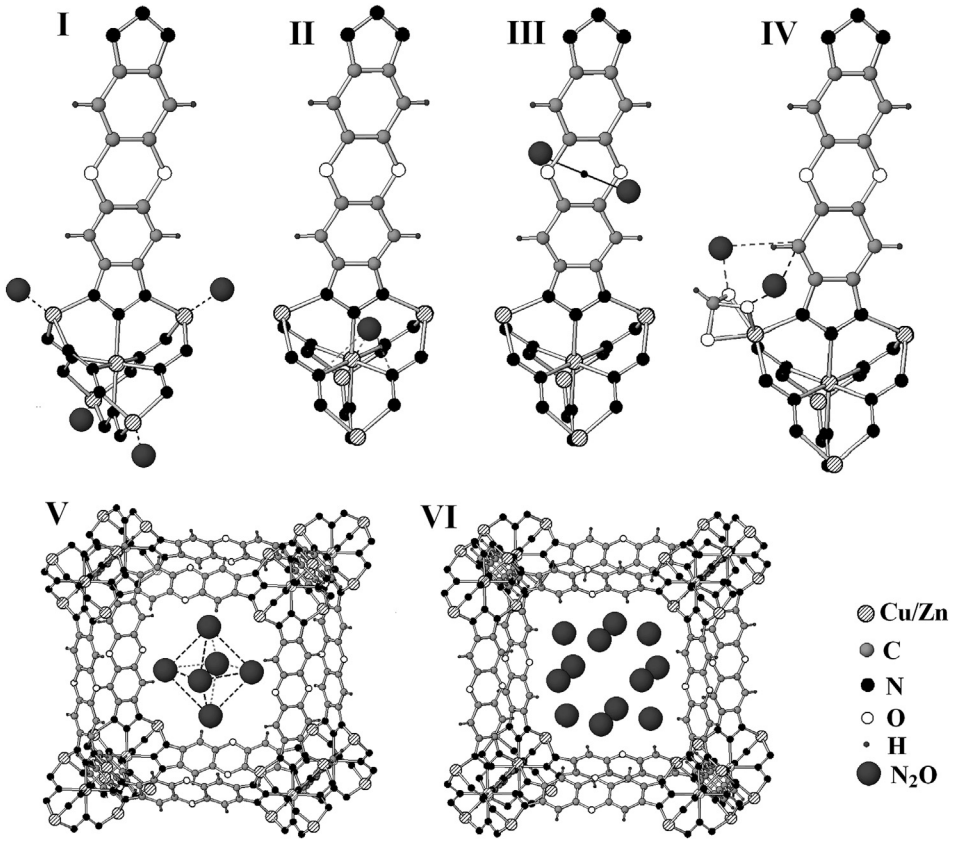

Fig. 6. Six symmetry-independent adsorption sites occupied by N_2O molecule (shown by large spheres) in the pores of Cu^I-MFU-4*l*. These include two sites (I and II) associated with secondary building unit, three sites (III, IV, and V) associated with the organic linker, and one site (VI) forming second adsorption layer within the large pores.

molecule is located near the formate ligand coordinating statistically disordered Zn ions as well as nitrogen and carbon atoms of the triazole- and benzole-rings of the organic linker, respectively (Fig. 6, IV, large cavity). In the fifth position the N_2O molecule is close to the oxygen atoms of the 1,4-dioxane ring of the organic linker (Fig. 6, V, small cavity). A further increase of pressure leads to the formation of the disordered second adsorption layer in the large cavity (Fig. 6, VI). All located positions of N_2O molecule in large and small cavities of Cu^I-MFU-4*l* are consistent with the previously found positions for noble gas atoms Xe and Ke in Cu^I-MFU-4*l* [52]. However, the order of their filling is different. No preferential filling of the large cavity in comparison to the small cavity was found for N_2O molecules, and the strongest adsorption site is located near coordinatively unsaturated Cu^I sites.

4. Conclusion

We have studied the interaction strength of N_2O and CO_2 molecules with different Lewis-acidic sites within the MFU-4*l* metal-organic framework *via* gas sorption measurements and density-functional theory calculations. Zn^{II}–Cl units appeared to possess only very weak Lewis acidity, such that only physisorption of both gases has been observed. Li^I centers, in contrast, show considerable Lewis acidity and similar binding strength toward N_2O and CO_2 molecules in the gas phase (22.7 and 23.6 kJ mol^{-1} at 0.35 mmol g^{-1} loading, respectively). Cu^I-MFU-4*l* shows quite strong binding of N_2O, whereas CO_2 doesn't bind to Cu^I centers. Preferential binding of N_2O to Cu^I centers was also confirmed by *in situ* synchrotron X-ray powder diffraction measurements. Thus, Cu^I-MFU-4*l* can be considered as a potential candidate for selective N_2O adsorption.

Acknowledgments

We gratefully acknowledge funding by the priority program 1362 “Porous Metal-Organic Frameworks (MOFs)” of the Deutsche Forschungsgemeinschaft (DFG). Support with synchrotron measurements at ESRF, ID22 (proposal ch4161) to Dr. C. Drathen (ESRF, Grenoble, France), Mr. F. Adams (Max Planck Institute for Solid State Research, Stuttgart, Germany), and with synchrotron measurements at Diamond, I12 (cm4963) to Dr. M. Drakopoulos (Diamond Light Source, UK) is gratefully acknowledged.

Appendix A. Supplementary data

Supplementary data related to this article can be found at http://dx.doi.org/10.1016/j.micromeso.2015.03.014.

References

[1] H. Furukawa, K.E. Cordova, M. O'Keeffe, O.M. Yaghi, Science 341 (2013) 1230444.
[2] K. Sumida, D.L. Rogow, J.A. Mason, T.M. McDonald, E.D. Bloch, Z.R. Herm, T.-H. Bae, J.R. Long, Chem. Rev. 112 (2012) 724–781.
[3] E. Barea, C. Montoro, J.A.R. Navarro, Chem. Soc. Rev. 43 (2014) 5419–5430.
[4] J.-R. Li, J. Sculley, H.-C. Zhou, Chem. Rev. 112 (2012) 869–932.
[5] M.P. Suh, H.J. Park, T.K. Prasad, D.-W. Lim, Chem. Rev. 112 (2012) 782–835.
[6] Y. Peng, V. Krungleviciute, I. Eryazici, J.T. Hupp, O.K. Farha, T. Yildirim, J. Am. Chem. Soc. 135 (2013) 11887–11894.
[7] D. Saha, Z. Bao, F. Jia, S. Deng, Environ. Sci. Technol. 44 (2010) 1820–1826.
[8] D.O. Shiels, J. Phys. Chem. 33 (1929) 1386–1397.
[9] H. Marsh, T.E. O'Hair, Fuel 45 (1966) 301–309.
[10] Y. Peng, F. Zhang, C. Xu, Q. Xiao, Y. Zhong, W. Zhu, J. Chem. Eng. Data 54 (2009) 3079–3081.
[11] V. Rakić, V. Dondur, S. Gajinov, A. Auroux, Thermochim. Acta 420 (2004) 51–57.
[12] V. Rakić, V. Rac, V. Dondur, A. Auroux, Catal. Today 110 (2005) 272–280.
[13] B.R. Wood, J.A. Reimer, A.T. Bell, J. Catal. 209 (2002) 151–158.
[14] Y. Wang, Z. Lei, B. Chen, Q. Guo, N. Liu, Appl. Surf. Sci. 256 (2010) 4042–4047.
[15] G. Domínguez, R. Hernández-Huesca, G. Aguilar-Armenta, J. Mex. Chem. Soc. 54 (2010) 111–116.
[16] O. Hinrichsen, T. Genger, M. Muhler, Chem. Eng. Technol. 23 (2000) 956–959.
[17] A.V. Zeigarnik, Kinet. Catal. 44 (2003) 233–246.
[18] D.A. Lashof, D.R. Ahuja, Nature 344 (1990) 529–531.
[19] A.R. Ravishankara, J.S. Daniel, R.W. Portmann, Science 326 (2009) 123–125.
[20] V.I. Sobolev, L.V. Pirutko, in: J.C. Taylor (Ed.), Advances in Chemistry Research, vol. 19, Nova Science Publishers, New York, 2013, pp. 1–24.
[21] G. Centi, S. Perathoner, F. Vazzana, CHEMTECH 29 (1999) 48–55.
[22] M.W. Ackley, S.U. Rege, H. Saxena, Micropor. Mesopor. Mat. 61 (2003) 25–42.
[23] G. Centi, P. Generali, L. dall'Olio, S. Perathoner, Ind. Eng. Chem. Res. 39 (2000) 131–137.
[24] D. Denysenko, M. Grzywa, M. Tonigold, B. Streppel, I. Krkljus, M. Hirscher, E. Mugnaioli, U. Kolb, J. Hanss, D. Volkmer, Chem. Eur. J. 17 (2011) 1837–1848.
[25] S. Biswas, M. Grzywa, H.P. Nayek, S. Dehnen, I. Senkovska, S. Kaskel, D. Volkmer, Dalton Trans. (2009) 6487–6495.
[26] J. Teufel, H. Oh, M. Hirscher, M. Wahiduzzaman, L. Zhechkov, A. Kuc, T. Heine, D. Denysenko, D. Volkmer, Adv. Mater. 4 (2013) 635–639.
[27] G. Sastre, J. van den Bergh, F. Kapteijn, D. Denysenko, D. Volkmer, Dalton Trans. 43 (2014) 9612–9619.
[28] A. Soleimani Dorcheh, D. Denysenko, D. Volkmer, W. Donner, M. Hirscher, Micropor. Mesopor. Mat. 162 (2012) 64–68.
[29] A. Soleimani-Dorcheh, R.E. Dinnebier, A. Kuc, O. Magdysyuk, F. Adams, D. Denysenko, T. Heine, D. Volkmer, W. Donner, M. Hirscher, Phys. Chem. Chem. Phys. 14 (2012) 12892–12897.
[30] S. Biswas, M. Tonigold, D. Volkmer, Z. Anorg. Allg. Chem. 634 (2008) 2532–2538.
[31] S. Biswas, M. Tonigold, M. Speldrich, P. Kögerler, M. Weil, D. Volkmer, Inorg. Chem. 49 (2010) 7424–7434.
[32] Y.-Y. Liu, M. Grzywa, M. Tonigold, G. Sastre, T. Schüttrigkeit, N.S. Leeson, D. Volkmer, Dalton Trans. 40 (2011) 5926–5938.
[33] S. Trofimenko, Chem. Rev. 93 (1993) 943–980.
[34] D. Denysenko, T. Werner, M. Grzywa, A. Puls, V. Hagen, G. Eickerling, J. Jelic, K. Reuter, D. Volkmer, Chem. Commun. 48 (2012) 1236–1238.
[35] D. Denysenko, M. Grzywa, J. Jelic, K. Reuter, D. Volkmer, Angew. Chem. 126 (2014) 5942–5946;
Angew. Chem. Int. Ed. 53 (2014) 5832–5836.
[36] D. Denysenko, J. Jelic, K. Reuter, D. Volkmer, Postsynthetic Metal and Ligand Exchange in MFU-4*l*: a Screening Approach toward Functional Metal-Organic Frameworks Comprising Single-Site Active Centers, Chem. Eur. J. (2015) [accepted].
[37] C. Lamberti, S. Bordiga, M. Salvalaggio, G. Spoto, A. Zecchina, F. Geobaldo, G. Vlaic, M. Bellatreccia, J. Phys. Chem. B 101 (1991) 344–360.
[38] V. Blum, R. Gehrke, F. Hanke, P. Havu, V. Havu, X. Ren, K. Reuter, M. Scheffler, Comp. Phys. Commun. 180 (2009) 2175–2196.
[39] X. Ren, P. Rinke, V. Blum, J. Wieferink, A. Tkatchenko, A. Sanfilippo, K. Reuter, M. Scheffler, New. J. Phys. 14 (2012) 053020.
[40] J.P. Perdew, K. Burke, M. Ernzerhof, Phys. Rev. Lett. 77 (1996) 3865–3868.
[41] A.D. Becke, J. Chem. Phys. 98 (1993) 5648–5652.
[42] P.J. Stephens, J.F. Devlin, C.F. Chabalowski, M.J. Frisch, J. Chem. Phys. 98 (1993) 11623–11627.
[43] A. Tkatchenko, M. Scheffler, Phys. Rev. Lett. 102 (2009) 073005.
[44] Y. Motoyama, H. Nishiyama, in: H. Yamamoto (Ed.), Lewis Acids in Organic Synthesis, vol. 1, WILEY-VCH, Weinheim, 2000, pp. 59–88.
[45] U. Olsher, Chem. Rev. 91 (1991) 137–164.
[46] R.G. Pearson, J. Am. Chem. Soc. 85 (1963) 3533–3539.
[47] R.G. Pearson, Inorg. Chem. 27 (1988) 734–740.
[48] W.B. Tolman, Angew. Chem. 122 (2010) 1034–1041;
Angew. Chem. Int. Ed. 49 (2010) 1018–1024.
[49] J.N. Armor, H. Taube, J. Am. Chem. Soc. 91 (1969) 6874–6876.
[50] C.B. Pamplin, E.S.F. Ma, N. Safari, S.J. Rettig, B.R. James, J. Am. Chem. Soc. 123 (2001) 8596–8597.
[51] N.A. Piro, M.F. Lichterman, W.H. Harman, C.J. Chang, J. Am. Chem. Soc. 133 (2011) 2108–2111.
[52] O.V. Magdysyuk, D. Denysenko, I. Weinrauch, D. Volkmer, M. Hirscher, R.E. Dinnebier, Chem. Commun. 51 (2015) 714–717.

Elucidating Lewis Acidity of Metal Sites in MFU-4*l* Metal-Organic Frameworks: N_2O and CO_2 Adsorption in MFU-4*l*, Cu^{I}-MFU-4*l* and Li-MFU-4*l*

Dmytro Denysenko,[a] Jelena Jelic,[b] Oxana V. Magdysyuk,[c] Karsten Reuter,[b] and Dirk Volkmer*[a]

Supplementary Data

Table of Contents

TGA measurements

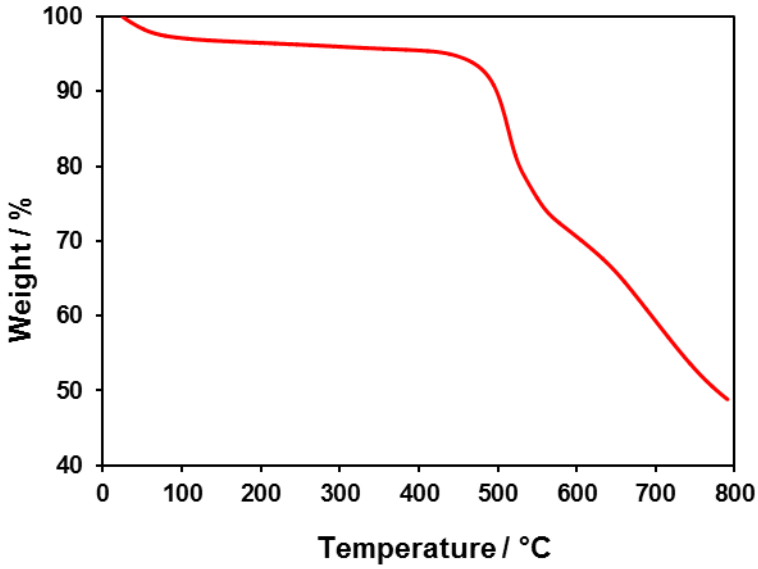

Fig. S1. TGA curve for Li-MFU-4*l* under N_2 flow.

FT-IR Spectra

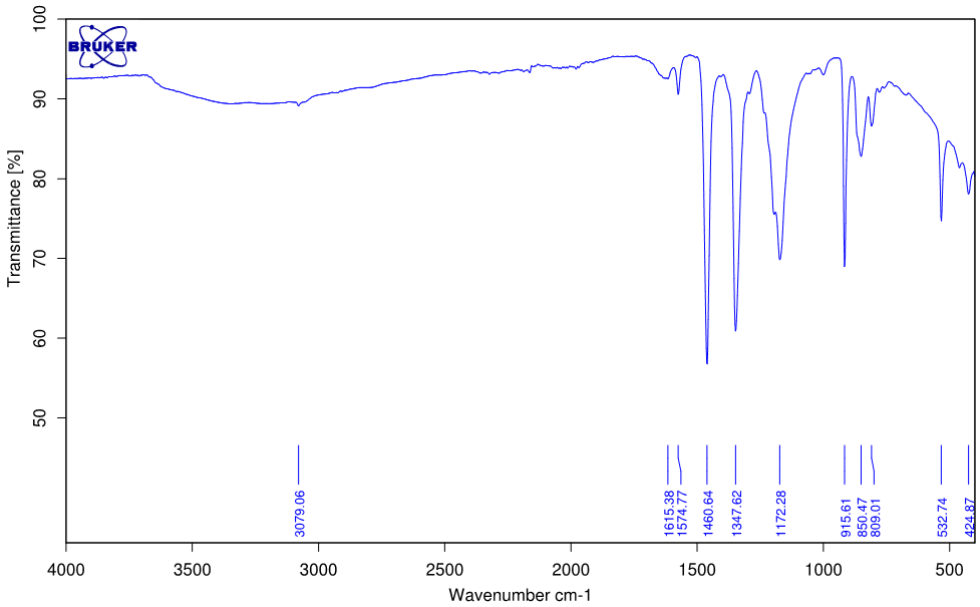

Fig. S2. FT-IR spectrum of Li-MFU-4*l*.

Gas sorption measurements

The isosteric heats of adsorption were calculated from the measured isotherms (Figs. S4-6) using the Clausius-Clapeyron equation (**I**). The slopes of linear plots lnP versus 1/RT for different loadings (Figs. S7-11) give the adsorption enthalpies, according to the equation (**II**).

$$Q_{st} = -R\left(\frac{\partial(\ln P)}{\partial(1/T)}\right)_{\theta}$$ (**I**), θ – surface coverage

$$\ln P = -\frac{Q_{st}}{R}\left(\frac{1}{T}\right) + C$$ (**II**), C – integration constant

The isosteric heats of adsorption at zero limit surface coverage (initial heat of adsorption) have been determined using Henry's constants K_H, obtained as a slope from the linear ranges of isotherms at low pressure (Tables S1-2 and Figs. S12-13). In this range the dependence of amount adsorbed (n) on the pressure can be expressed with Henry's law (**III**). The initial isosteric heat of adsorption can be obtained in a similar way by using the Clausius-Clapeyron equation (**IV**) (Fig. S14).

$n = K_H \bullet P$ (**III**)

$$\lim_{n\to 0}(Q_{st}) = Q_{st}^{0} = R\left(\frac{\partial(\ln K_H)}{\partial(1/T)}\right)$$ (**IV**)

Table S1. Henry's constants for N_2O adsorption on MFU-4*l*, $cm^3\ g^{-1}\ kPa^{-1}$

T / K	243	253	263	273
K_H	1.5551	1.0565	0.7563	0.5583

Table S2. Henry's constants for N_2O adsorption on Cu^{I}-MFU-4*l*, $cm^3\ g^{-1}\ kPa^{-1}$

T / K	263	273	283	293
K_H	4.6759	2.5883	1.5714	1.0033

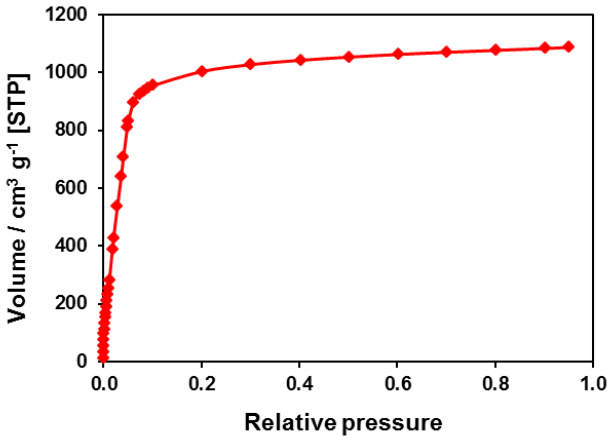

Fig. S3. Argon adsorption isotherm at 87.3 K for Li-MFU-4*l*.

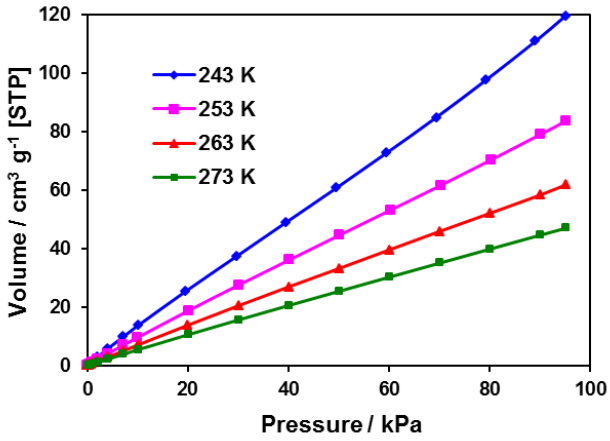

Fig. S4. N_2O adsorption isotherms for MFU-4*l* at different temperatures for the determination of the isosteric heat of adsorption.

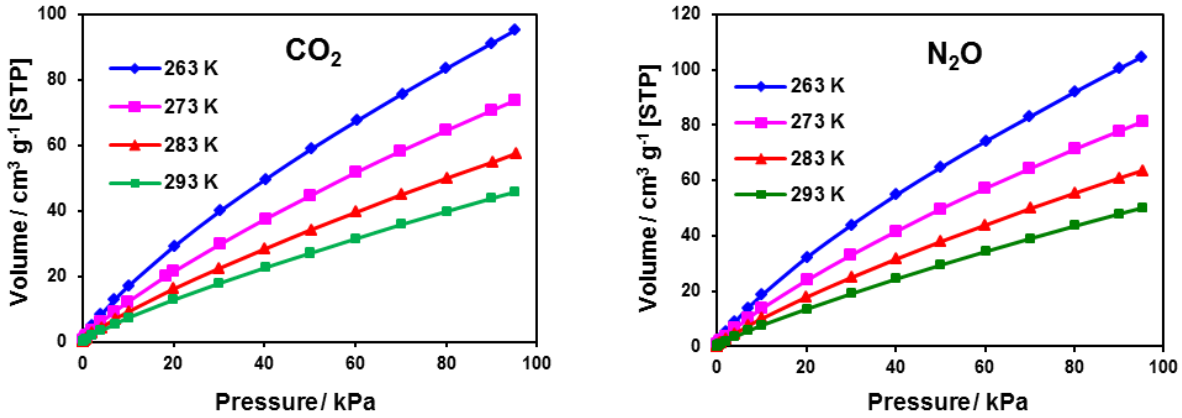

Fig. S5. CO_2 and N_2O adsorption isotherms for Li-MFU-4*l* at different temperatures for the determination of the isosteric heats of adsorption.

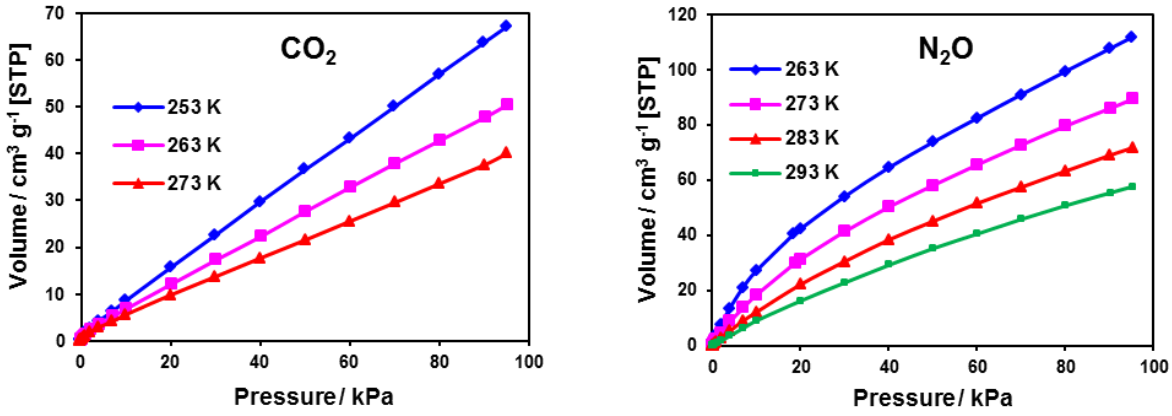

Fig. S6. CO_2 and N_2O adsorption isotherms for Cu^{I}-MFU-4*l* at different temperatures for the determination of the isosteric heats of adsorption.

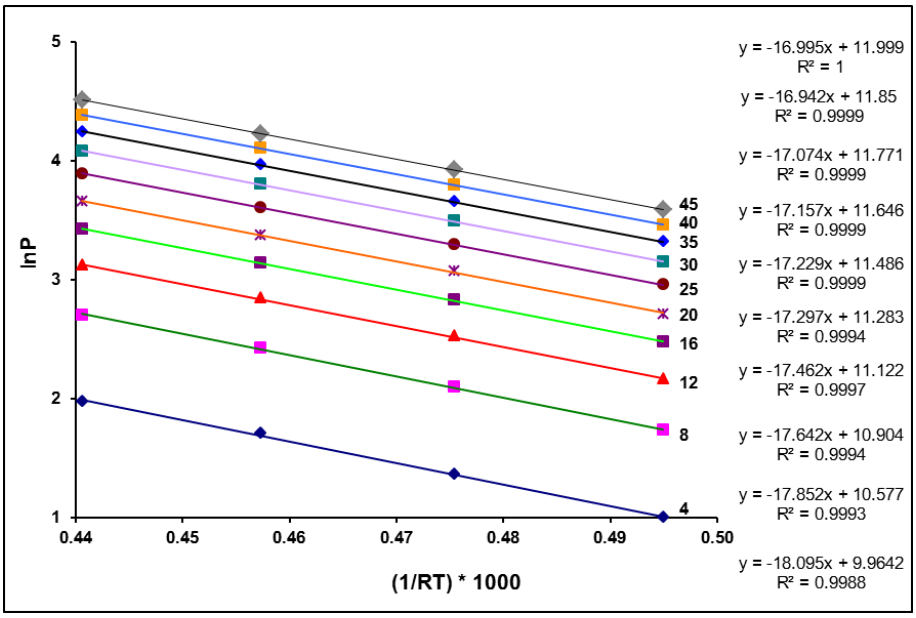

Fig. S7. lnP versus 1/RT plots for different loadings for N_2O adsorption on MFU-4*l*. The numbers near the lines correspond to the loading in $cm^3\ g^{-1}$.

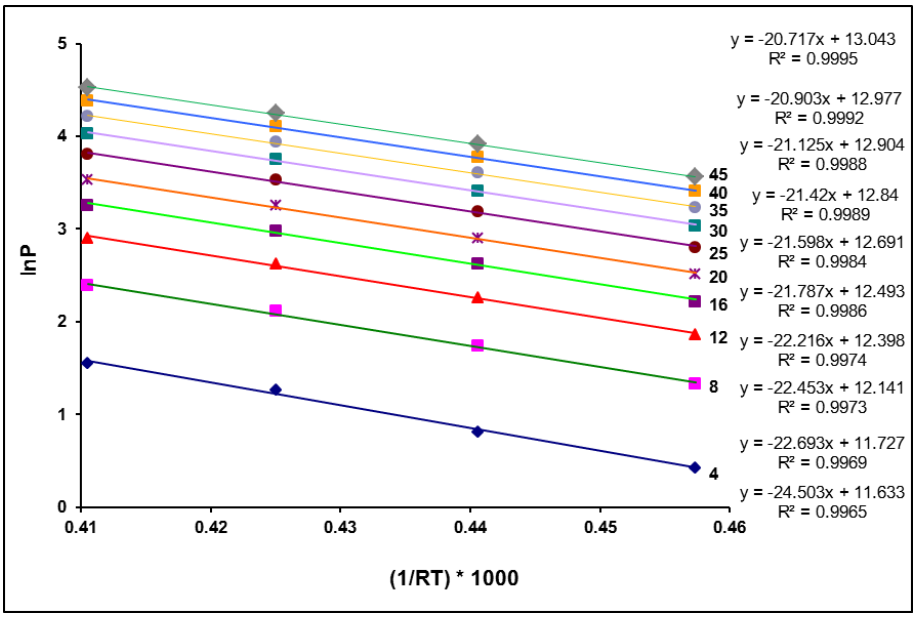

Fig. S8. lnP versus 1/RT plots for different loadings for CO_2 adsorption on Li-MFU-4*l*. The numbers near the lines correspond to the loading in $cm^3\ g^{-1}$.

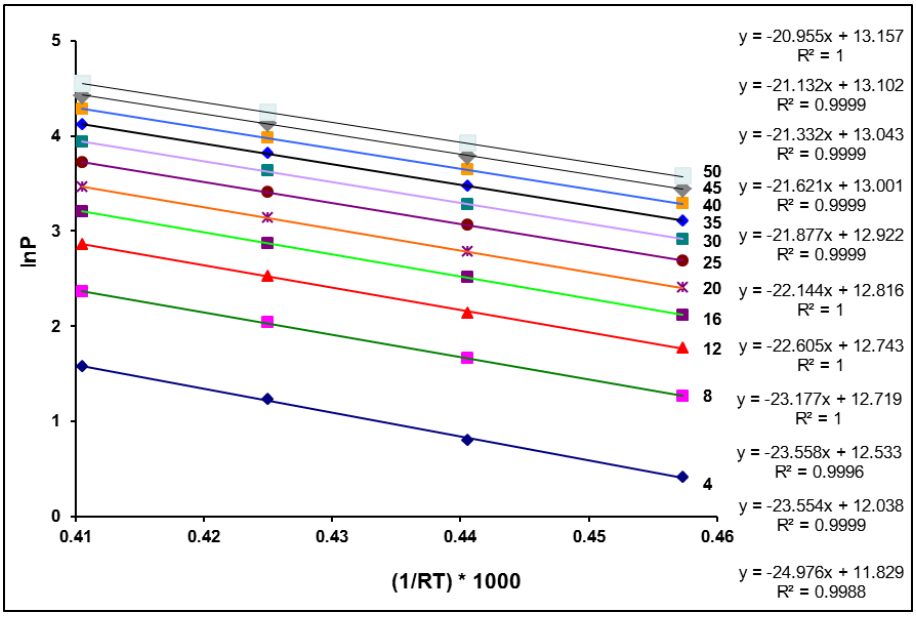

Fig. S9. lnP versus 1/RT plots for different loadings for N_2O adsorption on Li-MFU-4*l*. The numbers near the lines correspond to the loading in $cm^3\ g^{-1}$.

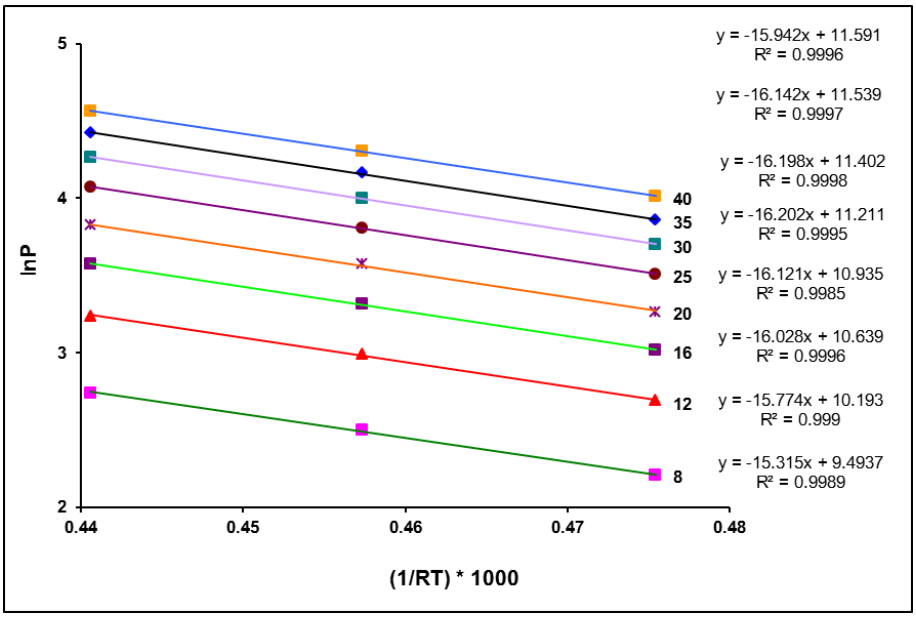

Fig. S10. lnP versus 1/RT plots for different loadings for CO_2 adsorption on Cu^{I}-MFU-4*l*. The numbers near the lines correspond to the loading in $cm^3\ g^{-1}$.

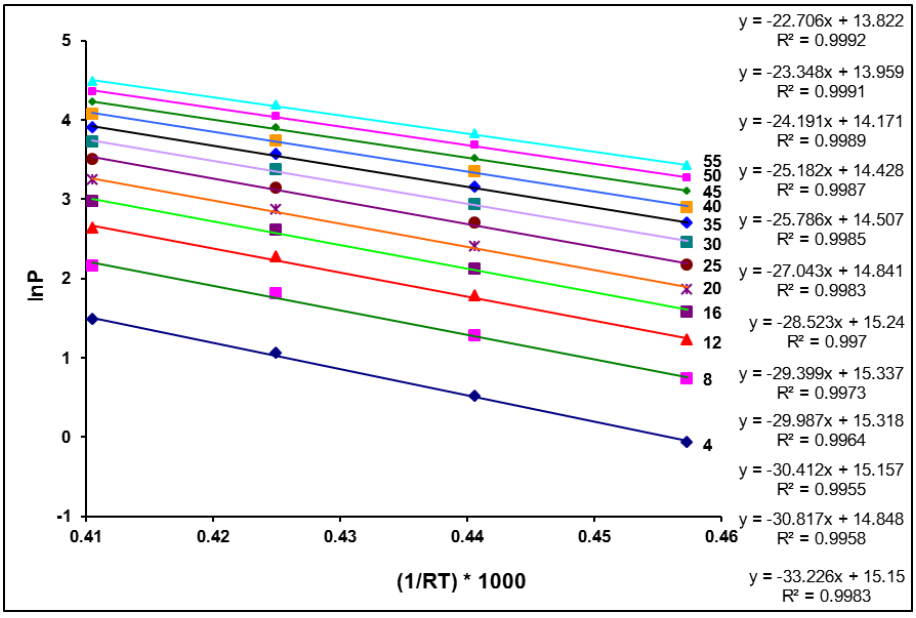

Fig. S11. lnP versus 1/RT plots for different loadings for N_2O adsorption on Cu^{I}-MFU-4*l*. The numbers near the lines correspond to the loading in $cm^3\ g^{-1}$.

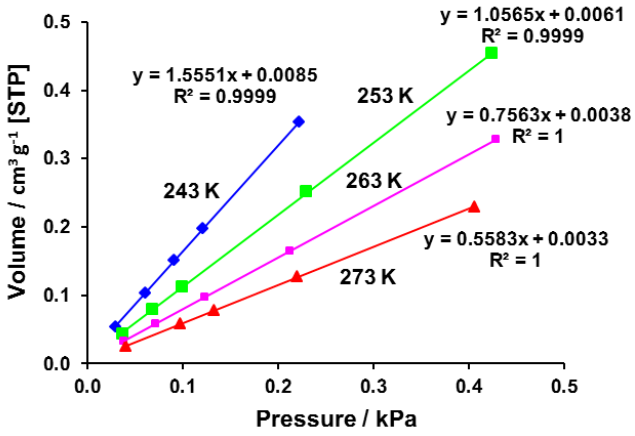

Fig. S12. Determination of Henry's constants for N_2O adsorption on MFU-4*l*.

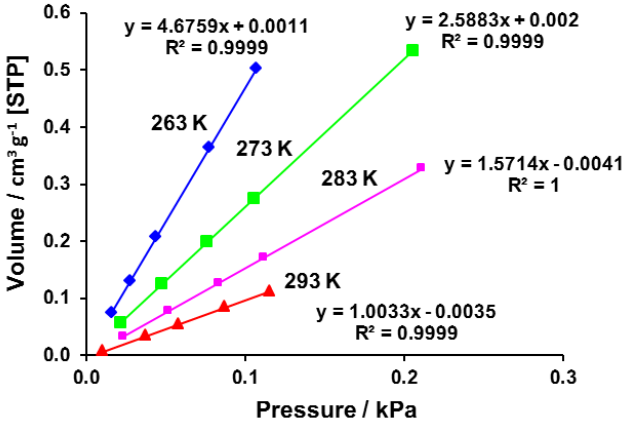

Fig. S13. Determination of Henry's constants for N_2O adsorption on Cu^{I}-MFU-4*l*.

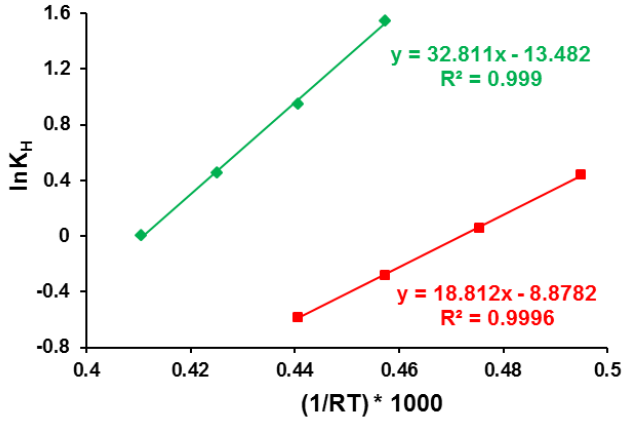

Fig. S14. $\ln K_H$ versus 1/RT plots for N_2O adsorption on MFU-4*l* (red) and Cu^{I}-MFU-4*l* (green).

Powder X-ray diffraction measurements

Crystalline samples of Li-MFU-4*l* and Cu^{II}-MFU-4*l*-formate were ground using an agate mortar and pestle, and filled into the quartz capillary of 1 mm diameter, then evacuated at 180 °C for 1 h and finally cooled down to 250 K (Li-MFU-4*l*) or 253, 288 and 183 K (Cu^{I}-MFU-4*l*). Diffraction data for Li-MFU-4*l* were collected in vacuum in the 2θ range of 0.5–15° with 0.005° steps, λ = 0.4 Å, at the high-resolution powder diffractometer ID22 [1] at ESRF (Grenoble, France). Diffraction data for N_2O adsorption in Cu^{I}-MFU-4*l* were collected in the 2θ range of 0.5–10°, λ = 0.2224 Å, at the powder diffractometer I12 at Diamond (United Kingdom). For the Rietveld refinement [2] of Li-MFU-4*l*, the crystal structure of MFU-4*l* was used as a starting crystal model. The Rietveld refinement was carried out using the Topas 4.2 program [3]. Powder diffraction pattern was characterized by strong anisotropic peak asymmetry, which was corrected by spherical harmonics, and strong anisotropic peak broadening, which was described by phenomenological model of Stephens [4]. Weak geometric restrains on bond distances were used during the refinement process. The experimental details and crystal data are listed in Tables S3-4. The final Rietveld refinement plot is presented in Fig. S15. Simulated annealing and Rietveld refinement of Cu^{I}-MFU-4*l* were applied to X-ray powder diffraction data for localization of positions of intercalated N_2O molecules. The program Topas 4.2 was used for powder data analysis. The crystal data are listed in Table S5.

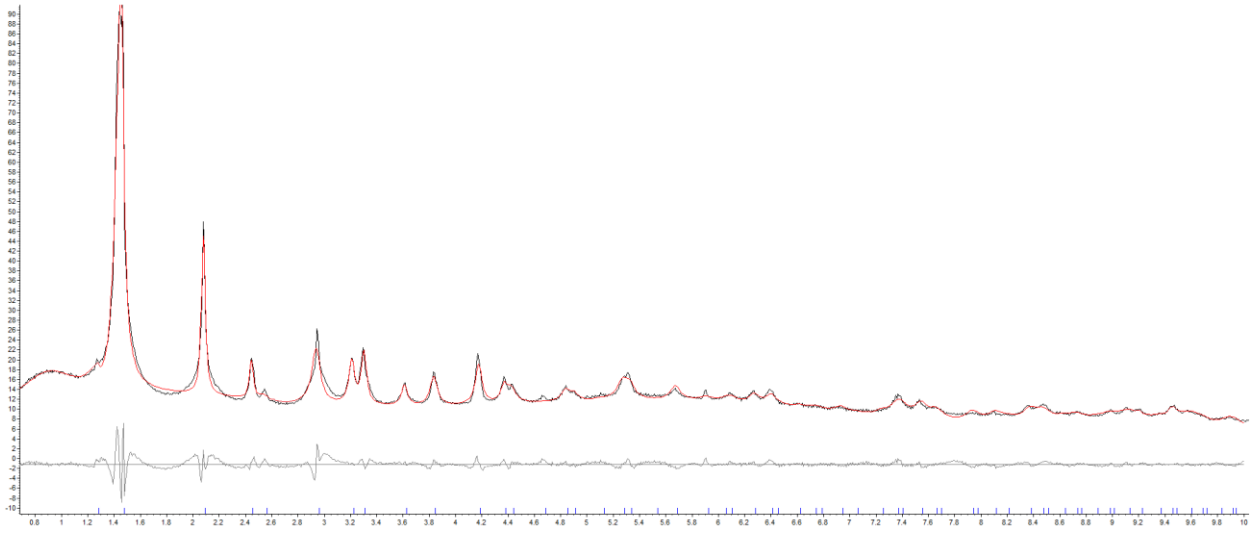

Fig. S15. Rietveld plot of evacuated Li-MFU-4*l* at 250K. Y-axis scale – square root of X-ray counts for better visibility of low-intensity reflections.

Table S3. Experimental details and crystal data for Li-MFU-4*l*.

Compound	Li-MFU-4*l*
Diffractometer	ID22, ESRF
X-ray source/wavelength/ Å	Synchrotron, 0.4
T/K	250(1)
Empirical formula	
Formula	$C_{36}H_{12}Cl_2N_{18}O_6Li_2Zn_3$
Crystal system	cubic
Space group (no)	$Fm\bar{3}m$ (no. 225)
a/Å	31.961(12)
V/Å^3	29681(32)
Z	8
D_c/g cm^{-3}	0.541
2θ Range/°	0.5-10
R_{wp}	10.54
R_p	8.53
R_{Bragg}	1.93

Table S4. Atomic coordinates for Li-MFU-4*l*.

Atom	x	y	z	U_{iso}
N1	0.337(5)	0.275(4)	0.225	0.08(2)
C1	0.383(3)	0.266(4)	0.234	0.01(2)
N2	0.316(6)	0.25	0.25	0.07(2)
C2	0.421(6)	0.283(4)	0.217	0.01(2)
C3	0.461(4)	0.267(4)	0.233	0.07(2)
O1	0.5	0.283(5)	0.217	0.08 (2)
Zn1	0.25	0.25	0.25	0.01(2)
Cl1	0.151(6)	0.151(6)	0.151(6)	0.01(2)
Zn2	0.311(8)	0.311(8)	0.189	0.08(2)
H2	0.4207	0.3037	0.1963	0.04

Table S5. Atomic positions and occupancies of intercalated N_2O molecules (center of mass) in Cu^I-MFU-4*l*. $U_{iso}(N_2O)$=0.127 Å^3.

T / K	P / kPa	N_2O (1) x,y,z,Occ	N_2O (2) x,y,z,Occ	N_2O (3) x,y,z,Occ	N_2O (4) x,y,z,Occ	N_2O (5) x,y,z,Occ	N_2O (6) x,y,z,Occ
Multiplicity		32	32	96	48	24	48
253	20	0.145(4) 0.145(4) 0.145(4) 0.37(5)					
	50	0.146(4) 0.146(4) 0.146(4) 0.38(5)					
	100	0.141(5) 0.141(5) 0.141(5) 0.53(6)	0.337(2) 0.337(2) 0.337(2) 0.30(3)	0.209(3) 0 0.291(3) 0.20(2)			
188	20	0.152(4) 0.152(4) 0.152(4) 0.53(7)	0.330(2) 0.330(2) 0.330(2) 0.32(7)	0.199(2) 0 0.199(2) 0.24(3)	0.119(2) 0.221(3) 0.119(2) 0.31(3)	0 -0.151(2) -0.151(2) 0.20(3)	
	100	0.141(4) 0.141(4) 0.141(4) 0.50(6)	0.331(1) 0.331(1) 0.331(1) 0.37(6)	0.197(2) 0 0.303(2) 0.33(2)	0.118(2) 0.223(4) 0.118(2) 0.35(3)	0 -0.153(3) -0.153(3) 0.21(2)	
183	100	0.144(3) 0.144(3) 0.144(3) 0.50(6)	0.372(2) 0.372(2) 0.372(2) 0.49(6)	0.174(2) 0 0.326(2) 0.63(4)	0.100(2) 0.246(4) 0.100(2) 0.34(4)	0 -0.101(2) -0.101(2) 0.59(6)	0 0 0.391(3) 0.77(7)

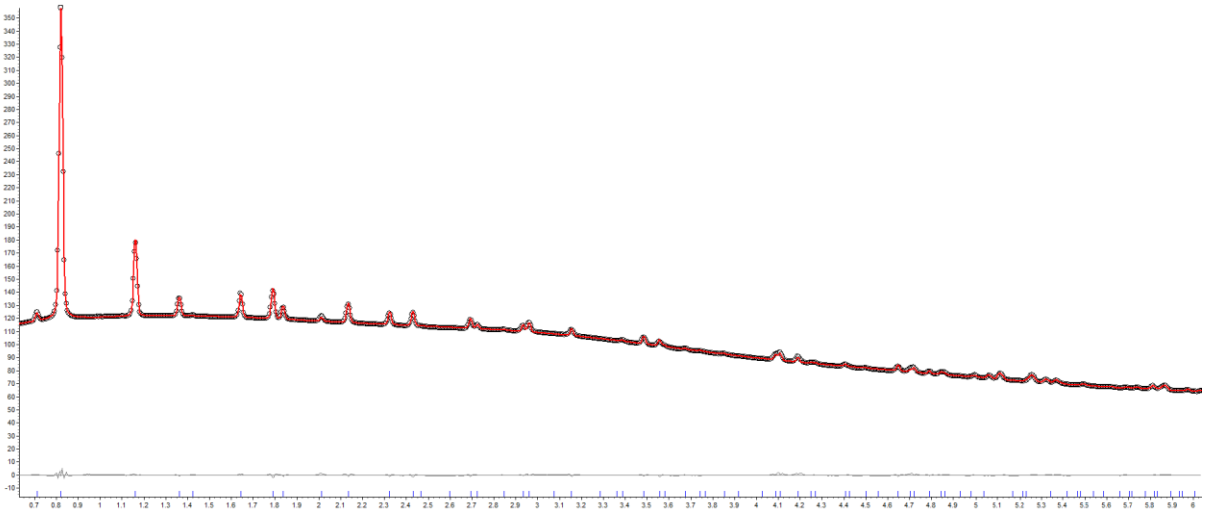

Fig. S16. Rietveld plot of Cu^I-MFU-4*l* with 20 kPa of N_2O, 253 K. Y-axis scale – square root of X-ray counts for better visibility of low-intensity reflections.

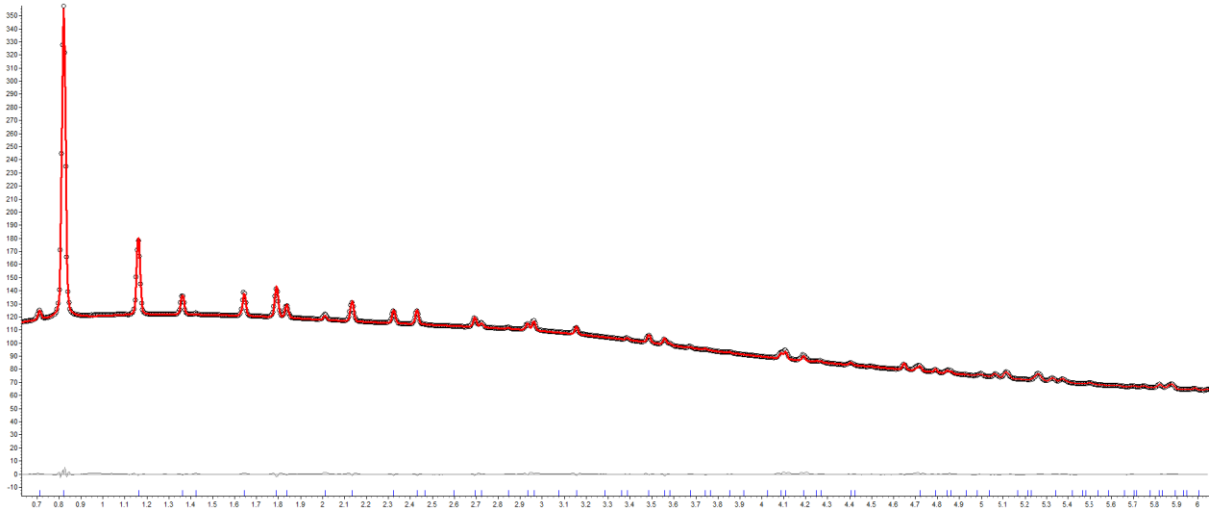

Fig. S17. Rietveld plot of Cu^{I}-MFU-4*l* with 50 kPa of N_2O, 253 K. Y-axis scale – square root of X-ray counts for better visibility of low-intensity reflections.

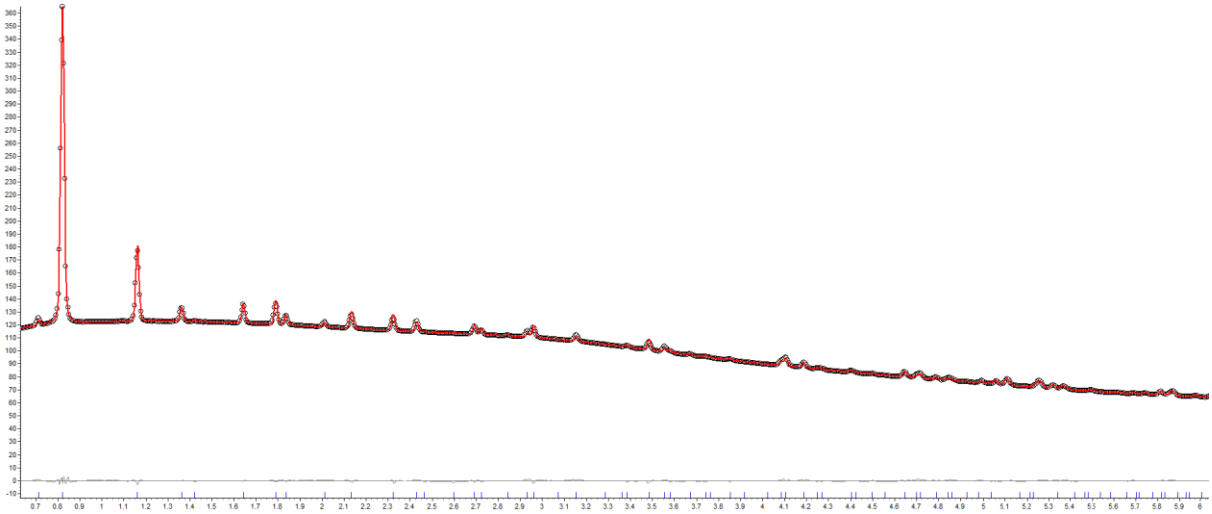

Fig. S18. Rietveld plot of Cu^{I}-MFU-4*l* with 100 kPa of N_2O, 253 K. Y-axis scale – square root of X-ray counts for better visibility of low-intensity reflections.

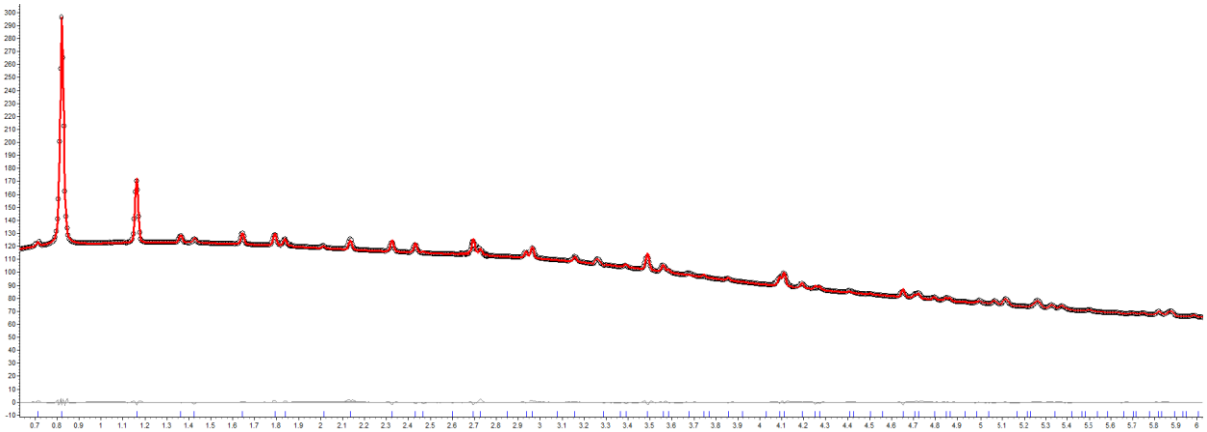

Fig. S19. Rietveld plot of Cu^{I}-MFU-4*l* with 20 kPa of N_2O, 188 K. Y-axis scale – square root of X-ray counts for better visibility of low-intensity reflections.

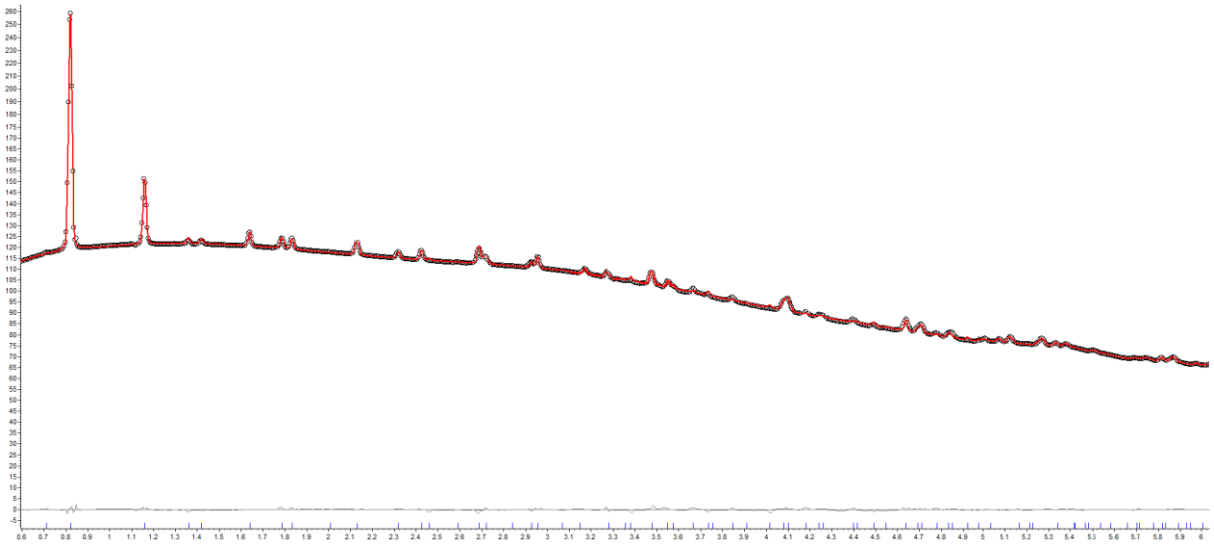

Fig. S20. Rietveld plot of Cu^{I}-MFU-4*l* with 100 kPa of N_2O, 188 K. Y-axis scale – square root of X-ray counts for better visibility of low-intensity reflections.

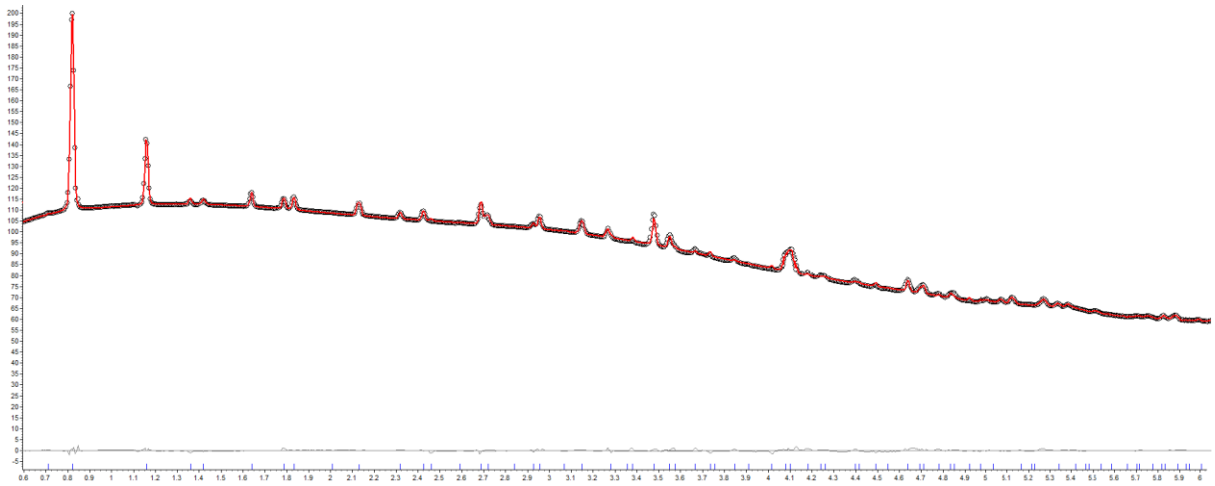

Fig. S21. Rietveld plot of Cu^{I}-MFU-4*l* with 100 kPa of N_2O, 183 K. Y-axis scale – square root of X-ray counts for better visibility of low-intensity reflections.

[1] a) J.-L. Hodeau, P. Bordet, M. Anne, A. Prat, A.N. Fitch, E. Dooryhee, G. Vaughan, A. Freund, Proc. SPIE, **1998**, 3448, 353; b) J.P. Wright, G.B.M. Vaughan, A.N. Fitch, IUCr Computing Commission Newsletter, **2003**, 1, 92.

[2] a) H.M. Rietveld, *Acta Cryst.* **1967**, *22*, 151–152; b) H.M. Rietveld, *J. Appl. Cryst*. **1969**, *2*, 65–71.

[3] A.A. Coelho, 2007. TOPAS. Version 4.1. Coelho Software, Brisbane, Australia.

[4] P.W. Stephens, *J. Appl. Cryst.* **1999**, *32*, 281–289.